CREEP OF CYLINDRICAL SHELLS SUBJECT TO AXISYMMETRIC LOADING

by

T. P. BYRNE

T H E S I S

submitted

to

THE UNIVERSITY OF GLASGOW

for the degree of

Doctor of Philosophy

February, 1967.

NAME	ADDRESS AND AFFILIATION	DA

ACKNOWLEDGMENTS

The author is grateful to the University of Glasgow for the provision of services and equipment necessary for the performance of this research, and wishes to express his thanks for support and assistance to Professor G.D.S. MacLellan and Professor J.D. Robson.

The author is very much indebted to Dr. A.C. Mackenzie for advice, encouragement and many stimulating discussions during the course of this work.

The experimental apparatus was made in the Engineering Workshop of the University, and thanks are due to the staff and Superintendent, Mr. I.D. Cameron.

N O T A T I O N

A	Physical constant.
A_1, A_2, A_3, A_4	Integration constants.
A_o	Initial cross- sectional area of tensile specimen.
a	Radius of shell.
a_1, a_2, a_3, a_4	Integration constants.
B	Physical constant.
B_1, B_2, B_3, B_4	Integration constants.
b	Value of $\bar{x}$; finite difference interval; distance.
C_1, C_2, C_3, C_4	Integration constants.
c	Integer; distance.
c_1, c_2	Coefficients of $\bar{x}$.
D	Differential operator $\frac{\partial}{\partial \bar{t}^*}$.
D_1	Differential operator $\frac{\partial}{\partial \bar{x}}$.
D_1, D_2, D_3, D_4	Integration constants
D_i	Denominator in numerical calculations.
d	Integer.
d_1, d_2	Coefficients of $\bar{x}$.
E	Young's modulus.
$e_x, e_\theta, e_{cx}, e_{c\theta}$	Non-dimensional middle surface strains.
$F_1(D), F_2(D)$	Differential operators.
$f(\beta)$	Function of β.
G	Function of m, e_x, e_θ, k_x.

G_c	Function of $m, e_{cx}, e_{c\theta}, k_{cx}, R$.
$H(\bar{t}^*)$	Heavyside step function.
h, h_c	Shell thicknesses.
$I_1^{\pm}, I_2^{\pm}$	Integration functions.
I_2	Second invariant of strain tensor.
i	$\sqrt{-1}$; integer.
J_2	Second invariant of deviatoric stress tensor.
j	Integer.
k_x, k_{cx}	Non-dimensional curvature change.
k_1	Function of m.
k_2	Function of m, p, n_a.
k_3	Function of m, λ, n_a.
k_{c1}	Function of m, R.
k_{c2}	Function of m, p, n_a, R.
k_i	Vector representing right hand side of finite difference equations.
l	Length of cylindrical shell.
$\bar{l}$	Non-dimensional length of cylindrical shell.
l_o	Effective length of tensile specimen.
M	Moment.
M_x, M_θ	Stress resultants.
m	Stress exponent.
m_1, m_2	Arbitrary functions of $\bar{x}$.
m_x, m_{cx}, m_θ	Non-dimensional stress resultants.

$m_{xo}, m_{\theta o}$	Initial elastic stress resultants.
$m_{x\infty}$	Steady state stress resultant.
m_x^c	Integral of creep strains $\varepsilon_x^c, \varepsilon_\theta^c$.
m_{xi}	Vector representing m_x in finite difference equations.
$N_{i,j}$	Matrix of finite difference coefficients.
N_x, N_θ	Stress resultants.
N_a	Axial stress resultant applied to shell.
n	Integer; distance.
$n_x, n_\theta, n_{cx}, n_{c\theta}$	Non-dimensional stress resultants.
n_a	Non-dimensional applied axial stress resultant.
$n_{xo}, n_{\theta o}$	Initial elastic stress resultants.
$n_{\theta\infty}$	Steady state stress resultant.
n_x^c, n_θ^c	Integrals of creep strains $\epsilon_x^c, \epsilon_\theta^c$.
$n_{xi}, n_{\theta i}$	Vectors representing n_x, n_θ in finite difference equations.
P	Uniform radial loading and internal pressure.
P_o	Initial load on tensile specimen.
P_1	Particular integral.
p	Non-dimensional radial loading and internal pressure.
Q_x	Shear stress resultant.
q	Time exponent; strain rate vector.
q_x, q_{cx}	Non-dimensional shear stress resultants.

R	Thickness ratio $=h_c/h$.
R_i	Residue.
r	Radial co-ordinate; integer.
S_{ij}	Deviatoric stress tensor.
S_1, S_2, S_{1i}, S_{2i}	Integration constants.
s	Proportionality factor.
T, T_i	Time functions.
t	Time.
$\bar{t}$	Non-dimensional time.
$\bar{t}^*$	Time variable $= \frac{\bar{t}^{q+1}}{q+1}$
$t_r, \bar{t}_r^*$	Redistribution times.
t_o	Reference time.
u	Axial displacement.
$\bar{u}, \bar{u}_c$	Non-dimensional axial displacements.
$\bar{u}_o$	Initial elastic axial displacement.
$\bar{u}_i$	Vector representing $\bar{u}$ in finite difference equations.
v	Integer.
W, w	Masses
w	Radial displacement.
$\bar{w}, \bar{w}_c$	Non-dimensional radial displacements.
$\bar{w}_1, \bar{w}_2$	Radial displacement functions.
$\bar{w}_o$	Initial elastic radial displacement.
$\bar{w}_\infty$	Steady state radial displacement.
$\bar{w}_i$	Vector representing $\bar{w}$ in finite difference equations.

$w_{mem}, \bar{w}_{mem}, \bar{w}_{cmem}$	Radial displacements of membrane region of shell.
X, X_i	Functions of $\bar{x}$.
x	Axial co-ordinate.
$\bar{x}$	Non-dimensional form of x.
$\bar{x}_i$	Vector representing $\bar{x}$ in finite difference equations.
z	Distance from middle surface of shell.
$\bar{z}$	Non-dimensional form of z.
α	Angle.
α_1, α_2	Coefficients of $\bar{x}$.
β, β_i	Roots of characteristic equation.
$\gamma_1, \gamma_2, \gamma_{1i}, \gamma_{2i}$	Coefficients of $\bar{t}^*$.
γ_{10}, γ_{20}	Coefficients of $\bar{t}^*$.
δ	Deflection of tensile specimen.
δ_{ij}	Kronecker delta.
$\varepsilon, \varepsilon_x, \varepsilon_\theta$	Strains.
ε_{ij}	Strain tensor.
ε^e_{ij}	Elastic strain tensor.
ε^c_{ij}	Creep strain tensor.
$\bar{\varepsilon}_x, \bar{\varepsilon}_\theta$	Non-dimensional strains.
$\varepsilon_{mx}, \varepsilon_{m\theta}$	Middle surface strains.
$\bar{\varepsilon}^c_x, \bar{\varepsilon}^c_\theta$	Non-dimensional creep strains.
ε_o	Reference strain.
$\dot{\varepsilon}_o$	Reference strain rate.
$\frac{\partial \varepsilon^*}{\partial t}$	Effective strain rate.

$\bar{\dot{\varepsilon}}^*$	Non-dimensional effective strain rate.
ε^*	Effective strain = $\int \frac{\partial \varepsilon^*}{\partial t}\, dt$.
$\bar{\varepsilon}^*$	Non-dimensional effective strain.
ε^*_{mem}	Effective strain in membrane region of shell.
$\bar{\varepsilon}^*_{max}$	Greatest effective strain in shell.
$\bar{\varepsilon}^*_d$	Greatest effective strain at shell discontinuity.
θ	Angular co-ordinate.
$\varkappa_x, \varkappa_\theta$	Middle surface curvature changes.
λ	Positive parameter; finite deformation parameter.
ν	Poisson's ratio.
ς	Small quantity.
σ_{ij}	Stress tensor.
σ_x, σ_θ	Stresses.
$\bar{\sigma}_x, \bar{\sigma}_\theta$	Non-dimensional stresses.
σ^*	Effective stress.
$\bar{\sigma}^*$	Non-dimensional effective stress.
σ^*_{mem}	Effective stress in membrane region of shell.
$\bar{\sigma}^*_{max}$	Greatest effective stress in shell.
$\bar{\sigma}^*_d$	Greatest effective stress at shell discontinuity.
σ_o	Reference stress.
ϕ	Function of $\bar{u}, \bar{w}, m$; angle.
ϕ_c	Function of $\bar{u}_c, \bar{w}_c, m, R$.

ϕ_i	Vector representing ϕ in finite difference equations.
ψ	Energy dissipation rate per unit surface area.

C O N T E N T S

CHAPTER 1

INTRODUCTION

At the elevated temperatures at which an increasing number of structures are now required to operate their materials exhibit significant creep. In consequence, an understanding of the effect of creep on the stresses and strains occurring within these structures is important, if their safe, economic design is to be achieved.

The creep deformation of most materials is affected not only by the prevailing temperature and stress system, but also by strain and thermal history. The influence of these factors on deformation is extremely complex, and it has not proved possible to represent adequately material behaviour under arbitrary variations of stress and temperature. However, some important structures, e.g. pressure vessels, are subject to almost constant loading and temperature during their working lives. Under these conditions creep behaviour can be fairly well described, and it is to problems of this type that the present work is directed.

Fig. 1.1 shows the strain-time dependence typical of many structural materials subject to constant tensile stress at a fixed temperature. In the absence of any initial plastic deformation the strain path can be con-

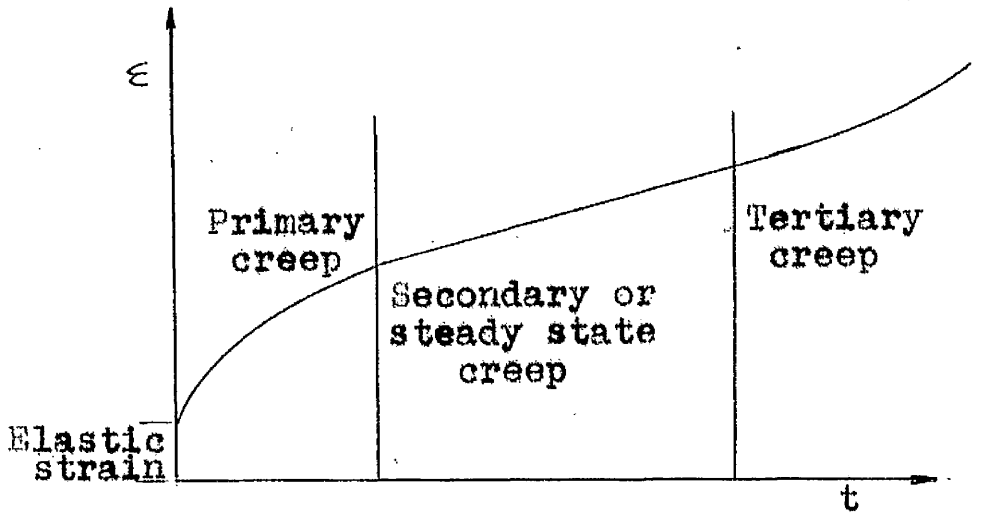

Fig. 1.1

veniently divided into four sections:

a) An initial elastic response governed by Hooke's law.

b) A primary creep region of decreasing strain rate.

c) A secondary or "steady state" region of minimum creep rate.

d) A tertiary region of increasing strain rate preceding fracture.

Many relationships have been proposed to describe creep behaviour during tensile and other more complex constant stress tests (see, for example, references [1] and [2]). However, the most comprehensive experimental work in this field has been carried out by Johnson and his co-workers. They have shown [3] that at practical stress levels the strain rate of a wide range of materials is well represented during primary creep by the equation

$$\frac{\partial \varepsilon}{\partial t}_{ij} = A J_2^m s_{ij} t^q \qquad (1.1)$$

The corresponding equation for steady state creep is

$$\frac{\partial \varepsilon}{\partial t}_{ij} = B J_2^m S_{ij} \qquad (1.2)$$

the transition from primary to steady state creep being at time

$$t = \left(\frac{B}{A}\right)^{1/q}$$

(Representation of tertiary creep is less important for stress analysis since the design life of a structure is unlikely to extend into this region.) In the above equations the stress deviator

$$S_{ij} = \sigma_{ij} - \frac{1}{3}\sigma_{kk}\delta_{ij}$$

where δ_{ij} is the Kronecker delta, and the second invariant of the deviatoric stress tensor

$$J_2 = \frac{1}{2} S_{ij} S_{ij}$$

Materials described by equations (1.1) and (1.2) are isotropic and deform during creep without change of volume.

If the stress system is varied continuously during creep the pattern of Fig.1.1 is obscured. Several 'mechanical theories of creep' have been proposed to describe material behaviour under varying stress conditions. The most common are the time hardening law, corresponding to equation (1.1), and the strain hardening law, viz.

$$\frac{\partial \varepsilon}{\partial t}_{ij} = \left[A(q+1)^q I_2^{q/2} J_2^{(m-q/2)}\right]^{1/(q+1)} S_{ij} \qquad (1.3)$$

where $I_2 = \frac{1}{2}\varepsilon_{ij}\varepsilon_{ij}$ is the second strain invariant.

Under conditions of constant stress equation (1.3) reduces to (1.1). In extensive tests involving periodic increases of load, Johnson et al[4] have shown that neither of these laws adequately predicts material behaviour. The investigations of Marriott and Leckie[5], however, encourage the use of equations (1.1) and (1.3) in the analysis of structures subject to constant loading, where the only stress changes are those required to make the stress distribution, initially elastic, consistent with the equations of creep. These writers analysed a number of simple structures under constant loading using the time hardening and strain hardening equations, and obtained results with both laws which were remarkably similar. This similarity, they suggest, is produced by the existence in the structures of regions where the stress remains almost constant during stress redistribution. If this hypothesis is correct it would be reasonable to expect that the actual strain and stress distributions would not differ greatly from those predicted by the two hardening laws.

Of the two constitutive equations the time hardening law (1.1) is the simpler, and it has been widely used in structural analysis[3],[6],[7]. During stress redistribution the total strain rate is assumed to have separate elastic and creep components:

$$\frac{\partial \varepsilon_{ij}}{\partial t} = \frac{\partial \varepsilon^e_{ij}}{\partial t} + \frac{\partial \varepsilon^c_{ij}}{\partial t} \qquad (1.4)$$

The elastic strain $$\varepsilon^e_{ij} = \left(\frac{1+\nu}{E}\right)\sigma_{ij} - \frac{\nu}{E}\sigma_{kk}\delta_{ij} \qquad (1.5)$$

and the creep strain rate

$$\frac{\partial \varepsilon^c_{ij}}{\partial t} = A J_2^m S_{ij} t^q \qquad (1.6)$$

On loading the structure responds elastically governed by (1.5), and then creeps in accordance with equations (1.4)-(1.6). The stresses tend asymptotically to steady state values determined by the creep equation (1.6), as has been formally proved by Leckie and Martin [8]. In a structure with no non-zero displacement boundary conditions and a stress system of at least two dimensions, two factors determine the amount of stress redistribution: the elastic Poisson's ratio ν, and the creep stress exponent m. The value of m controls the final, steady state stress distribution, while the initial, elastic distribution is governed by ν. As mentioned previously, the form of the creep equation (1.6) implies that creep deformation occurs without increase of volume i.e. the equivalent of Poisson's ratio equals a half. Consequently, when the elastic ratio $\nu \neq \frac{1}{2}$ stress redistribution takes place even when m=0, because of the change in time of the effective Poisson's ratio. This statement is, of course, not applicable to a simple structure in which the stress

system is one-dimensional, and ν in consequence disappears from the constitutive equations.

The most general method of solving structural problems governed by constitutive equations such as (1.4) is that described by Mendelson, Hirschberg and Manson[9]. The method employs the integrated form of equation (1.4), which may be written

$$\varepsilon_{ij} = \left(\frac{1+\nu}{E}\right)\sigma_{ij} - \frac{\nu}{E}\sigma_{kk}\delta_{ij} + \varepsilon^{c}_{ij} \qquad (1.7)$$

where the creep strain $\varepsilon^{c}_{ij} = A\int J_2^m S_{ij} t^q . dt \qquad (1.8)$

From the initial elastic stresses and equations (1.8) the creep strain occurring in a small time interval is estimated. Equations (1.7) can then be solved numerically with those of equilibrium and compatibility for total strains and a new set of stresses. With these stresses a further set of creep strains is obtained from (1.8), and the process repeated until satisfactory convergence is achieved. In a similar way the solution can be extended through further time intervals.

With this method the complete solution of the creep problem is obtained. The strains occurring during primary creep and the steady state stresses are determined from the analysis directly, while the steady state strain rates are calculated from equation (1.2), or obtained from a seperate analysis with the time exponent q=0. Mendelson

et al applied the method to plate and rotating disc problems, and their procedure has been followed by Poritsky[10] and others, who describe how shells of revolution may be analysed. To the author's knowledge, however, there are no results of such shell analyses recorded in the literature.

An alternative approach to the investigation of structures under constant loading ignores the elastic and primary regions, and uses the steady state law (1.2) with the field equations to obtain steady state creep rates and stresses. Such an analysis is independent of time, and, as pointed out by Hoff[11], is analagous to that of a structure with constitutive equation

$$\varepsilon_{ij} = BJ_2^m s_{ij} \qquad (1.9)$$

The stress distribution in a structure governed by equation (1.2) is identical with that in a structure governed by (1.9), while strain rates in the former correspond to strains in the latter.

Steady state analysis requires considerably less effort than the incremental method of Mendelson, and results from it should be adequate when the steady state creep strains are much greater than the elastic and primary creep components. Further, the investigations of Wahl[12], Gubser, Sidebottom and Shammamy[13], and Marriott and

Leckie[5], show that in some cases at least, the stress redistribution has little influence on the deformations, and the steady state solution can be used to give good approximations to the total strains occurring at any time. Primary creep strains are calculated from equation (1.1) with the steady state stresses, and total strains estimated by adding the creep strain to the initial elastic strain.

The first steady state analysis was carried out on thick walled tubes by Bailey[14], and since then solutions have been obtained analytically and numerically to a wide range of problems[1],[15],[16]. However, when the method is applied to shell structures, axisymmetric in geometry and loading, non-linear differential equations containing definite integrals in the thickness co-ordinate are obtained. While it should be possible to solve these equations by some numerical technique, the computations would be greatly complicated by the presence of the integrals. The analysis can be simplified by working with approximate relations between stress resultants and middle surface deformations. Several forms of approximate relations have been used by Bieniek and Freudenthal[17], Onat and Yuksel[18], Calladine[19] and Gemma[20]. A more general set has been derived by Rozenblium[21] and Mackenzie[22] from an approximate expression for an energy function based on the two

dimensional form of the steady state equation (1.2).

In this thesis the creep behaviour of a simple shell structure, a cylindrical shell with fixed ends subject to uniform axial and radial loading, is investigated in two distinct ways: with the "exact" constitutive equations (1.4)-(1.6), and with the approximate relations between stress resultants and middle surface deformations proposed in references[21] and [22].

A closed form solution is obtained using the exact equations (1.4)-(1.6) with the stress exponent m=0, and numerical solutions are computed with non-zero values of m. The solutions are examined to determine the influence of the material parameters, particularly the stress exponent m and Poisson's ratio ν, on structural behaviour. The effect of the stress redistribution is investigated, and the accuracy, with which total strains can be estimated using steady state stresses, assessed.

Steady state solutions obtained from the exact analysis and with the approximate relations are compared, and the usefulness of the latter discussed. The approximate relations are then used in the analysis of a more practical problem, a cylindrical shell with an abrupt change of wall thickness.

Reports of creep experiments on shell structures are almost non-existent; the only test of which the author is

aware is one on a lead cylinder mentioned very briefly in reference[17]. As part of this research a small series of short term creep tests on pressurised polypropylene cylindrical shells was carried out. Polypropylene was chosen as the test material from an examination of the tensile creep behaviour of several commercially available plastics. In this thesis the design of a tensile testing machine and apparatus for measuring the deformation of pressurised cylindrical shells is described. Tensile creep data from polypropylene, perspex, PVC and nylon are discussed, and the measured deformation patterns of the polypropylene shells presented.

In all the theoretical analyses so far mentioned the usual assumptions of small deflection shell theory (see, for example, Flügge[23]) are made; in particular, the equilibrium equations are set up with regard to the geometry of the undeformed shell. It emerges that this simplification is too severe to allow the experimental measurements to be adequately predicted. The equilibrium equations are modified to take some account of the "finiteness" of the shell deformations, and satisfactory agreement with experiment is obtained.

CHAPTER 2

SOME BASIC EQUATIONS AND THEIR NON-DIMENSIONALIZATION

2.1 Equations of Cylindrical Shell

Fig. 2.1 shows a thin cylindrical shell of length l and defines the co-ordinate system. Movement of a point on the mid-surface from S in the undeformed shell to S' after deformation defines the positive axial and radial displacements u and w respectively.

Fig. 2.2 shows an element of the shell at x and defines the positive stress resultants

$$N_x = \int_{-\frac{h}{2}}^{\frac{h}{2}} \sigma_x \, dz \quad , \qquad M_x = \int_{-\frac{h}{2}}^{\frac{h}{2}} \sigma_x \, z \, dz, \text{ etc.} \tag{2.1}$$

acting on the element. Forces N_x, N_θ, Q_x and moments M_x, M_θ as defined are per unit length of mid-surface. Radial loading P is per unit area of mid-surface.

In constructing the equations governing the behaviour of the loaded shell the usual assumptions of small deflection shell theory - see, for example,[23] - are made. The governing equations are formulated in terms of the stress resultants, the mid-surface strains ε_{mx} , $\varepsilon_{m\theta}$ and the mid-surface curvature change λ_x ($\lambda_\theta = 0$). The strains ε_x and ε_θ at distance z from the

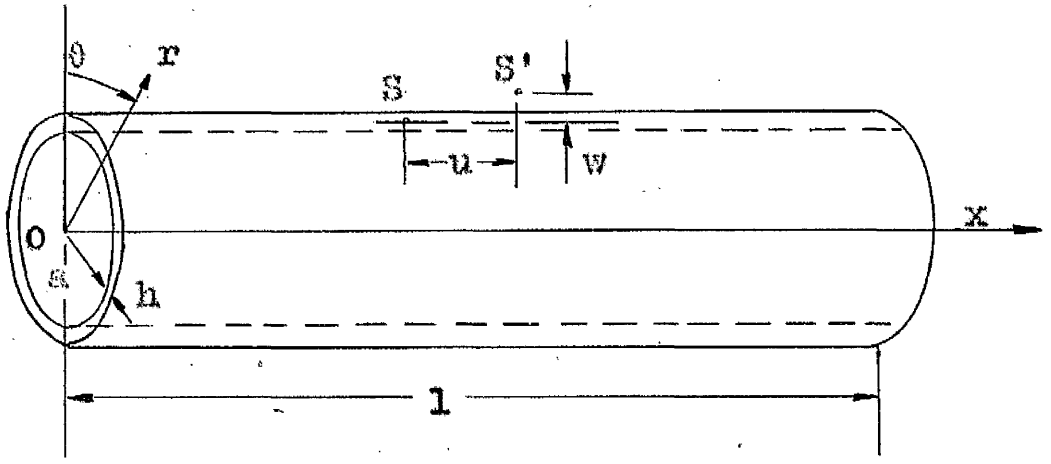

Fig. 2.1

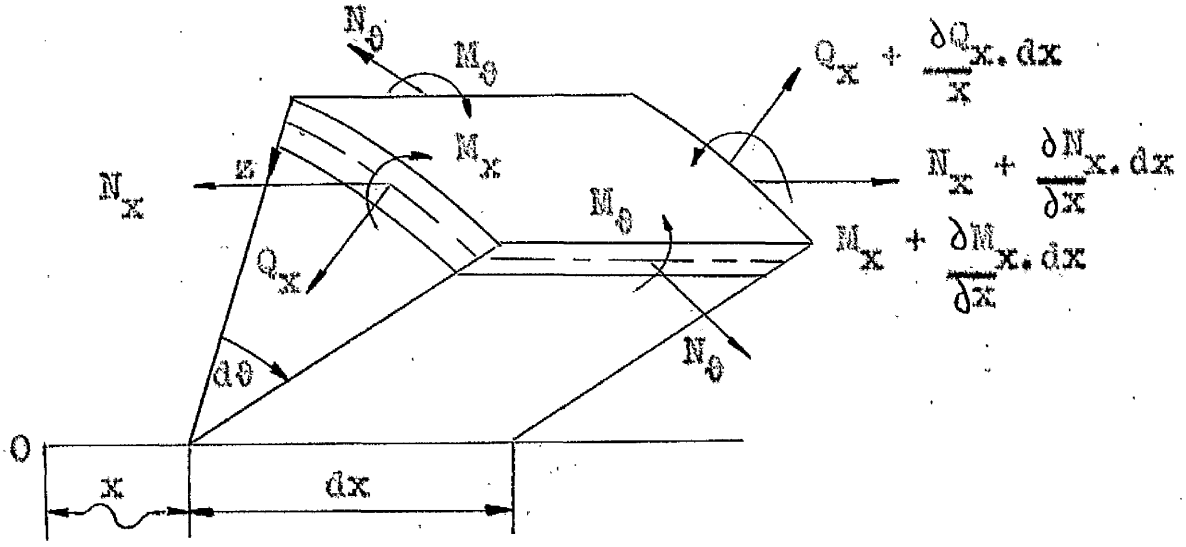

Fig. 2.2

mid-surface are assumed to be

$$\varepsilon_x = \varepsilon_{mx} + z\,\gamma_x$$
$$\varepsilon_\theta = \varepsilon_{m\theta} \qquad (2.2)$$

It is convenient in the theoretical analyses of this thesis to work with dimensionless variables. These are defined as follows:

$$n_{x,\theta} = \frac{N_{x,\theta}}{\sigma_o h} ; \qquad m_{x,\theta} = \frac{M_{x,\theta}}{\sigma_o h^2} ;$$

$$q_x = \frac{Q_x \sqrt{ah}}{\sigma_o h^2} ; \qquad p = \frac{Pa}{\sigma_o h} ;$$

$$\bar{\varepsilon}_{x,\theta} = \frac{\varepsilon_{x,\theta}}{\varepsilon_o} ; \qquad \bar{\sigma}_{x,\theta} = \frac{\sigma_{x,\theta}}{\sigma_o} ; \tag{2.3}$$

$$e_{x,\theta} = \frac{\varepsilon_{mx,m\theta}}{\varepsilon_o} ; \qquad k_x = \frac{h\mathcal{H}_x}{\varepsilon_o} ;$$

$$\bar{u} = \frac{u}{\varepsilon_o \sqrt{ah}} ; \qquad \bar{w} = \frac{w}{a\varepsilon_o} ;$$

$$\bar{x} = \frac{x}{\sqrt{ah}} \left(\bar{l} = \frac{l}{\sqrt{ah}}\right) ; \quad \bar{z} = \frac{z}{h} ;$$

$$\bar{t} = \frac{t}{t_o}$$

(For brevity, a comma between suffices is used to indicate that one equation is formed with the first suffix in each term, and a second equation with the second suffix.) In these definitions (2.3) σ_o is an arbitrary reference stress; ε_o and t_o are obtained from the constitutive equations of the material.

With these variables equations (2.1) and (2.2) become

$$n_x = \int_{-\frac{1}{2}}^{\frac{1}{2}} \bar{\sigma}_x \, d\bar{z} ; \qquad m_x = \int_{-\frac{1}{2}}^{\frac{1}{2}} \bar{\sigma}_x \, \bar{z} \, d\bar{z} , \text{ etc.} \tag{2.4}$$

$$\epsilon_x = e_x + \bar{z}\, k_x$$

$$\epsilon_\theta = e_\theta \qquad (2.5)$$

Force equilibrium of the shell element - Fig. 2.2 - requires that

$$\begin{aligned} n_x' &= 0 \\ q_x' - n_\theta &= -p \\ m_x' + q_x &= 0 \end{aligned} \qquad (2.6)$$

In these equations, and those that follow, a prime denotes differentiation with respect to $\bar{x}$. Equations (2.6) may be rewritten as

$$\begin{aligned} n_x &= n_a \\ m_x'' + n_\theta &= p \end{aligned} \qquad (2.7)$$

where n_a, an integration constant, is the axial stress resultant applied to the ends of the shell.

The mid-surface deformations are expressed in terms of the displacements by

$$\begin{aligned} e_x &= \bar{u}' \\ e_\theta &= \bar{w} \\ k_x &= \bar{w}'' \end{aligned} \qquad (2.8)$$

With the fundamental equations of the cylindrical shell (2.4) - (2.8) and the constitutive equations of the material, a complete mathematical description of structural behaviour is obtained.

2.2 Constitutive Equations

The elastic-time hardening equations (1.4) - (1.6) may be written, in terms of the strains and stresses occurring in the shell, thus:

$$\frac{\partial \varepsilon_{x,\theta}}{\partial t} = \frac{1}{E}\frac{\partial}{\partial t}\left(\sigma_{x,\theta} - \nu\sigma_{\theta,x}\right) + A\,\frac{2}{3}\left(\frac{1}{3}\right)^{m}\sigma^{*2m}\left(\sigma_{x,\theta} - \frac{\sigma_{\theta,x}}{2}\right)t^{q} \qquad (2.9)$$

where the "effective stress"

$$\sigma^{*} = \left(\sigma_x^2 - \sigma_x\sigma_\theta + \sigma^2\right)^{\frac{1}{2}} \qquad (2.10)$$

(Note: The shear stress associated with Q_x is assumed to have no influence on the strain components.) In non-dimensional form equations (2.9) and (2.10) become

$$\frac{\partial \bar{\varepsilon}}{\partial \bar{t}}_{x,\theta} = \frac{\partial}{\partial \bar{t}}\left(\bar{\sigma}_{x,\theta} - \nu\bar{\sigma}_{\theta,x}\right) + \bar{\sigma}^{*2m}\left(\bar{\sigma}_{x,\theta} - \frac{\bar{\sigma}_{\theta,x}}{2}\right)\bar{t}^{\,q} \qquad (2.11)$$

$$\bar{\sigma}^{*} = \left(\bar{\sigma}_x^2 - \bar{\sigma}_x\bar{\sigma}_\theta + \bar{\sigma}_\theta^2\right)^{\frac{1}{2}} \qquad (2.12)$$

where the reference strain and time have been chosen such that

$$\varepsilon_o = \frac{\sigma_o}{E} \quad ; \quad t_o = \left[EA\,\frac{2}{3}\left(\frac{1}{3}\right)^{m}\sigma_o^{2m}\right]^{-\frac{1}{q+1}} \qquad (2.13)$$

Equations (2.11) may be simplified by changing the time variable. If a new variable $\bar{t}^{*}$ is defined by

$$\bar{t}^{*} = \int \bar{t}^{q}\,.\,d\bar{t} = \frac{\bar{t}^{\,q+1}}{q+1} \qquad (2.14)$$

equations (2.11) become

$$\dot{\bar{\varepsilon}}_{x,\theta} = \dot{\bar{\sigma}}_{x,\theta} - \upsilon\dot{\bar{\sigma}}_{\theta,x} + \bar{\sigma}^{*2m}\left(\bar{\sigma}_{x,\theta} - \frac{\bar{\sigma}_{\theta,x}}{2}\right) \tag{2.15}$$

where a dot indicates differentiation with respect to $\bar{t}^*$. The modified constitutive equations (2.15) do not involve the time exponent q. Solutions obtained with these equations can be converted to solutions for any value of q by a simple alteration of the time scale in accordance with equation (2.14).

(It should be noted that the reduction of the elastic-time hardening equations (2.11) to (2.15) is not dependent on the time function being of the form $\bar{t}^q$. Whatever the time function, a change of variable similar to (2.14) produces equations (2.15), and results obtained with the latter can, therefore, be more generally applied.)

Integrated with respect to $\bar{t}^*$ equations (2.15) may be written

$$\bar{\varepsilon}_{x,\theta} = \bar{\sigma}_{x,\theta} - \upsilon\bar{\sigma}_{\theta,x} + \bar{\varepsilon}^{c}_{x,\theta} \tag{2.16}$$

where $$\bar{\varepsilon}^{c}_{x,\theta} = \int\left(\bar{\sigma}^{*2m}\left(\bar{\sigma}_{x,\theta} - \frac{\bar{\sigma}_{\theta,x}}{2}\right)\right) d\bar{t}^* \tag{2.17}$$

The steady state equations (1.2) can be adapted to suit shell analysis and written in the non-dimensional form,

$$\dot{\bar{\varepsilon}}_{x,\theta} = \bar{\sigma}^{*2m}\left(\bar{\sigma}_{x,\theta} - \frac{\bar{\sigma}_{\theta,x}}{2}\right) \tag{2.18}$$

Here, $$\frac{\varepsilon_o}{t_o} = \dot{\varepsilon}_o = B\,\frac{2}{3}\left(\frac{1}{3}\right)^m \sigma_o^{2m+1} \tag{2.19}$$

Rates of deformation resulting from different stress systems can be usefully compared by associating an effective strain rate with the effective stress. The effective strain rate is defined as

$$\frac{\partial \varepsilon^*}{\partial t} = \frac{2}{\sqrt{3}}\left[\left(\frac{\partial \varepsilon_x}{\partial t}\right)^2 + \frac{\partial \varepsilon_x}{\partial t}\cdot\frac{\partial \varepsilon_\theta}{\partial t} + \left(\frac{\partial \varepsilon_\theta}{\partial t}\right)^2\right]^{\frac{1}{2}} \tag{2.20}$$

or, in non-dimensional form

$$\dot{\bar{\varepsilon}}^* = \frac{2}{\sqrt{3}}\left(\dot{\bar{\varepsilon}}_x^2 + \dot{\bar{\varepsilon}}_x\dot{\bar{\varepsilon}}_\theta + \dot{\bar{\varepsilon}}_\theta^2\right)^{\frac{1}{2}} \tag{2.21}$$

From the definitions (2.12) and (2.21), and the constitutive equations (2.18), or, under constant stress, (2.15), it can be shown that

$$\dot{\bar{\varepsilon}}^* = \bar{\sigma}^{*\,2m+1} \tag{2.22}$$

2.3 Choice of Reference Stress

The arbitrary stress σ_o can be chosen such that, for any combination of the loading parameters p and n_a, the radial velocity $\dot{\bar{w}}$ in the membrane region of the shell is independent of the stress exponent m. (The word membrane is used to denote uniformly stressed sections of the shell.) In the membrane region the stresses are independent of time and position, and can be determined from equilibrium considerations alone. Equations (2.4) and (2.7) simplify to yield

$$\bar{\sigma}_x = n_x = n_a$$
$$\bar{\sigma}_\theta = n_\theta = p \qquad (2.23)$$

From the time derivatives of equations (2.5) and (2.8)

$$\dot{\bar{w}} = \dot{\bar{\varepsilon}}_\theta$$

and hence, equations (2.15) or (2.18) yield

$$\dot{\bar{w}} = \bar{\sigma}^{*2m} (\bar{\sigma}_\theta - \tfrac{1}{2}\bar{\sigma}_x)$$
$$= (\bar{\sigma}_\theta - \tfrac{1}{2}\bar{\sigma}_x)$$

if $\bar{\sigma}^* = 1$.

Equations (2.12) and (2.23) combine to give

$$\bar{\sigma}^* = (n_a^2 - n_a p + p^2)^{\frac{1}{2}}$$

and therefore $\dot{\bar{w}}$ is independent of m provided that

$$n_a^2 - n_a p + p^2 = 1 \qquad (2.24)$$

In this study three types of loading are considered, uniform radial loading, axial loading and internal pressure. In these cases the parameters p, n_a take the following values:

(a) Uniform radial loading	$n_a = 0$	from (2.24)	$p = 1$
(b) Axial loading	$p = 0$	" "	$n_a = 1$
(c) Internal pressure	$n_a = \frac{p}{2}$	" "	$p = \frac{2}{\sqrt{3}}$

(2.25)

For any real loads P and N_a, p $(= \frac{Pa}{\sigma_o h})$ and n_a $(= \frac{N_a}{\sigma_o h})$ can be given the desired values by appropriate choice of σ_o e.g. in case (c) above

$$\sigma_o = \frac{Pa}{ph} = \frac{\sqrt{3}}{2} \cdot \frac{Pa}{h}$$

CHAPTER 3

LINEAR CREEP OF A CYLINDRICAL SHELL

3.1 Introductory Remarks

The linear form of the constitutive equations(2.15) is

$$\dot{\bar{\varepsilon}}_{x,\theta} = \dot{\bar{\sigma}}_{x,\theta} - \nu\dot{\bar{\sigma}}_{\theta,x} + \bar{\sigma}_{x,\theta} - \tfrac{1}{2}\bar{\sigma}_{\theta,x} \qquad (3.1)$$

(With a constant stress system these equations provide a good description of the behaviour of certain alloys[24].)

On loading, the shell is assumed to respond elastically in accordance with Hooke's Law i.e.

$$\bar{\varepsilon}_{x,\theta} = \bar{\sigma}_{x,\theta} - \nu\bar{\sigma}_{\theta,x} \qquad (3.2)$$

and then to creep governed by equations (3.1). The stresses tend to steady state values, which, with these simplified creep equations, can be obtained from the elastic solution by putting Poisson's ratio ν equal to a half. The extent of the stress redistribution during creep is determined, therefore, by the amount that ν differs from a half.

To illustrate this susceptibility to ν, the greatest bending moment in a cylindrical shell with fixed ends (at $\bar{x}$ 0) is plotted against ν for three loading conditions in Fig. 3.1.* As can be seen the

* Figures not included in the text appear at the end of the relevant chapter.

influence of ν on the bending moment is small for radial loading ($p=1, n_a=0$) and internal pressure ($p=\frac{2}{\sqrt{3}}, n_a=\frac{1}{\sqrt{3}}$), but substantial when axial loading ($p=0, n_a=1$) alone is applied. (In this and subsequent figures involving m_x and k_x at $\bar{x}=0$, the values for axial loading, though negative, are shown on the positive scale for direct comparison with those of the other loading systems.) A creep analysis with axial loading and a low value of ν should clearly demonstrate the effect of the stress redistribution.

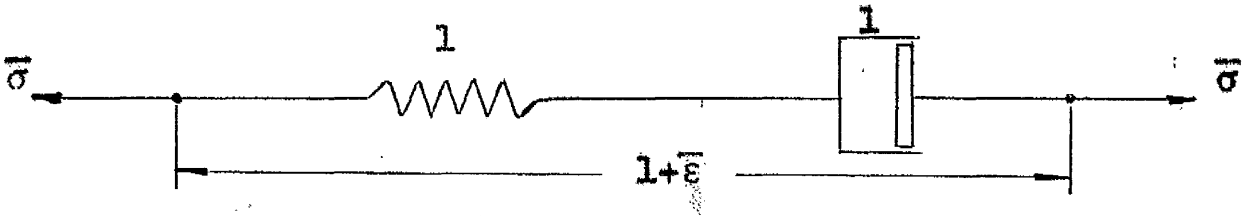

(With non-dimensional stress and strain the spring and dashpot constants are unity.)

Fig. 3.2 Maxwell model

For simple tension equation (3.1) describes the Maxwell model of viscoelastic theory – Fig. 3.2. The neatest method of solving linear viscoelastic problems is through use of the Laplace transform; a transformed set of field and constitutive equations, analogous to the set governing the corresponding elastic problem, is obtained, and hence a transformed solution. Unfortunately with many problems, such as those provided by shell structures, the transformed solution cannot be

easily inverted to give the true solution. Shinozuka and Spillers[25] have produced a few results by expanding a transformed solution as an infinite series and inverting term by term. This process, however, obscures the functional form of the true solution, from which the influence of material and geometric parameters can often be assessed.

An alternative method, and that employed here for a cylindrical shell with fixed ends, is to solve the governing differential equations directly.

3.2 Method of Solution

Equations (3.1) may be rearranged and written in the form,

$$F_1(D)\,\bar{\sigma}_{x,\theta} = (D+1)\,\dot{\bar{\varepsilon}}_{x,\theta} + (\nu D+\tfrac{1}{2})\,\dot{\bar{\varepsilon}}_{\theta,x} \qquad (3.3)$$

where $F_1(D) = (D+1)^2 - (\nu D+\tfrac{1}{2})^2$, D being the operator $\partial/\partial\bar{t}^*$, ~~and the subscripts x, θ replace 1, 2.~~ (In this analysis it is convenient to use both a dot above a variable and D to indicate differentiation with respect to $\bar{t}^*$.)

The stress resultants may be expressed in terms of the displacements using equations (2.4), (3.3) and the time derivatives of (2.5), (2.8):

$$F_1(D)n_x = (D+1)\,\dot{\bar{u}}' + (\nu D+\tfrac{1}{2})\,\dot{\bar{w}}$$

$$F_1(D)n_\theta = (D+1)\,\dot{\bar{w}} + (\nu D+\tfrac{1}{2})\,\dot{\bar{u}}' \qquad (3.4)$$

$$F_1(D)m_x = (D+1)\,\frac{\dot{\bar{w}}''}{12}$$

Loading applied suddenly is usually represented by the Heavyside step function

$$H(\bar{t}^*) = 0 \quad , \quad \bar{t}^* < 0$$

$$= 1 \quad , \quad \bar{t}^* > 0$$

Since this function has non-zero time derivatives at $\bar{t}^* = 0$, and zero derivatives for $\bar{t}^* > 0$, it is convenient in this analysis to associate the initial values of the dependent variables with $\bar{t}^* = 0^+$, and to obtain solutions for $\bar{t}^* \geqslant 0^+$.

When the relations (3.4) are substituted into the equilibrium equations (2.7) there results:

$$(D+1)\,\dot{\bar{u}}' + (\nu D+\tfrac{1}{2})\,\dot{\bar{w}} = F_1(D)\,n_a = \tfrac{3}{4}\,n_a \qquad (3.5)$$

$$(D+1)\,\frac{\dot{\bar{w}}''''}{12} + (D+1)\,\dot{\bar{w}} + (\nu D+\tfrac{1}{2})\,\dot{\bar{u}}' = F_1(D)p = \tfrac{3}{4}\,p$$

since p and n_a are independent of time for $\bar{t}^* \geqslant 0^+$. Equations (3.5) may be combined by the elimination of $\dot{\bar{u}}'$ to give the partial differential equation,

$$F_2(D)\,\dot{\bar{w}}'''' + 12F_1(D)\,\dot{\bar{w}} = 9\,(p-\tfrac{1}{2}n_a) \qquad (3.6)$$

where $F_2(D) = (D+1)^2$. Equation (3.6), governing the radial velocity $\dot{\bar{w}}\,(\bar{x},\bar{t}^*)$, is of the fourth order in $\bar{x}$ and of the second order in $\bar{t}^*$. Solutions are

sought which can satisfy the conditions at the fixed ends, i.e. $\dot{\bar{w}}(0,\bar{t}^*) = \dot{\bar{w}}'(0,\bar{t}^*) = \dot{\bar{w}}(\bar{1},\bar{t}^*) = \dot{\bar{w}}'(\bar{1},\bar{t}^*) = 0$ and can describe the initial velocity and acceleration functions, $\dot{\bar{w}}(\bar{x}, 0^+)$ and $\ddot{\bar{w}}(\bar{x}, 0^+)$, the latter functions being specified through the initial elastic stress distribution.

As equation (3.6) is inhomogeneous, the familiar method of solving partial differential equations by separation of variables cannot be directly applied. If, however, the solution is assumed to have the form

$$\dot{\bar{w}}(\bar{x}, \bar{t}^*) = \dot{\bar{w}}_1(\bar{x}, \bar{t}^*) + \dot{\bar{w}}_2(\bar{x}) \qquad (3.7)$$

equation (3.6) can be divided into two equations, one homogeneous and the other independent of time:

$$F_2(D)\,\dot{\bar{w}}_1'''' + 12\,F_1(D)\,\dot{\bar{w}}_1 = 0 \qquad (3.8)$$

$$\dot{\bar{w}}_2'''' + 9\,\dot{\bar{w}}_2 = 9\left(p - \frac{n_a}{2}\right) \qquad (3.9)$$

Equation (3.9) is the same as that describing a purely viscous shell. Its time-independent (i.e. steady state) solution and the initial elastic solution are given in Appendix 2.1. Steady state variables are denoted by subscript '∞', and those associated with initial conditions by subscript 'o'. Hence,

$$\dot{\bar{w}}_2(\bar{x}) = \dot{\bar{w}}_\infty(\bar{x}) \qquad (3.10)$$

Equation (3.8) can be solved by assuming a velocity function of the form

$$\dot{\bar{w}}_1(\bar{x},\bar{t}^*) = T(\bar{t}^*).X(\bar{x}) \qquad (3.11)$$

Substitution of this expression in equation (3.8) yields

$$X''''.F_2(D)T + 12X.F_1(D)T = 0$$

which becomes, when the variables are separated,

$$\frac{X''''}{X} = -\frac{12F_1(D)T}{F_2(D)T} = \beta^4 \qquad (3.12)$$

The positive sign with the constant β^4 is chosen as it leads to a non-trivial solution.

The resulting equation in X,

$$X'''' - \beta^4 X = 0 \qquad (3.13)$$

has the solution

$$X = a_1\cosh\beta\bar{x} + a_2\sinh\beta\bar{x} + a_3\cos\beta\bar{x} + a_4\sin\beta\bar{x} \qquad (3.14)$$

where a_1, ... a_4 are constants to be found from the boundary conditions. For a shell with fixed ends these are $X(0) = X'(0) = X(\bar{l}) = X'(\bar{l}) = 0$

and therefore

$$\begin{aligned} 0 &= a_1 + a_3 \\ 0 &= a_2 + a_4 \\ 0 &= a_1\cosh\beta\bar{l} + a_2\sinh\beta\bar{l} + a_3\cos\beta\bar{l} + a_4\sin\beta\bar{l} \\ 0 &= a_1\sinh\beta\bar{l} + a_2\cosh\beta\bar{l} - a_3\sin\beta\bar{l} - a_4\cos\beta\bar{l} \end{aligned} \qquad (3.15)$$

This set of homogeneous equations has a non-trivial solution only if,

$$\cosh\beta\bar{l}\,.\cos\beta\bar{l} = 1 \qquad (3.16)$$

The roots β_i of this characteristic equation are given in

Table 3.1. From equation (3.15) a_2, a_3, a_4 can be expressed in terms of a_1 and β; a_1 can be set equal to unity without loss, and from equation (3.14) the solutions X_i associated with each β_i obtained:

$$X_i = \cosh\beta_i\bar{x} - \cos\beta_i\bar{x} + f(\beta_i)(\sinh\beta_i\bar{x} - \sin\beta_i\bar{x}) \qquad (3.17)$$

where

$$f(\beta_i) = \frac{\cos\beta_i\bar{l} - \cosh\beta_i\bar{l}}{\sinh\beta_i\bar{l} - \sin\beta_i\bar{l}}$$

These functions X_i, which also occur in beam vibration problems, form an orthogonal set i.e.

$$\int_0^{\bar{l}} X_i \, X_j \, d\bar{x} = 0 \quad , \quad i \neq j \qquad (3.18)$$

Proof of this property and other useful relationships can be found in texts on vibrations, for example, Timoshenko[26].

$\beta_1\bar{l}$	4.730
$\beta_2\bar{l}$	7.853
$\beta_3\bar{l}$	10.996
$\beta_4\bar{l}$	14.137
$\beta_5\bar{l}$	17.279

Higher roots can be obtained with sufficient accuracy from the formula

$$\beta_i l = 17.279 + \pi(i-5)$$

Table 3.1

The time equation (3.12) is

$$F_1(D)T + \frac{\beta^4}{12} F_2(D)\,T = 0$$

which may be expanded as

$$(1 - \nu^2 + \frac{\beta^4}{12})\ddot{T} + (2 - \nu + \frac{\beta^4}{6})\dot{T} + \tfrac{1}{4}(3 + \frac{\beta^4}{3})T = 0 \qquad (3.19)$$

The solution of this equation is

$$T = S_1\, e^{-\gamma_1 \bar{t}^*} + S_2\, e^{-\gamma_2 \bar{t}^*} \qquad (3.20)$$

where S_1, S_2 are constants and

$$\gamma_{1,2} = \frac{1}{2(1 - \nu^2 + \frac{\beta^4}{12})} \left[(2 - \nu + \frac{\beta^4}{6}) \pm (1 - 2\nu) \sqrt{1 + \frac{\beta^4}{12}} \right] \qquad (3.21)$$

As is readily confirmed by examining equation (3.21) for the range $0 \leqslant \nu \leqslant \frac{1}{2}$, which embraces all material values, γ_1 and γ_2 are real and positive. Hence $T(\bar{t}^*)$, and therefore $\dot{\bar{w}}_1(\bar{x}, \bar{t}^*) \longrightarrow 0$ as $\bar{t}^* \longrightarrow \infty$.

There exists a function T_i of the form of equation (3.20) for each root β_i, and from equation (3.11) the general expression for $\dot{\bar{w}}_1$ may be written,

$$\dot{\bar{w}}_1(\bar{x}, \bar{t}^*) = \sum_{i=1}^{\infty} T_i \cdot X_i = \sum_{i=1}^{\infty} (S_{1i} e^{-\gamma_{1i} \bar{t}^*} + S_{2i} e^{-\gamma_{2i} \bar{t}^*}) X_i$$

From equations (3.7) and (3.10) the total radial velocity function then becomes

$$\dot{\bar{w}}(\bar{x}, \bar{t}^*) = \dot{\bar{w}}(\bar{x}) + \sum_{i=1}^{\infty} (S_{1i} e^{-\gamma_{1i} \bar{t}^*} + S_{2i} e^{-\gamma_{2i} \bar{t}^*}) X_i \qquad (3.22)$$

The constants S_{1i} and S_{2i} are evaluated from the initial

velocity and acceleration functions, $\dot{\bar{w}}_o(\bar{x})$ and $\ddot{\bar{w}}_o(\bar{x})$.

From equation (3.22) *

$$\dot{\bar{w}}\,(\bar{x}, 0^+) = \dot{\bar{w}}_o(\bar{x}) = \dot{\bar{w}}_\infty(\bar{x}) + \sum_{i=1}^{\infty}(S_{1i} + S_{2i})X_i$$

$$\ddot{\bar{w}}\,(\bar{x}, 0^+) = \ddot{\bar{w}}_o(\bar{x}) = - \sum_{i=1}^{\infty}(\gamma_{1i}S_{1i} + \gamma_{2i}S_{2i})X_i$$

When each of these equations is multiplied by X_j and integrated from 0 to $\bar{l}$, the orthogonality property (3.18) allows the constants to be obtained:

$$S_{1i} + S_{2i} = \frac{1}{\int_0^{\bar{l}} X_i^2 \, d\bar{x}} \left[\int_0^{\bar{l}} (\dot{\bar{w}}_o - \dot{\bar{w}}_\infty) \, X_j \, d\bar{x} \right]$$

$$\gamma_{1i}S_{1i} + \gamma_{2i}S_{2i} = - \frac{1}{\int_0^{\bar{l}} X_i^2 \, d\bar{x}} \left[\int_0^{\bar{l}} \ddot{\bar{w}}_o \, X_i \, d\bar{x} \right] \qquad (3.23)$$

With the function $\dot{\bar{w}}\,(\bar{x}, \bar{t}^*)$ known the stress resultants at any time can be obtained by integrating the differential equations (3.4). These solutions are given in Appendix 2.4.

3.3 Determination of Initial Functions

Immediately after loading i.e. at $\bar{t}^* = 0^+$, the elastic stress distribution exists throughout the structure. The stresses in the constitutive relations (3.1) are therefore known, and the latter can be solved for stress rates:

---

* That an arbitrary function can be represented by an infinite series of orthogonal functions is demonstrated by Rayleigh (27).

$$\dot{\bar{\sigma}}_{x,\theta} = \frac{1}{1-\nu^2}\left(\dot{\bar{\varepsilon}}_{x,\theta} + \nu\dot{\bar{\varepsilon}}_{\theta,x}\right) - \frac{1}{1-\nu^2}\left[\left(1-\tfrac{1}{2}\nu\right)\bar{\sigma}_{x,\theta} + \left(\nu-\tfrac{1}{2}\right)\bar{\sigma}_{\theta,x}\right]$$

With the time derivatives of equations (2.4), (2.5), (2.8) the initial stress resultant rates can then be obtained:

$$\dot{n}_{xo} = \frac{1}{1-\nu^2}\left(\dot{\bar{u}}_o' + \nu\dot{\bar{w}}_o\right) - \frac{1}{1-\nu^2}\left[\left(1-\tfrac{1}{2}\nu\right)n_{xo} + \left(\nu-\tfrac{1}{2}\right)n_{\theta o}\right]$$

$$\dot{n}_{\theta o} = \frac{1}{1-\nu^2}\left(\dot{\bar{w}}_o + \nu\dot{\bar{u}}_o'\right) - \frac{1}{1-\nu^2}\left[\left(1-\tfrac{1}{2}\nu\right)n_{\theta o} + \left(\nu-\tfrac{1}{2}\right)n_{xo}\right] \qquad (3.24)$$

$$\dot{m}_{xo} = \frac{1}{12(1-\nu^2)}\dot{\bar{w}}_o'' - \frac{1}{1-\nu^2}\left(1-\nu+\nu^2\right)m_{xo}$$

In the last equation the relation $m_{\theta o} = \nu m_{xo}$ has also been used.

The equilibrium equations (2.7) can be differentiated with respect to time and written

$$\begin{aligned} \dot{n}_{xo} &= 0 \\ \dot{m}_{xo}'' + \dot{n}_{\theta o} &= 0 \end{aligned} \qquad (3.25)$$

When the relations (3.24) are introduced into equations (3.25) there results:

$$\dot{\bar{u}}_o' = \left(1-\tfrac{1}{2}\nu\right)n_a + \left(\nu-\tfrac{1}{2}\right)n_{\theta o} - \nu\dot{\bar{w}}_o \qquad (3.26)$$

$$\dot{\bar{w}}_o'''' + 12(1-\nu^2)\dot{\bar{w}}_o = 12\left[\left(1-\nu+\nu^2\right)m_{xo}'' + (1-\nu^2)\left(n_{\theta o} - \tfrac{1}{2}n_a\right)\right] \qquad (3.27)$$

The right hand side of equation (3.27) consists of known functions, so that the solution can be readily

found. Details of this solution are given in Appendix 2.2.

The differential equation controlling the initial radial acceleration is obtained from equation (3.27) by differentiating with respect to time:

$$\ddot{\bar{w}}_o'''' + 12(1-\nu^2)\ddot{\bar{w}}_o = 12\left[(1-\nu+\nu^2)\dot{m}''_{xo} + (1-\nu^2)\dot{n}_{\theta o}\right] \qquad (3.28)$$

Again, the right hand side consists of known functions, obtained from equations (3.24), (3.26) and the solution of (3.27). Details of the solution of equation (3.28) also appear in Appendix 2.2.

When the initial velocity and acceleration functions are found, the series constants S_{1i}, S_{2i} can be calculated from equations (3.23). This process is described in Appendix 2.3.

3.4 Results and Discussion

The large number of arithmetic calculations involved in the evaluation of the arbitrary constants of both the series and the time independent functions (Appendices 2.1, 2.2, 2.4), made the use of a computer essential. An English Electric Leo KDF9 computer was used to calculate these constants, and to provide the desired solutions.

It was found that a fairly large number of terms was required to produce satisfactory convergence of the series representing $\dot{\bar{w}}\ (\bar{x}, \bar{t}^*)$ - equation (3.22). The

velocity and acceleration functions obtained from this equation at $\bar{t}^* = 0$, $\dot{\bar{w}}(\bar{x}, 0)$, $\ddot{\bar{w}}(\bar{x}, 0)$, were compared with with their prescribed values, $\dot{\bar{w}}_o$, $\ddot{\bar{w}}_o$, and good agreement achieved when the first forty non-zero terms of the series were included.

In Figs. 3.3 - 3.8 the redistribution in time of the functions $\dot{\bar{w}}$, n_θ, m_x are shown for a shell with fixed ends, $\bar{l} = 15$ units (a length sufficiently great to avoid interaction of the end effects), $\nu = 0.1$, and subject to the loadings $p = \frac{2}{\sqrt{3}}$, $n_a = \frac{1}{\sqrt{3}}$ (internal pressure) and $p = 0$, $n_a = 1$ (axial loading).

From Figs. 3.5 - 3.8 it can be seen that the stress distribution changes little during creep for internal pressure loading, but alters considerably when axial loading alone is applied. However, in neither case is there significant change in the radial velocity $\dot{\bar{w}}$ - Figs. 3.3 and 3.4.

This insensitivity of the deformation rate to stress changes is also shown by Figs. 3.9 and 3.10, where the greatest bending moment and curvature change (at $\bar{x} = 0$) are plotted against $\bar{t}^*$ for several values of ν and loading conditions. Despite the changes in the moments with time, particularly for axial loading, the curvature rate is almost constant.

It is useful to study the functional form of the

series solution, and in particular the dependence of the time coefficients $\gamma_{1,2}$ on β and ω - equation (3.21). The variations of $\gamma_{1,2}$ with β for $\omega = 0.1, 0.3$ are shown in Fig. 3.11. As can be seen γ_1 and γ_2 lie above and below the line $\gamma = 1$, to which they tend asymptotically as β increases. This suggests that the time dependence of the dependent variables may be approximately predicted by setting $\gamma_1 = \gamma_2 = 1$, and assuming, e.g. for the bending moment:

$$m_x(\bar{x}, \bar{t}^*) = (m_{xo} - m_{x\infty})\, e^{-\bar{t}^*} + m_{x\infty} \qquad (3.29)$$

This function, at $\bar{x} = 0$, is shown as a dashed line for several loading conditions and values of ω in Fig. 3.9; in all cases it is seen to agree reasonably well with the exact function.

Equation (3.29) may also be used to estimate the time in which stress redistribution occurs. If it is assumed to be complete when $m_x(\bar{x}, \bar{t}^*) - m_{x\infty} < \xi$, then redistribution time

$$\bar{t}_r^* \doteq \log_e \left[\frac{m_{xo} - m_{x\infty}}{\xi} \right]$$

From the definition of $\bar{t}^*$, $\bar{t}$ and t_o - equations (2.14), (2.3) and (2.13) - the real redistribution time may be written

$$t_r = \left[\frac{3(q+1)}{2\, E\, A} \cdot \bar{t}_r^* \right]^{1/(q+1)}$$

For real materials the time exponent q lies in the range $-1 < q < 0$, so that t_r is inversely related to E and A. As E increases the elastic strains diminish, and - equations (2.9) - as A increases the creep strain rates increase. Thus, the smaller the elastic strains and the larger the creep strain rates, the shorter is the redistribution time; a result which might be expected intuitively. The influence of q on t_r is more complex and depends on the ratio $\frac{t_r^*}{EA}$.

This analysis, though restricted to materials with a linear stress dependence, has shown that considerable stress redistribution can take place within a shell structure without the deformation rates deviating significantly from their steady state values.

Some of the features of the analytical approach should be useful for the analysis of cylindrical shells governed by more complex linear viscoelastic laws, though direct extension of the method is not possible because the initial functions are not readily obtained when higher order differential operators appear in the constitutive equations.

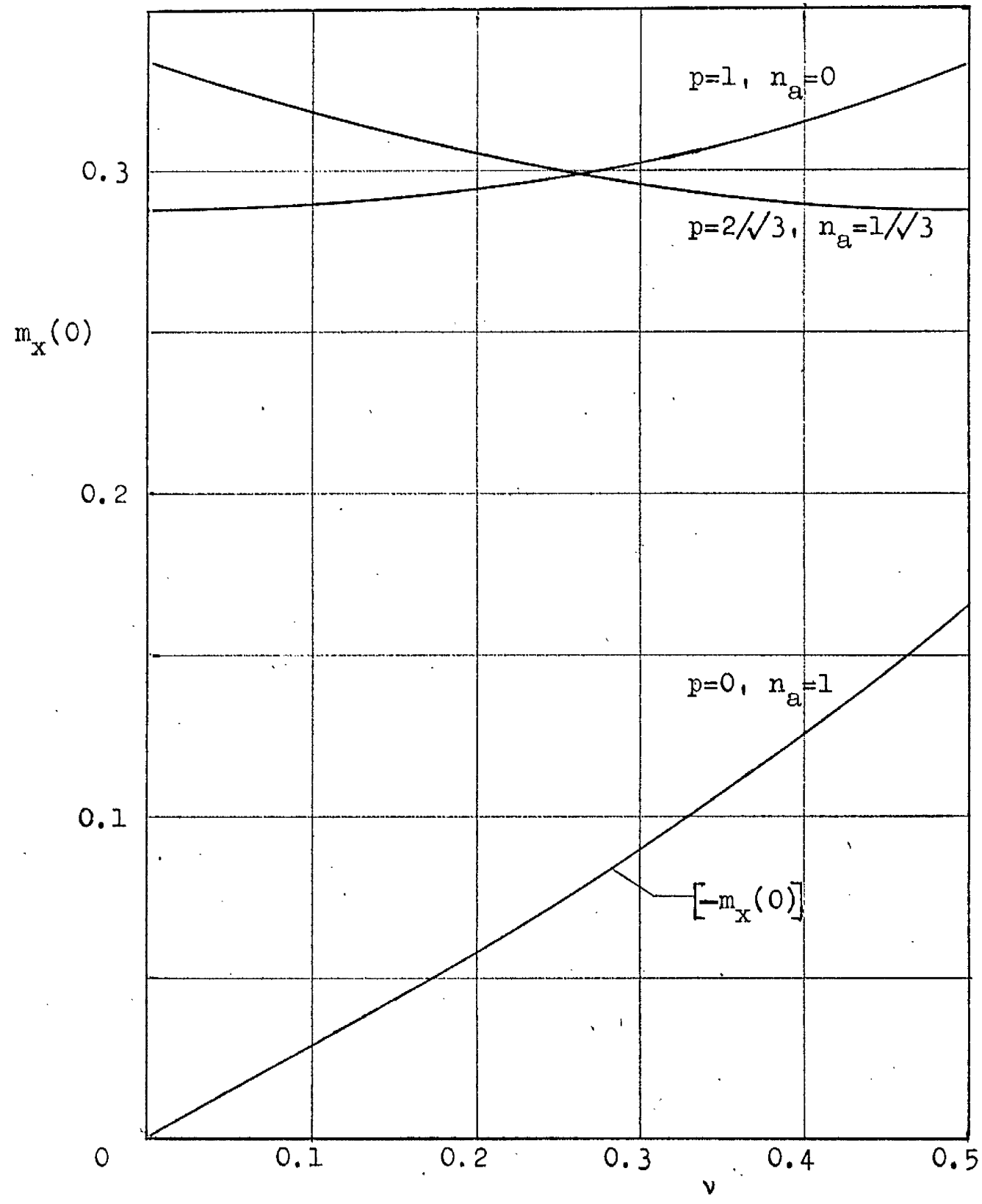

Fig. 3.1 Variation of greatest bending moment with ν

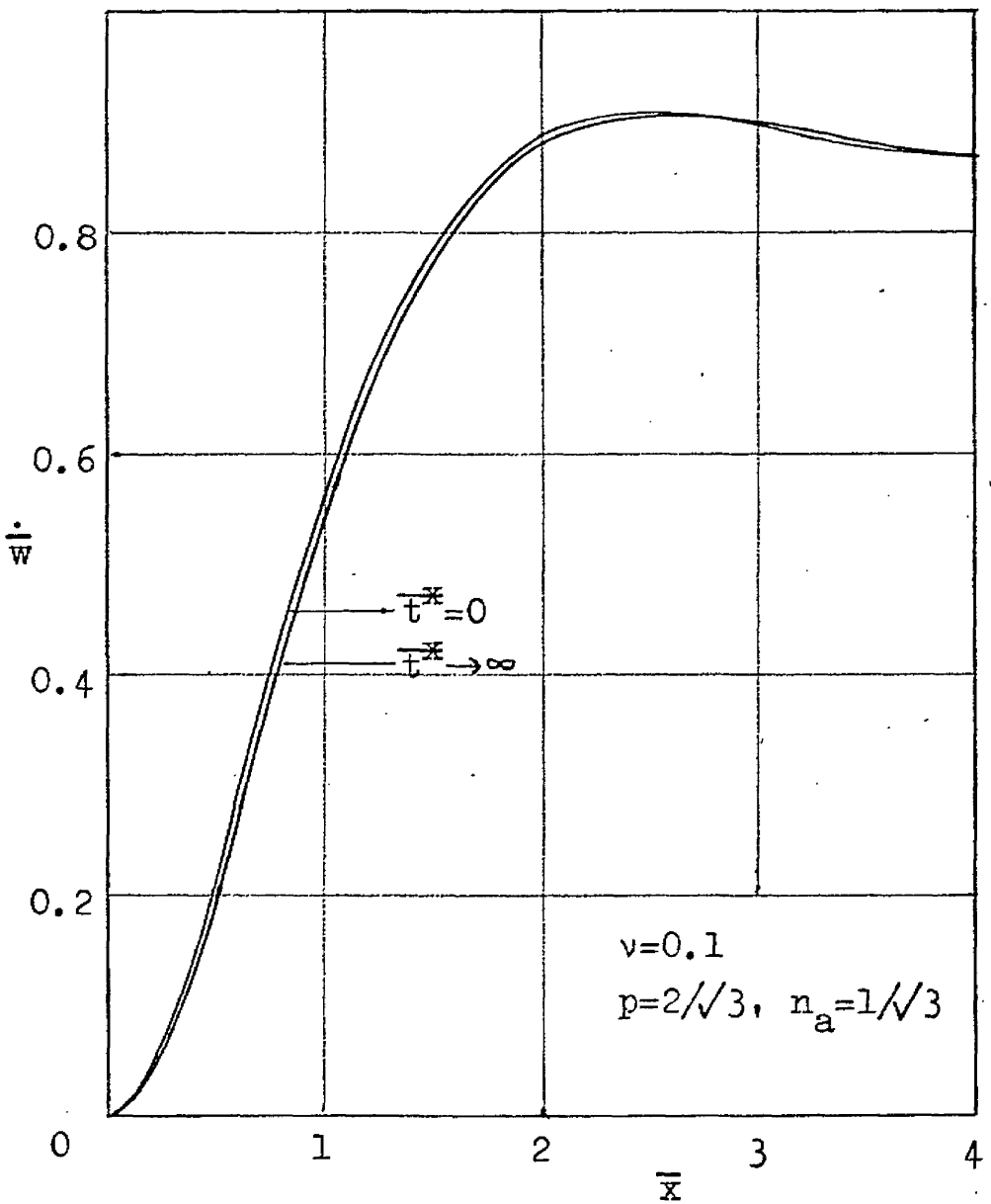

Fig. 3.3 Variation of radial velocity along shell

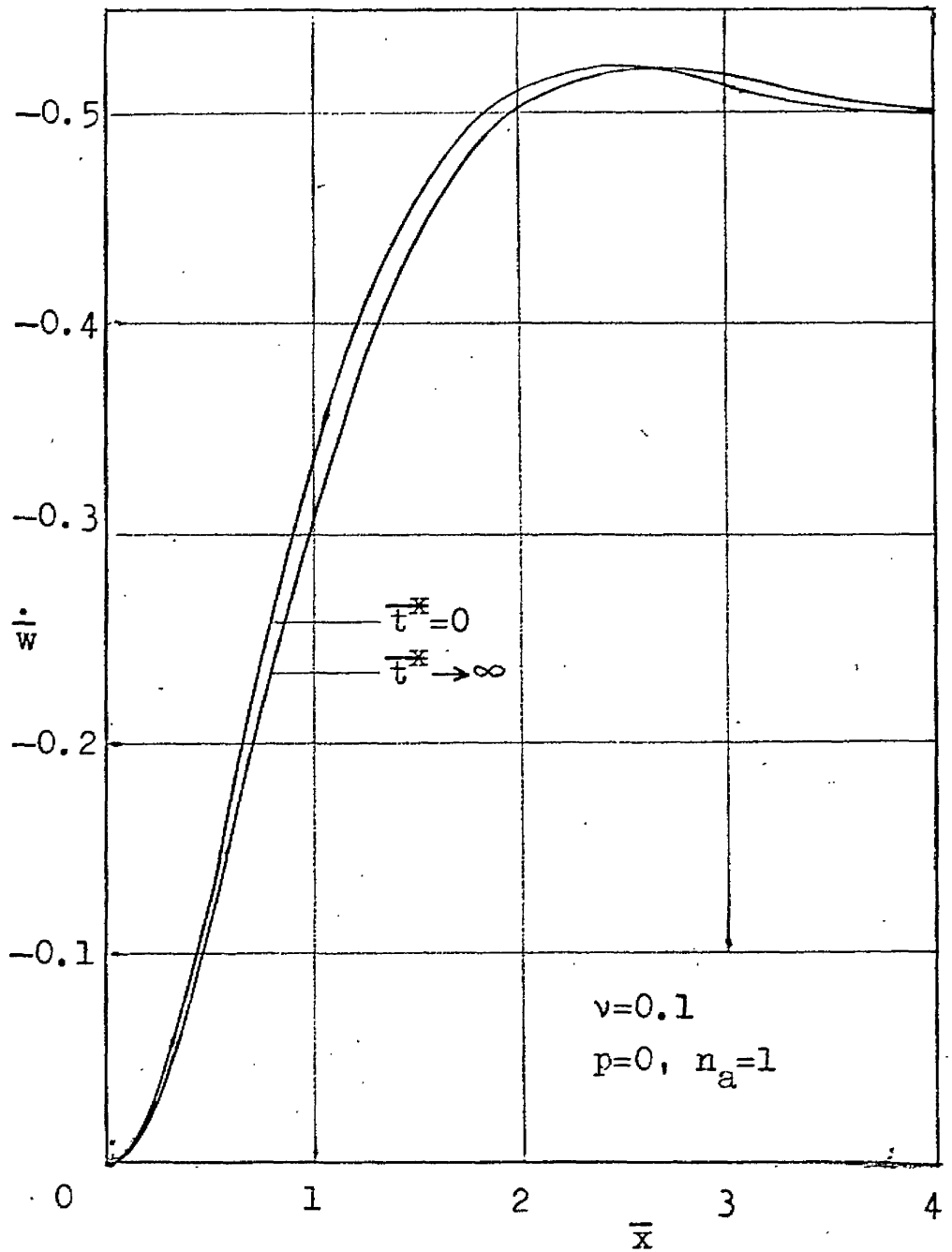

Fig. 3.4 Variation of radial velocity along shell

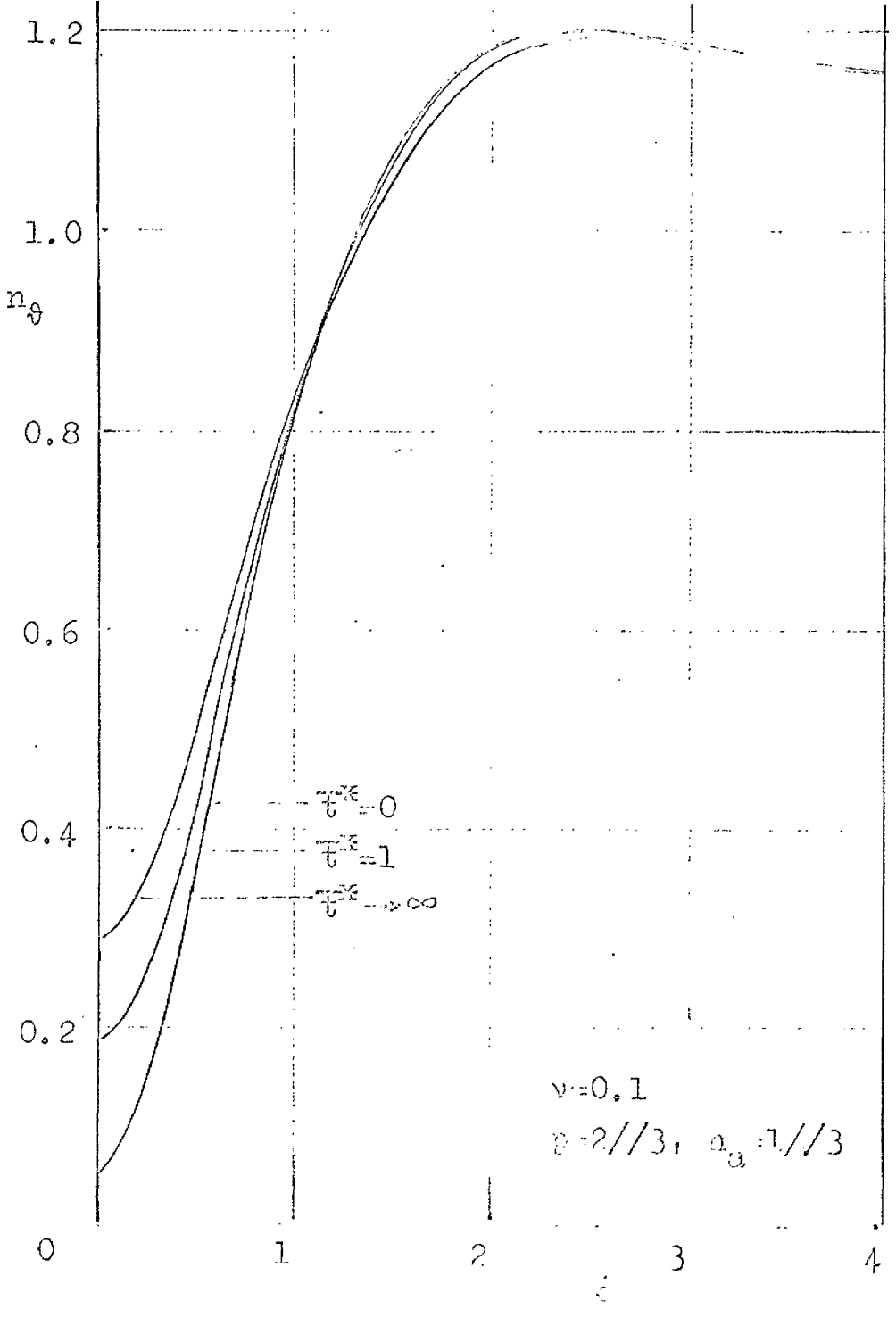

Fig. 3.5 Variation of hoop stress resultant along shell

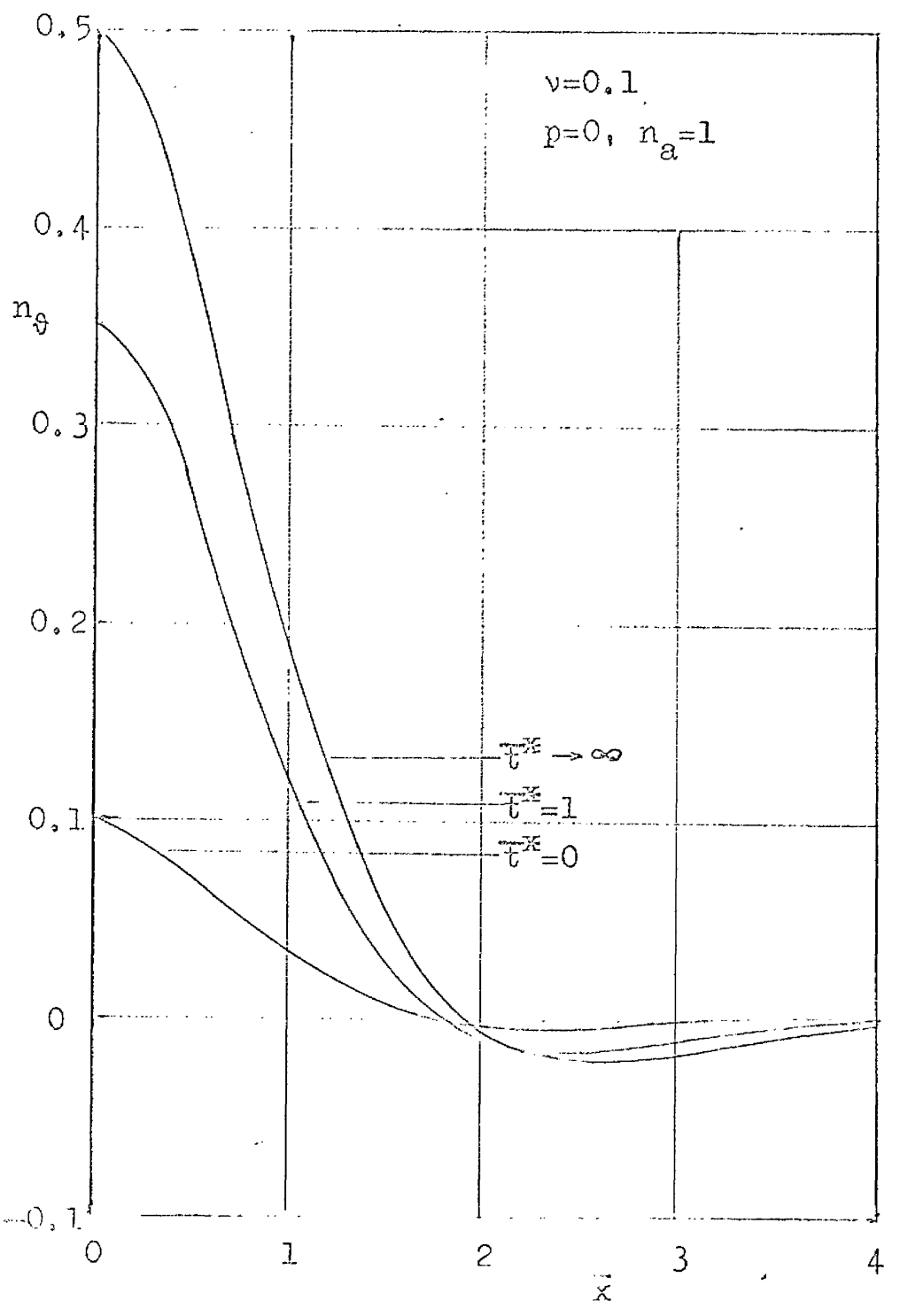

Fig. 3.6 Variation of hoop stress resultant along shell

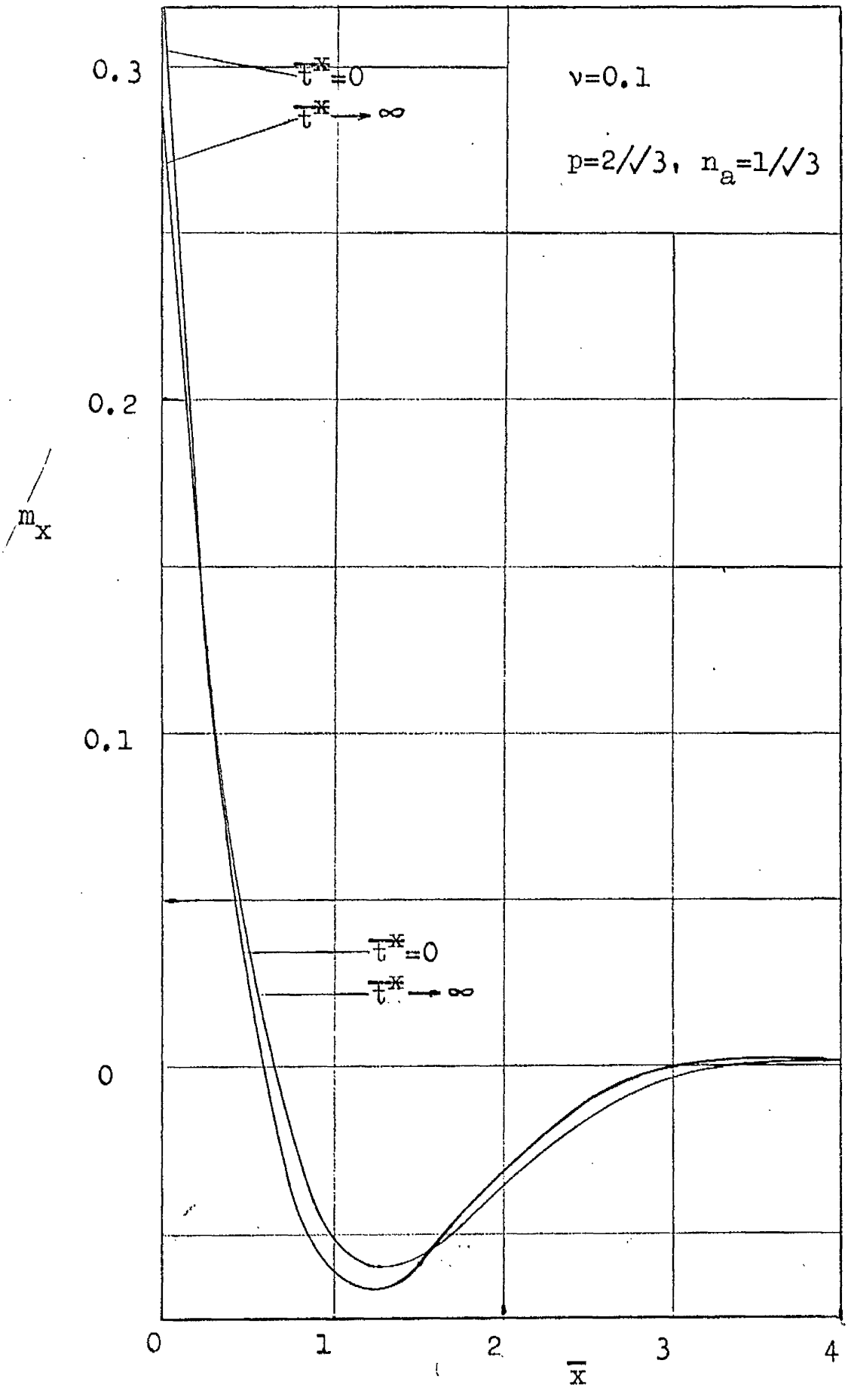

Fig. 3.7 Variation of bending moment along shell

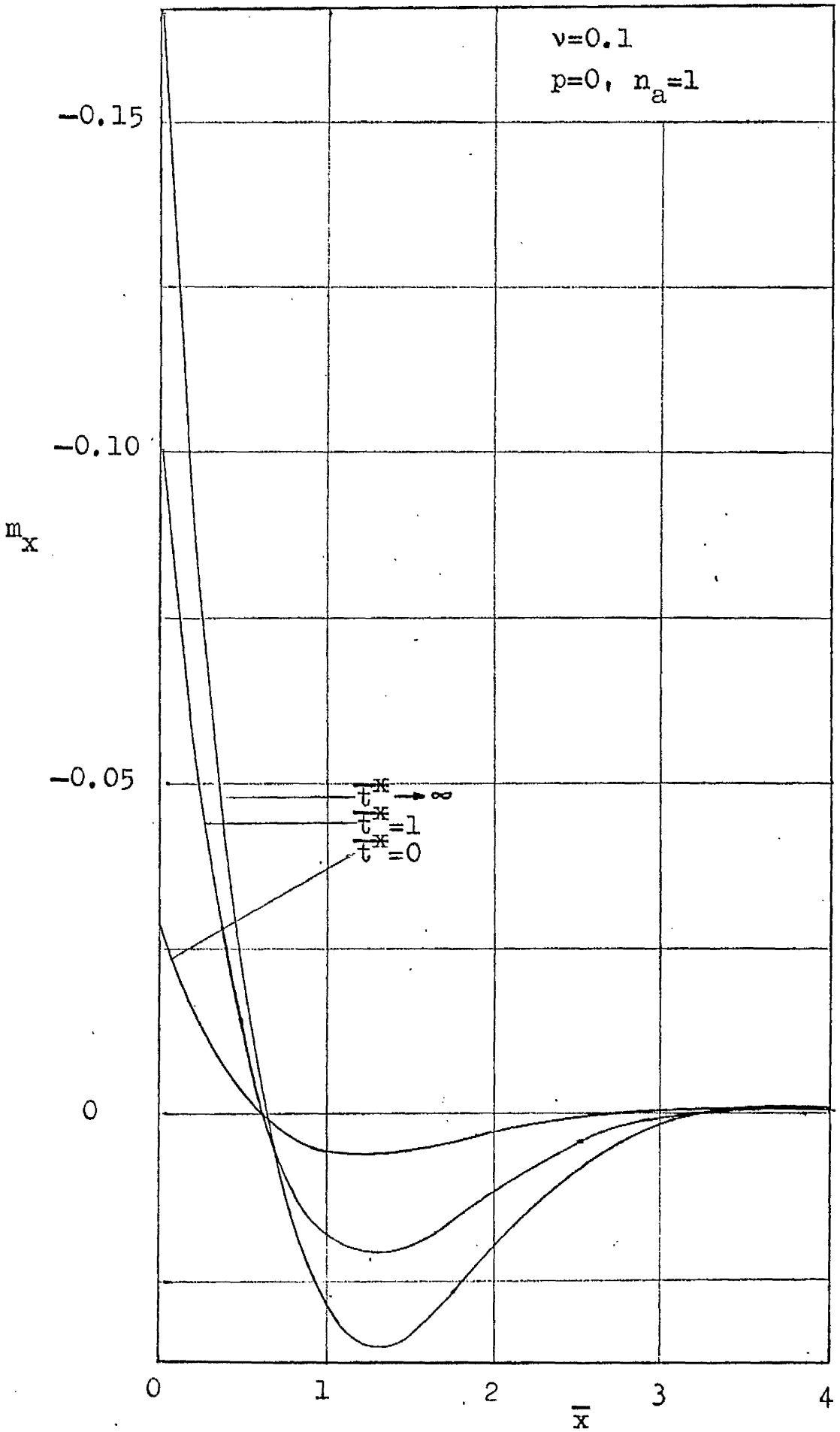

Fig. 3.8 Variation of bending moment along shell

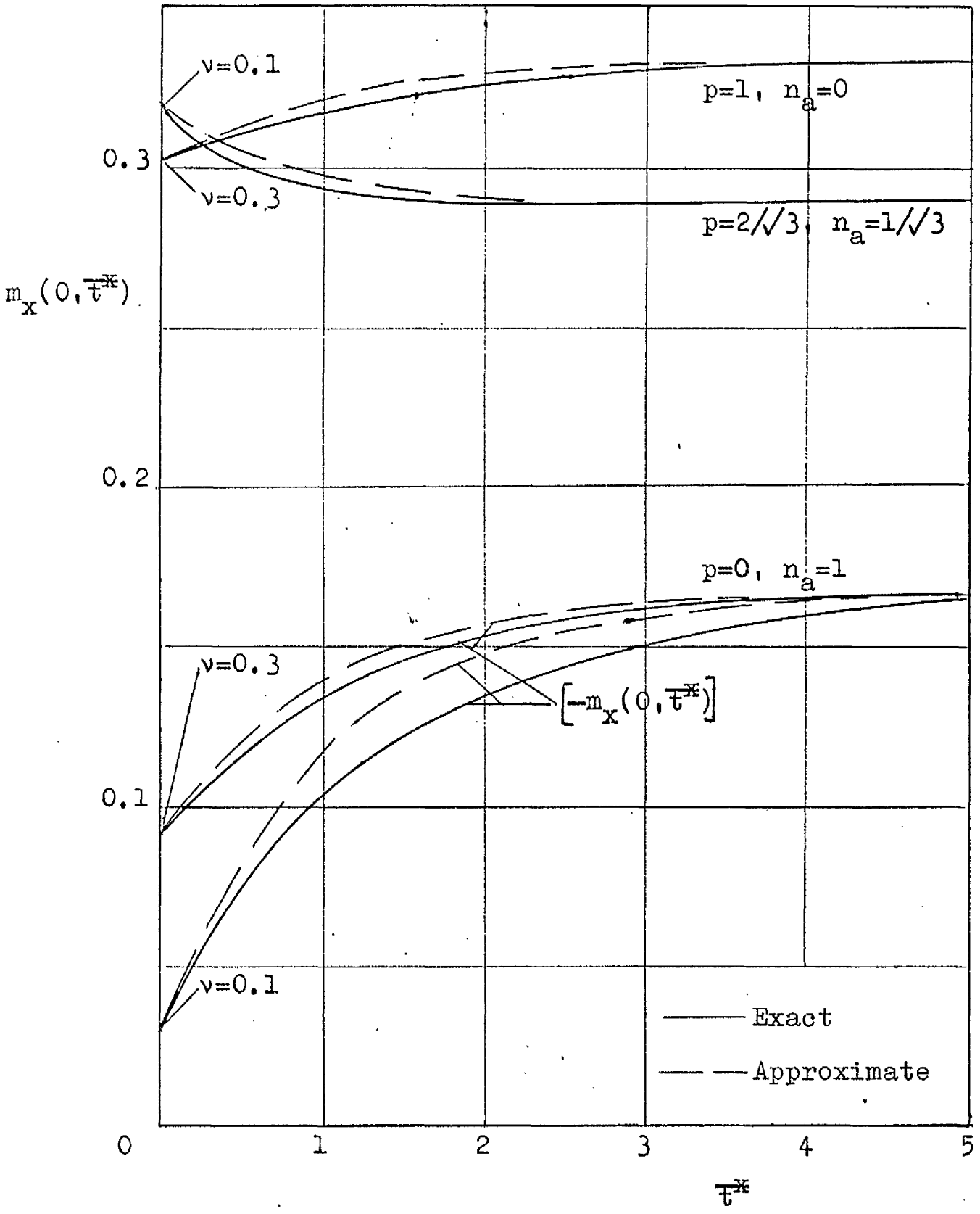

Fig.3.9 Variation of greatest bending moment with time

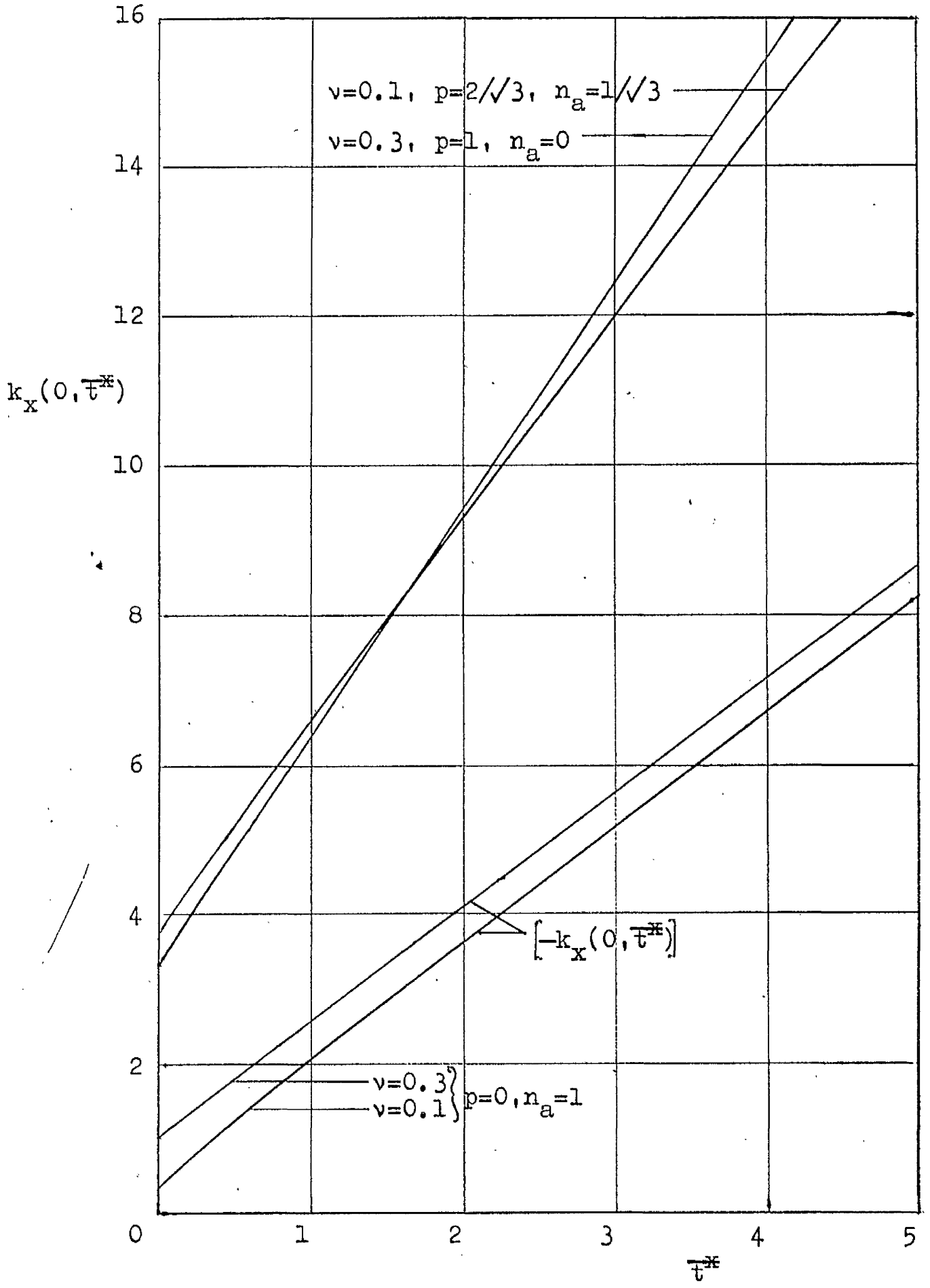

Fig. 3.10 Variation of greatest curvature with time

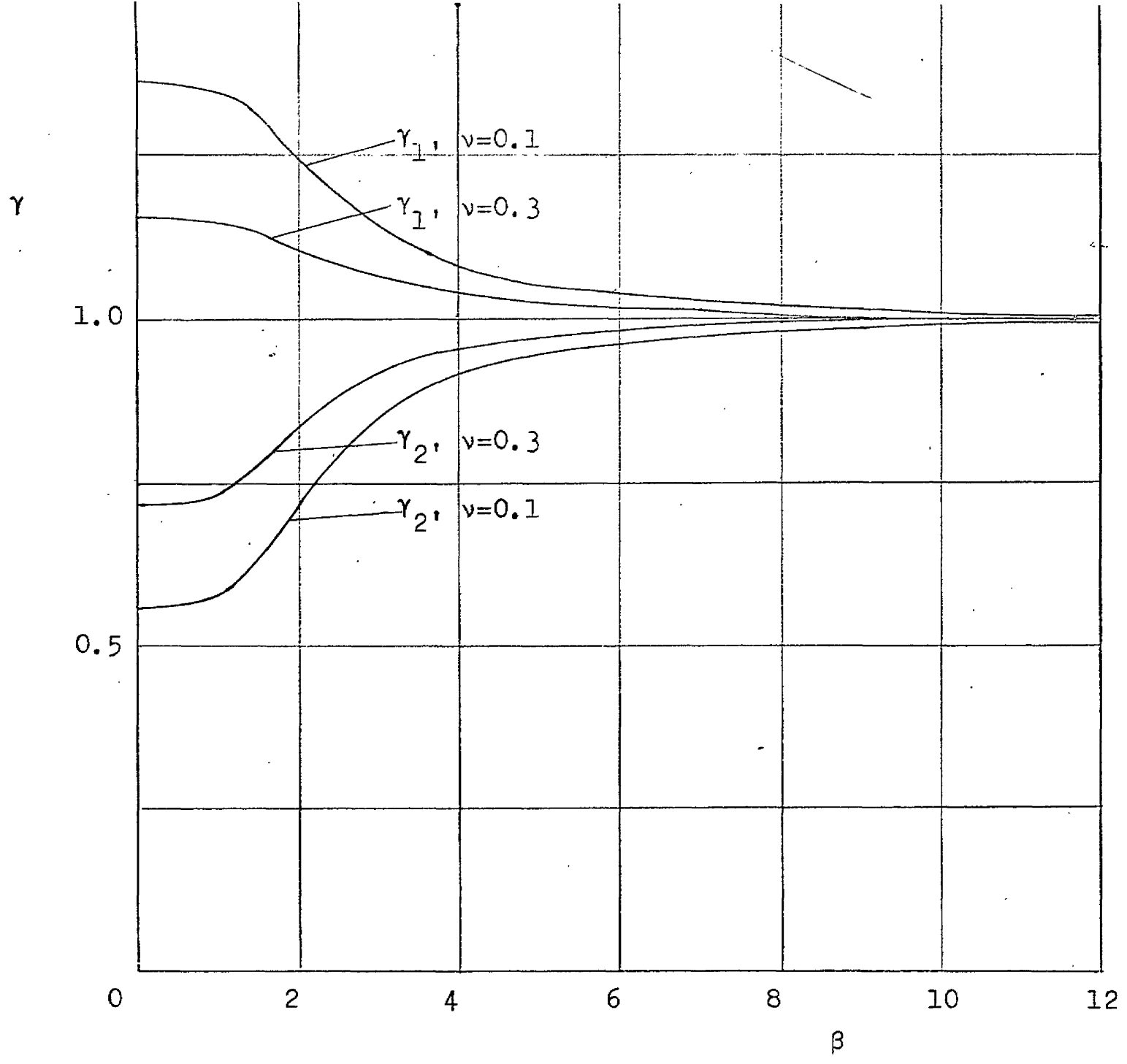

Fig. 3.11 Dependence of time coefficients on roots of characteristic equation

CHAPTER 4
NON-LINEAR CREEP OF A CYLINDRICAL SHELL

NON-LINEAR CREEP OF A CYLINDRICAL SHELL

4.1 Formulation of Problem and Method of Solution

With the general form of the constitutive equation (2.15) there is no prospect of obtaining a closed form solution to the cylindrical shell problem, and some numerical method of analysis is required. The method presented here is in essence the same as that of Mendelson et al [9].

The total strain equations (2.16) may be solved for stresses to yield

$$\bar{\sigma}_{x,\theta} \quad \frac{1}{1-\nu^2}\left(\bar{\varepsilon}_{x,\theta} + \nu\,\bar{\varepsilon}_{\theta,x}\right) - \frac{1}{1-\nu^2}\left(\bar{\varepsilon}^{c}_{x,\theta} + \nu\,\bar{\varepsilon}^{c}_{\theta,x}\right) \tag{4.1}$$

When these equations are combined with (2.4) and (2.5) the stress resultants become,

$$n_{x,\theta} = \frac{1}{1-\nu^2}\left(e_{x,\theta} + \nu\, e_{\theta,x}\right) - n^{c}_{x,\theta}$$

$$m_x = \frac{1}{12(1-\nu^2)} \cdot k_x - m^{c}_{x} \tag{4.2}$$

where

$$n^{c}_{x,\theta} = \frac{1}{1-\nu^2}\int_{-\frac{1}{2}}^{\frac{1}{2}}\left(\bar{\varepsilon}^{c}_{x,\theta} + \nu\bar{\varepsilon}^{c}_{\theta,x}\right)\, d\bar{z}$$

$$m^{c}_{x} = \frac{1}{1-\nu^2}\int_{-\frac{1}{2}}^{\frac{1}{2}}\left(\bar{\varepsilon}^{c}_{x} + \nu\bar{\varepsilon}^{c}_{\theta}\right)\,\bar{z}\, d\bar{z} \tag{4.3}$$

With equations (4.2), the equilibrium equations (2.7) and the deformation-displacement equations (2.8), two differential equations in total displacements are obtained:

$$\bar{u}' = (1-\upsilon^2)(n_a - n_x^c) - \upsilon\bar{w} \tag{4.4}$$

$$\bar{w}'''' + 12(1-\upsilon^2)\bar{w} = 12(1-\upsilon^2)\left[p-\upsilon n_a+m_x^{c''} + n_\theta^c - \upsilon n_x^c\right] \tag{4.5}$$

These equations in displacements and creep strain integrals must be satisfied at all times. The creep strain terms $n_{x,\theta}^c$, $m_x^{c''}$ in equations (4.4) and (4.5) have the form of additional loads, and the equations themselves are equivalent to those governing a purely elastic shell (c.f. equation (A2.2)) subject to non-uniform loading.

From equation (2.17) the creep strain increments occurring in a short time interval $\delta\bar{t}^*$ may be expressed approximately as

$$\delta\bar{\varepsilon}_{x,\theta}^c = \bar{\sigma}^{*2m}\,(\bar{\sigma}_{x,\theta} - \tfrac{1}{2}\bar{\sigma}_{\theta,x})\,.\,\delta\bar{t}^* \tag{4.6}$$

The total creep strains at time $\bar{t}^* + \frac{1}{2}\delta\bar{t}^*$ can then be written

$$(\bar{\varepsilon}_{x,\theta}^c)_{\bar{t}^*+\frac{1}{2}\delta\bar{t}^*} = (\bar{\varepsilon}_{x,\theta}^c)_{\bar{t}^*} + \tfrac{1}{2}\delta\bar{\varepsilon}_{x,\theta}^c \tag{4.7}$$

If total displacements and creep strains are known at any time, corresponding stresses may be calculated from equations (4.1), (2.5), (2.8); the latter may be combined to yield

$$\bar{\sigma}_x = \frac{1}{1-\nu^2}\left(\bar{u}' + \bar{z}\,\bar{w}'' + \nu\bar{w}\right) - \frac{1}{1-\nu^2}\left(\bar{\varepsilon}_x^c + \nu\bar{\varepsilon}_\theta^c\right)$$

$$\bar{\sigma}_\theta = \frac{1}{1-\nu^2}\left(\bar{w} + \nu\bar{u}' + \nu\bar{z}\,\bar{w}''\right) - \frac{1}{1-\nu^2}\left(\bar{\varepsilon}_\theta^c + \nu\bar{\varepsilon}_x^c\right) \qquad (4.8)$$

With equations (4.5) and (4.8) and the appropriate boundary conditions expressed in finite difference form, the solution at time $\bar{t}^*$ may be extended to $\bar{t}^* + \delta\bar{t}^*$ by the following iterative technique:

(1) Assume a set of stresses to act during the interval $\delta\bar{t}^*$, and estimate the creep strains occurring therein from equations (4.6). For the first interval the initial elastic values of the stresses are used; thereafter, the stresses assumed are those of the preceding time interval.

(2) Obtain the total creep strains at $\bar{t}^* + \frac{1}{2}\delta\bar{t}^*$ from equations (4.7).

(3) Calculate $n^c_{x,\theta}$, m^c_x by the numerical integration of equations (4.3).

(4) Solve equation (4.5) for $\bar{w}$ and obtain $\bar{u}'$ from (4.4).

(5) With these total displacements and the creep

strains calculate another set of stresses from equations(4.8).

(6) Use these stresses in equations (4.6) to re-estimate the creep strain increments.

(7) Repeat steps (2) - (6) until successive values of $\bar{w}$ are satisfactorily close.

When convergence has been obtained the total creep strains at $\bar{t}^* + \delta\bar{t}^*$ can be calculated from

$$(\bar{\varepsilon}^c_{x,\theta})_{\bar{t}^* + \delta\bar{t}^*} = (\bar{\varepsilon}^c_{x,\theta})_{\bar{t}^*} + \delta\varepsilon^c_{x,\theta}$$

and the entire iteration procedure applied to the next time interval.

The finite difference form of equations (4.5) and (4.8) and the fixed end boundary conditions, together with the integration formula for equations (4.3) and other details of the calculations are given in Appendix 3.

4.2 Accuracy and Range of Iteration Process

A computer programme was written to carry out the sequence of operations of the preceding section and provide the variation in time and space of the displacements, stress resultants, etc. The programme proved to be rather large, occupying almost all of the storage capacity of the KDF9 computer, and had a typical running time of thirty minutes.

Some criterion was required to measure the

convergence of the iteration process at each time interval. Convergence at the n^{th} iteration was assumed if

$$\frac{\bar{w}_n - \bar{w}_{n-1}}{\bar{w}_n} < \xi$$

It was found that with $\xi = 0.0002$ the error from this source was negligible.

As in the analysis of Chapter 3, solutions were obtained with a shell of length $\bar{l} = 15$ units, and, because of the longitudinal symmetry, integration performed over the range $0 - \frac{1}{2}\bar{l}$. To express equations (4.5) and (4.8) in finite difference form the shell was divided into equal intervals b near the fixed end, while at points away from the end, where the variables change less rapidly, the interval was doubled to 2b and then to 4b. It was found that with $b = 0.05$ three figures of agreement were obtained between the initial elastic solution as obtained numerically (i.e. with $\bar{\varepsilon}^c_{x,\theta} = 0$) and the closed form solution - equation (A2.3). In addition, numerical solutions with the stress exponent $m = 0$ agreed well with the closed form linear solutions of Chapter 3. As integration advanced in time the numerical solutions tended to drift slightly from the exact forms, though this divergence did not become significant until the stress redistribution was complete, and the steady state solution clearly established.

However, when non-zero values of the stress exponent m were used the drift in time increased considerably. It was most pronounced at the fixed end of the shell where the stresses are highest. This deviation was not affected by reductions in the time interval $\delta\bar{t}^*$ or the convergence parameter ξ, but was influenced by the size of the space interval b. Figs. 4.1 and 4.2 show for internal pressure loading and $m = 2$, the variation with time of the moment m_x and curvature k_x at $\bar{x} = 0$, as obtained with $b = 0.05$ and 0.02. With the former value m_x decreases continuously and the rate of increase of k_x never becomes constant. When $b = 0.02$, on the other hand, the steady state values of m_x and k_x are fairly well established. With higher values of m the drift again becomes significant even with this smaller interval. The storage capacity of the computer prevented a still smaller value of b from being used, and, indeed, with $b = 0.02$ the shell length was limited to 7.6 units. This reduction in length causes some interaction of the end effects, but it does not alter significantly the values of the stresses and strains at the fixed ends.

This type of instability is to be found in results from similar methods of analysis applied to other structures [7], [29]. The most obvious source of

cumulative error is the calculation of stresses from the difference of total and creep strains - equations (4.8). As these strains increase the accuracy with which their difference can be computed diminishes. The stresses are raised effectively to the power 2m+1 for the re-calculation of creep strains - equation (4.6), and the error consequently enlarged.

4.3 Results and Discussion

Solutions were obtained with m values up to 2 and several values of υ for the cylindrical shell subject to internal pressure, axial loading, and radial loading, the values of the parameters p, n_a being chosen as described in Section 2.3. The results are presented for the shell of length 15 units, although the maximum values of m_x and k_x were actually calculated with $\bar{I} = 7.6$ units.

The influence of m on the stress distribution depends very much on the loading system. This dependence is illustrated in Fig. 4.3 where the steady state values of m_x at $\bar{x} = 0$ are plotted against m. The influence of m on $m_x(0,\infty)$ increases with the axial load n_a. When $n_a = 0$ the moment at m = 2 is 88% of the value at m = 0; while, with $n_a = \frac{1}{\sqrt{3}}$ and 1, this ratio is 80% and 59% respectively.

In Fig. 4.4 the steady state curvature rate at

$\bar{x} = 0$ is plotted against m for the three loading systems. In each case $\dot{k}_x(0,\infty)$ increases with m, the increase being greatest for axial loading and least for internal pressure. The curves shown were determined by calculation only as far as m = 1. With m = 2, $\dot{k}_x(0,\infty)$ for each loading obtained a constant value during the iteration process as reported in the last section; but for radial loading and internal pressure these values (marked x in Fig. 4.4) were below those calculated with m = 1. It was considered very unlikely that the shell would behave in this way, and the result was attributed to the drift of the iteration process. The calculated value with m = 2 for axial loading was also judged unreliable, and all the curves were extended to m = 2 by extrapolation.

The characteristic influence of the stress exponent m on the steady state distribution along the shell of $\dot{\bar{w}}$, m_x and n_θ is shown in Figs. 4.5 - 4.7 for internal pressure loading. As m increases, the maximum values of the stress resultants are reduced, and the stress distribution becomes more uniform. The decay length, or the distance from the fixed end at which the radial velocity becomes virtually constant, increases with m, but the maximum value of $\dot{\bar{w}}$ is insensitive to variations of m.

Shell behaviour during the transition from initial elastic to steady state distribution is illustrated in Figs. 4.8 - 4.11, where the variations with time of n, m_x, e_θ, k_x at several values of $\bar{x}$ are shown for $p = 0$, $n_a = 1$, $m = 1$, and $\nu = \frac{1}{2}$. With these parameter values the redistribution of the stress resultants, particularly m_x, is considerable. Despite this, however, the total deformations e_θ and k_x are almost linear functions of time, their rates of increase during stress redistribution differing little from the steady state values.

This feature of the results is also shown in Figs. 4.12 and 4.13 where the greatest values of effective stress $\bar{\sigma}^*$ and effective strain $\bar{\epsilon}^*$ $(= \int \dot{\bar{\epsilon}}^* \, d\bar{t}^*)$ occurring in the shell (at $\bar{x} = 0$, and, depending on the loading system, $\bar{z} = -\frac{1}{2}$ or $\bar{z} = \frac{1}{2}$) are plotted against time for two loading conditions, $\nu = \frac{1}{2}$ and several values of m. The decrease in $\bar{\sigma}^*_{max}$ with time is much greater than the decrease in the greatest bending moment, because the distribution of the bending stresses through the thickness of the shell changes with time in a manner which reduces the greatest values. Nevertheless, the higher stresses which exist during the early stages of creep do not affect substantially the growth of total strains. The total strain can be fairly well estimated at any time by assuming a simple relationship with the initial elastic

strain and the steady state strain rate:

$$\bar{\varepsilon}^*_{\text{total}} = \bar{\varepsilon}^*_{\text{initial elastic}} + \bar{t}^* \, \dot{\bar{\varepsilon}}^*_{\text{steady state}} \qquad (4.9)$$

Approximations obtained with equation (4.9) for each loading system with m = 1, 2 are represented by dotted lines in Fig. 4.13. The accuracy of the numerical calculations is such that the steady state strain rates with m = 1 and 2 are virtually the same, and consequently the approximate lines for each loading system are indistinguishable. Underestimates of the total strain are provided by equation (4.9) in all cases. The approximation is poorest for internal pressure loading with m = 2, where during stress redistribution the estimate can be 20% below the true value. This discrepancy diminishes rapidly, however, and when the total strain is four times the initial elastic strain the error is only 6%.

The relative insensitivity of total strains to stress variation may be qualitatively explained as follows. The stress redistribution is accomplished fairly quickly - when (Fig. 4.13) the creep strains are about twice the initial elastic strains - so that the high stresses, and therefore high creep rates, present at the onset of creep act for only a short time. In addition, the elastic strain components decrease with the

stresses, and the net result is a mean total strain rate during redistribution which does not differ very greatly from the steady state strain rate. When the steady state stresses exceed the initial elastic values (as in Fig. 3.9), creep strain rates are low during stress redistribution, elastic strains increase, and the net result again is a mean total strain rate (Fig. 3.10) similar to the steady state rate.

The dominating influence of the steady state stress distribution on the growth of total strains has been observed in analyses of spinning discs[12], prismatic bars under torsion[13], pressurised thick cylinders[5]. It would appear, therefore, to be a general feature of structural behaviour, and one which increases the value of analyses based on the simpler steady state equation (1.2).

In all the figures so far presented in this chapter which show the time dependence of stresses and strains, Poisson's ratio ν has equalled a half. The value of ν determines the initial elastic stresses, and consequently, with m, the amount of stress redistribution during creep. In Fig. 4.14 the variation with time of the greatest bending moment is shown for the three loading cases and several values of m and ν. For internal pressure loading the effect of $\nu < \frac{1}{2}$ is to increase the elastic moment (see Fig. 3.1), and hence the change

during creep. With the other loading systems $m_x(0,\bar{t}^*)$ diminishes with ω as well as m so that for certain combinations of these parameters $m_x(0,\bar{t}^*)$ is almost independent of time.

The numerical solutions do not, of course, provide the functional relationship between dependent and independent variables. However, from an examination of the numerical results, approximate relationships can be constructed. For example, the linear analysis of Chapter 3 suggests - equation (3.29) - an exponential relationship between the moment at any time and its initial elastic and steady state values. In the non-linear case it is found that $m_x(\bar{x},\bar{t}^*)$ is well represented by the formula,

$$m_x(\bar{x},\bar{t}^*) = (m_{xo} - m_{x\omega})e^{-2\sqrt{m}.\bar{t}^*} + m_{x\infty} \qquad (4.10)$$

In Fig. 4.15 this expression is shown to agree closely with the actual moment/time dependence at $\bar{x} = 0$ for the three loading systems, m = 1 and 2.

As in Chapter 3, equation (4.10) may be used to estimate the period during which stress redistribution occurs. If the latter is considered complete when $m_x(\bar{x},\bar{t}^*) - m_{x\infty} < \varsigma$, then the redistribution time

$$\bar{t}_r^* = \frac{1}{2\sqrt{m}} \cdot \log_e \left| \frac{m_{xo} - m_{x\infty}}{\varsigma} \right|$$

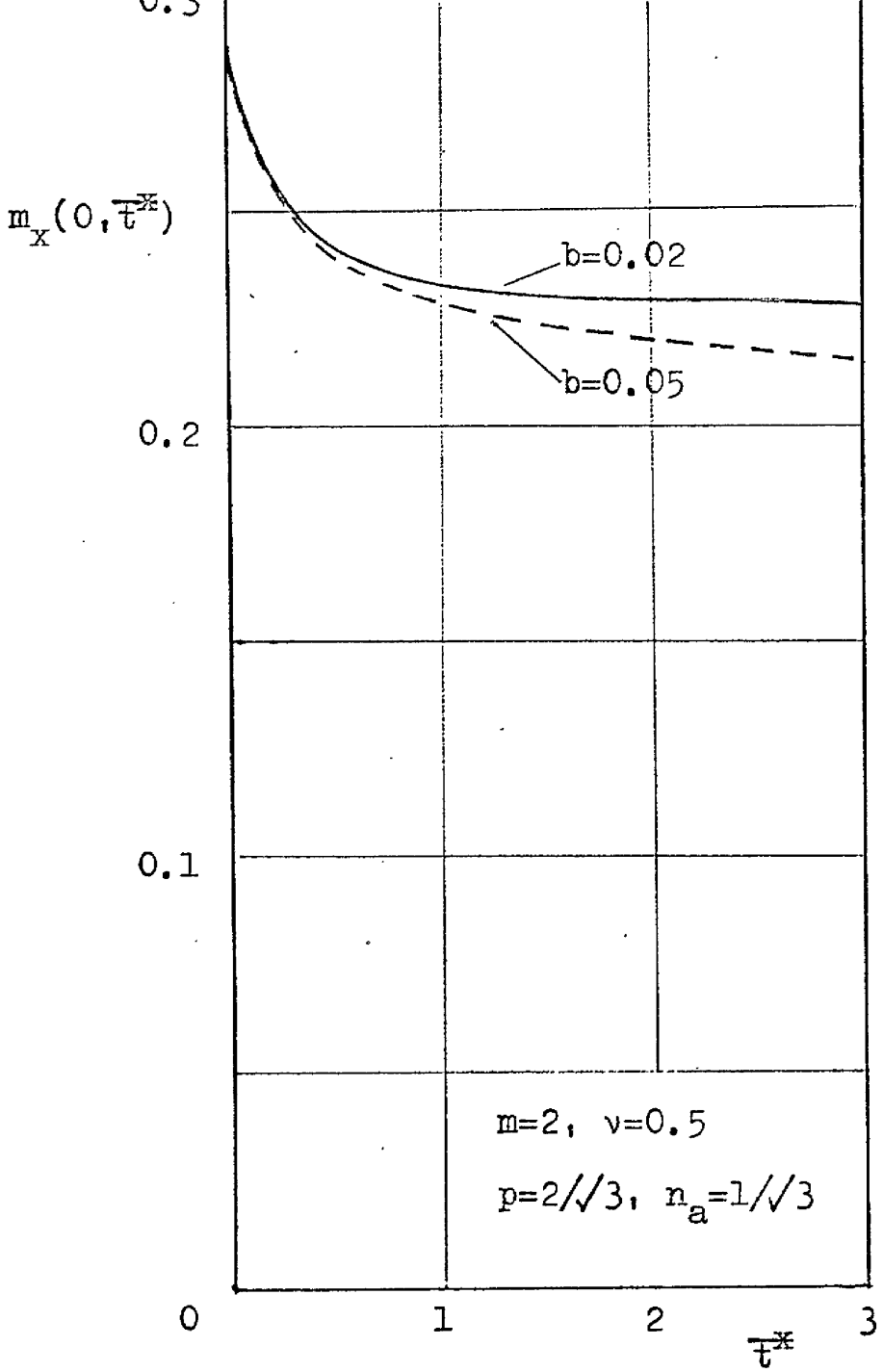

Fig.4.1 Influence of interval b on greatest bending moment

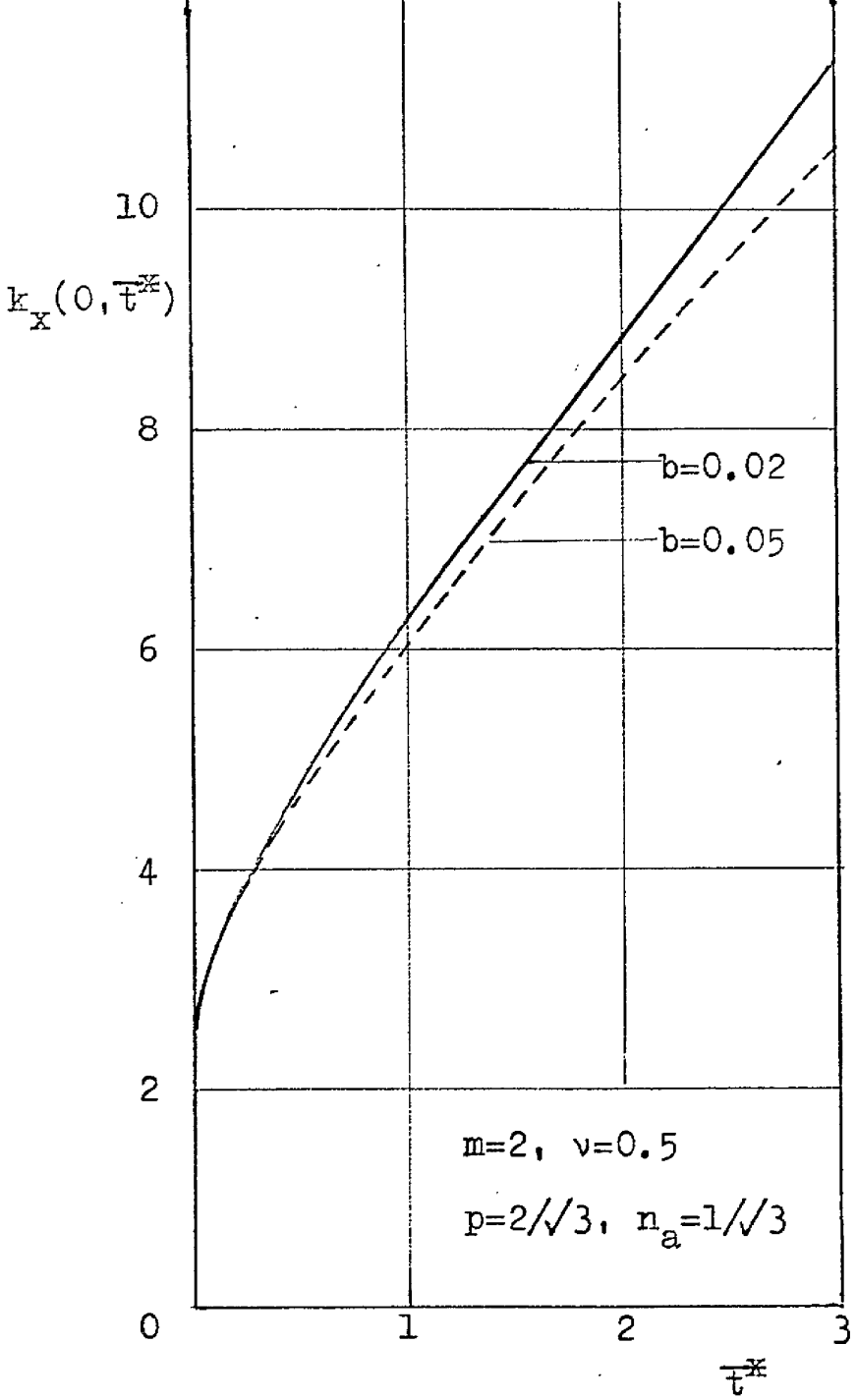

Fig.4.2 Influence of interval b on greatest curvature

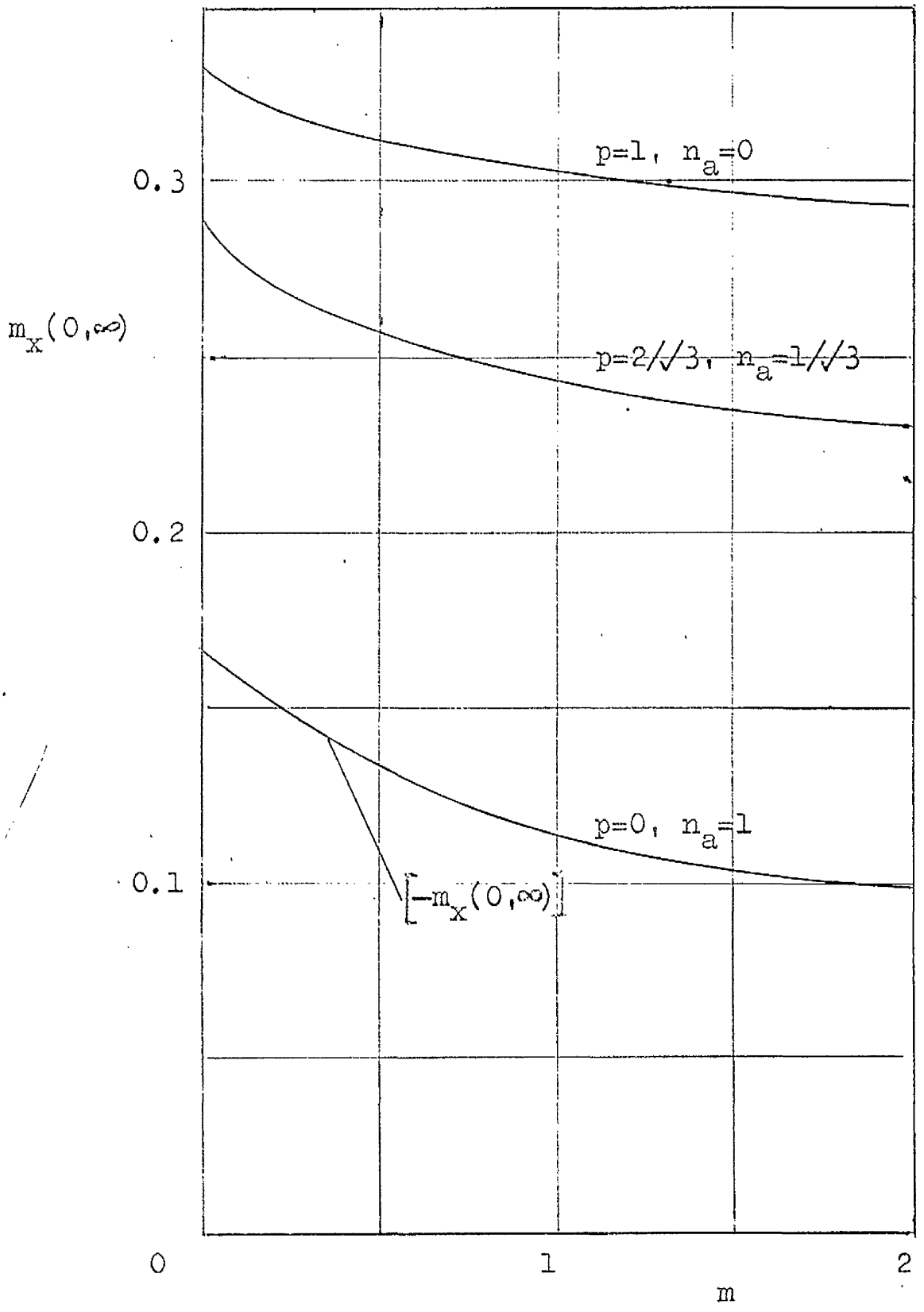

Fig. 4.3 Dependence of greatest steady state moment on stress exponent

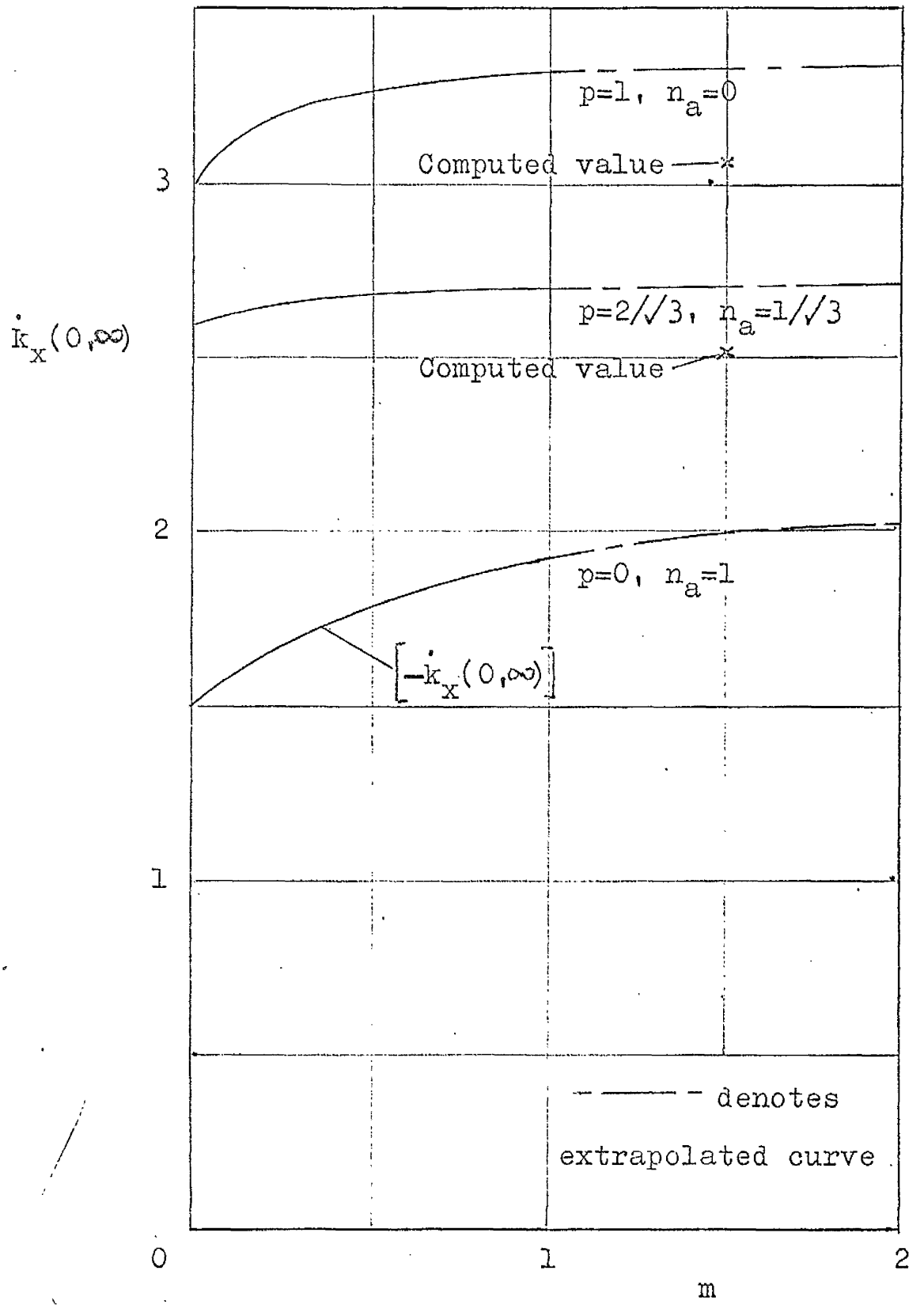

Fig.4.4 Dependence of greatest steady state curvature rate on stress exponent

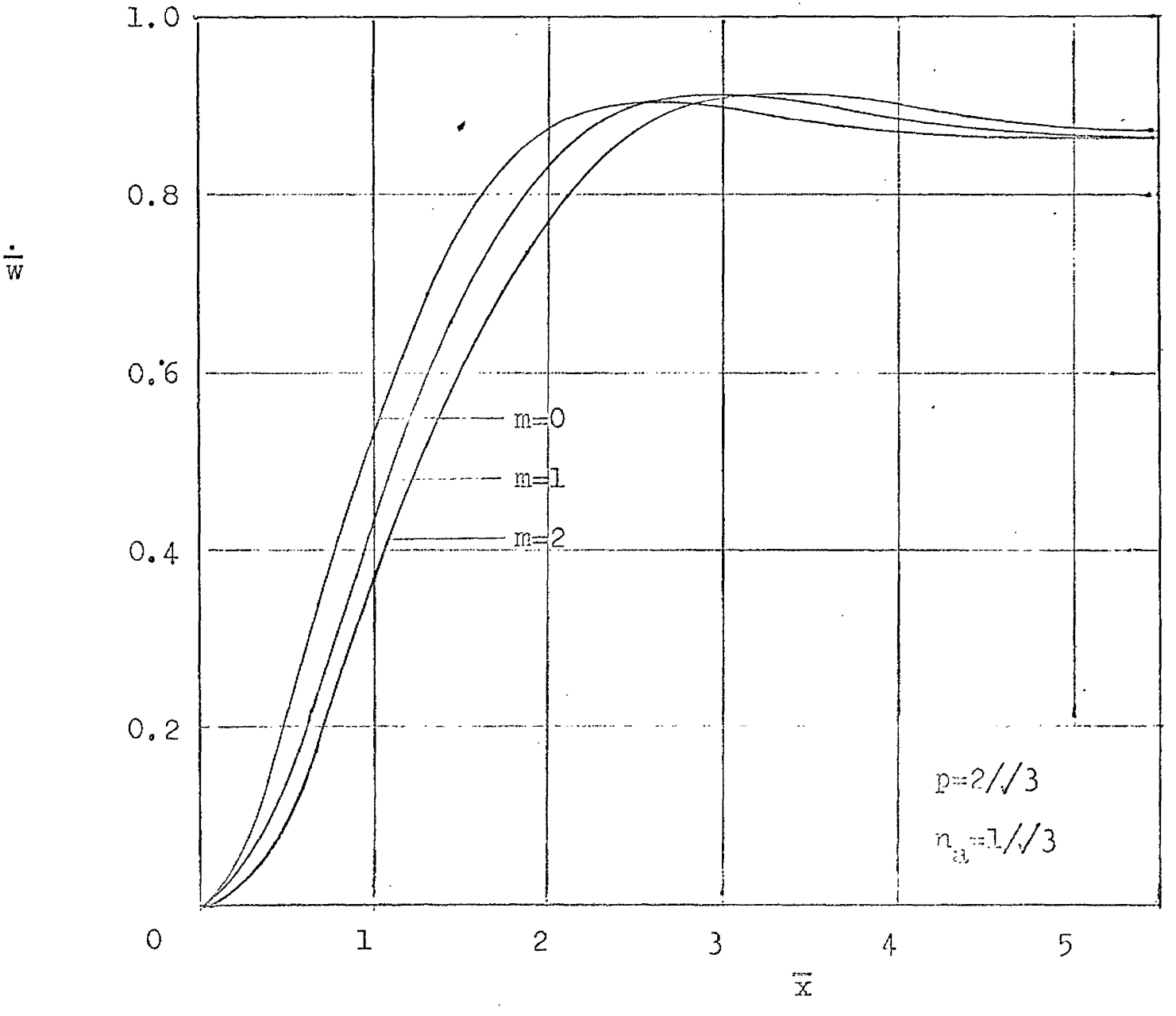

Fig.4.5 Variation of steady state radial velocity along shell

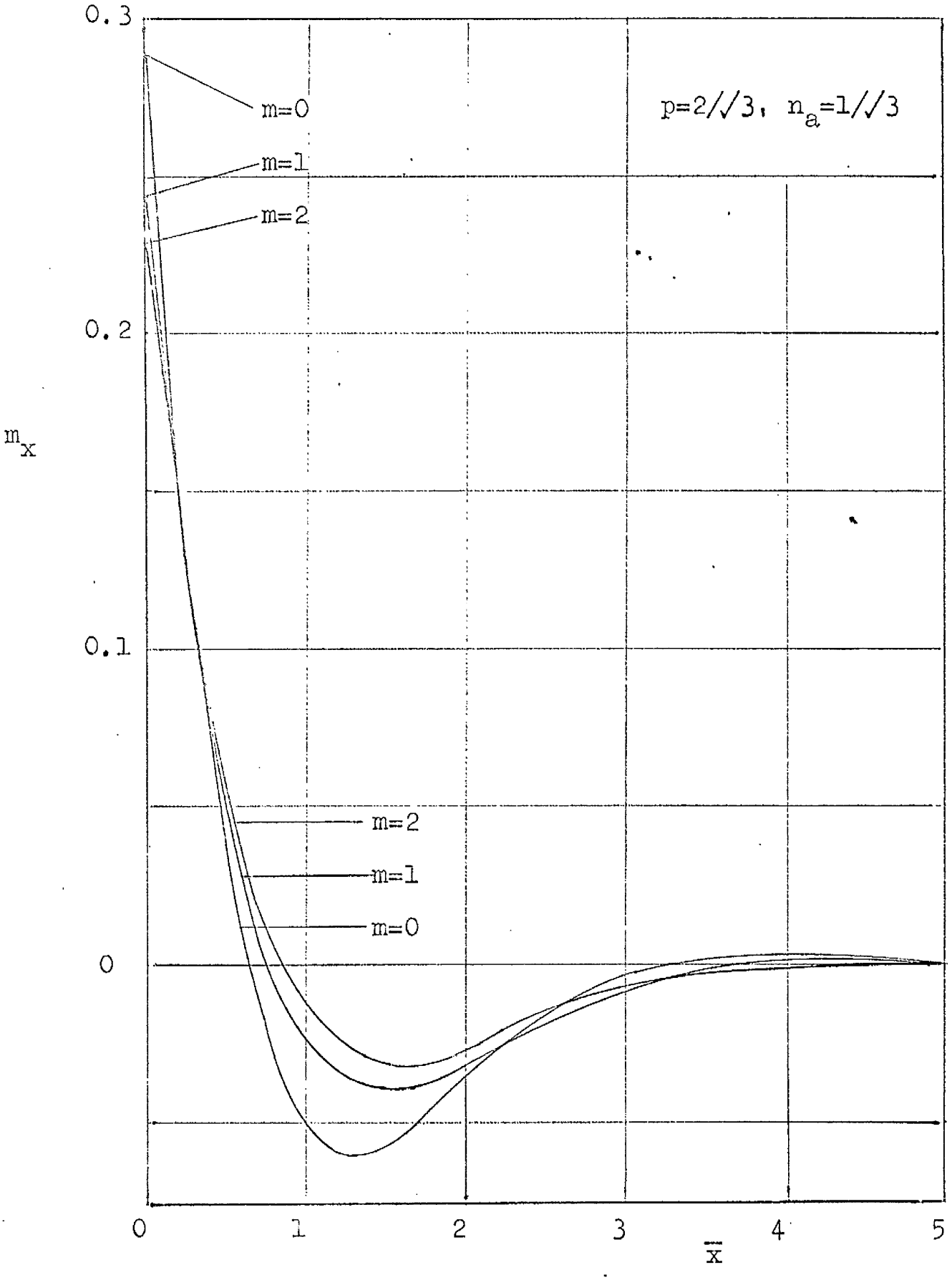

Fig.4.6 Variation of steady state bending moment along shell

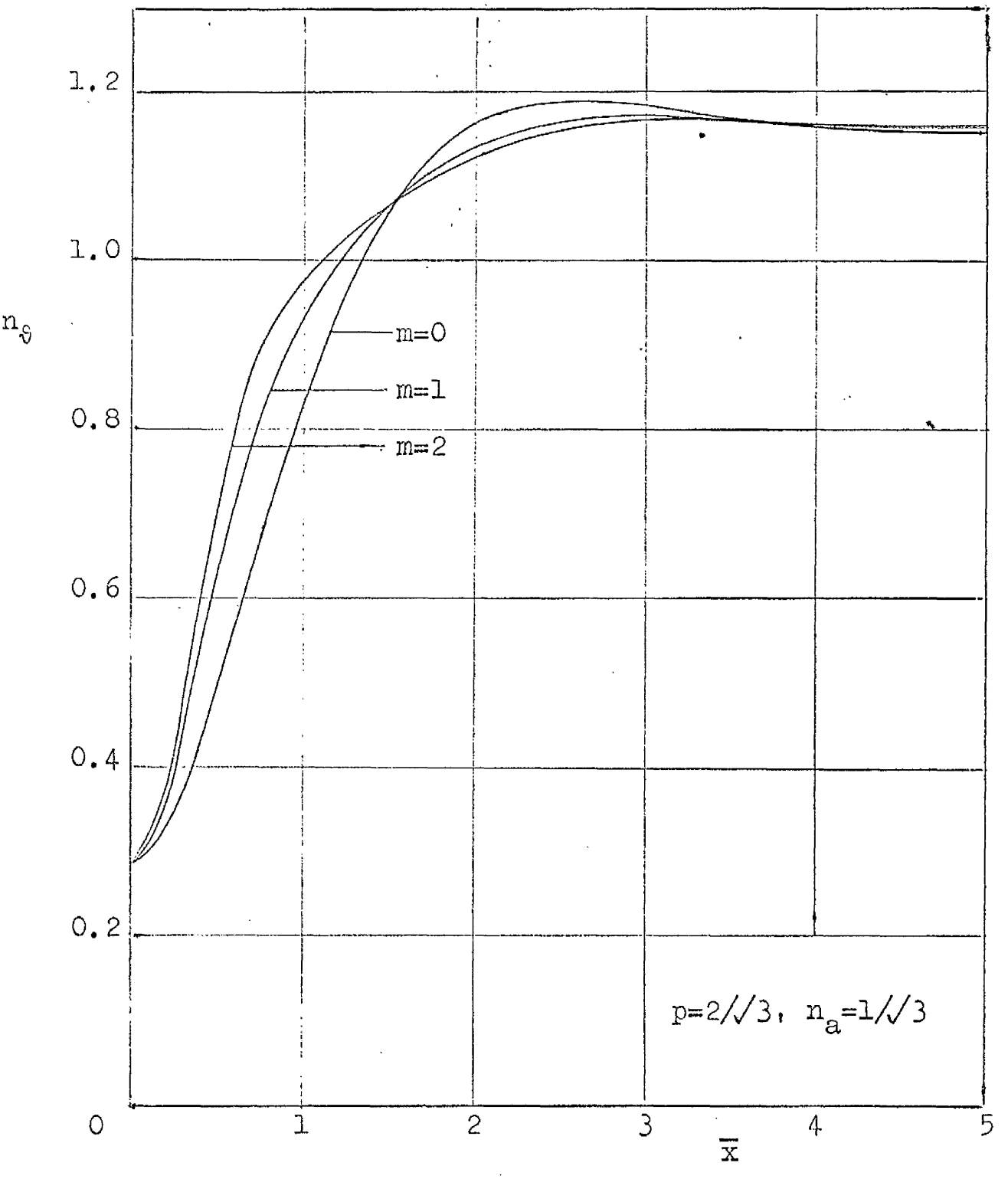

Fig.4.7 Variation of steady state hoop stress resultant along shell

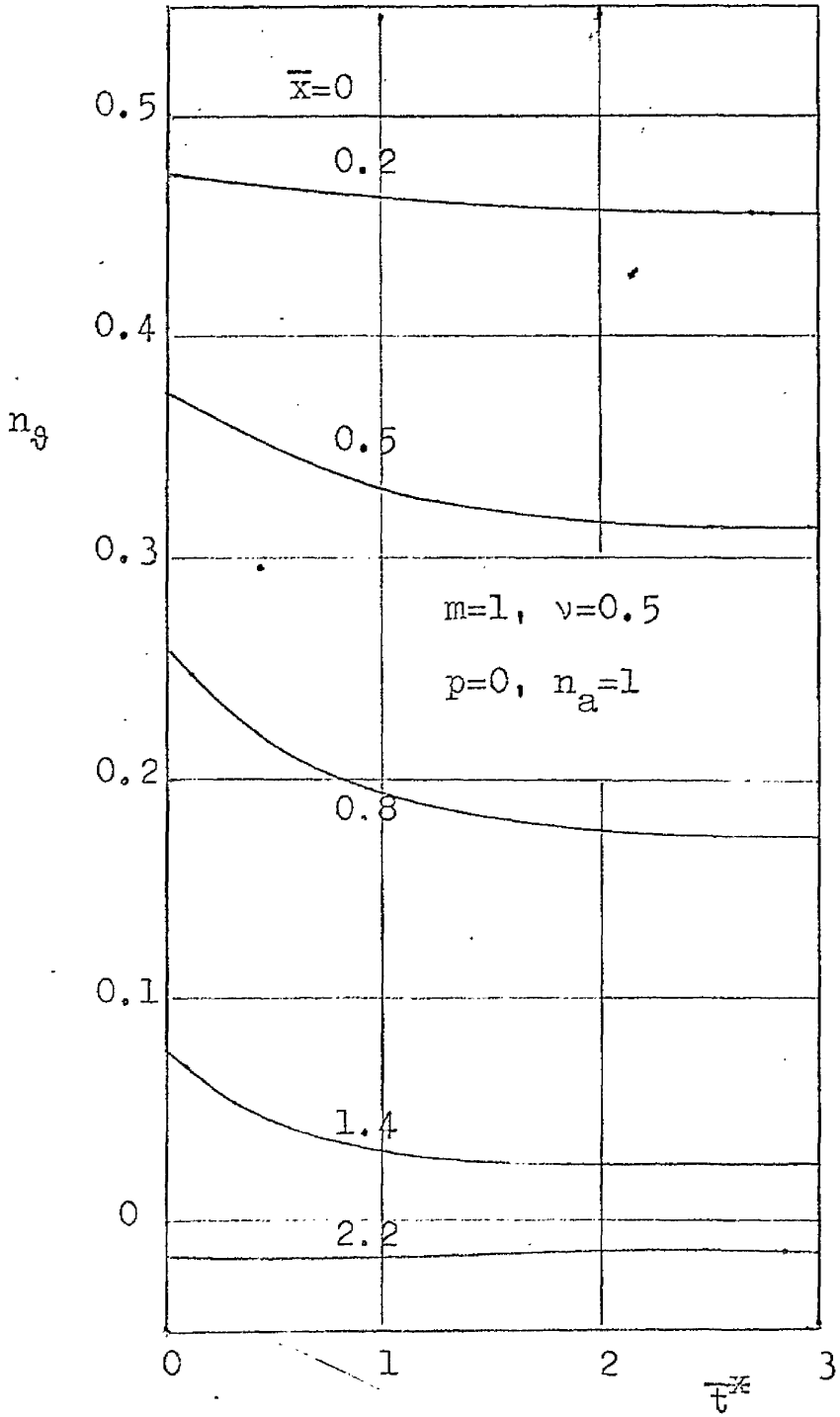

Fig.4.8 Redistribution of hoop stress resultant with time

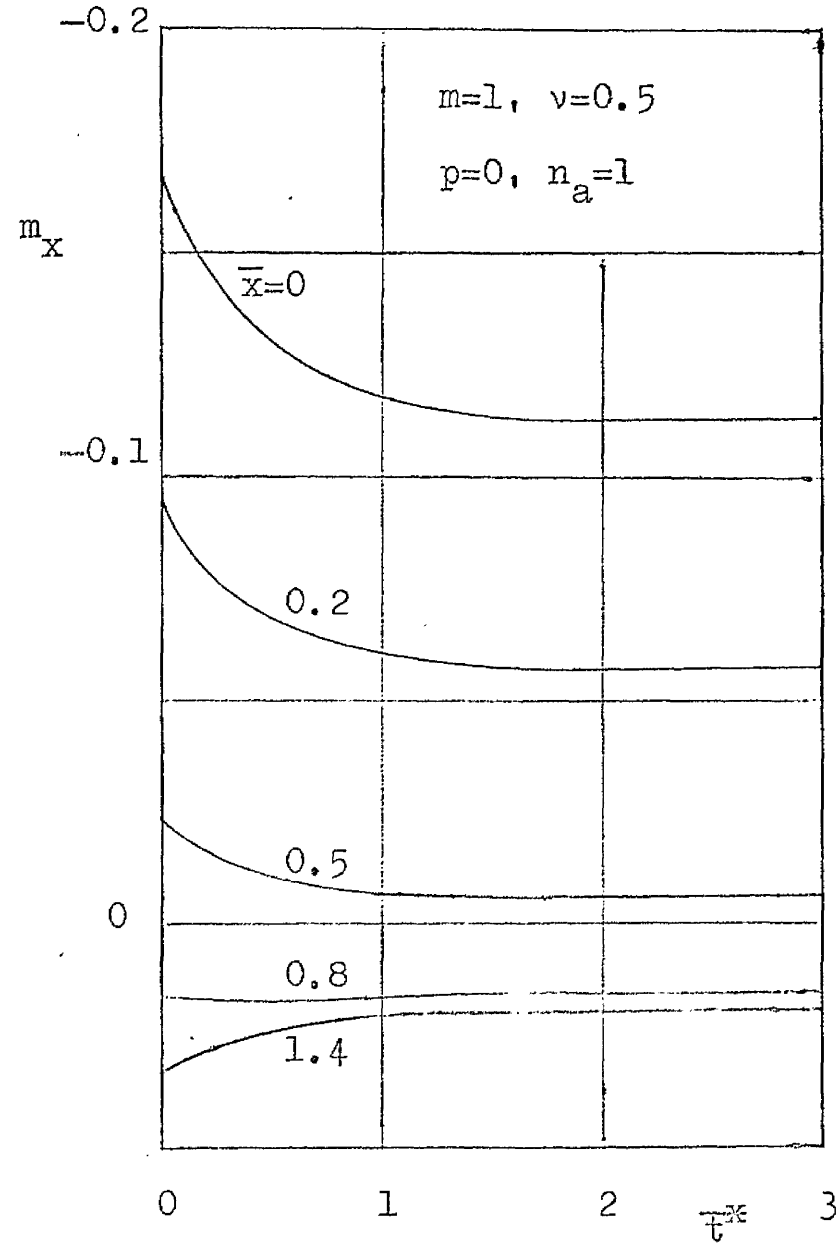

Fig.4.9 Redistribution of bending moment with time

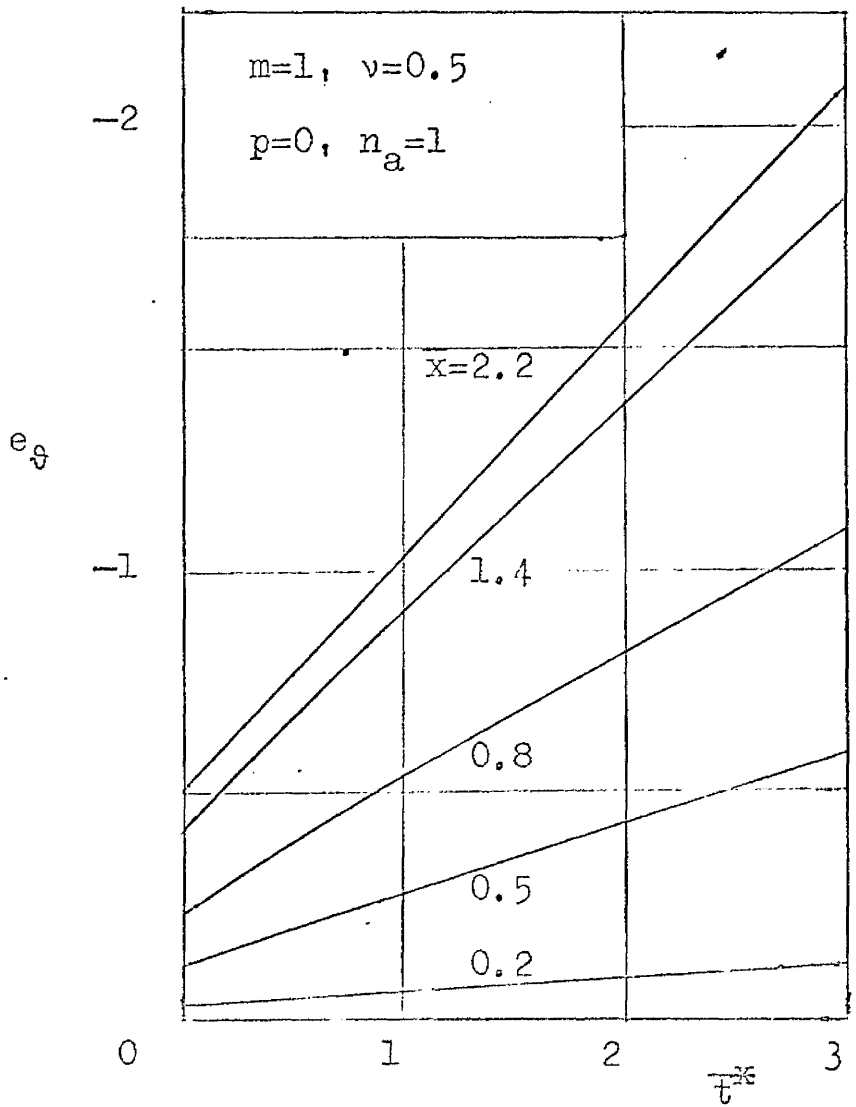

Fig.4.10 Development of hoop strain with time

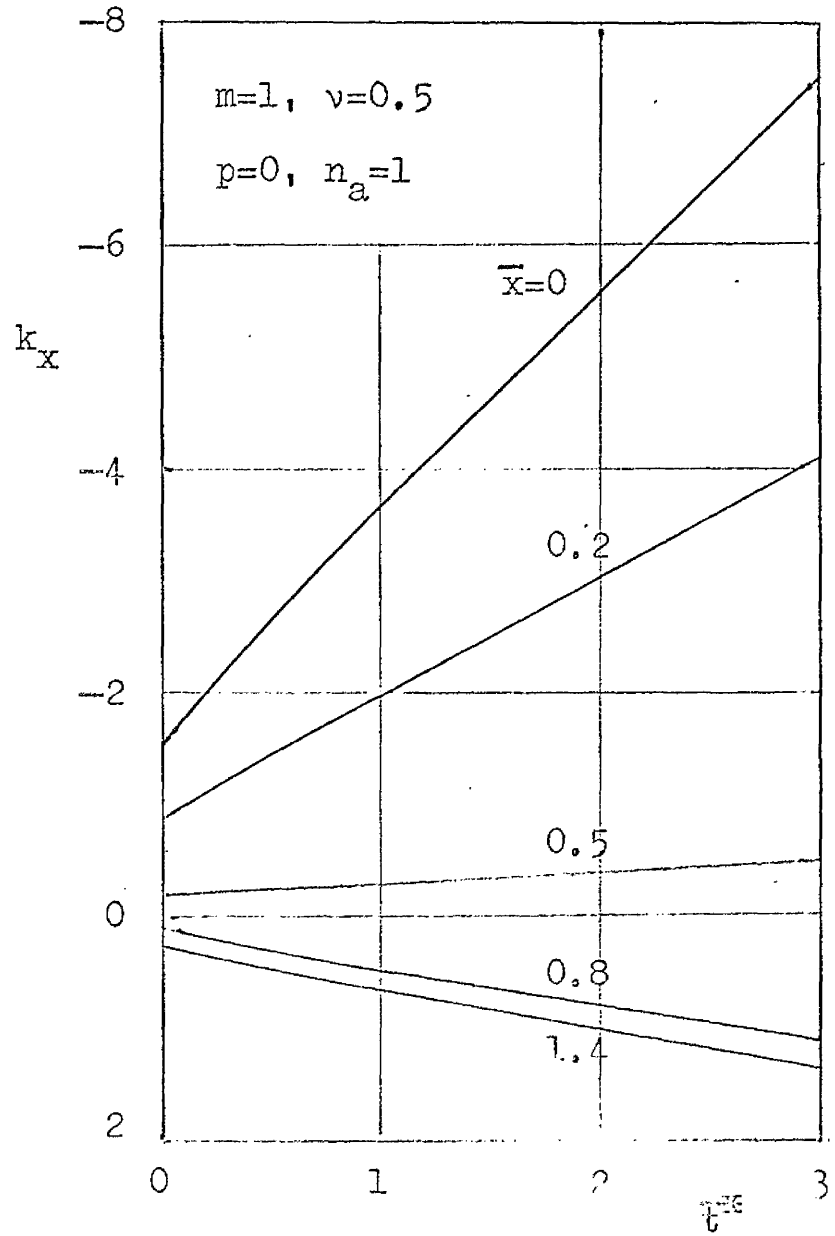

Fig.4.11 Development of curvature with time

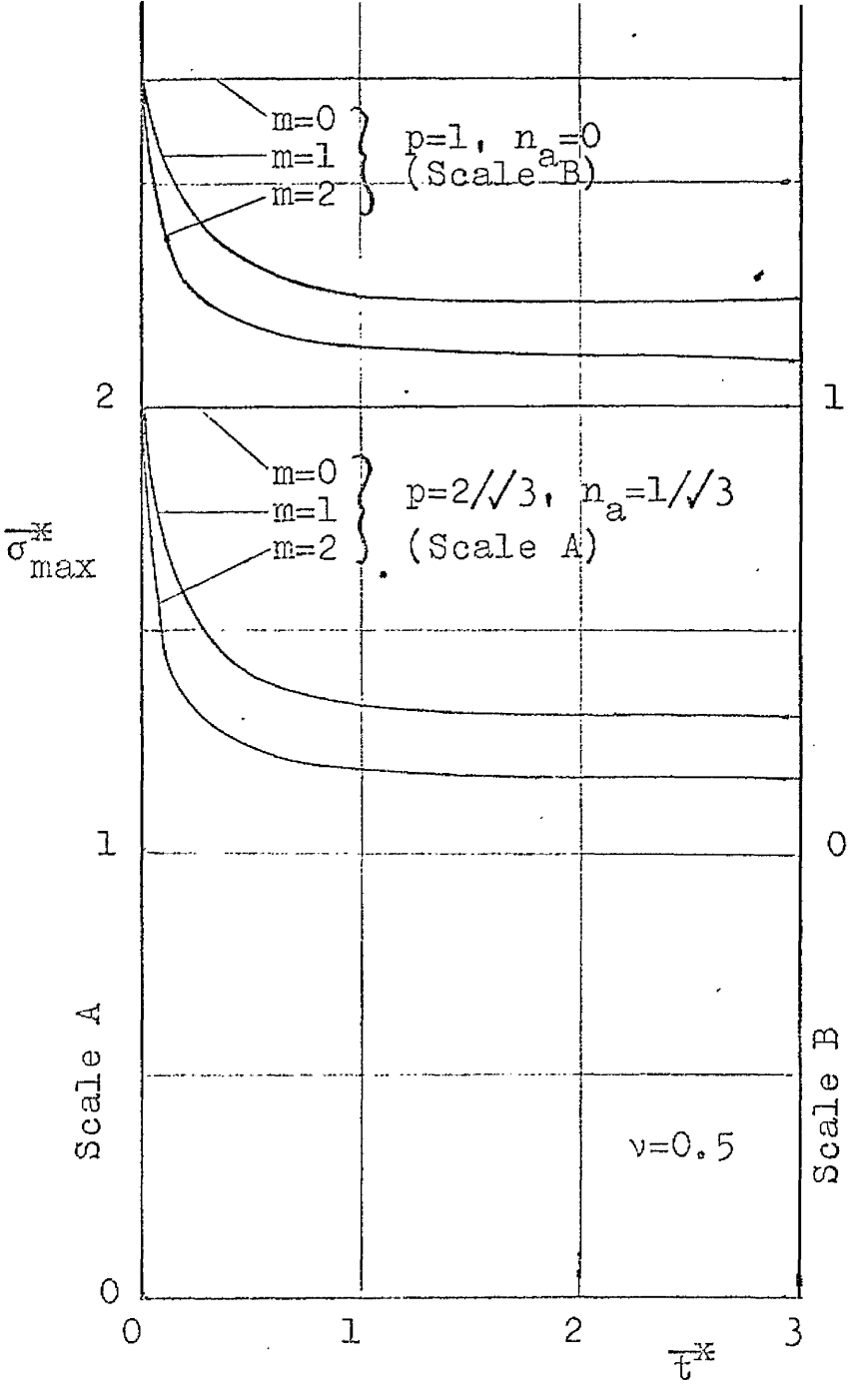

Fig.4.12 Variation of greatest effective stress with time

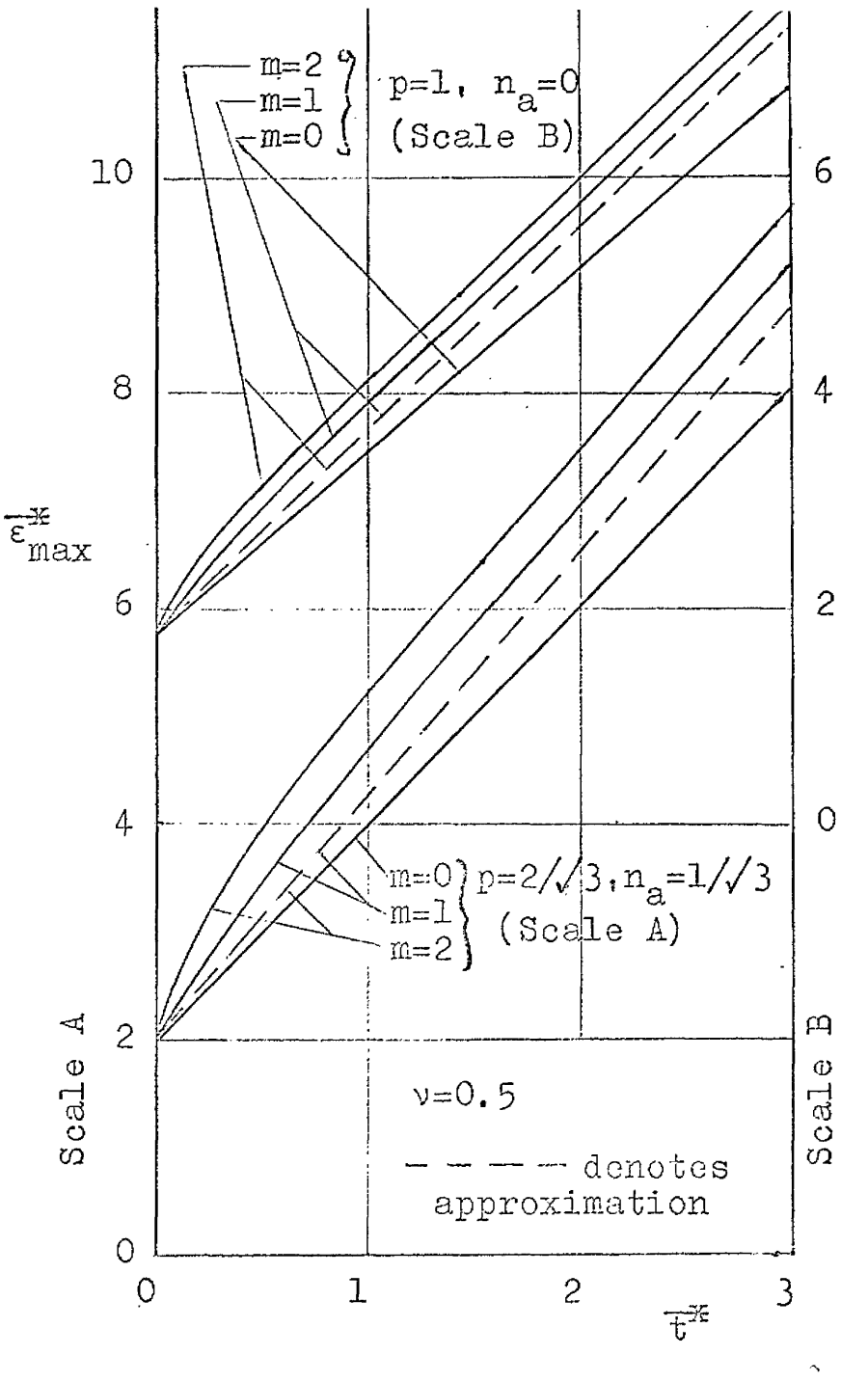

Fig.4.13 Variation of greatest effective strain with time

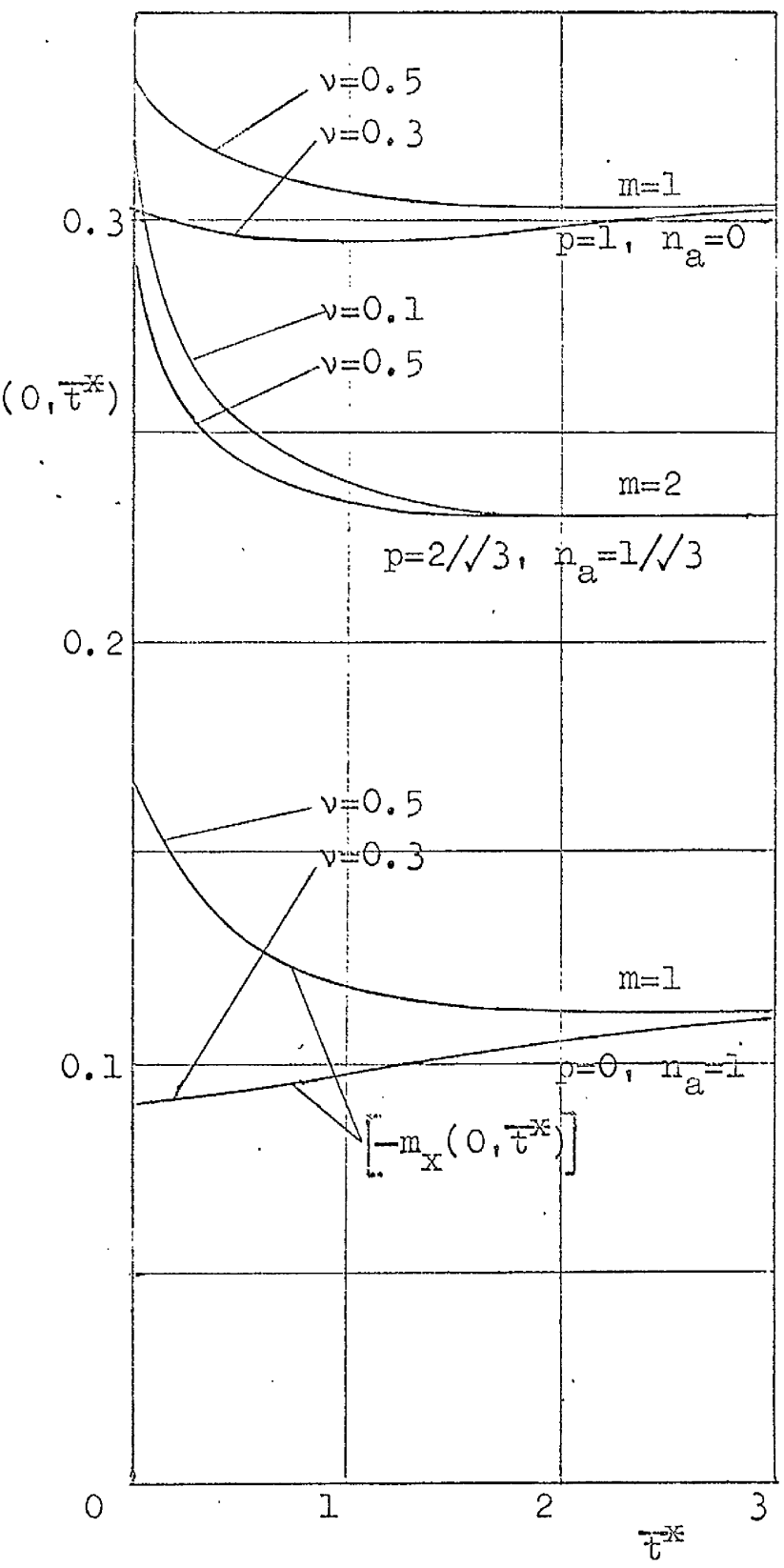

Fig.4.14 Influence of Poisson's ratio on greatest bending moment

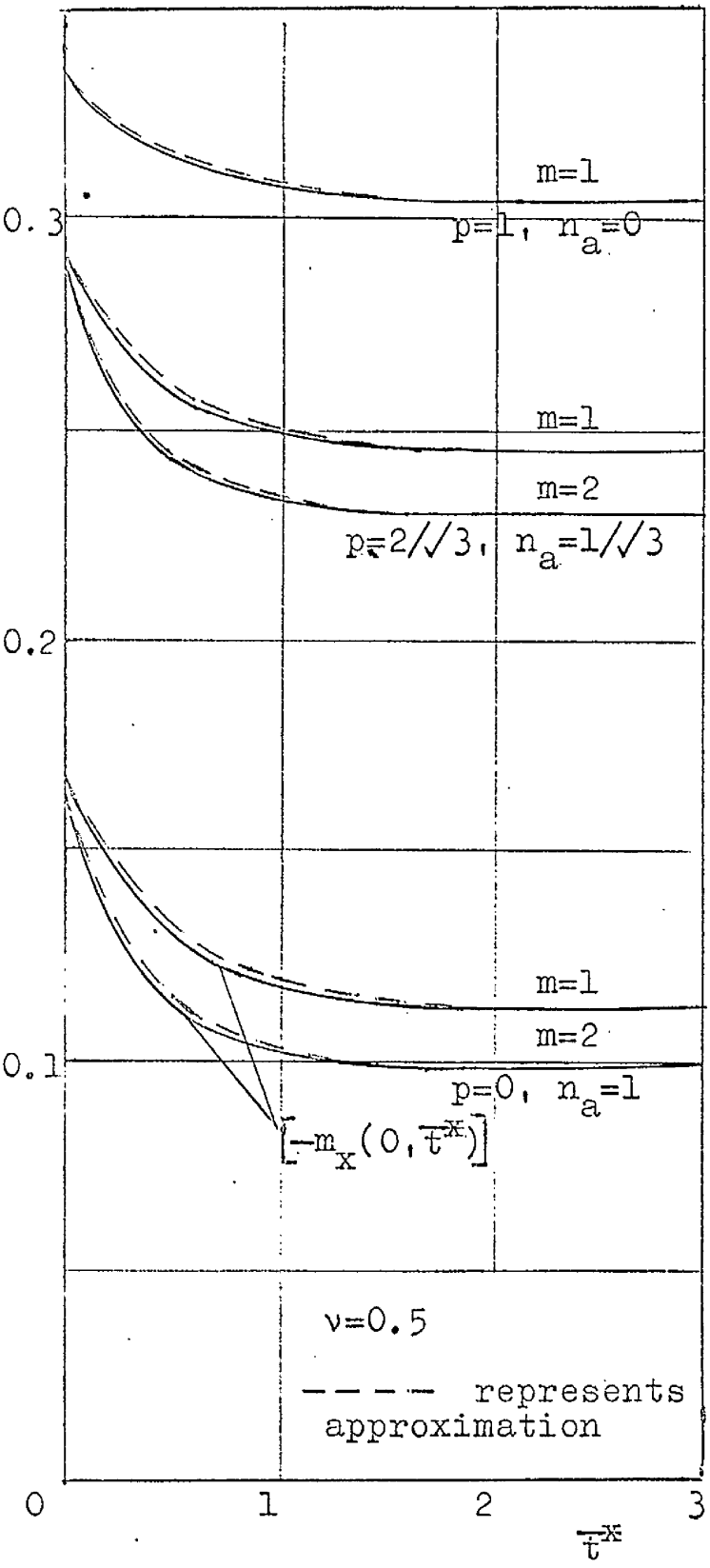

Fig.4.15 Comparison of exact and approximate variations of greatest bending moment

CHAPTER 5

APPROXIMATE STEADY STATE ANALYSIS OF A CYLINDRICAL SHELL

5.1 Formulation of Problem and Method of Solution

As indicated in Chapter 1 the steady state creep analysis of shell structures requires the use of simplified material equations if lengthy calculations are to be avoided. The authors of [21] and [22] have suggested a set of approximate relations between stress resultants and mid-surface deformation rates. These relations contain a feature of the exact expressions connecting resultants and deformation rates (obtained from equations (2.4),(2.5),(2.18)), which is not found in the linear form of the expressions - coupling between mid-surface stretching and bending actions. In non-dimensional form the approximate relations are

$$
\begin{aligned}
n_x &= \frac{4}{3}\, G^{\left(-\frac{m}{2m+1}\right)} \cdot \left(\dot{\epsilon}_x + \frac{1}{2}\dot{\epsilon}_\theta\right) \\
n_\theta &= \frac{4}{3}\, G^{\left(-\frac{m}{2m+1}\right)} \cdot \left(\dot{\epsilon}_\theta + \frac{1}{2}\dot{\epsilon}_x\right) \\
m_x &= \frac{1}{3}\, G^{\left(-\frac{m}{2m+1}\right)} \cdot \left(\frac{2m+1}{4m+3}\right)^{\left(\frac{2m+1}{m+1}\right)} \cdot \dot{k}_x
\end{aligned}
\qquad (5.1)
$$

where

$$
G = \frac{4}{3}\left[\dot{\epsilon}_x^2 + \dot{\epsilon}_x\dot{\epsilon}_\theta + \dot{\epsilon}_\theta^2 + \left(\frac{2m+1}{4m+3}\right)^{\left(\frac{2m+1}{m+1}\right)} \cdot \frac{1}{4}\dot{k}_x^2\right]
$$

Substitution of equations (5.1) and the time derivatives of the deformation-displacement equations (2.8) into

the equilibrium equations (2.7), yields the non-linear differential equations

$$4\left(\frac{1}{3}\right)^{\left(\frac{m+1}{2m+1}\right)} \phi\left(\dot{\bar{u}}' + \frac{1}{2}\dot{\bar{w}}\right) = n_a$$

$$\left(\frac{1}{3}\right)^{\left(\frac{m+1}{2m+1}\right)} \left\{\left(\frac{2m+1}{4m+3}\right)^{\left(\frac{2m+1}{m+1}\right)} \left[\phi \dot{\bar{w}}''\right]'' + 4\phi\left(\dot{\bar{w}} + \frac{1}{2}\dot{\bar{u}}'\right)\right\} = p \qquad (5.2)$$

where

$$\phi = \left[4\left(\dot{\bar{u}}'^2 + \dot{\bar{u}}'\dot{\bar{w}} + \dot{\bar{w}}^2\right) + \left(\frac{2m+1}{4m+3}\right)^{\left(\frac{2m+1}{m+1}\right)} \dot{\bar{w}}''^2\right]^{\left(-\frac{m}{2m+1}\right)} \qquad (5.3)$$

and n_a, as before, is the applied axial stress resultant. From the first of equations (5.2),

$$\dot{\bar{u}}' = \frac{3}{4}^{\left(\frac{m+1}{2m+1}\right)} \cdot \frac{n_a}{\phi} - \frac{1}{2}\dot{\bar{w}} \qquad (5.4)$$

and, when $\dot{\bar{u}}'$ is eliminated from the second of (5.2),

$$\left[\phi \dot{\bar{w}}''\right]'' + k_1 \phi \dot{\bar{w}} = k_2 \qquad (5.5)$$

where $k_1 = 3\left(\frac{4m+3}{2m+1}\right)^{\left(\frac{2m+1}{m+1}\right)}$, and $k_2 = k_1(3)^{\left(\frac{m}{2m+1}\right)}\left(p - \frac{1}{2}n_a\right)$.

The governing equation (5.5) is evidently too complex to allow closed form solution, and some iteration procedure is required. With equations (5.3), (5.5) and the boundary conditions expressed in finite difference form, a possible iteration scheme is as follows:

(1) Introduce approximate values of the function ϕ into equation (5.5).

(2) Solve (5.5) with the boundary conditions for $\dot{\bar{w}}$.

(3) Calculate $\dot{\bar{u}}'$ from equation (5.4).

(4) Obtain a new set of values for Φ from equation (5.3).

(5) Repeat steps (1)-(4) until successive values of $\dot{\bar{w}}$ are satisfactorily close.

Details of the numerical calculations are given in Appendix 4.1.

It is not possible to determine at the outset whether an iteration procedure such as that outlined will converge. Convergence in this case will depend on the sensitivity of the function ϕ to variations in $\dot{\bar{w}}$, and this cannot be discovered until solution is attempted.

For a linear material ($m=0$), $\phi=1$ for all $\bar{x}$, and, for materials with low m values, unity may be taken as a first approximation for ϕ. Where solutions are required for a range of m, ϕ functions from solutions with low m values may be used as initial approximations in iteration cycles with higher m values.

5.2 Results of Approximate Analysis and Comparison with "Exact" Solutions

Solutions were computed, as before, for a cylindrical shell with fixed ends, of length $\bar{l}=15$, and subject to the three loading systems: internal pressure, axial load-

ing and radial loading. The loading parameters p, n_a were chosen in each case as described in Section 2.3.

The accuracy of the finite difference approximation to the differential equation was estimated as before by comparing, for the linear case (m=0), the values of $\bar{\bar{w}}$ obtained from the analytical solution with those from the finite difference equations. Three figures of agreement were obtained at all stations. With this estimate of accuracy, the iteration process was continued until the first three figures of $\bar{\bar{w}}$ from several successive cycles were the same.

For low values of m, it was found that increasing numbers of iterations produced greater and greater convergence, but about m=2 the convergence of the solution reached a limit, and further iterations produced divergence. For m=3 with internal pressure and axial loading, and m=2 with radial loading, three figures of agreement of successive cycles were reached before divergence occurred, and that $\bar{\bar{w}}$ was selected which produced the least sum of the squares of the residues of the difference equations (Appendix 4.2). For values of m greater than those presented, sufficient convergence was not obtained before instability developed for the solutions to be of much value.

The extent of the agreement between the approximate solutions and the "exact" solutions of Chapter 4 is most

easily judged from Figs. 5.1 and 5.2, where, for the three loading systems, the approximate and exact steady state values of m_x and $\dot{k}_x$ at $\bar{x}=0$ are plotted against m. The comparison is seen to depend very much on the loading system, the approximations deteriorating as the axial loading n_a becomes more dominant. Agreement is good for radial loading $p=1, n_a=0$, the deviation nowhere exceeding 2.5%, but poor for axial loading $p=0, n_a=1$, the approximate moment when m=2 being 50% greater than the exact value. The approximate moment and curvature rate change relatively little as m increases, and in most cases their dependence on m is less than that of the exact functions.

The effect of the approximate relations on the distribution along the shell of the resultants and deformation rates is illustrated in Figs. 5.3-5.5 where the exact and approximate forms of m_x, n_θ and $\dot{\bar{w}}$ are plotted against $\bar{x}$ for internal pressure loading, m=1 and 2. The functions n_θ and $\dot{\bar{w}}$ are quite well estimated, the approximate decay length being slightly greater than the exact value. The greatest deviation occurs in the moment distribution, the approximate function lying for the most part above the exact curve. These features also appear with the other loading systems, although the comparison is better under radial loading, and worse under axial loading.

While the approximate solutions can be considerably

in error, they do indicate in all the cases investigated the general influence of the stress exponent m on shell behaviour: the greatest stresses diminish as m increases; the greatest strains and the decay length increase with m. In addition, they give conservative estimates of the highest stresses, though not necessarily of the highest strains. It would appear, therefore, that the approximate constitutive equations (5.1) are of some use for the investigation of the creep behaviour of other more complex shell structures, but the results they provide must clearly be used with caution.

5.3 Discussion of Approximate Solutions as $m \to \infty$

As mentioned previously, instability of the iteration process prevented solutions being obtained for large m values and the interesting limiting case of $m \to \infty$ could not be approached. As $m \to \infty$ the stress-strain rate relations (5.1) are replaced by a yield criterion and flow law which approximate to those for a shell of rigid-perfectly plastic material obeying the von Mises yield condition and associated flow rule. Complete solutions of rigid-perfectly plastic shell problems involving non-linear yield criteria are in most cases difficult to obtain[32]; however, useful information on shell behaviour can be extracted from an examination of the governing equations.

The energy dissipation rate per unit surface area is

$$\Psi = n_x \dot{e}_x + n_\theta \dot{e}_\theta + \dot{k}_x m_x \tag{5.6}$$

If the relations (5.1) are solved for deformations, and the resulting expressions introduced into (5.6), the latter becomes

$$\Psi = \left[n_x^2 - n_x n_\theta + n_\theta^2 + 3\left(\frac{4m+3}{2m+1}\right)\left(\frac{2m+1}{m+1}\right) m_x^2 \right]^{m+1}$$

As $m \to \infty$ Ψ can have a non-zero or non-infinite value only if

$$n_x^2 - n_x n_\theta + n_\theta^2 + 12 m_x^2 = 1 \tag{5.7}$$

This equation defines the yield criterion in (n_x, n_θ, m_x) space.

In limit analysis (see Hodge[32]) the deformation of a structure is assumed to be such that the strain rate vector $q(\dot{e}_x, \dot{e}_\theta, \dot{k}_x)$ is always normal to the yield surface. Thus, the components of q in the directions of the resultants are

$$\dot{e}_x = \dot{\bar{u}}' = \lambda \frac{\partial}{\partial n_x}(n_x^2 - n_x n_\theta + n_\theta^2 + 12 m_x^2) = \lambda(2n_x - n_\theta)$$

$$\dot{e}_\theta = \dot{\bar{w}} = \lambda \frac{\partial}{\partial n_\theta}(n_x^2 - n_x n_\theta + n_\theta^2 + 12 m_x^2) = \lambda(-n_x + 2n_\theta) \tag{5.8}$$

$$\dot{k}_x = \dot{\bar{w}}'' = \lambda \frac{\partial}{\partial m_x}(n_x^2 - n_x n_\theta + n_\theta^2 + 12 m_x^2) = \lambda 24 m_x$$

where λ is a positive parameter.

The cylindrical shell being considered has $n_x(\bar{x})=n_a$ and $\dot{\bar{w}}(0)=0$; hence, from the second of equations (5.8)*,

$$n_\theta(0) = \tfrac{1}{2}n_a \tag{5.9}$$

and from the yield criterion (5.7),

$$m_x(0) = \pm \frac{1}{2\sqrt{3}}\sqrt{1-\tfrac{3}{4}n_a^2} \tag{5.10}$$

The values of the loading parameters p,n_a which cause the shell with fixed ends to collapse depend on its length $\bar{l}$; however, as $\bar{l}$ increases the critical values of p,n_a tend rapidly towards those which produce collapse when the shell has unrestrained boundaries, as is shown on page 63 of reference[32]. For a shell with free edges $n_x=n_a$, $n_\theta=p, m_x=0$ for all $\bar{x}$ and from the yield criterion (5.7),

$$n_a^2 - n_a p + p^2 = 1$$

This equation is the same as (2.24) -the condition that the loading parameters must satisfy for $\dot{\bar{w}}$ to be independent of m. Hence, the numerical values of p and n_a used for the three types of loading (a),(b) and (c) -equations (2.25)- are collapse loads for the unrestrained shell. Furthermore, these values are extremely close to those causing the collapse of a long shell with fixed ends, and they may be used to calculate the edge moment. Thus, from equations (2.25)

---

* The possibility of having $\lambda(0)=0$, and hence all the deformation rates at $\bar{x}=0$ zero, is discounted, since for all finite values of m, $\dot{\bar{w}}(0)=0$ implies the result (5.9).

and (5.10),

$$\begin{aligned} &\text{(a)} \quad n_a = 0; && m_x(0) = \frac{1}{2\sqrt{3}} \\ &\text{(b)} \quad n_a = 1; && m_x(0) = -\frac{1}{4\sqrt{3}} \\ &\text{(c)} \quad n_a = \frac{1}{\sqrt{3}}; && m_x(0) = \frac{1}{4} \end{aligned} \tag{5.11}$$

The sign of $m_x(0)$ is chosen to be the same as that expected of $\dot{\bar{w}}''$ when the shell moves radially outwards in cases (a) and (c), and inwards in case (b). (It should be noted that in case (a), since there is no axial load, $m_x(0)$ is independent of the shell length.) The values (5.11) are shown in Fig. 5.1, and in each loading case they put a close lower bound on the approximate moment function.

It can be shown by examination of the exact steady state stress resultant/deformation rate equations (obtained from equations (2.4),(2.18) and (2.5)) that, when $n_a=0$, the exact edge moment is the same as that given above.

The equations governing problems of limit analysis do not, in general, restrict all the dependent variables to being continuous functions -Section 1.7, reference[32]. For example, in the cylindrical shell a discontinuity in $\dot{\bar{w}}'$ (implying infinite $\dot{\bar{w}}''$) is permissible. However, all the variables in the problem under consideration can be shown to be continuous by the following somewhat intuitive argument.

Equilibrium considerations require that the stress

resultants m_x, q_x be continuous functions -page 4, reference[32], and from the yield criterion (5.7), n_θ^2 must also be continuous. From the loading systems applied to the shell there is no reason to expect an abrupt change in the sign of n_θ, which must therefore be a continuous function. The flow law (5.8) then requires that all the deformations also be continuous.

That it is finite, is all that can be inferred about $\dot{k}_x(0)$ from examination of the governing equations. However, an interesting result of the computed solutions is that the energy dissipation rate per unit area, ψ, at $\bar{x}=0$ deviates very little from unity for all loadings and values of m investigated. (It can be shown -Appendix 4.3- that when m=0 and the shell is very long, $\psi(0)=1$ for any ratio p/n_a.) In addition, the value of $\dot{\epsilon}_x$ at $\bar{x}=0$ is found to remain almost constant at its linear (m=0) value as m increases. These computed values of $\psi(0)$ and $\dot{\epsilon}_x(0)$ are shown in Table 5.1. From consideration of the probable accuracy of these numerical values it can be concluded that $\psi(0)$ and $\dot{\epsilon}_x(0)$ are either independent of, or very insensitive to, m.

If $\psi(0)$ and $\dot{\epsilon}_x(0)$ are assumed independent of m, and ψ is expressed in terms of the deformations, $\dot{k}_x(0)$ can be calculated. From equations (5.1) and (5.6),

$$\psi = \frac{2}{\sqrt{3}} \left(\dot{\epsilon}_x^2 + \dot{\epsilon}_x\dot{\epsilon}_\theta + \dot{\epsilon}_\theta^2 + \frac{1}{16}\dot{k}_x^2\right)^{\frac{1}{2}}$$

	$p=1,\ n_a=0$		$p=\frac{2}{\sqrt{3}},\ n_a=\frac{1}{\sqrt{3}}$		$p=0,\ n_a=1$	
m	$\psi(0)$	$\dot{\bar{u}}'(0)$	$\psi(0)$	$\dot{\bar{u}}'(0)$	$\psi(0)$	$\dot{\bar{u}}'(0)$
0	1	0	1	0.433	1	0.750
0.25	0.999	0	0.999	0.433	0.999	0.750
1	0.996	0	0.995	0.432	0.999	0.750
2	0.995	0	0.997	0.432	0.996	0.748
3	-	0	0.991	0.430	0.991	0.745

Table 5.1

as $m\to\infty$. At $\bar{x}=0$, $\dot{\epsilon}_e=0, \psi=1$ and therefore,

$$1 = \frac{4}{3}\left(\dot{\epsilon}_x^2(0) + \frac{1}{16}\dot{k}_x^2(0)\right) \tag{5.12}$$

With the linear value of $\dot{\epsilon}_x(0)$ corresponding to the loading system, $\dot{k}_x(0)$ can be obtained from equation (5.12):

$$\text{(a)}\quad p=1, n_a=0;\quad \dot{\epsilon}_x(0)=0,\quad \therefore \dot{k}_x(0) = 2\sqrt{3}$$

$$\text{(b)}\quad p=0, n_a=1;\quad \dot{\epsilon}_x(0)=\frac{3}{4},\quad \therefore \dot{k}_x(0) = \sqrt{3} \tag{5.13}$$

$$\text{(c)}\quad p=\frac{2}{\sqrt{3}}, n_a=\frac{1}{\sqrt{3}};\quad \dot{\epsilon}_x(0)=\frac{\sqrt{3}}{4},\quad \therefore \dot{k}_x(0) = 3$$

In Fig. 5.2 it can be seen that these values of $\dot{k}_x(0)$ put close upper bounds on the approximate curvature rate functions.

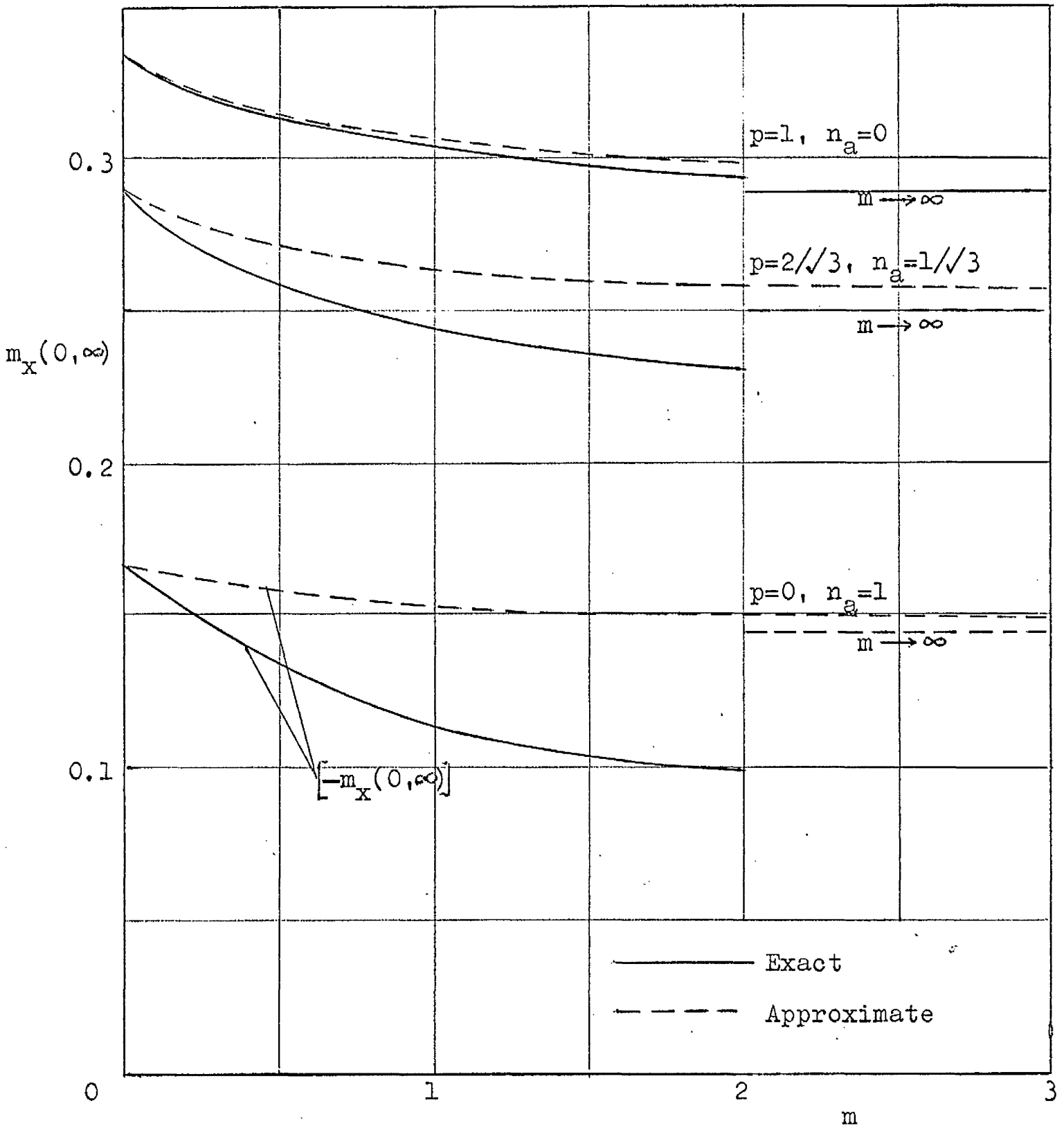

Fig.5.1 Comparison of approximate and exact steady state values of greatest bending moment

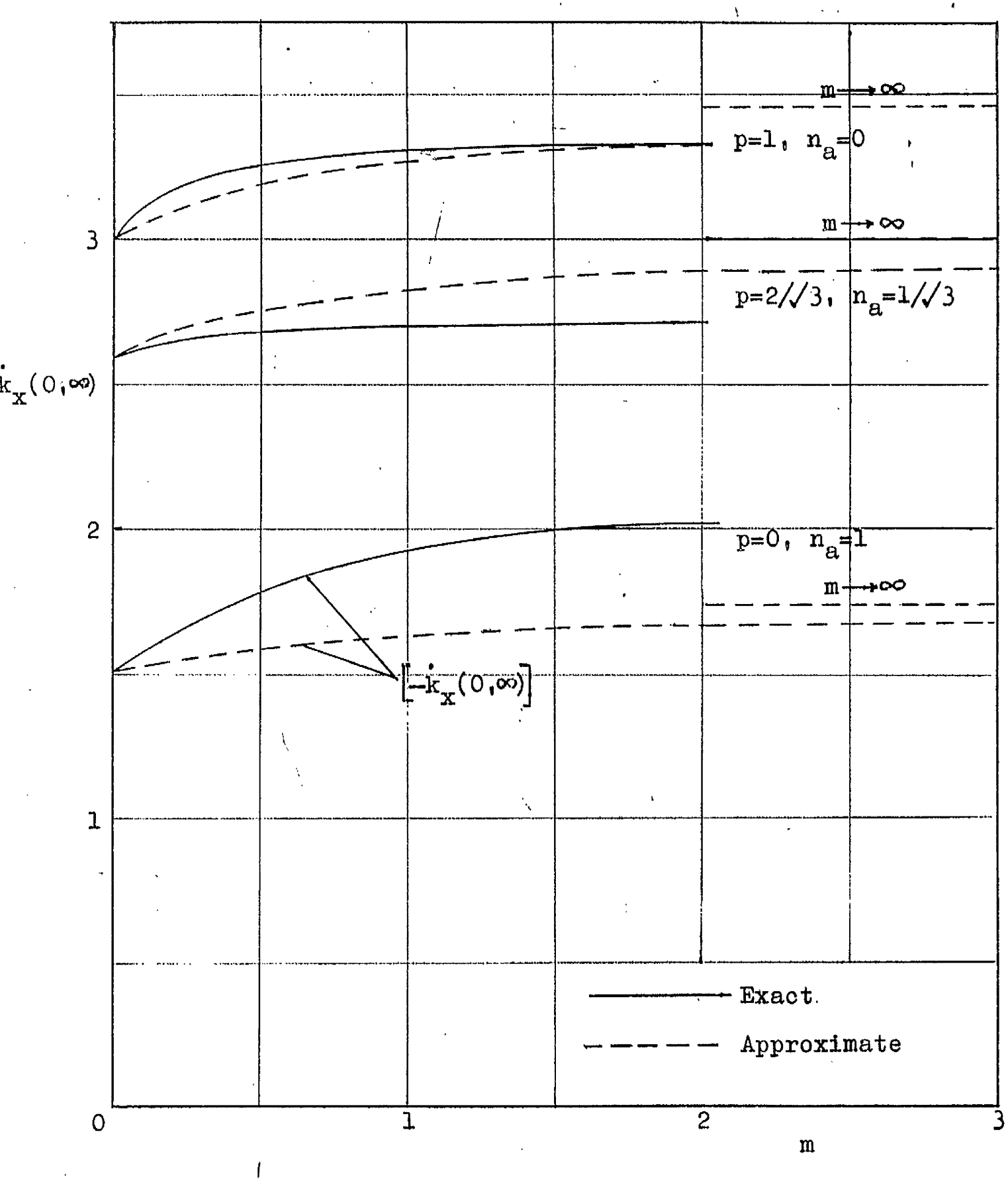

Fig. 5.2 Comparison of approximate and exact steady state values of greatest curvature rate

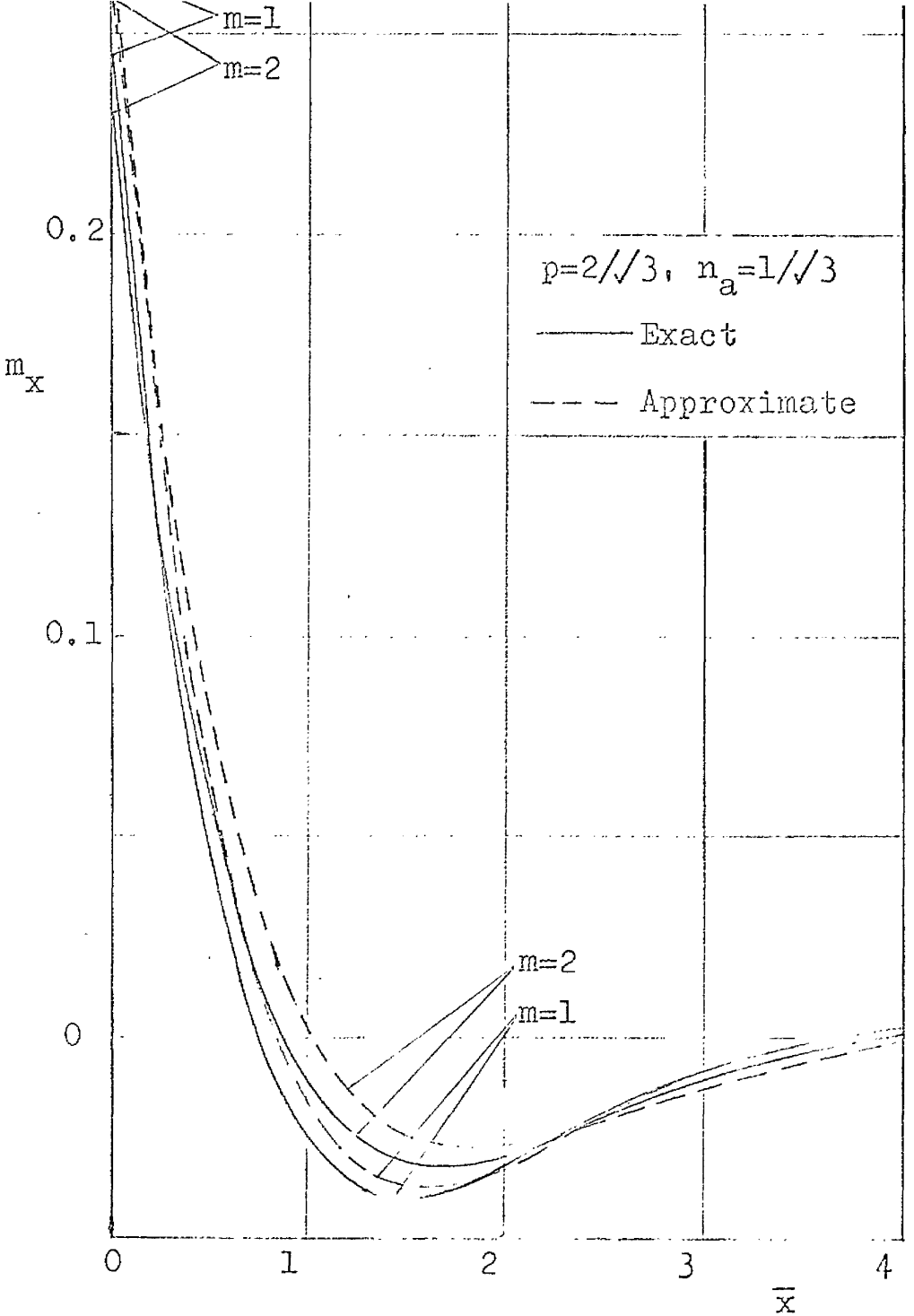

Fig.5.3 Comparison of approximate and exact variations along shell of steady state bending moment

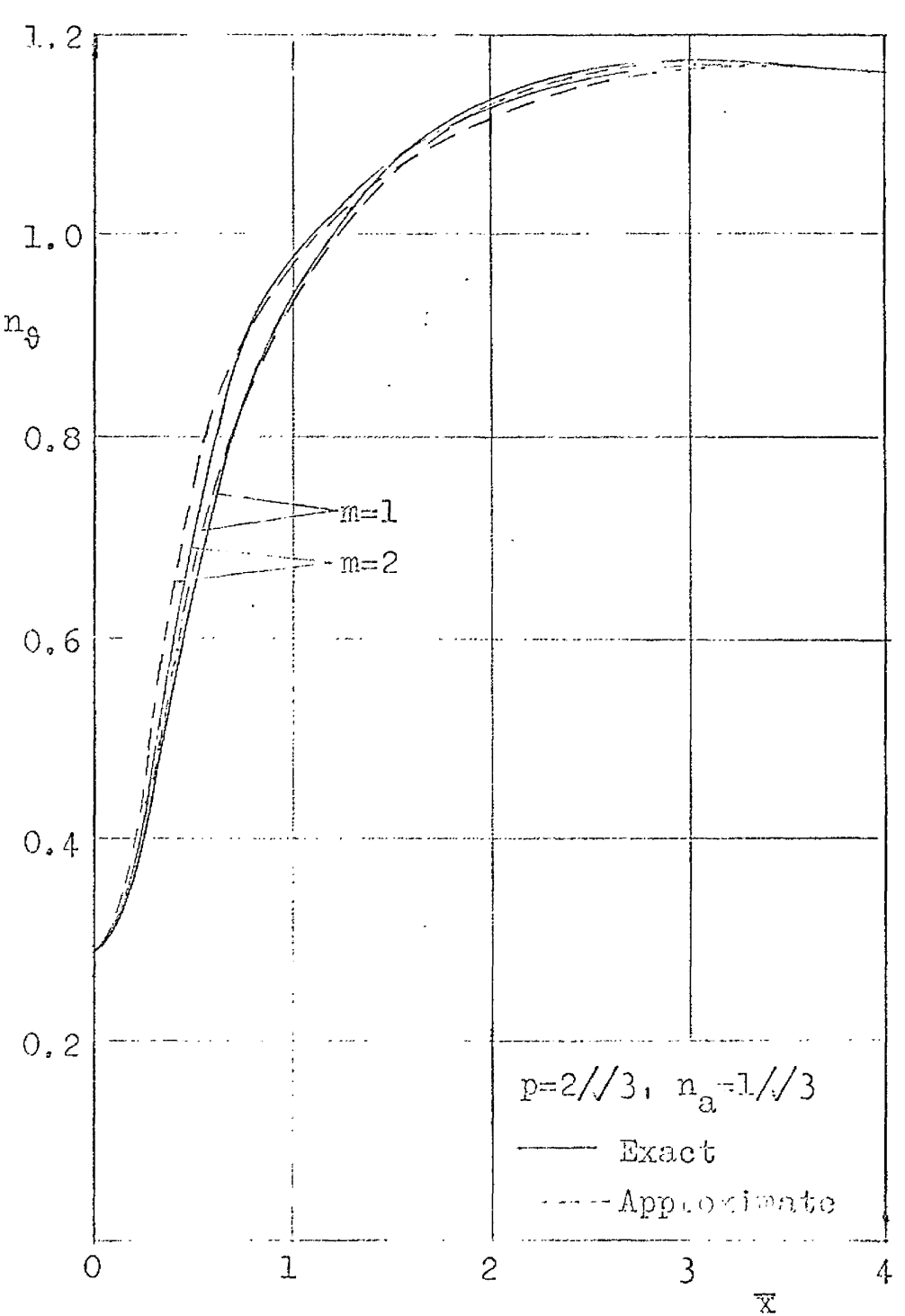

Fig.5.4 Comparison of approximate and exact variations along shell of steady state hoop stress resultant

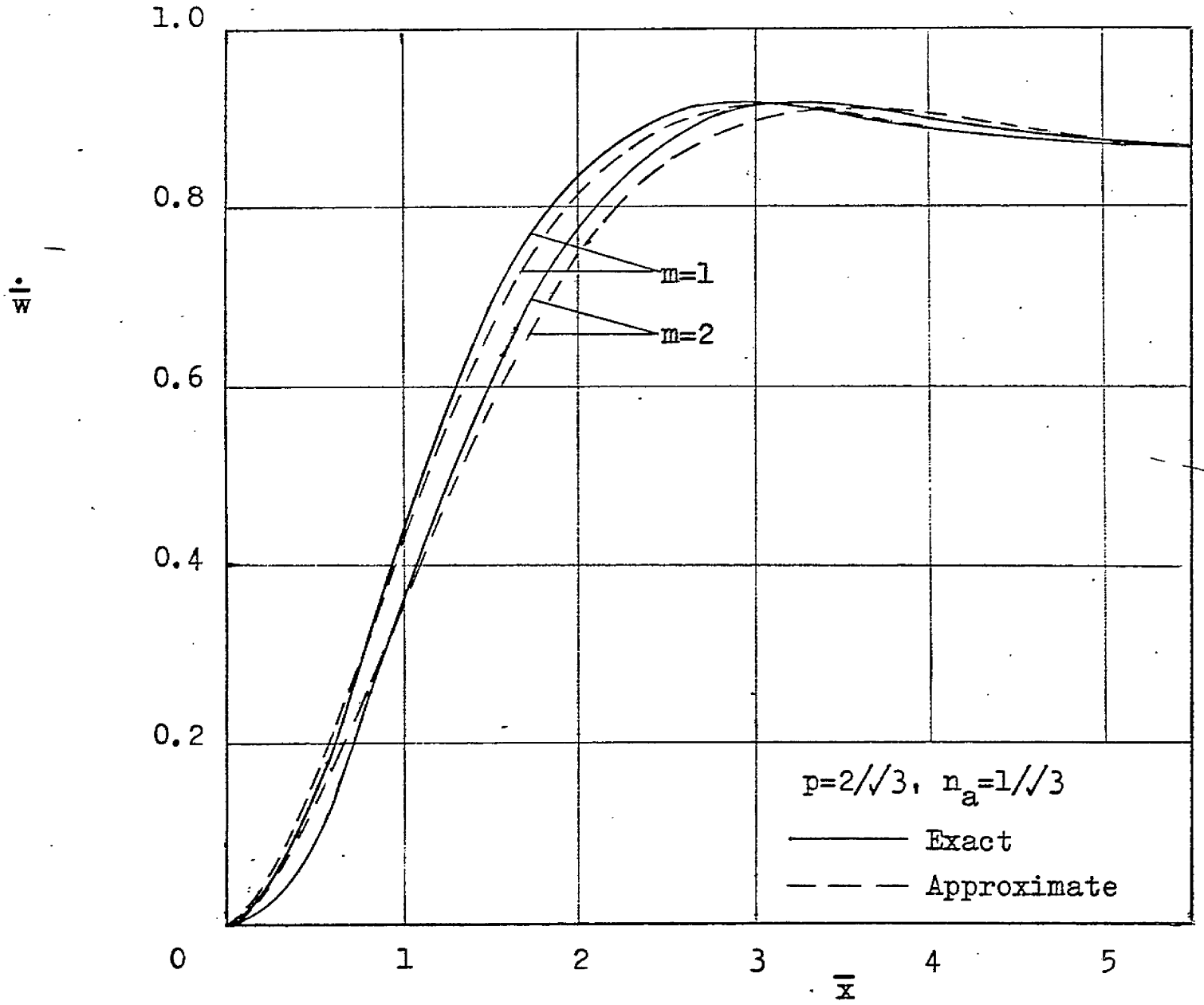

Fig.5.5 Comparison of approximate and exact variations along shell of steady state radial velocity

CHAPTER 6

APPROXIMATE STEADY STATE ANALYSIS OF A CYLINDRICAL SHELL WITH AN ABRUPT THICKNESS CHANGE

6.1 Formulation of Problem and Method of Solution

Since the approximate constitutive equations used in the previous chapter provide solutions which are qualitatively similar to those obtained with the exact constitutive equations, it was considered worthwhile to extend the simpler steady state analysis to the problem of a cylindrical shell with a thickness discontinuity subject, as before, to uniform axial and radial loading-Fig. 6.1.

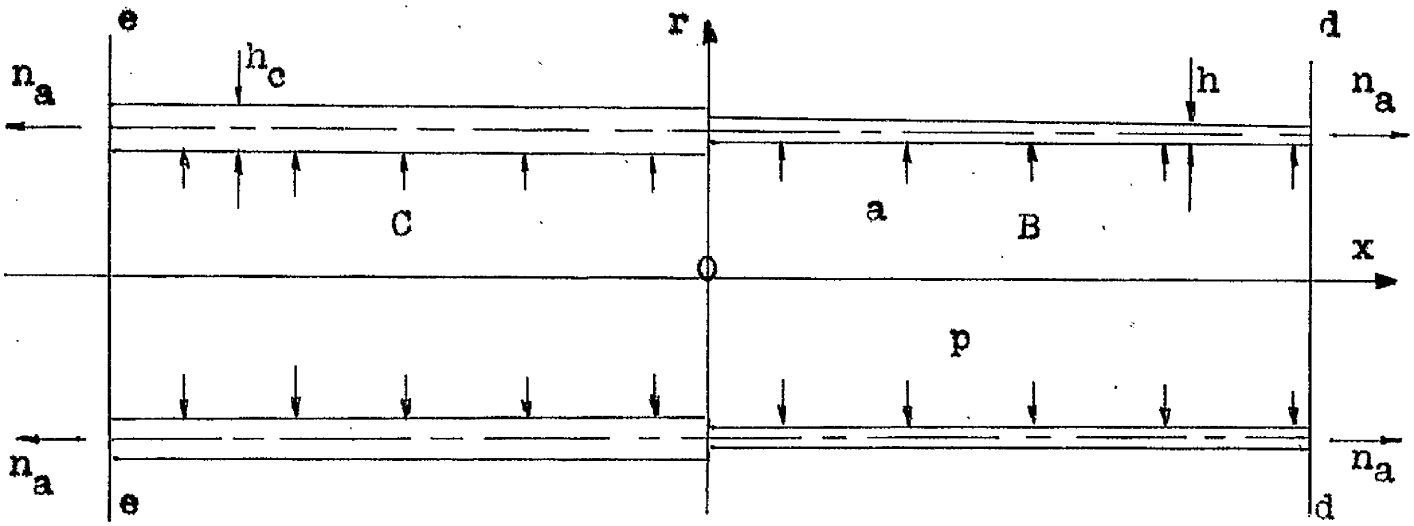

B and C denote the thin and thick portions of the shell, respectively.

Fig. 6.1

If all the variables are non-dimensionalized (as in Chapter 2) with the thickness h of shell B, the equations

governing the latter are (5.1),(5.3),(5.4),(5.5), and the corresponding equations for shell C may be written

$$n_{cx} = \frac{4}{3}G_c\left(\frac{m}{2m+1}\right).R\left(\dot{e}_{cx}+\frac{\dot{e}_{ce}}{2}\right)$$

$$n_{ce} = \frac{4}{3}G_c\left(\frac{m}{2m+1}\right).R\left(\dot{e}_{ce}+\frac{\dot{e}_{cx}}{2}\right)$$

$$m_{cx} = \frac{1}{3}G_c\left(\frac{m}{2m+1}\right).R^3\left(\frac{2m+1}{4m+3}\right)\left(\frac{2m+1}{m+1}\right).\dot{k}_{cx} \qquad (6.1)$$

where,

$$G_c = \frac{4}{3}\left[\dot{e}_{cx}^2 + \dot{e}_{cx}\dot{e}_{ce} + \dot{e}_{ce}^2 + \frac{R^2}{4}\left(\frac{2m+1}{4m+3}\right)\left(\frac{2m+1}{m+1}\right)\dot{k}_{cx}^2\right]$$

$$\phi_c = R\left[4\left(\dot{\bar{u}}_c'^2 + \dot{\bar{u}}_c'\dot{\bar{w}}_c + \dot{\bar{w}}_c^2\right) + R^2\left(\frac{2m+1}{4m+3}\right)\left(\frac{2m+1}{m+1}\right)\dot{\bar{w}}_c''^2\right]^{\left(\frac{m}{2m+1}\right)} \qquad (6.2)$$

$$\dot{\bar{u}}_c' = \frac{3}{4}\left(\frac{m+1}{2m+1}\right).\frac{n_a}{\phi_c} - \frac{\dot{\bar{w}}_c}{2} \qquad (6.3)$$

$$\left[\phi_c\dot{\bar{w}}_c''\right]'' + k_{c1}\phi_c\dot{\bar{w}}_c = k_{c2} \qquad (6.4)$$

where $k_{c1} = \frac{k_1}{R^2}$, and $k_{c2} = \frac{k_2}{R^2}$

In the above equations the subscript 'c' denotes variables of shell C, and the thickness ratio $R = \frac{h_c}{h}$.

To ensure that the two shells remain attached during deformation and that the junction strain rates are finite, the radial velocities must be such that

$$\dot{\bar{w}}(0) = \dot{\bar{w}}_c(0) \;; \quad \dot{\bar{w}}'(0) = \dot{\bar{w}}_c'(0) \qquad (6.5)$$

In addition, equilibrium considerations require that

$$m_x(0) = m_{cx}(0) \; ; \quad q_x(0) = q_{cx}(0) \qquad (6.6)$$

These junction forces may be expressed in terms of velocities by means of equations (2.6),(2.8),(5.1) and (6.1):

$$\begin{aligned}
m_x(0) &= (\tfrac{1}{3})(\tfrac{m}{2m+1}) \cdot \frac{\phi(0)}{k_1} \dot{\bar{w}}''(0) \\
q_x(0) &= -(\tfrac{1}{3})(\tfrac{m}{2m+1}) \frac{1}{k_1} \left[\phi'(0)\dot{\bar{w}}''(0) + \phi(0)\dot{\bar{w}}'''(0)\right] \\
m_{cx}(0) &= (\tfrac{1}{3})(\tfrac{m}{2m+1}) \cdot \frac{\phi_c(0)}{k_{c1}} \dot{w}_c''(0) \\
q_{cx}(0) &= -(\tfrac{1}{3})(\tfrac{m}{2m+1}) \frac{1}{k_{c1}} \left[\phi_c'(0)\dot{w}_c''(0) + \phi_c(0)\dot{w}_c'''(0)\right]
\end{aligned} \qquad (6.7)$$

To avoid the additional computation which would be necessary if conditions different from those at the junction are specified at the far ends of the shell, the latter is assumed to be symmetrical about the lines dd and ee -Fig.6.1.

The method of solution is similar to that of Chapter 5, the iteration sequence being as follows:

(1) Introduce values of the functions ϕ and ϕ_c into equations (5.5)and(6.4) respectively.

(2) Solve equations (5.5) and (6.4) with the junction equations (6.5)-(6.7) for $\dot{\bar{w}}$ and $\dot{w}_c$.

(3) Calculate $\dot{\bar{u}}'$ and $\dot{u}_c'$ from equations (5.4) and (6.3) respectively.

(4) Obtain new estimates of ϕ and ϕ_c from equations

(5.3) and (6.2) respectively.

(5) Repeat stages (1)-(4) until successive values of $\dot{\bar{w}}$ and $\dot{\bar{w}}_c$ are satisfactorily close.

6.2 Results and Discussion

The lines of symmetry dd and ee were set at 8 units from the junction - a distance sufficient to allow regions of uniform strain to exist in both halves of the shell, and solutions were obtained for internal pressure loading and several values of R. Here, the values of the loading parameters p, n_a (Section 2.3) were chosen to make the radial velocity of the membrane region of shell B independent of m.

The divergence of the iteration process which limited the analysis of the shell with fixed ends (Chapter 5), also occurred in this problem. However, the value of m at which instability developed increased as the thickness ratio R decreased, so that when R=2 useful solutions were obtained with m values up to 4.

The variations of $\dot{\bar{w}}, n_\theta, m_x$ with $\bar{x}$ for internal pressure, R=2 and several values of m are shown in Figs. 6.2-6.4, and in Figs. 6.5 and 6.6 the greatest values of m_x and $\dot{k}_x$ occurring in the thinner shell are plotted against m for R=2,3,4 and $R \to \infty$. (As $R \to \infty$ the problem becomes that of a cylindrical shell with fixed ends; solutions shown for $R \to \infty$

in this chapter were obtained from the analyses of Chapter 5.)

The most striking feature of these solutions, contrasting with the behaviour at a clamped edge (where the approximate solutions are fairly insensitive to m), is the considerable change with m of the radial velocity and stress resultant distributions. This result could, of course, have been predicted, since the membrane velocity of the thinner shell is independent of m, while that of the thicker shell - proportional to $(\frac{1}{R})^{2m+1}$ - diminishes rapidly as m increases. The influence of m on the solutions can be further explained by considering the rigid-perfectly plastic ($m \to \infty$) response of the shell.

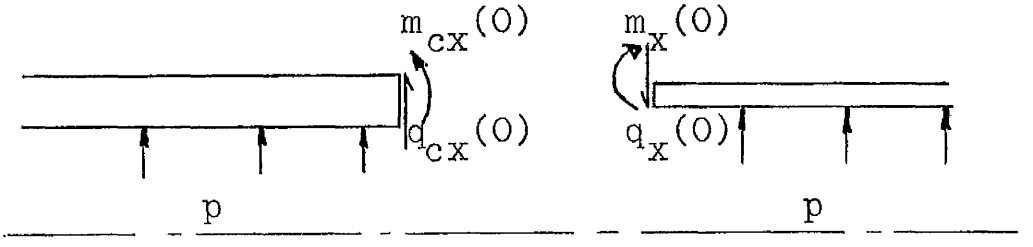

(a) Forces on shells at junction.

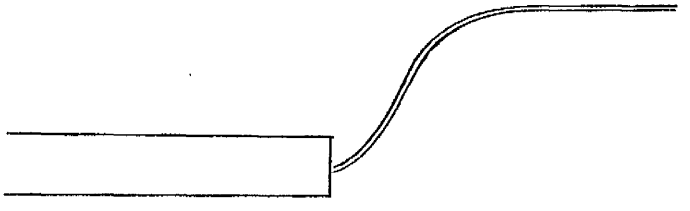

(b) Collapse mode for large thickness ratios.

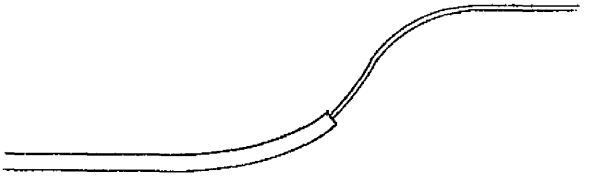

(c) Collapse mode for small thickness ratios.

Fig. 6.7

Fig. 6.7(a) shows the bending moments and shear stress resultants acting on the shells at the junction. When R is large the rigid-perfectly plastic behaviour of the thinner shell is the same as that of a shell with a clamped ($R\to\infty$) edge. This mode of deformation - Fig. 6.7(b) - will prevail as long as the thicker shell remains rigid under the action of internal pressure, and of junction forces equal to those at a clamped edge. At some small value of R the thicker shell will be unable to support this combined loading; yielding will occur in the region of the junction, and the deformation mode on collapse will be as shown in Fig. 6.7(c). In this second collapse mode the junction bending moment and the curvature rate of the thinner shell at the junction will be less than those at a clamped edge.

In Figs. 6.5 and 6.6 the moment and curvature rate functions when R=3 and 4 increase with m from fairly small linear (m=0) values, and rapidly approach the larger rigid-perfectly plastic values of the clamped ($R\to\infty$) edged shell. This suggests that these plastic limits are common to shells with thickness ratios of the order of three and above. When R=2 the behaviour as $m\to\infty$ is less certain. At m=4, $m_x(0)$ is 83% of the clamped edge plastic value, but $\dot{k}_x(0)$ is only 28% of the corresponding curvature rate. (The large peak values of m_x in Fig. 6.4 occur in the thicker shell, and are associated with stresses which are always

less than the greatest stress in the thinner shell.) To determine whether $m_x(0)$ and $\dot{k}_x(0)$ in this case tend to the clamped edge values, or to some lower limits would require numerical solutions with higher m values, or a full analysis of the rigid-perfectly plastic problem. It seems probable that it is in the region of the thickness ratio two that the change in the collapse mode occurs.

The manner in which $\dot{k}_x(0)$ increases with R and m directly affects the behaviour of the greatest effective strain rate, $\dot{\bar{\varepsilon}}_d^*$, at the discontinuity (i.e. $\bar{x}=0, \bar{z}=\frac{1}{2}$). (This quantity may be regarded as a strain rate concentration, since the effective strain rate in the membrane region of the shell is unity, with the loading parameters chosen as in Section 2.3) Fig. 6.3 shows the variation with m of $\dot{\bar{\varepsilon}}_d^*$ for internal pressure and several values of R. For all $R \geqslant 3$, previous discussion suggests that $\dot{\bar{\varepsilon}}_d^*$ tends, as $m \to \infty$, to the same rigid-perfectly plastic limit; calculated from equations (5.13) this value is $\sqrt{3}+\frac{1}{2}$. There is a pronounced difference between the strain rate curve for R=2 and those obtained with higher R values. When R=2, $\dot{\bar{\varepsilon}}_d^*$ at m=0 is less than unity, and it diminishes as m increases until about m=3. From the rate of increase of $\dot{\bar{\varepsilon}}_d^*$ beyond this value, it seems unlikely that, if the strain rate does eventually exceed unity and a concentration develops, it will do so until m is very large. With $R \geqslant 3$, on the other hand, $\dot{\bar{\varepsilon}}_d^*$ exceeds

unity when m=0, and it increases monotonically towards the plastic limit.

The spread of the effective strain rate curves contrasts with the fairly rapid convergence of the corresponding effective stress functions -Fig. 6.9. The effective stress $\bar{\sigma}^*$ is estimated from equation (2.22) i.e.

$$\bar{\sigma}^* = \dot{\bar{\epsilon}}^{*\frac{1}{2m+1}}$$

When m=2, $\bar{\sigma}^*_d$ is within 16% of the rigid-perfectly plastic value, unity, for all $2 \leq R < \infty$.

It would appear probable that the absence of strain rate concentrations over a large range of m values observed at the junction of the cylindrical shells for small, though in practice important, thickness ratios, will also be a feature, under certain conditions, of other shell intersections e.g. a cylindrical shell with a hemispherical end closure. In any particular case the junction strain rates will depend on the degree of mismatch of the membrane velocities of the mating shells, and the resistance of the latter to edge forces and moments. A rule of thumb suggested by Fig. 6.8 is that a strain rate concentration will not develop until m is very large, if one does not exist when m=0, or, by analogy, if a strain concentration does not exist in the elastic case (with $\nu = \frac{1}{2}$).

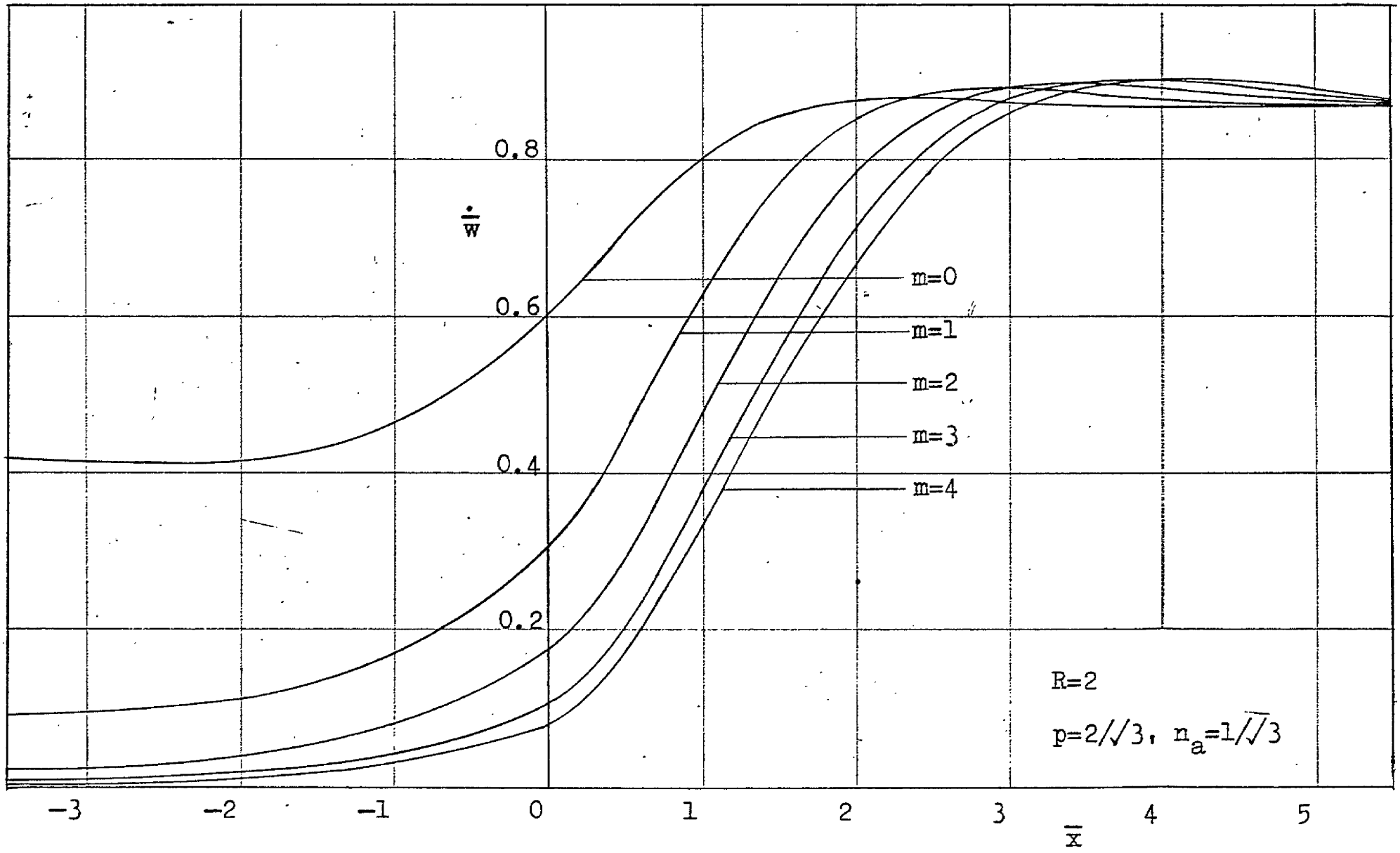

Fig.6.2 Variation of radial velocity along shell

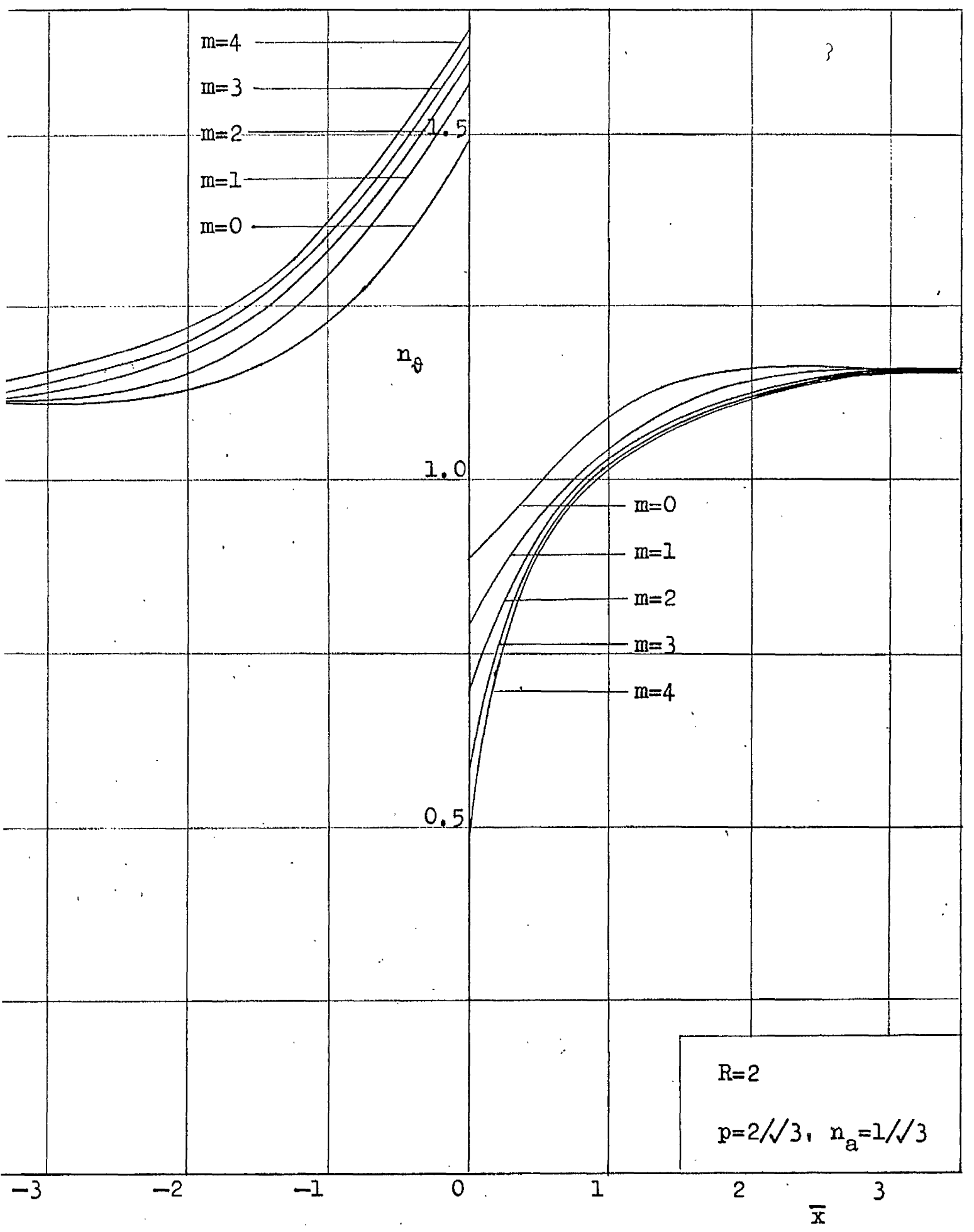

ig.6.3 Variation of steady state hoop stress resultant along shell

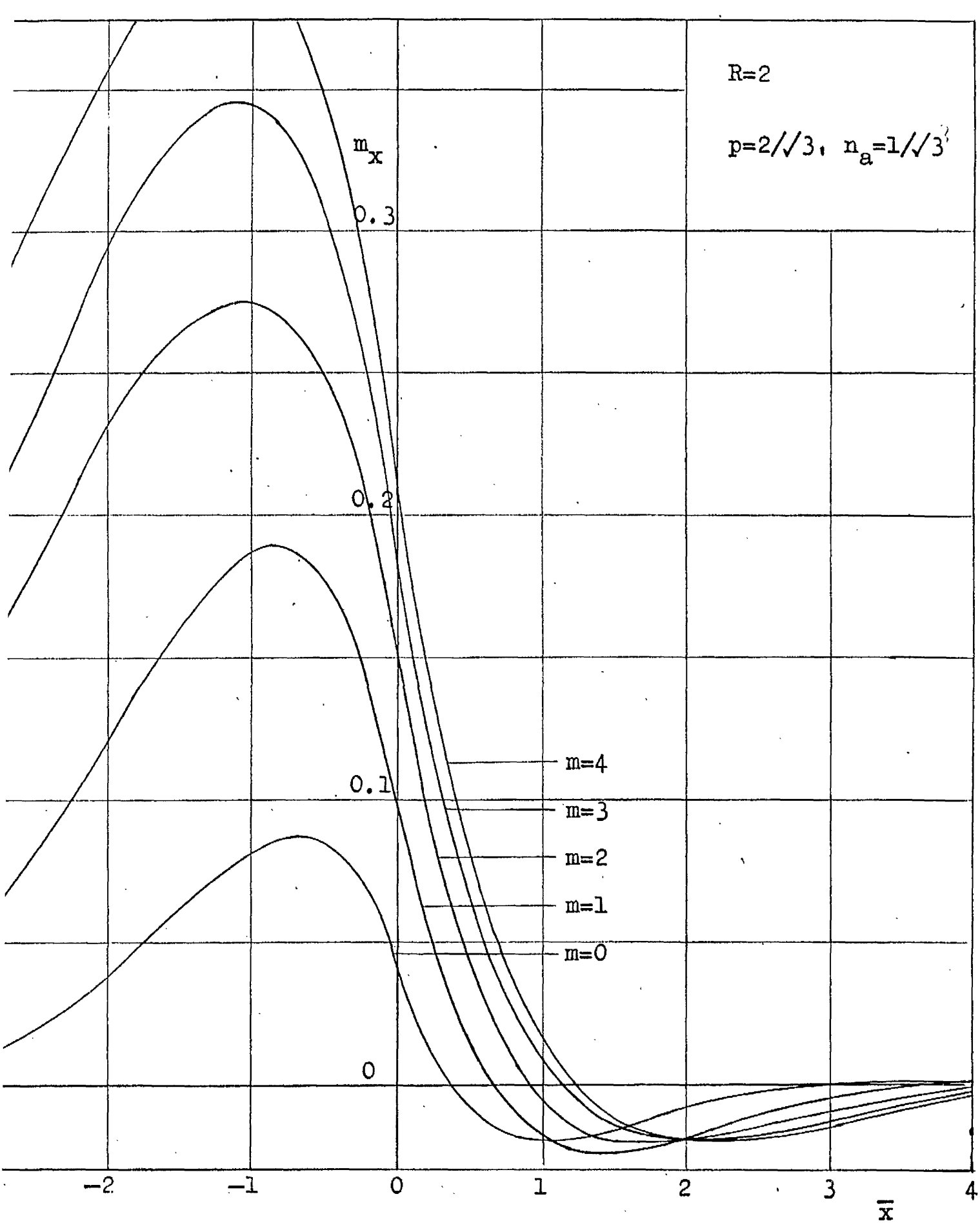

Fig.6.4 Variation of steady state bending moment along shell

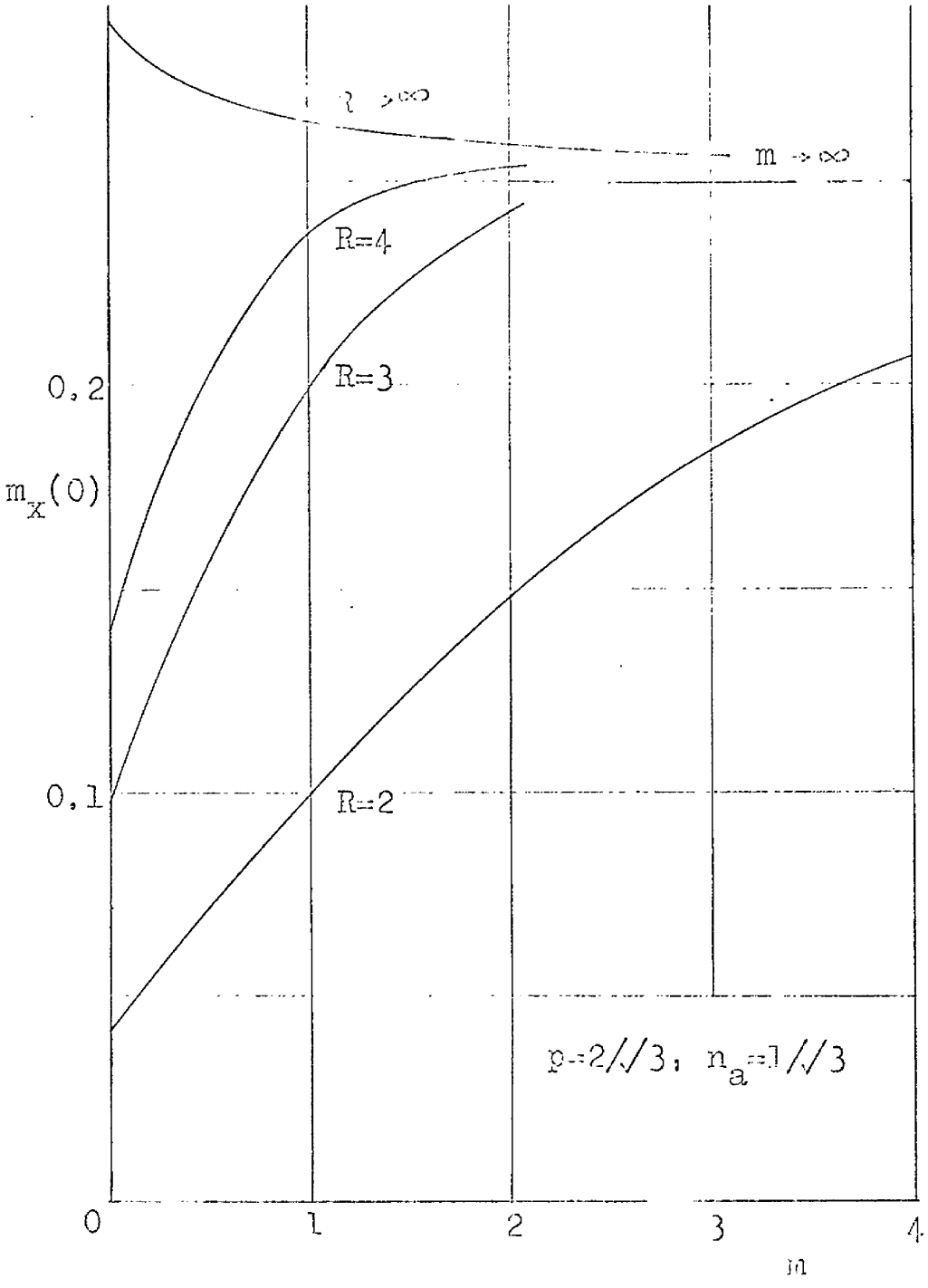

Fig.6.5 Dependence of greatest bending moment on stress exponent

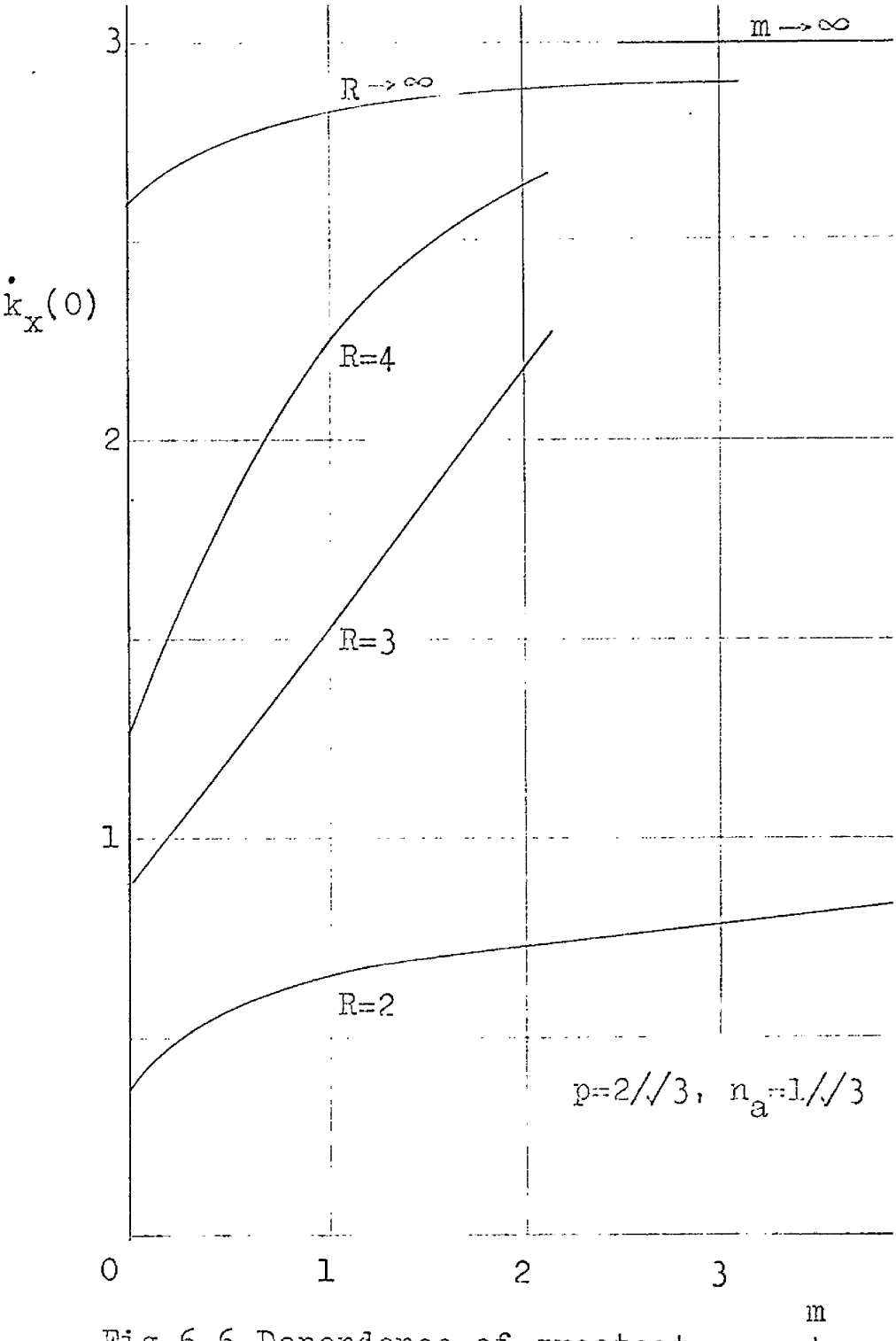

Fig.6.6 Dependence of greatest curvature rate on stress exponent

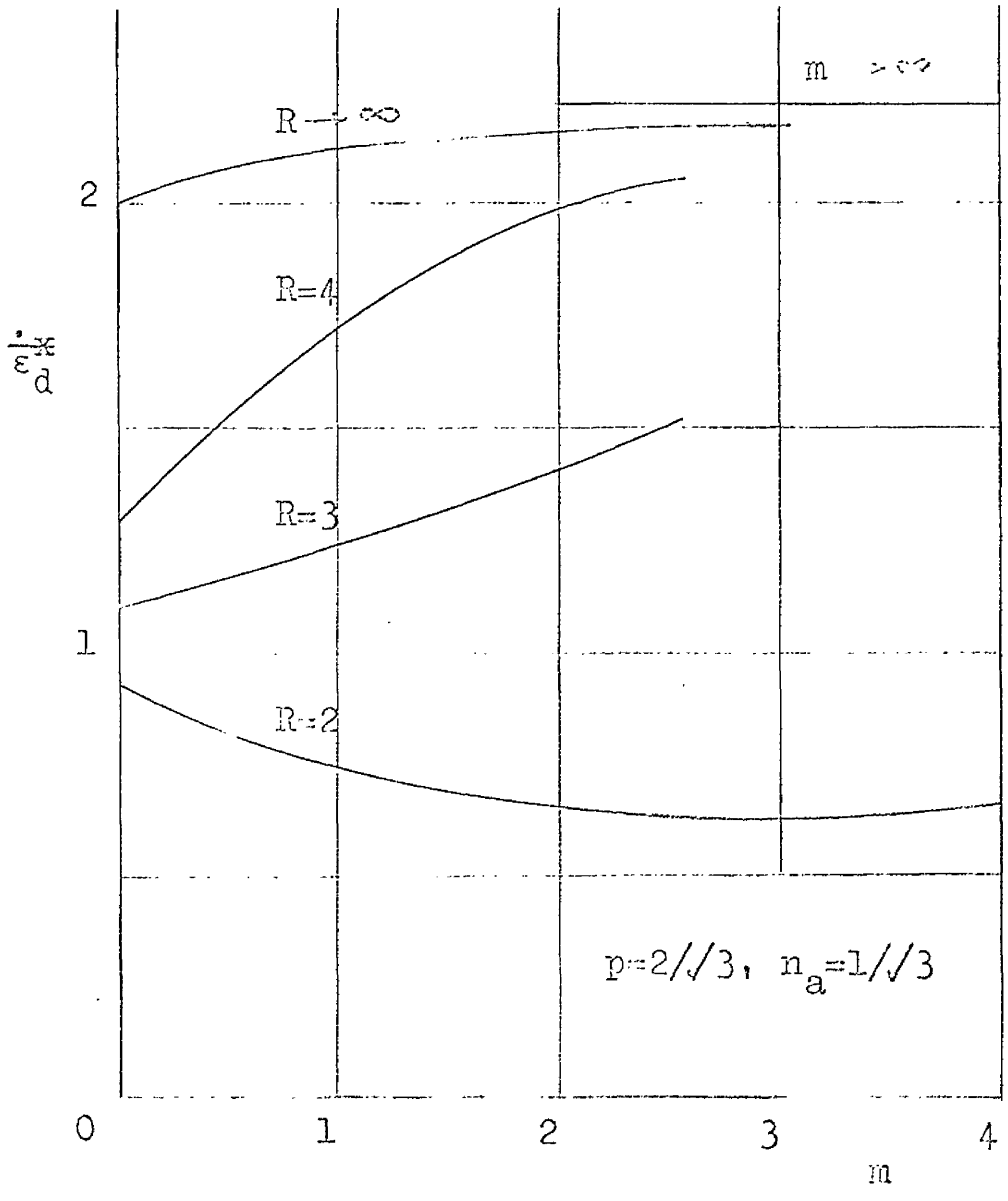

Fig.6.8 Dependence on stress exponent of greatest effective strain at discontinuity

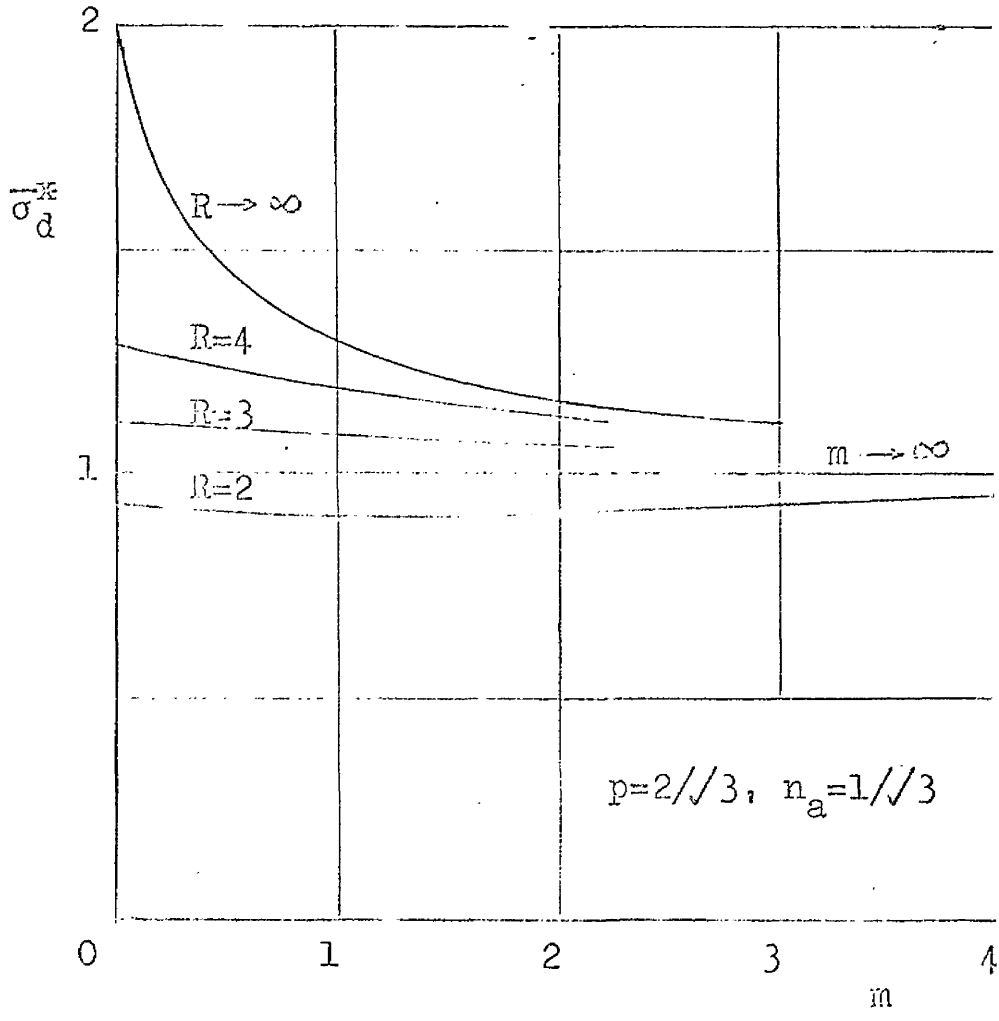

Fig.6.9 Dependence on stress exponent of greatest effective stress at discontinuity

CHAPTER 7

SCOPE OF EXPERIMENTAL WORK AND DESCRIPTION OF APPARATUS

7.1 General Remarks

Information on the actual behaviour of structures during creep is scarce, and to the author's knowledge there are no reports in the literature of creep experiments on shell structures with which theoretical analyses might be compared. Part of the reason for this lack is the expensive and time consuming nature of creep testing. Tests on structural materials at stress and temperature levels similar to those met in practice are especially demanding, requiring the continuous use of equipment over very long periods. While such long term tests are necessary, knowledge of structural behaviour can be obtained with comparative ease and speed from experiments on structures of materials which can be made to creep rapidly at moderate temperatures. The results from such tests will be useful for predicting the behaviour of practical structures (either by direct analogy, or through substantiation of theoretical analyses) provided the constitutive equations of the "model" material are similar to those of the structural material. A number of materials, mostly soft metals,

have been used in this rôle. Discs of lead (at 30°C) have been tested by Wahl[12], thick walled tubes, of lead (at 33°C) and magnesium (at 120°C) by Smith[33], and of aluminium (at 250°C) by King[34]. Polymeric materials have received less attention, although Gubser et al[13] report torsion tests on bars of polyethylene.

7.2 Experimental Programme

Because of the lack of experimental data it was decided to initiate a programme of creep tests on cylindrical shells with clamped ends and thickness discontinuities, and subject to internal pressure loading. One of the aims of the present project was to design and commission suitable apparatus, and to conduct a small exploratory series of short term creep tests on cylindrical shells under conditions of constant temperature and loading.

Of the metals mentioned above, lead with its high density is clearly an unsuitable material from which to make thin shells. Magnesium and aluminium alloys are more promising; their creep behaviour has been investigated by Johnson et al[3], and is similar to that of steel. In the event, it was decided to design apparatus suitable for testing both soft metals and plastics, but to concentrate initially on plastic materials. These have several very practical advantages over metals; they creep rapidly at

low stresses at temperatures around 100°C, and several types can be obtained fairly cheaply in a large tube form suitable for making cylindrical shells. The creep properties of polyethylene, polypropylene, PVC and nylon have been investigated by Turner et al[35],[36],[37],[38], and their strain rates show a non-linear stress and time dependence not unlike that of structural metals. The selection of the plastic most suited to the work envisaged, however, required more information than is available in the literature, and it was considered that this could be most simply obtained from tensile creep tests. As suitable apparatus was not available in the department it was decided to design a tensile creep machine to perform these tests.

7.3 Tensile Testing Machine

The general arrangement of this machine is shown in Plates 7.1 and 7.2. The load is applied to the specimen through the lever arm A which has a mechanical advantage of 10:1. At pivotal points on the lever system, knife edges are incorporated to make the inherent friction forces very small. To prevent any extraneous bending or twisting moments being transmitted along the loading column, a universal knife edged joint B and a thrust race C are fitted above the specimen. (Initially, a knife edged joint was also fitted below the specimen; however, the ex-

treme flexibility of the plastic specimens at test temperatures made it desirable to have the lower clamp firmly secured.) Though it was not possible with the measurement system used to detect any bending, examination of the specimens after testing produced no evidence of non-uniform straining. In addition, the tensile results (Chapter 8) showed good reproducibility, suggesting a lack of any random bending effects.

a) Clamping Arrangement

The test material was obtained in the form of cylindrical tubes of about 3/8in thick from which only flat tensile specimens could be conveniently cut. The geometry of these specimens and the clamping system are shown in Fig. 7.1. The specimen is positioned in the clamp by two pins A_1 which pass through the close fitting holes B_1. When the threaded collar C_1, which supports the conical block D_1, is rotated clockwise, the serrated jaws E_1 are pressed into the specimen. The slide and spring attachment F_1 ensures that the jaws are pushed apart when the collar is loosened.

b) Strain Measurement

The common, commercially available means of measuring strains on metals e.g. extensometers and strain gauges, are unsuited for application to thin plastics because they

disturb unduly the deformation of these comparatively weak materials.

All interference with free extension in this design is avoided by measuring with the horizontal arm D (Plate 7.1) and micrometer head E-calibrated in 0.0001in-the upward movement of the loading column. Contact between the micrometer spindle and the arm is indicated through the closing of an electric circuit containing a small bulb. Such a measurement, of course, contains the extension of the non-uniform sections of the specimen, and any relative movement between specimen and clamps. However, the desired strain can be obtained by testing two specimens, identical, but for a known difference in the length of their uniform sections. Subtraction of micrometer readings from the two specimens and division by the difference in length gives the strain in the uniform section.

c) Constant Stress Device

The apparatus was constructed with the intention of measuring strains up to about 5%. (In short term tests it is often necessary to produce total strains of this magnitude in order to obtain a dominance of creep strain over elastic strain.) A tensile strain of the order of 5% produces a similar increase in stress in constant load tests because of the reduction in the cross-sectional area of the specimen. This amount was considered too large to be

ignored, but not large enough to justify constant stress equipment as elaborate as that described by Sully[39].

If A_o and l_o are the initial cross-sectional area and "effective" length of the specimen, the reduction in area following an elongation δ is, to a first approximation, $A_o\delta/l_o$, provided deformation occurs without increase of volume. It follows that to maintain constant stress, the initial specimen load P_o must be reduced by $P_o\delta/l_o$. This reduction can be approximately obtained with a simple device based on the fact that a beam resting on a sharp edge has only one equilibrium position unless very carefully balanced. Fig. 7.2 shows a schematic drawing of a beam on a fulcrum A; the masses W,w of the portions of the beam on

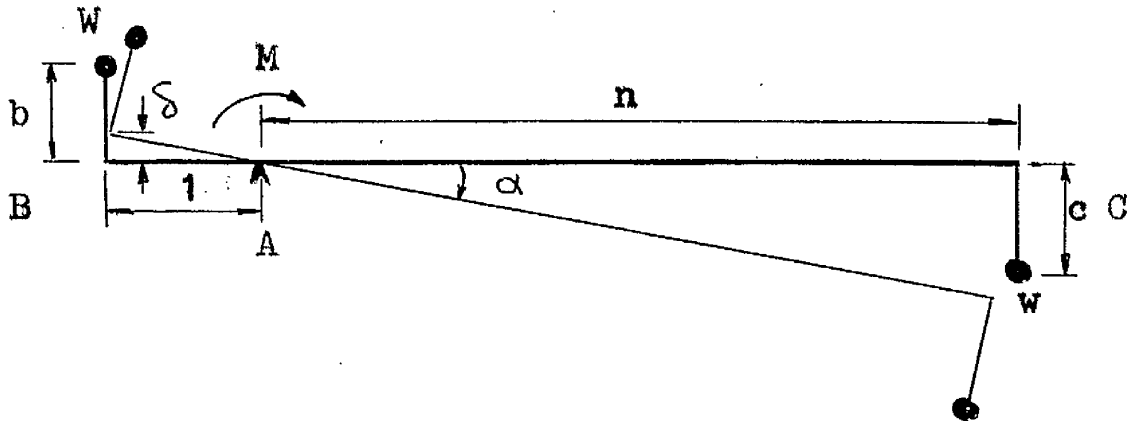

Fig. 7.2

either side of the fulcrum are located at their respective centres of mass. If the beam is in equilibrium in the horizontal position W = nw. To hold the beam in any other

position a moment

$$M = w(c-bn)\sin\alpha$$

is required; this moment is zero for all α only if $c = bn$.

If Fig. 7.2 is considered to represent the loading lever of a tensile machine, with the specimen at end B and the applied weights at C, M is provided by a change in the specimen load. If the lever is unbalanced such that $c > bn$ the specimen load is reduced, and when α is small ($\sin\alpha \doteq \alpha \doteq \delta$) this reduction is approximately a linear function of the specimen extension δ. Thus, by constructing a beam such that the unbalance, and hence the moment M, can be varied, the reduction in specimen load can be made equal to $P_o\delta/l_o$.

In Plate 7.2 the loading lever arrangement is shown. The mass F is mounted on a screwed rod, and mass G attached to a rod which can be inclined at any angle to the lever A. The positions of these masses can be adjusted such that for any P_o the reduction in load with elongation is $P_o\delta/l_o$. With the loading column replaced by known weights this system was calibrated for a range of loads. The masses F and G were adjusted by trial and error to give the desired load/deflection relationship, F being used to keep the balance position of the beam horizontal. A scale indicating the position of G for several values of P_o was marked off on a perspex sheet H. Calibration values are shown in

Table 7.1 where the reduction in load accompanying any deflection is seen to be always within 10% of that desired. This accuracy was considered sufficient to maintain the stress to within about $\pm$1% of the initial value.

P_o-lb	δ/l_o=0.0213		δ/l_o=0.0425		δ/l_o=0.0638	
	$P_o\delta/l_o$-lb					
	Desired	Actual	Desired	Actual	Desired	Actual
40	0.85	0.9	1.7	1.7	2.55	2.5
50	1.06	1.15	2.13	2.2	3.19	3.1
60	1.28	1.3	2.55	2.65	3.83	3.8
70	1.49	1.5	2.98	3.0	4.47	4.5
80	1.7	1.7	3.4	3.5	5.1	5.0

Table 7.1

d) Heating System

The creep deformation of materials is often very sensitive to temperature, and much of the scatter of experimental results is due to temperature fluctuations. To minimise temperature variation the specimen and clamps are totally immersed in liquid paraffin contained in the heating tank J (Plate 7.1, where it is shown in the lowered position), and the temperature controlled by a proportional controller.

Liquid paraffin has the properties which are necessary or desirable for the heating medium: that it should

be a good thermal and poor electrical conductor, non-inflammable and chemically inactive under test conditions. This specification is also met by methyl phenol silicone which was used by Finnie[40]. The silicone can be used at 250°C, but the paraffin with a flash point of 195°C, is restricted to lower temperatures. For testing plastics, however, temperatures near 195°C are not required, and the much cheaper liquid paraffin is adequate.

The tank is heated by an "Electrothermal" heating tape wound around the outside, and a uniform temperature distribution obtained inside the tank by continuous stirring of the paraffin. Automatic control of temperature is achieved with a "Sirect" proportional controller, which continuously varies the current being sent to the heating element in relation to changes in the resistance of a platinum thermometer K (Plate 7.1) placed close to the specimen. With this instrument temperature stability of $\pm 0.25^{\circ}C$ was achieved.

Temperatures were measured by thermocouples. Nine base metal couples, having a high e.m.f./°C output, were made from nickel chromium and nickel aluminium wire. They were calibrated against a platinum/platinum-13% rhodium couple which had itself been calibrated on the International Temperature Scale at the National Physical Laboratories. The calibration was carried out by placing the hot junc-

tions of all the couples in a narrow glass tube and immersing it to a depth of 10in in the liquid paraffin. The cold junctions were placed in crushed ice made from distilled water, and the voltage measured to within 2×10^{-6} volts with a Cambridge Slidewire Potentiometer and spot galvonometer. Two sets of readings were made at ten minute intervals at each temperature, and the measurements only accepted if they agreed. A typical calibration curve for the couples is shown in Fig. 7.3.

Thermocouples were attached to the specimen at three points along its length (Plate 7.1). The temperature difference indicated by these couples during the tests never exceeded $0.15^{\circ}C$.

7.4 Shell Testing Apparatus

Apparatus was built to test cylindrical shells with clamped ends subject to internal pressure loading. The equipment was designed to suit shell specimens of 4in nominal diameter. This dimension enabled a thickness/radius ratio of less than 0.1 (an arbitrary "thin" shell limit) to be employed without incurring the disadvantages associated with the use of very thin plastic sections. A specimen length of 17in (including a 1in clamping zone at each end) was chosen, since the theoretical analyses suggested, that, even with a central thickness discontinuity, this length would be sufficient to prevent interaction of edge

disturbances. A typical specimen is shown in Fig. 7.4.

a) Mounting of Specimens

In the design of the specimen fixture care was taken to ensure firm clamping of the ends, axial alignment of the clamps, and the free axial expansion of the specimen. A close-up view of the specimen fixture is shown in Plate 7.3, and a general view of the apparatus with a specimen in position in Plate 7.4. The clamps A,B have central spigots over which the specimen fits closely, and on to which it is pressed by twelve circumferential blocks formed to suit the outside of the specimen. The blocks are controlled independently by bolts mounted in solid supporting rings. The clamps are integral with hollow shafts which are supported in bearings C,D; the latter are mounted on a rigid table, and have welded to them the large end plates which carry the heating tank. Within the clamp-shaft A runs a central core E, which passes through the specimen and locates in clamp B, thus ensuring good axial alignment. Linear ball bearing races support the core in clamp-shaft B and the latter in bearing D. An oil seal between this clamp-shaft and its bearing is provided by the expansible "bellows" F, which were made from a silicone rubber solution. With the bellows and linear bearings, the forces resisting the movement of the right hand clamp assembly are negligible.

b) Measurement of Deformation

The radial deformation of the specimen is measured by means of the vertical probe G mounted in the horizontal rod H; this can be moved along the length of the specimen by the screw and anti-backlash nut arrangement J. A graduated ring attached to the handle K enables the probe to be positioned with an accuracy of 0.001in. The displacement of the probe is measured to 0.0001in by a micrometer head, contact, as with the tensile machine, lighting a small bulb.

It was not intended in the exploratory tests to attempt to measure local strains, for example, at the clamped edge, although in an extended programme such measurements would be desirable.

c) Heating System

The heating system is similar to that of the tensile machine. A liquid paraffin heating medium, continuously stirred, is again used with the proportional temperature controller. Readings of six of the calibrated thermocouples distributed about the specimen varied by only $\pm 0.3^{\circ}C$ during the tests.

d) Loading System

The specimen is filled with liquid paraffin by tubes passing through the core E. Pressure is provided by the dead weight piston-cylinder combination shown in Plate 7.5. Much effort has been expended on devices of this type[41],

(42), (43), which can be made to produce or measure high pressures very accurately. The main difficulty in their design is maintaining the clearance between the piston and the cylinder within tolerable limits as the pressure is increased. However, this problem only arises at high pressure, while the requirement here was for a low pressure device (0-200lb/in^2) with a fairly large volumetric capacity. It was found that, with a radial clearance of 0.001in and the piston continuously rotated, no change was produced in the reading of a pressure gauge having an accuracy of $\pm$ 0.25lb/in^2, when the piston travelled its full range. The volume displaced by the piston was made sufficient to prevent the latter having to be raised during a test.

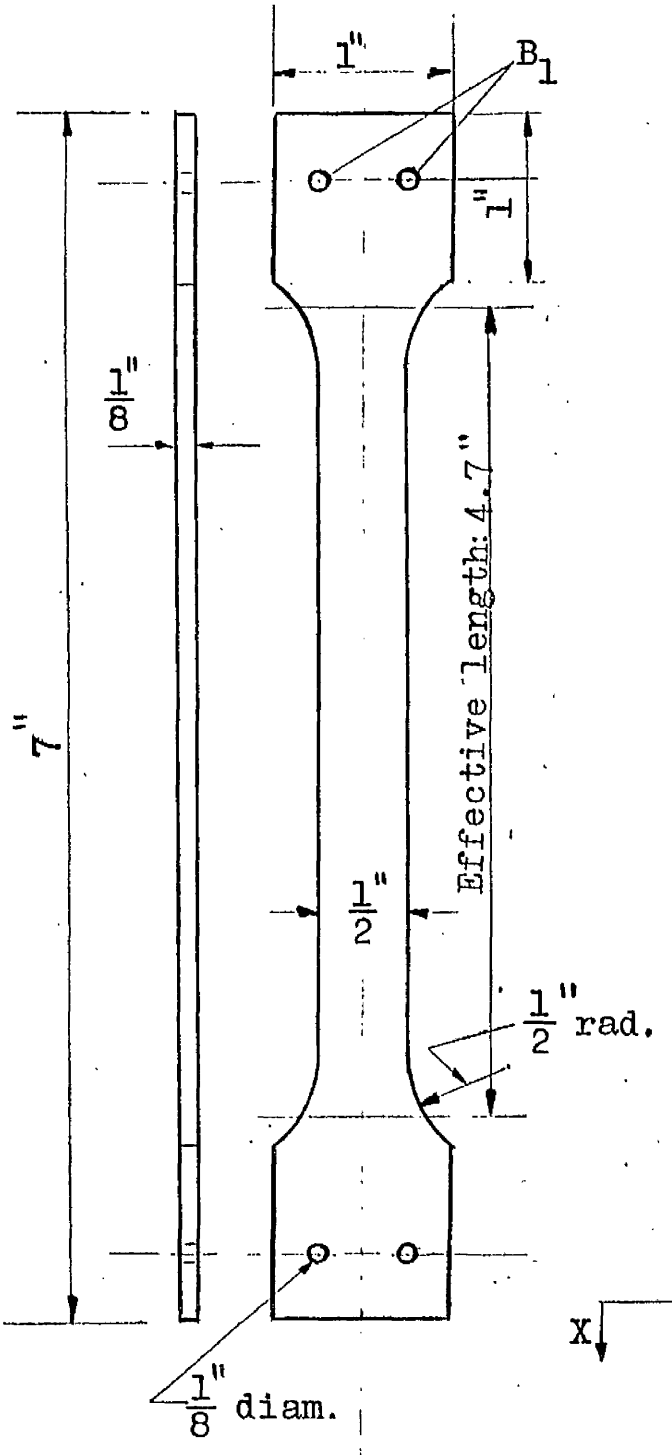

Standard Tensile Specimen

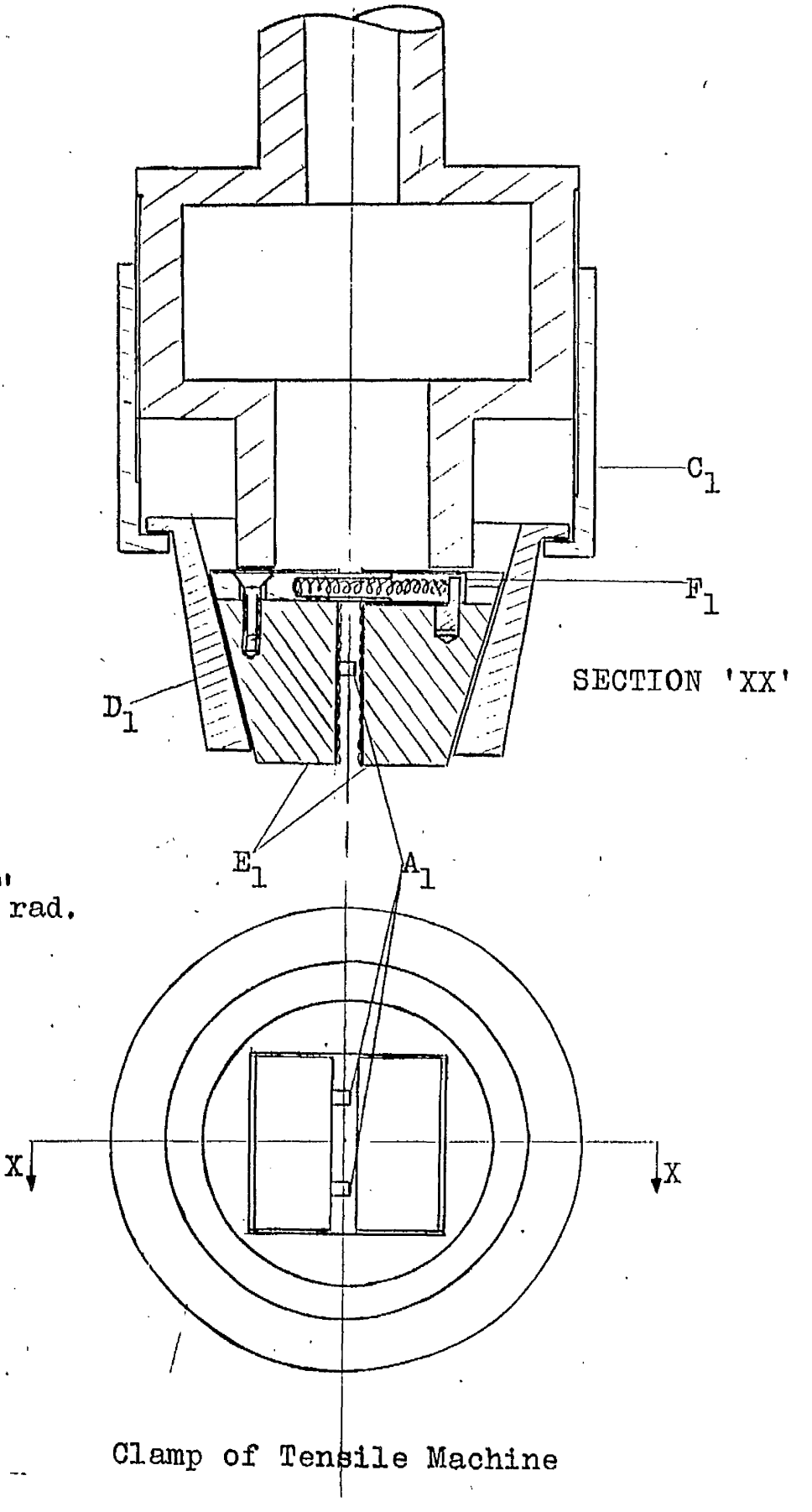

Clamp of Tensile Machine

Fig. 7.1

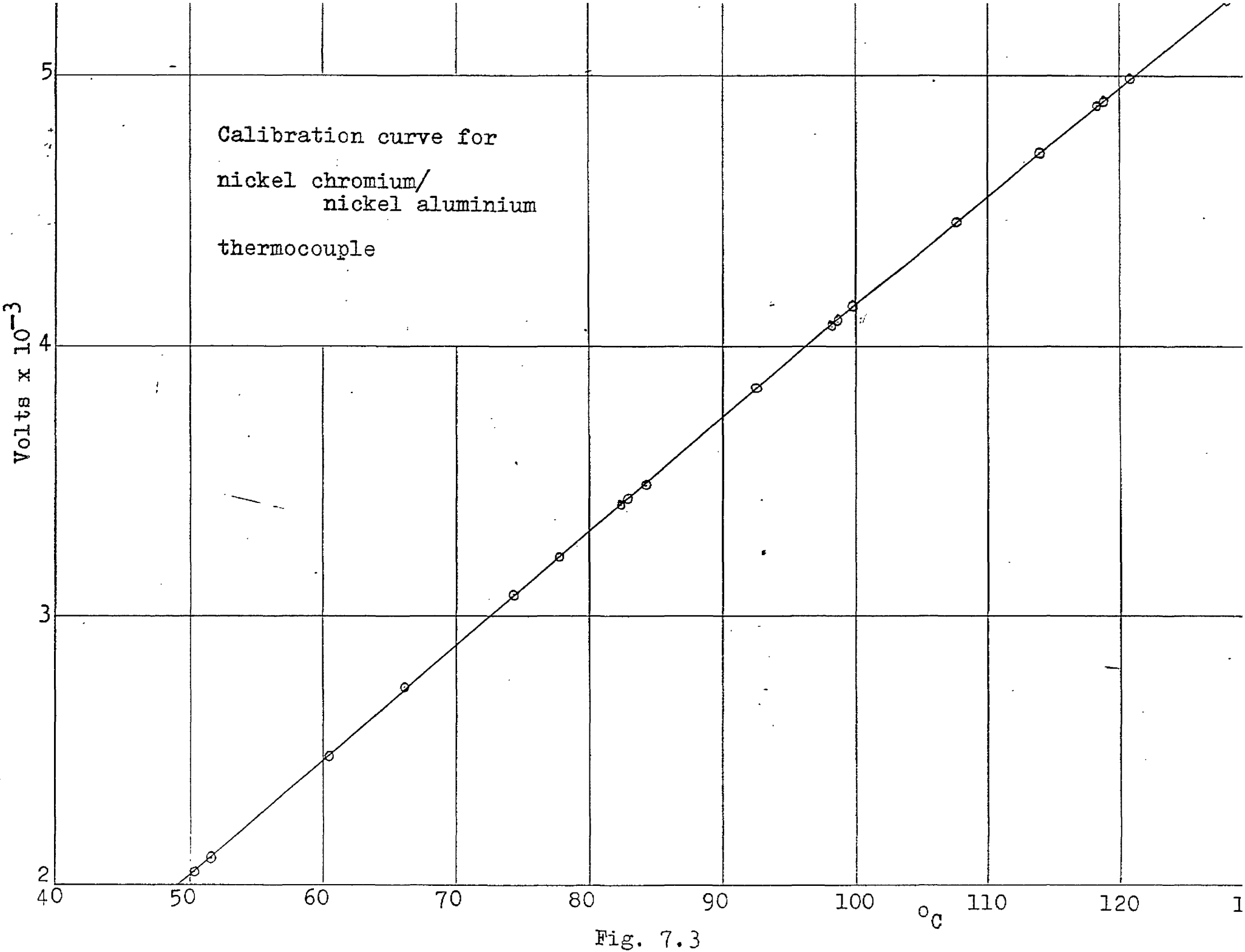
Calibration curve for
nickel chromium/
nickel aluminium
thermocouple
Volts x 10^{-3}
5
4
3
2
40
50
60
70
80
90
100
110
120
^{o}C

Fig. 7.3

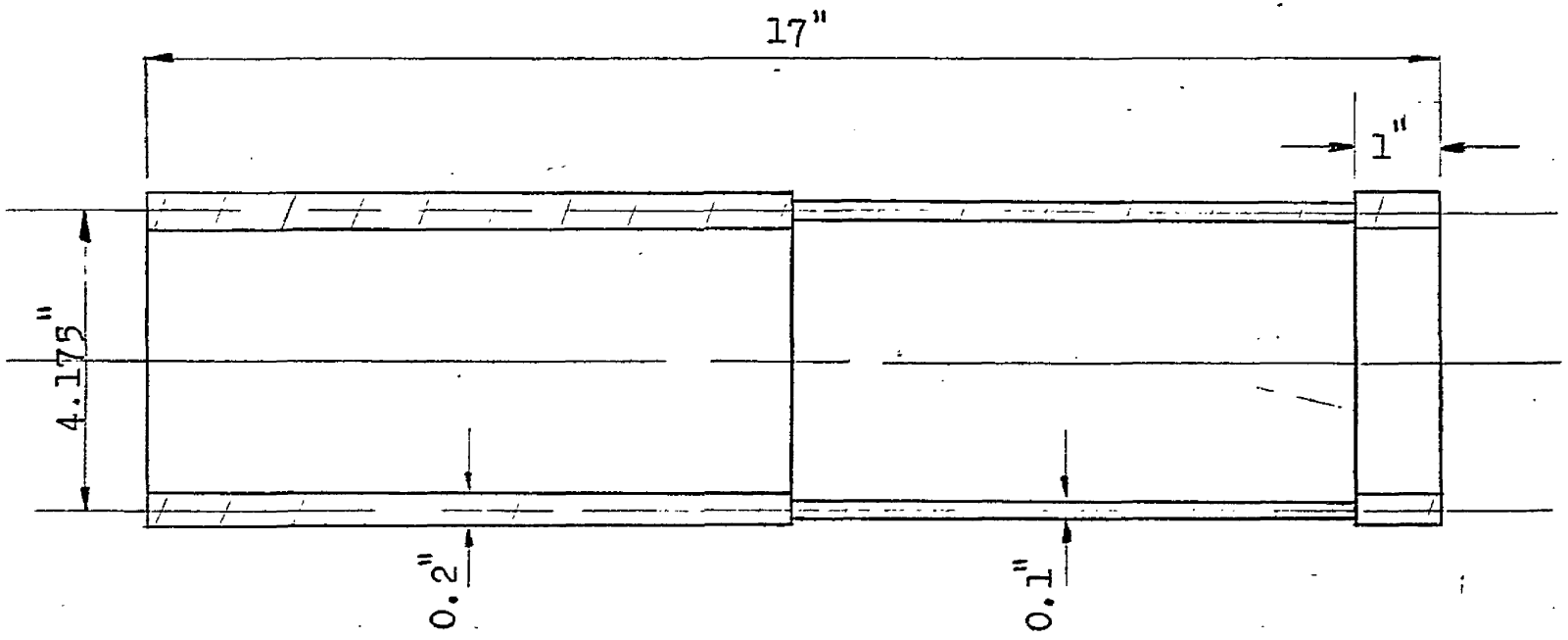

Fig. 7.4 Cylindrical shell specimen

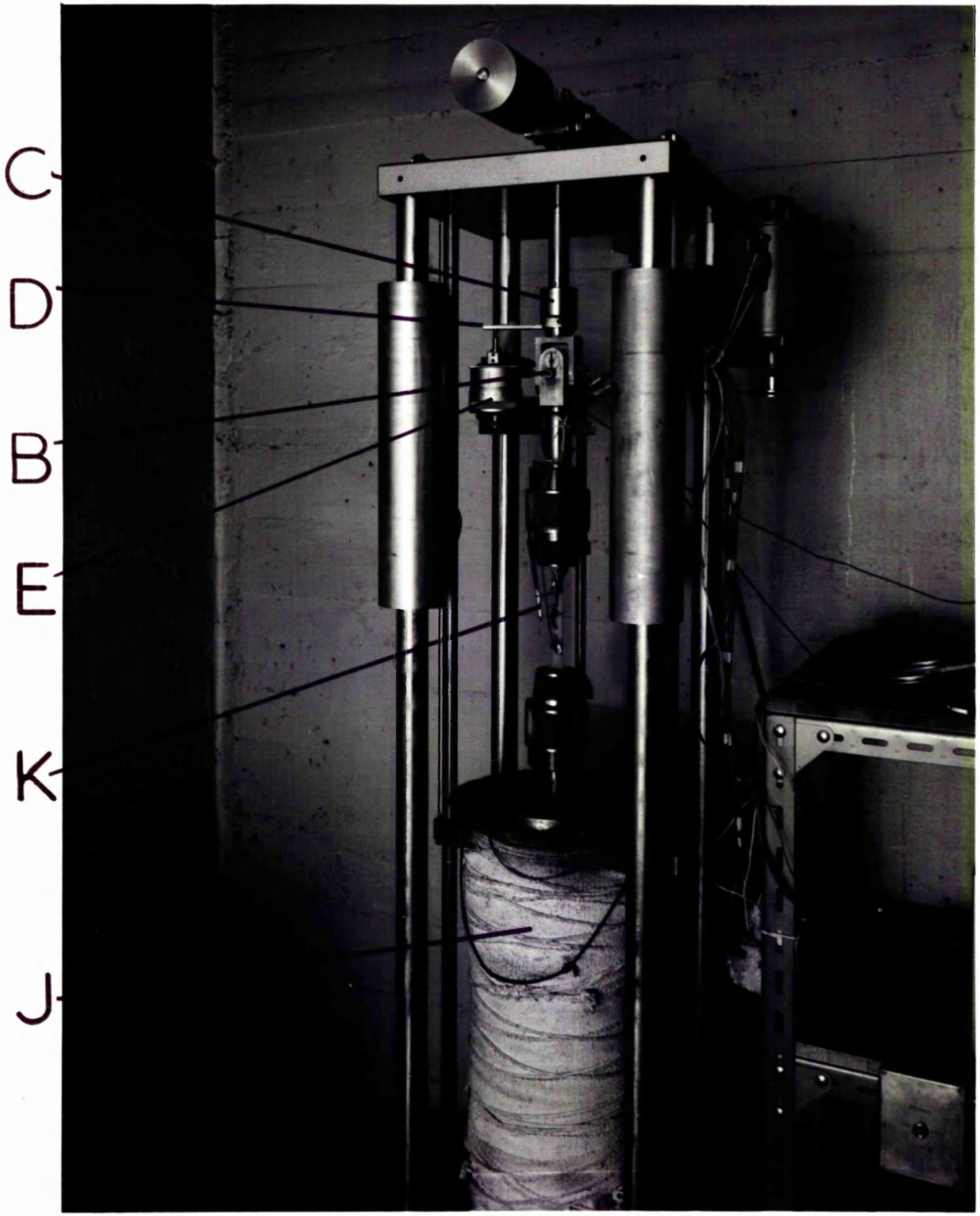

Tensile Testing Machine

Plate 7.1

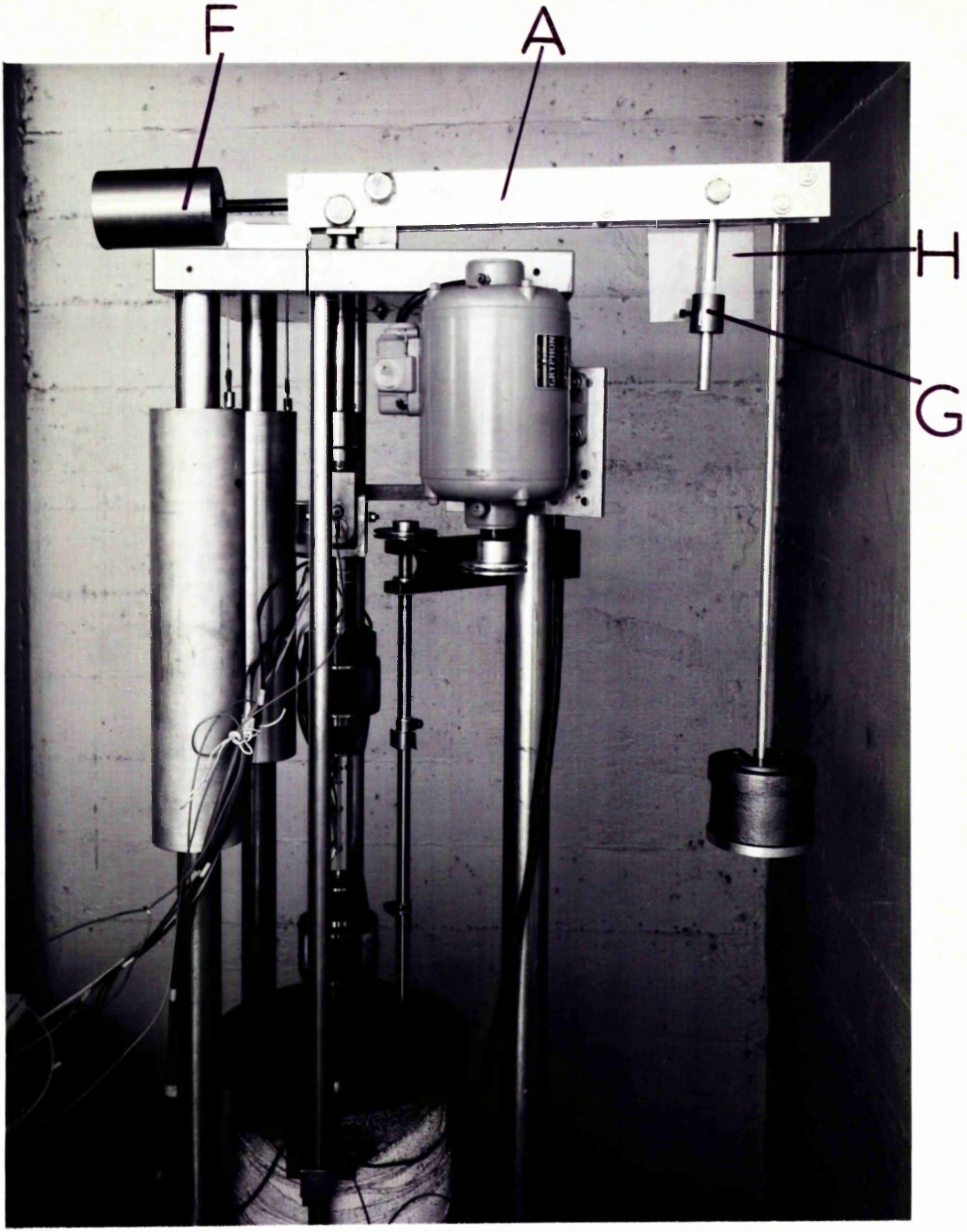

Tensile Testing Machine

Plate 7.2

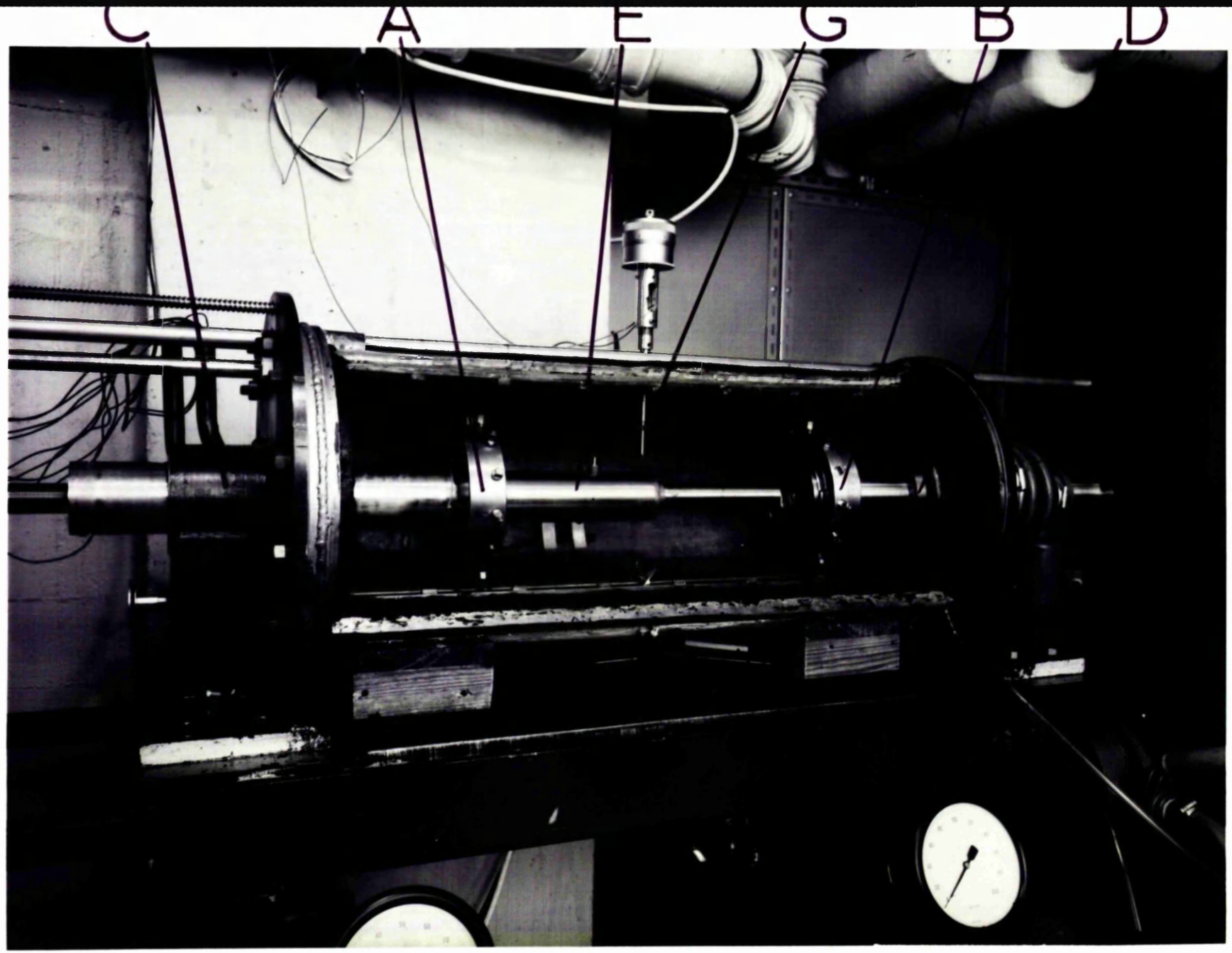

Shell Testing Machine

Plate 7.3

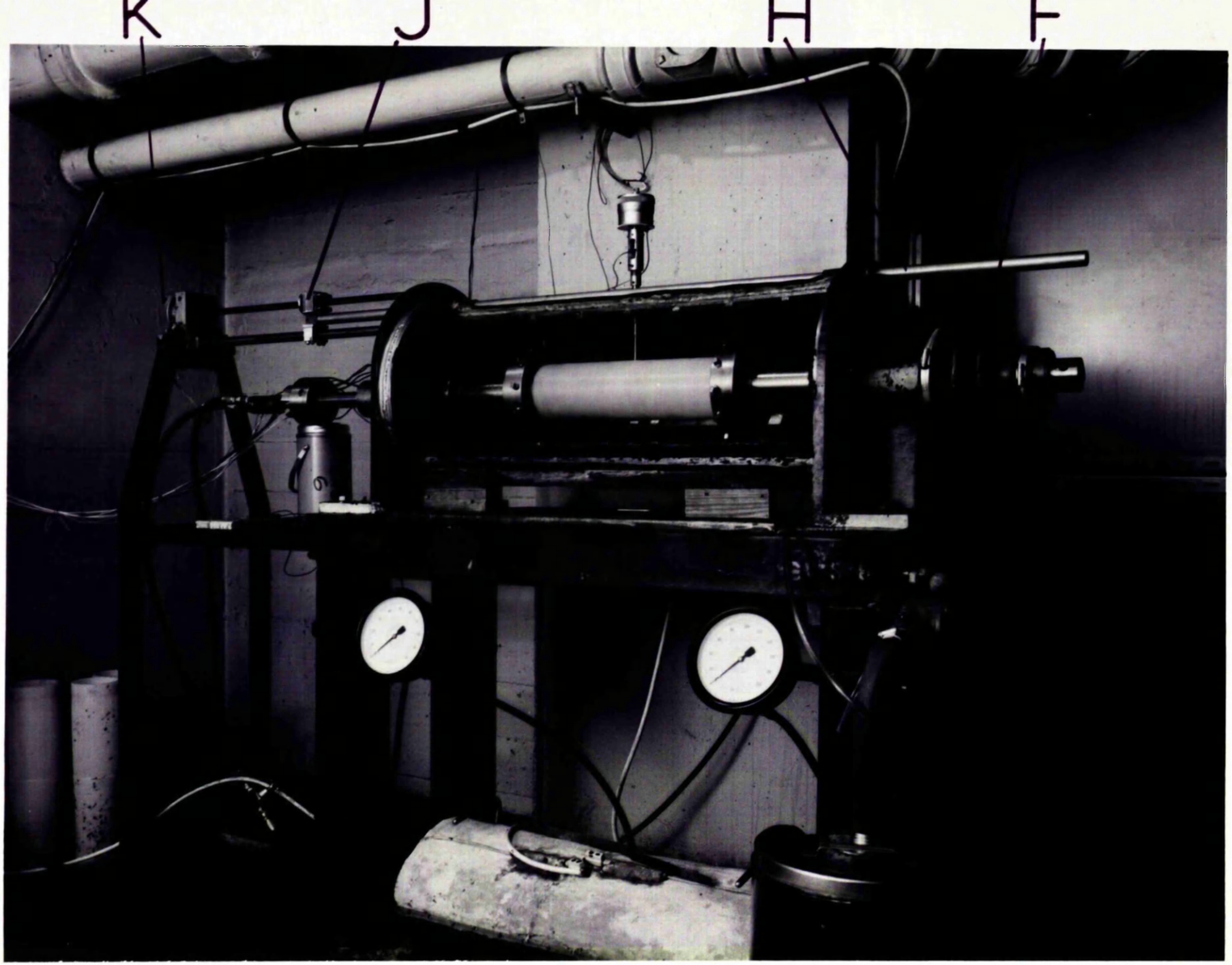

Shell Testing Machine

Plate 7.4

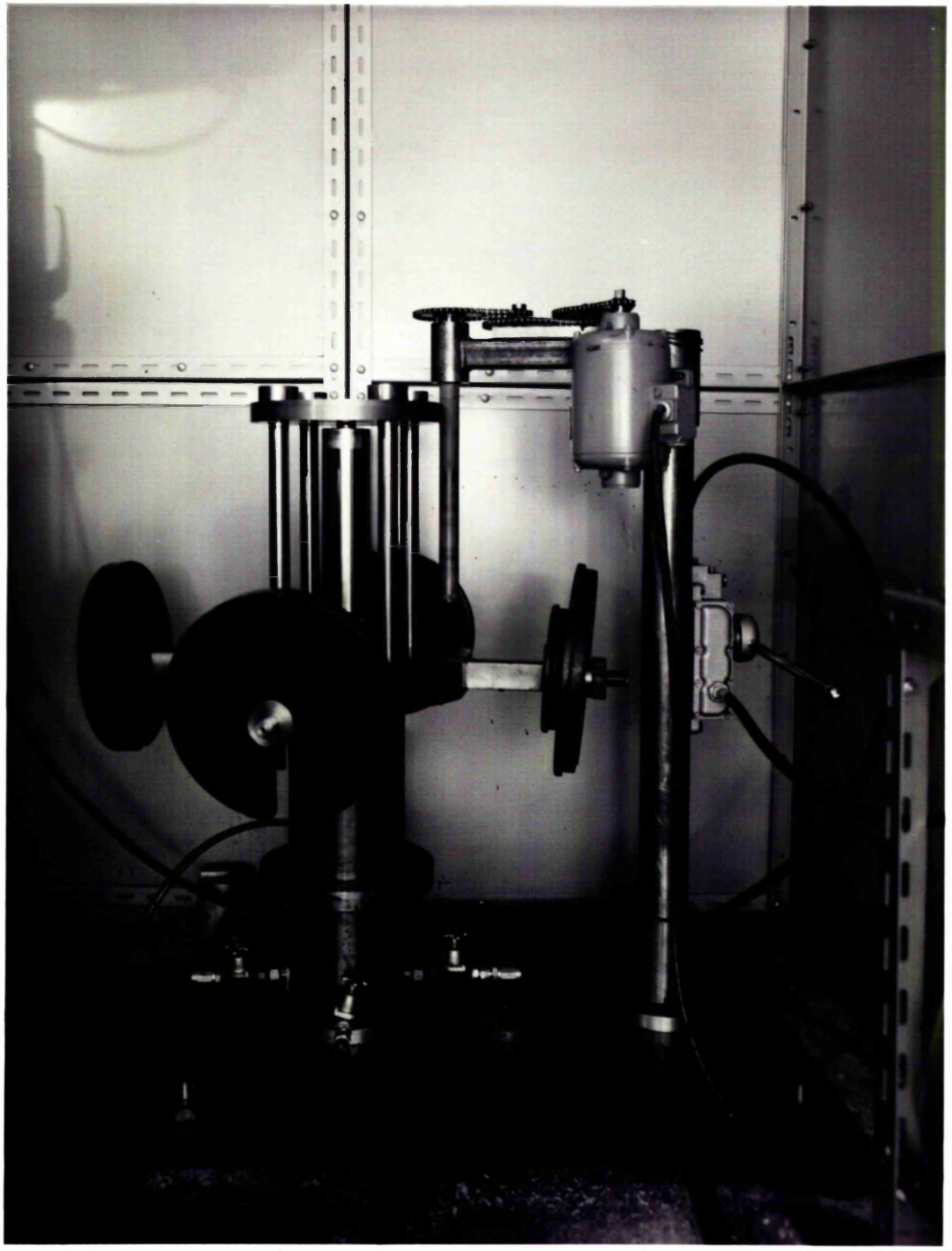

Dead Weight Pressure Intensifier

Plate 7.5

CHAPTER 8

DETAILS OF EXPERIMENTS AND RESULTS

8.1 Selection of Material

Preliminary tensile tests were carried out to select the plastic which would provide, from short-term tests, the most useful information on the behaviour of cylindrical shell structures during creep. Among features of material behaviour considered desirable were non-linear strain rate-stress dependence, and a dominance of creep strain over elastic strain.

Five polymeric materials were obtained in suitable tube form: polyethylene, perspex, PVC, nylon, and polypropylene. The polyethylene tubing was of the low density type, and much too flexible for making shells. The remaining materials were tested, and polypropylene chosen as most suitable. The tensile results from perspex, PVC and nylon, and the reasons for their rejection are given in Appendix 5. A more detailed investigation of polypropylene, a ductile polymer with a high degree of crystallinity, was then carried out, and this is described in succeeding sections.

8.2 Preparation of Polypropylene Specimens

Twenty feet of commercial polypropylene tubing 4.5in outside diameter and 0.370in wall thickness was ob-

tained; the tubing was made from Grade HPE.35 granules supplied by Imperial Chemical Industries. A length, sufficient to make eight tensile specimens, was cut from each end of the tube, and the remainder divided into portions from which shells of the desired size could be turned. All the tubing was placed in an oven and given a thirty hour heat treatment at 140°C. After thirty hours the heating was switched off, and the material allowed to cool slowly in the oven to room temperature. In consultation with the Materials Group in the Department it was decided that this treatment would make the plastic stable at test temperatures substantially below 140°C, and over long periods of time.

Difficulty was experienced at first in machining this rather flexible plastic which tended to be deflected by the cutting tool. The problem was largely overcome by providing substantial support for the material during machining through the use of special fixtures for milling the tensile specimens and large spigots for turning the cylindrical shells. Nevertheless, dimensional accuracy was less than would normally be achieved with metals. The cross-sectional area of the uniform portion of the tensile specimens varied by up to 2% of the nominal size. However, the variation in any one specimen was slight, and actual dimensions were used to determine initial stress.

With the shells the deviation from the desired size was more serious. Typical micrometer measurements of thickness and diameter at a number of positions on the shell are given in Table 8.1. As is shown, the variation in

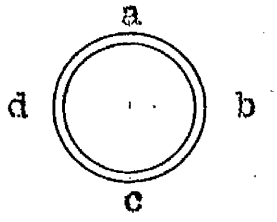

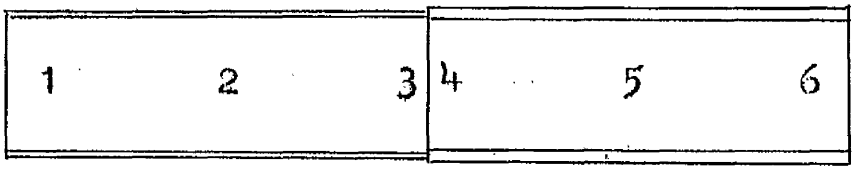

Circumferential Position / Axial Position	Thickness				Outside Diameter	
	a	b	c	d	ac	bd
1	0.104	0.103	0.102	0.104	4.275	4.276
2	0.103	0.102	0.101	0.103	4.272	4.277
3	0.103	0.103	0.101	0.102	4.269	4.278
4	0.200	0.200	0.201	0.200	4.372	4.373
5	0.200	0.200	0.200	0.201	4.372	4.375
6	0.203	0.202	0.202	0.203	4.371	4.378

All dimensions in inches.

Table 8.1

the thickness of the thinner portion can be as much as 3%, and in some positions there is slight ovality. This degree of dimensional variation had to be accepted, and it was considered to be the cause of differences in deformation measurements from separate tests, as reported in Section 8.4.

A test temperature of 60°C was adopted. At this temperature a reasonable creep strain/elastic strain ratio is obtained in a period of several hours (the tests were carried out over eight hours), and the strain rate is not too sensitive to temperature.

8.3 Tensile Test Results

Tests on the "standard" specimens (Fig. 7.1) were carried out for a range of loads, and measurements of deflection are plotted against time in Fig. 8.1. Three specimens were tested with initial stresses of 984 lb/in^2, and two with initial stresses of 1320 lb/in^2 (one specimen being taken from each end piece cut from the original tube), and, as can be seen in the figure, the consistency of the measurements is good.

Measurements were also obtained from specimens with a uniform section one inch less than the standard size, and comparison with the graphs of Fig. 8.1 revealed that the clamping regions of the specimen were making a substantial contribution to total deflection during the early stages of creep. Examination of the specimens after testing suggested that this was caused by the teeth of the jaws in the clamps digging into the plastic, on, and for a short time after, loading.

Estimates of total strains were made by subtracting

the deflections of the smaller from those of the larger (standard) specimens. However, strain values from several pairs of specimens tested at the same stress differed considerably, as can be seen in Fig. 8.2 where results obtained from combinations of three standard and two small specimens at a stress of 9841b/in^2 are shown. The spread of these results is, of course, caused by subtracting quantities of similar magnitude containing small errors, and could be reduced by using specimens with a greater length difference. However, though there is substantial disagreement in the total strain values, there is no detectable difference in the steady state strain rates. Further, it was found (Fig. 8.2) that the steady state rates could be well estimated by dividing the deflection measurements by an "effective" specimen length of 4.7in (Fig. 7.1). In this first experimental programme most interest lay in determining steady state strain rates, and therefore the deflection rates of the graphs of Fig. 8.1 were converted to strain rates by the simple expedient of dividing by the effective length.

Fig. 8.3 shows a log-log plot of the steady state strain rate against stress. (From the definitions (2.10) and (2.20) a pure tensile stress is equal to the effective stress σ^*, and, assuming flow to occur at constant volume, the tensile strain rate equals the effective strain rate,

$\frac{\partial \varepsilon^*}{\partial t}$.) The experimental points lie on a fairly well defined curve, which shows the strain rate to increase rapidly with stress, particularly at the higher stress levels. A simple m-power relationship clearly does not exist between strain rate and stress, and, consequently, the theoretical analyses of previous chapters cannot be expected to provide very good predictions of the behaviour of shells of this material.

8.4 Shell Test Results

Six shells, each with a central discontinuity, were tested. They all had a mean diameter of 4.175in and a load carrying length of 15in; in two of the shells the wall thicknesses were 0.1in/0.2in, and in the others, 0.1in/0.25in, 0.1in/0.15in, 0.133in/0.2in and 0.067in/0.2in.

When the specimens were heated in the apparatus the different coefficients of thermal expansion of the plastic shells and the steel clamps, caused a thermal stress field to be set up in the specimens. Readings from a specimen left unloaded for a long time at test temperature showed that these stresses produced extremely little creep strain. However, the thermal strain variation along the shell length was of some significance, and had to be included in total displacement profiles.

The effective stresses and strains in small regions midway between the discontinuity and the ends of the shell,

were estimated by assuming behaviour there to be the same as in an unrestrained membrane i.e.

$$\sigma_x = \frac{\sigma_\theta}{2} = \frac{Pa}{2h}, \qquad \therefore \sigma^*_{mem} = \frac{\sqrt{3}}{2}\frac{Pa}{h}$$

$$\frac{\partial \varepsilon_\theta}{\partial t} = \frac{1}{a}\frac{\partial w_{mem}}{\partial t}, \qquad \frac{\partial \varepsilon_x}{\partial t} = 0 \text{ (assuming flow to occur at constant volume)} \qquad (8.1)$$

$$\therefore \varepsilon^*_{mem} = \frac{2}{\sqrt{3}}\frac{w_{mem}}{a}$$

In Fig. 8.4 ε^*_{mem} is plotted against time for several values of effective stress. (The stress values shown, calculated from the dimensions of the undeformed shell, are but nominal, since, in these constant load tests, the stresses increase as the expansion of the shell proceeds.) Reproducibility of measurements from the thicker shell sections was good, but from the thinner sections, which were subject to the highest stresses, the results were not so consistent. The data shown as having been obtained at a stress of 11101b/in^2, came from tests on four similar shell halves (nominally 0.1in thickness). As the pressure and temperature during these tests were held within very close limits, the spread of the results had to be ascribed to the small, though not insignificant, dimensional differences between the specimens. This explanation became more likely when the sensitivity of the strain rate to stress at the existing stress level was considered.

With the tensile measurements in Fig. 8.3 are shown

steady state effective strain rate/stress data obtained from the shell tests. (For these results the stress values were calculated using estimates of the average shell thickness and diameter during steady state creep.) All the points lie fairly close to one curve suggesting a unique relationship between effective strain rate and effective stress. This relationship becomes increasingly non-linear as the stress is increased, and, if a power law of the form

$$\frac{\partial \varepsilon^*}{\partial t} = \sigma^{*2m+1}$$

is fitted to small regions of the curve, values of m range from 0.2 at low stresses, to about 5 at the highest stress levels. At the stresses prevailing in the four tests discussed above (about 1250lb/in^2 in the steady state) the strain rate/stress sensitivity is such that a 3% change in stress can produce a 20% increase in strain rate. This sensitivity and the tolerance on the specimen thickness discussed in Section 8.2 are sufficient to explain the inconsistency of these shell measurements.

Also shown in Fig. 8.3 are effective strain rate/stress data at time t = 50min. The determination of the stress and strain values at this time is less accurate than during steady state creep, but nevertheless the $\frac{\partial \varepsilon^*}{\partial t} - \sigma^*$ relationship is fairly well defined. The curve is similar to that governing steady state behaviour,

though the non-linearity is not so great, values of m increasing with stress from about 0 to 2.

Radial velocity distributions along the length of the specimen at time t = 50min and during steady state creep are shown in Figs. 8.5 and 8.6 respectively, for shells having wall thicknesses 0.1in/0.2in and 0.1in/0.25in, and subject to a pressure of 61.2lb/in^2. Also shown with these velocity variations are contemporaneous radial displacement profiles for the shell with thicknesses 0.1in/0.2in. The most striking feature of these results is the increase in the decay length as creep proceeds. The extent of the increase can best be judged by comparing the total displacement pattern at t = 50min (this being closest to the initial, almost linear elastic, distribution), and the steady state velocity profile. While the growth of the decay length during creep is predicted by the analyses of Chapters 4-6, there is a substantial difference between the measured velocity distributions and those obtained from theory.

The radial velocity profile for internal pressure loading, R = 2 and m = 1.4 (calculated as in Chapters 5 and 6), is given in Fig. 8.6 for comparison with the steady state measurements. In Fig. 8.7, the steady state velocity distribution of a shell of thickness ratio 0.133in/0.2in, under 61.2lb/in^2 pressure, is shown, and compared with a

theoretical curve obtained with R = 1.5 and m = 0.7. In both of these figures the values of m have been chosen to make the theoretical and experimental distributions agree at the points x = 4in and x = 11in (i.e. in the regions of almost uniform strain). Over the range of stress likely to exist in the shell of Fig. 8.7 (values in the membrane regions of the thin and thick sections are 830lb/in^2 and 550lb/in^2 respectively), the logarithmic steady state strain rate/stress graph (Fig. 8.3) is almost linear, and with m = 0.7 the power law provides a reasonable description of material behaviour. In the specimens of Fig. 8.6, however, the effective stress range extends over the whole of the strain rate/stress curve, which is poorly approximated by the line m = 1.4.

In Fig. 8.6 the difference between the experimental measurements and the theoretical curve is very considerable. The measured velocities in the thin section lie, for the most part, well below their predicted values on a somewhat parabolic curve, and there is no suggestion of the oscillation which characterises the theoretical solutions. At the fixed end of the shell m = 3 provides a better description of material behaviour at the prevailing stress level. However, although the solution with this value is closer to the experimental points, the disagreement is still very great. The difference in the distributions of

Fig. 8.7 is similar though less pronounced. The experimental profile in this case shows a "flat" region in agreement with theory over the central portion of the thin section, but in the vicinity of the maximum turning values of the theoretical curve the measured velocities are significantly lower.

Velocity profiles from the other specimens tested disagreed in a similar manner with the theoretical solutions.

The most probable cause of the difference between the experimental and theoretical results appeared to be the size of the total deformations of the plastic shells. During steady state creep the total circumferential strain of the shells of Fig. 8.6 was about 6%, and that of Fig. 8.7 about 3½%. This explanation was substantiated by the resemblance between the velocity profile of Fig. 8.6 and the deformed shape of a shell which had undergone 30% strain-Plate 8.1. (The shell ruptured locally, and the shape referred to is that opposite the bubble.) Plate 8.2 shows a shell which has experienced 6% strain; in this case, the substantial creep recovery which the material exhibits on unloading obscures the deformed profile.

All the analyses presented have been based on the assumptions of small deflection shell theory. Some of these assumptions are evidently too severe to allow reasonable

estimates of the experimentally measured deformations to be made. Some modification of the theory is necessary, and this is discussed in the next chapter.

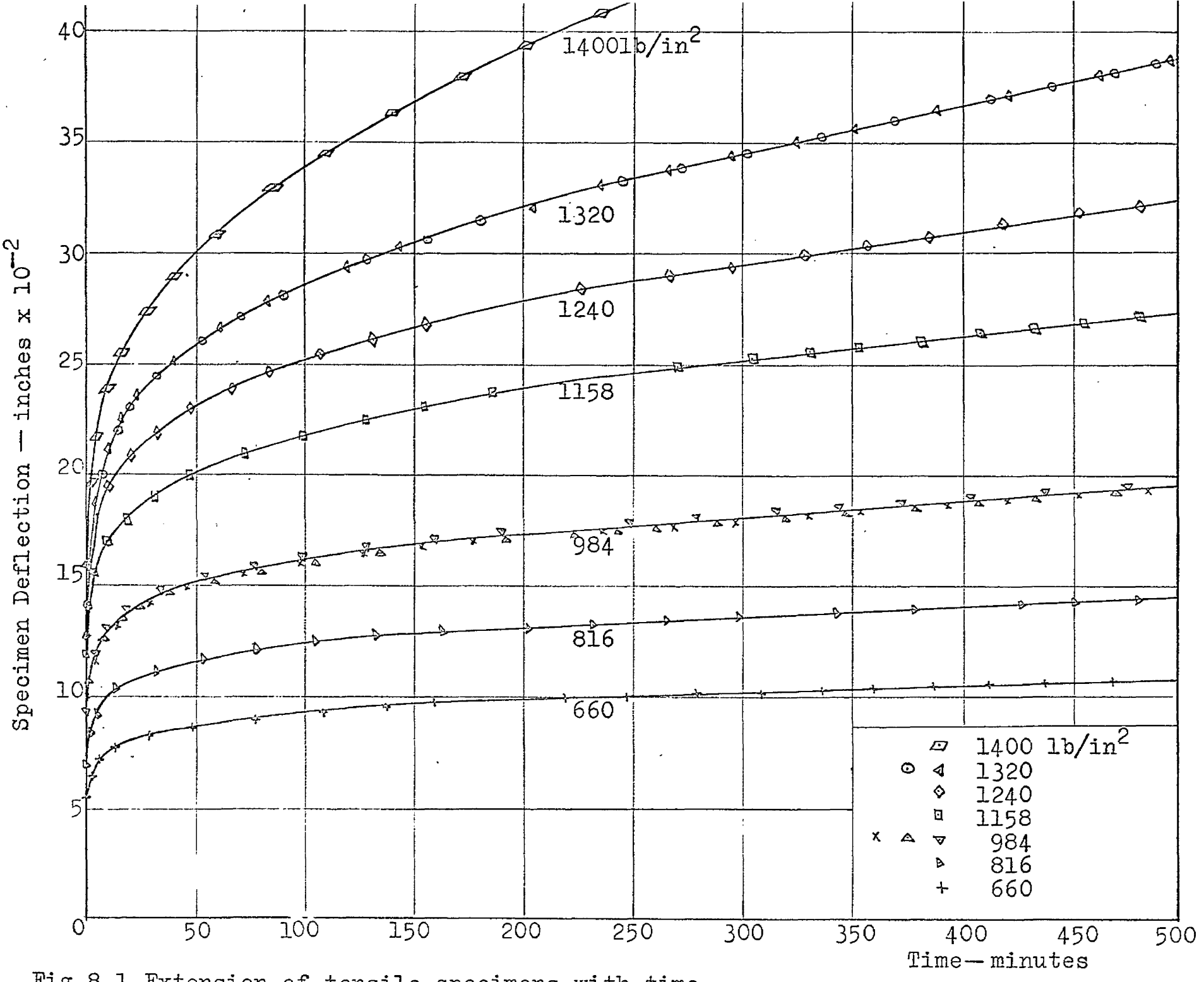

Fig.8.1 Extension of tensile specimens with time

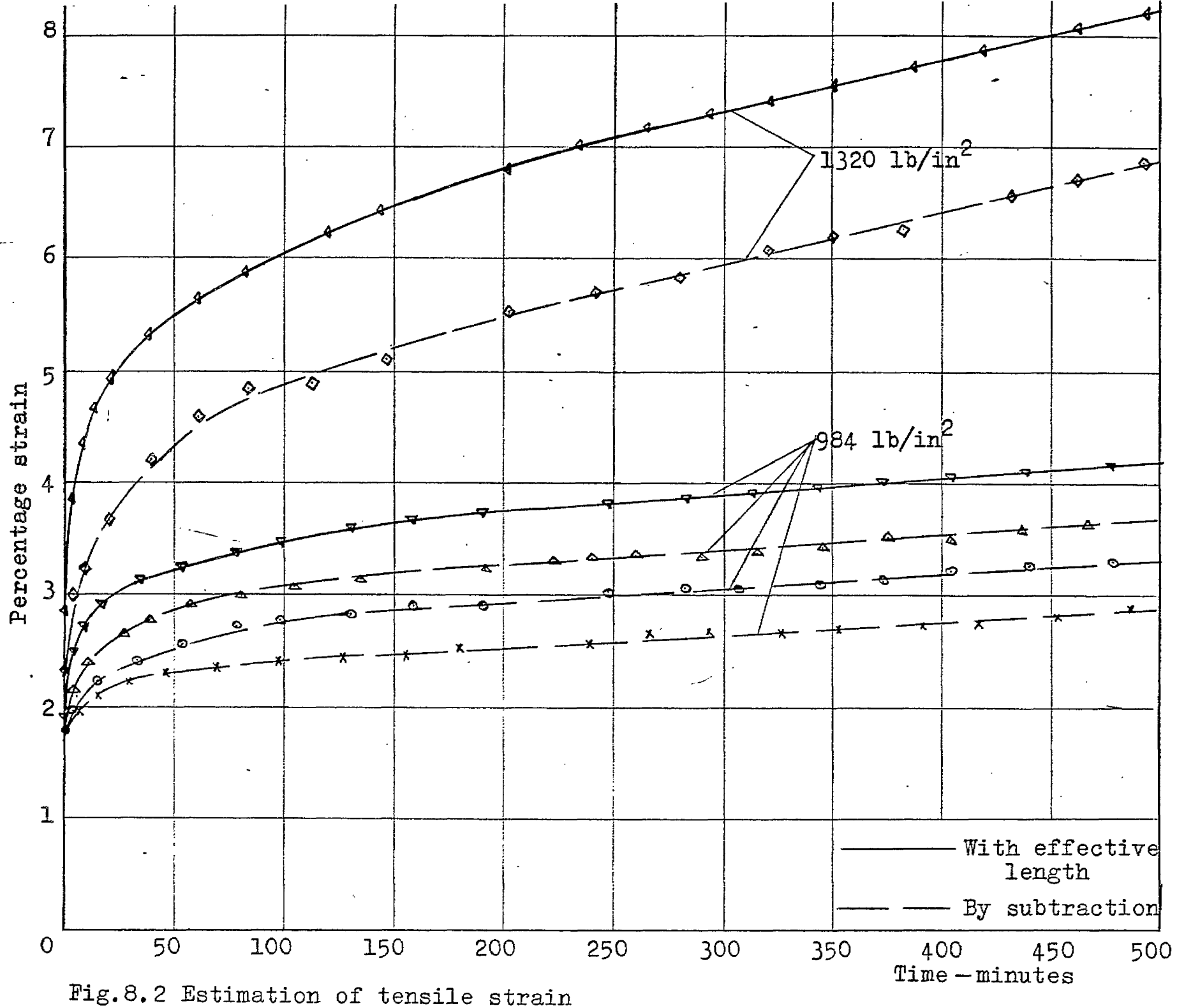

Fig.8.2 Estimation of tensile strain

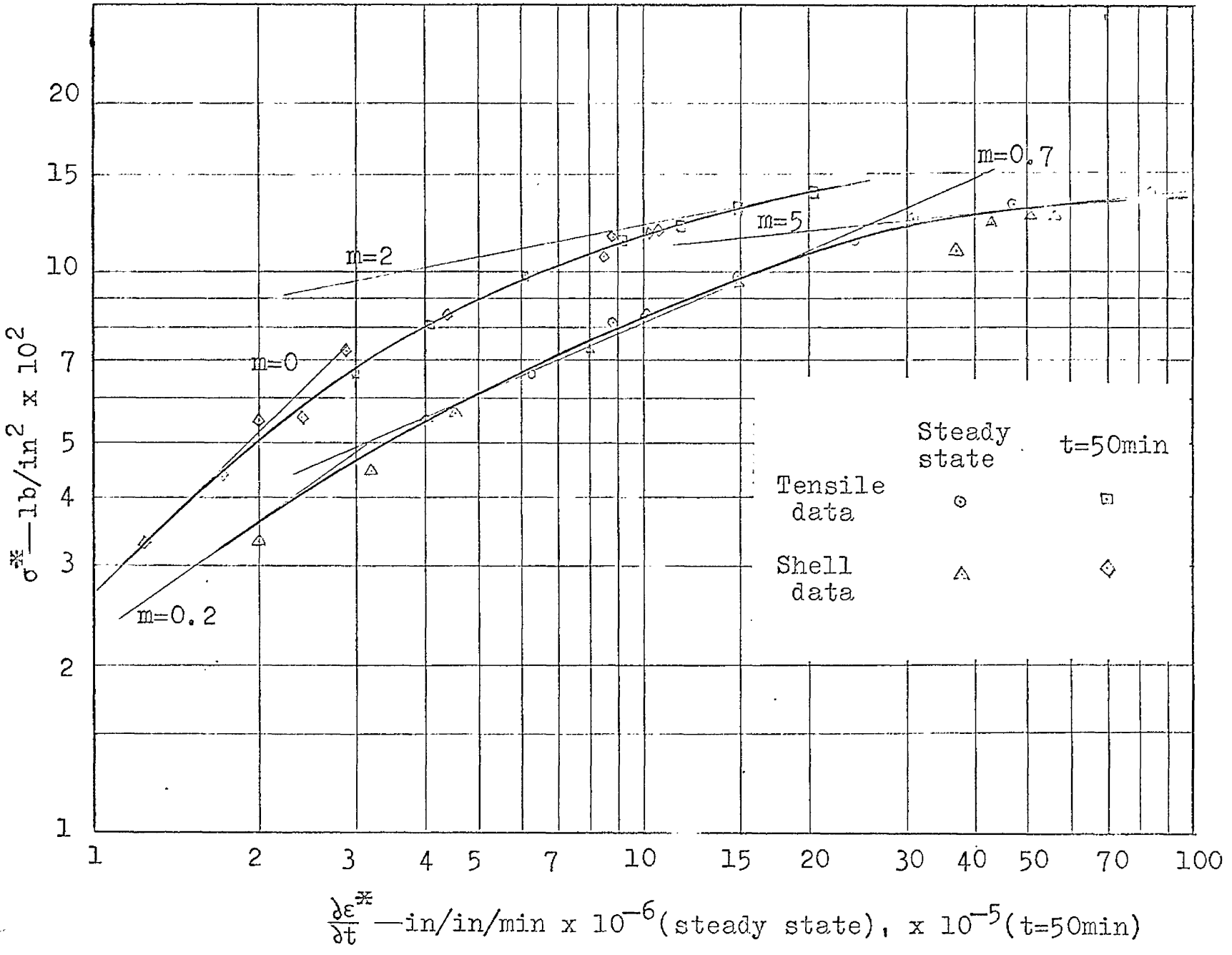

Fig.8.3 Effective strain rate/stress data from tensile and shell tests

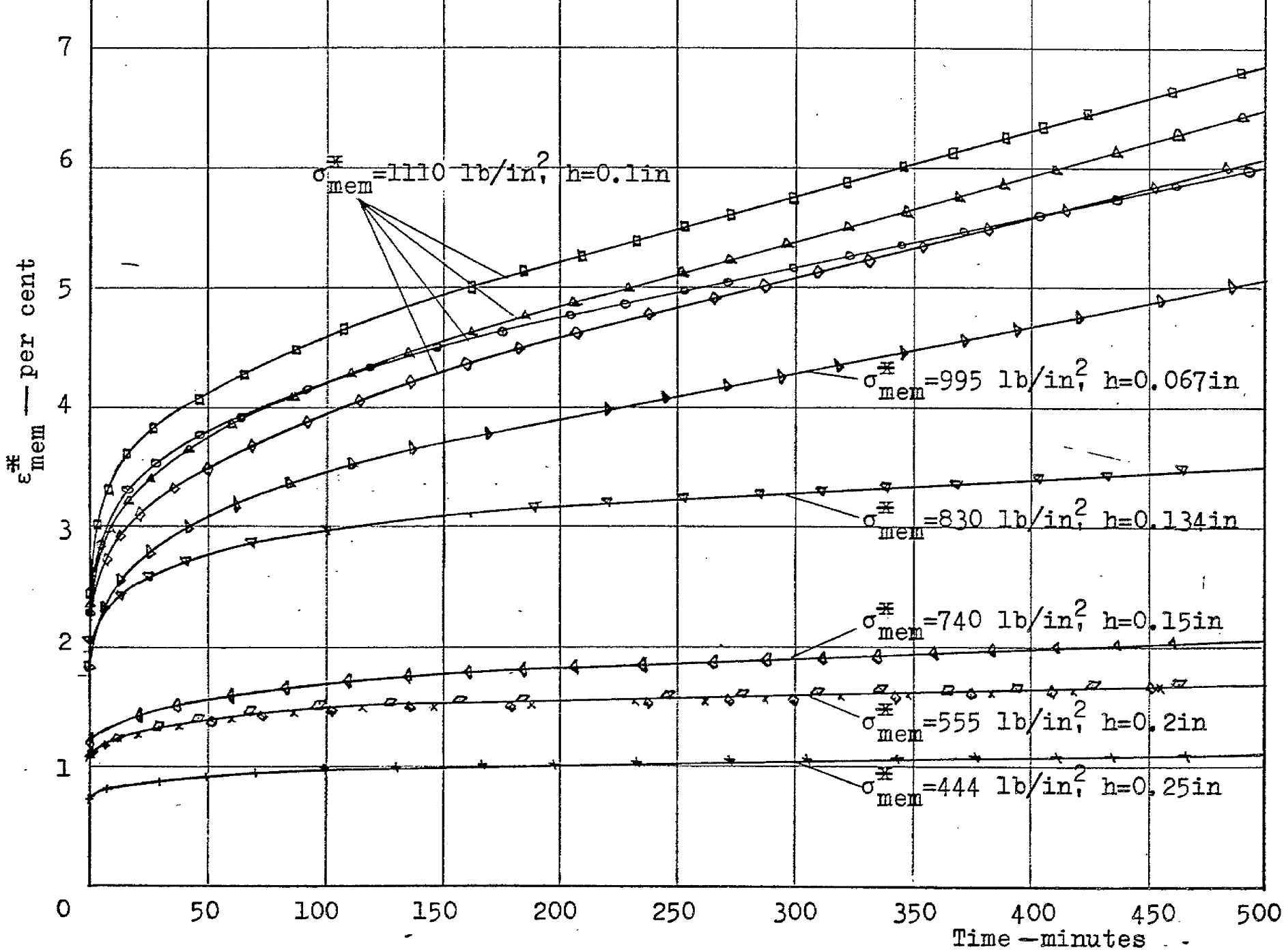

Fig.8.4 Increase of effective membrane strain with time

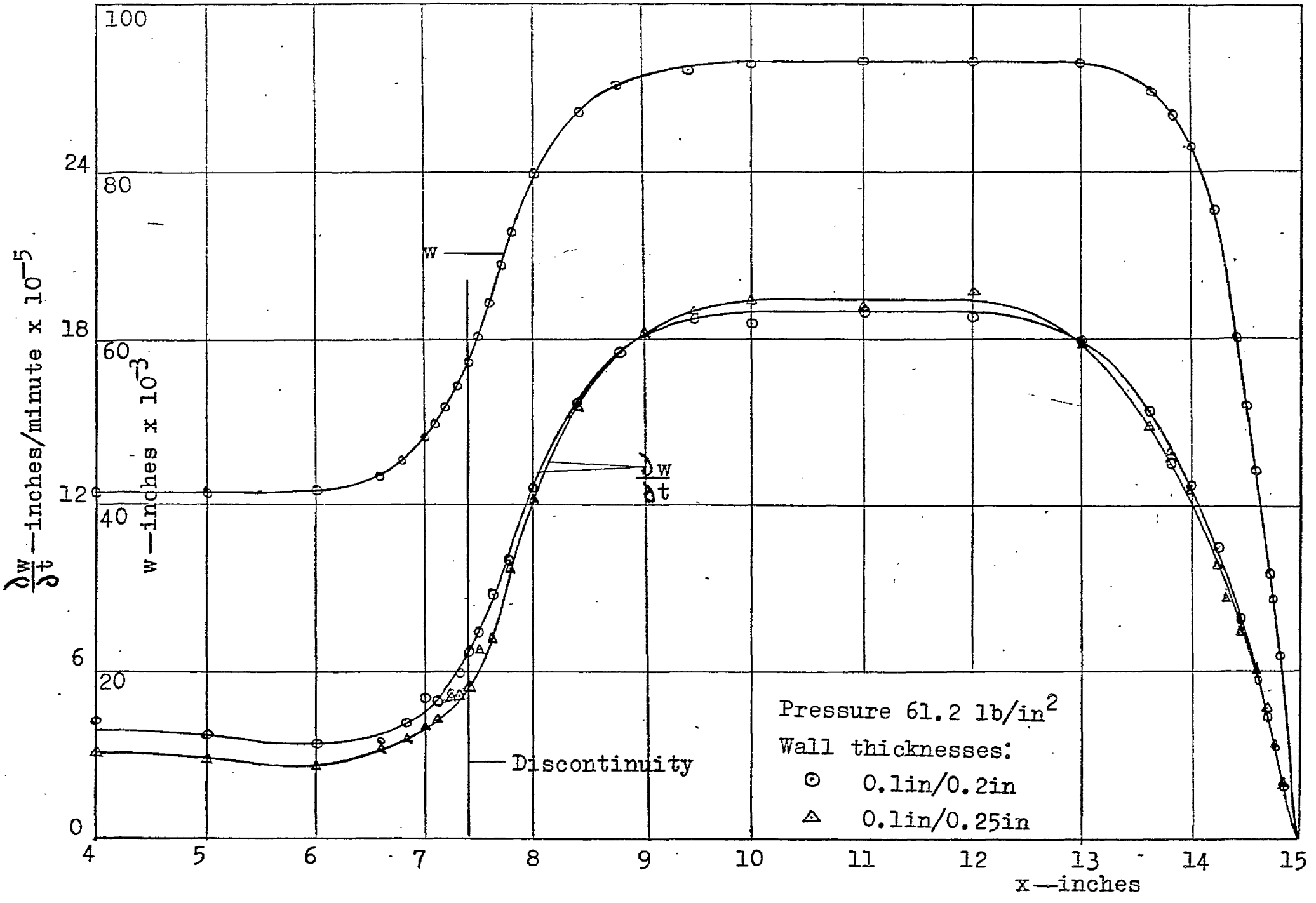

Fig.8.5 Variation of radial velocity and displacement along shell at time t=50minutes

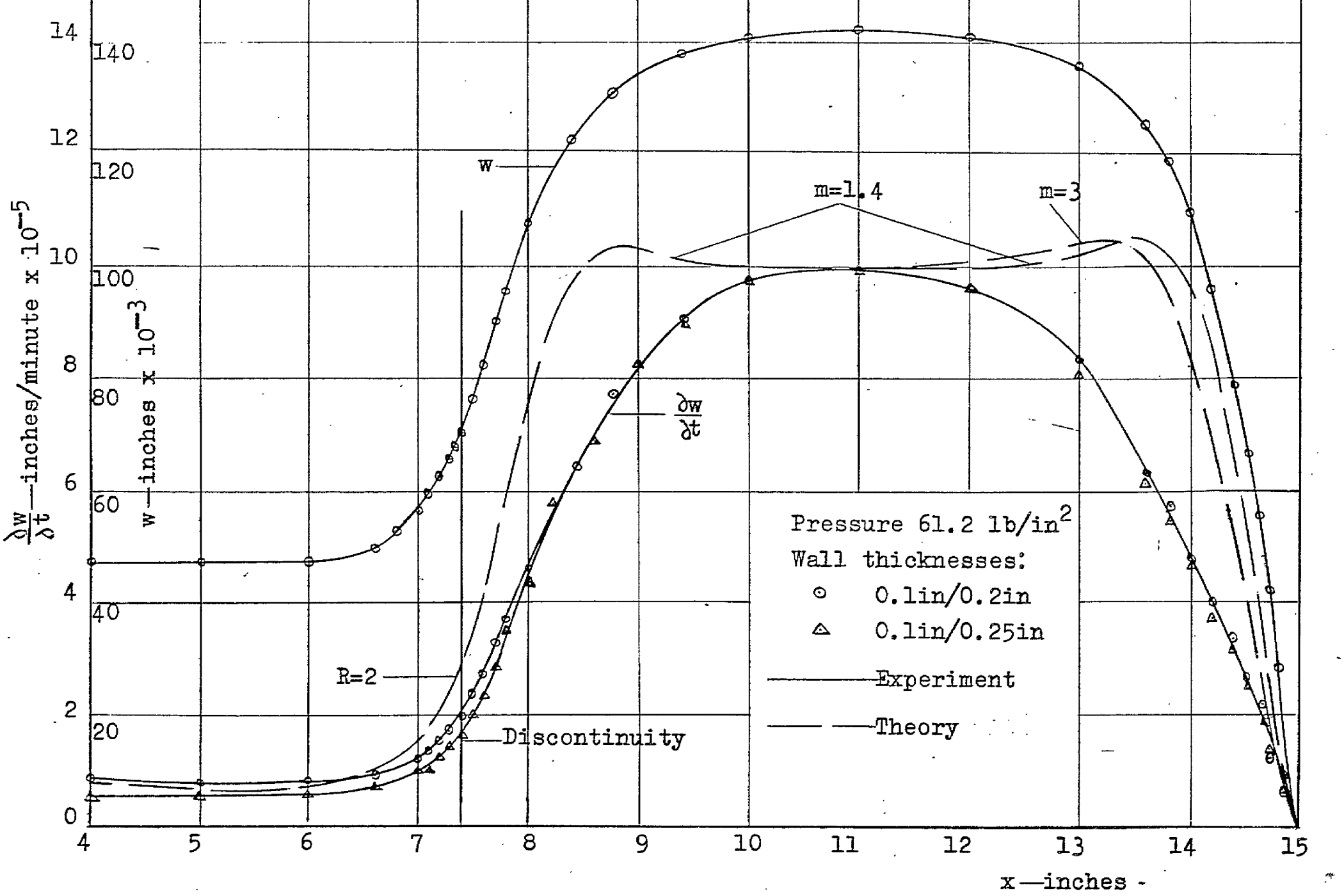

Fig.8.6 Steady state velocity and displacement profiles

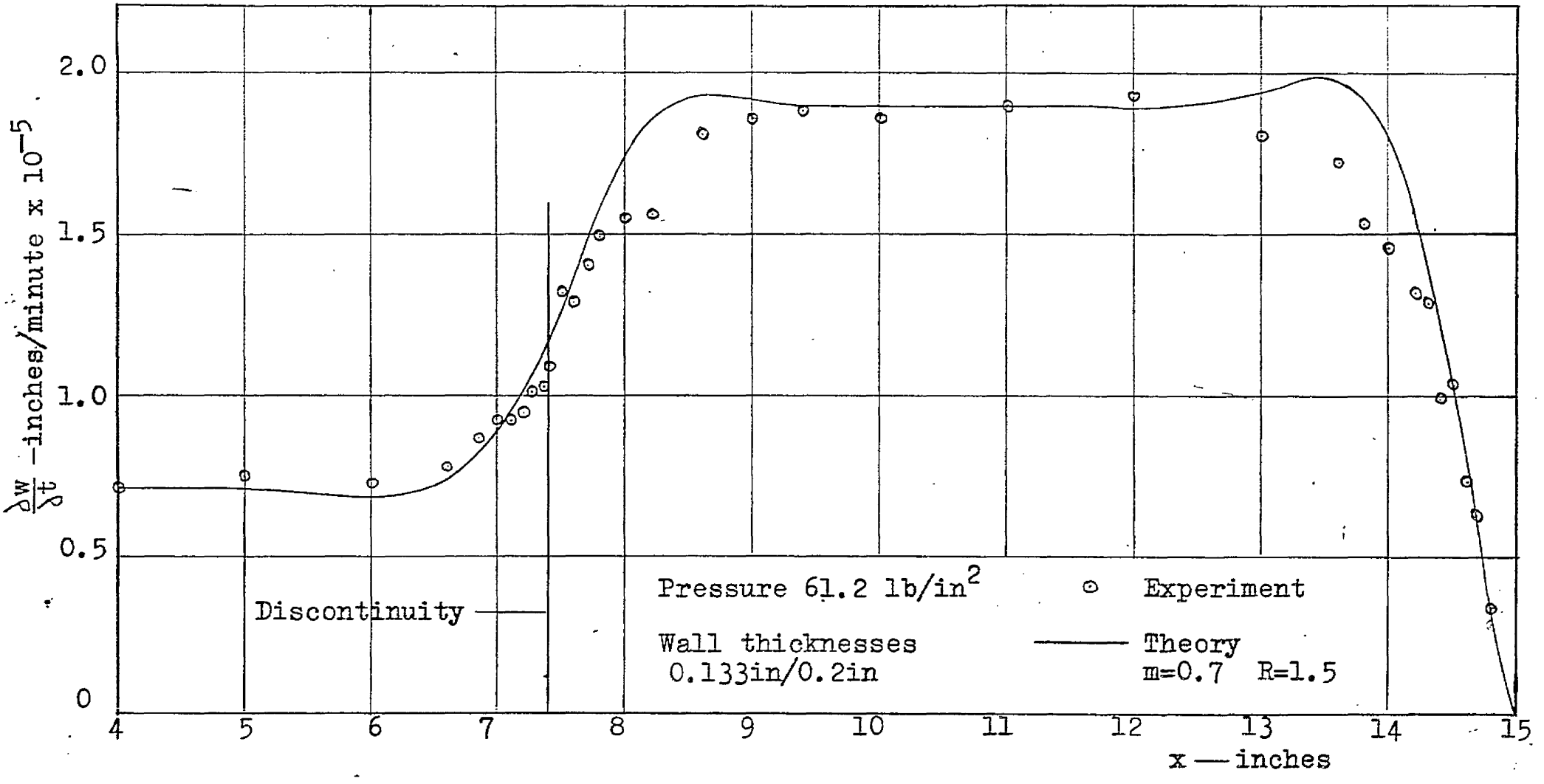

Fig.8.7 Steady state velocity profiles

Shell profile after 30% circumferential strain (opposite bubble)

Plate 8.1

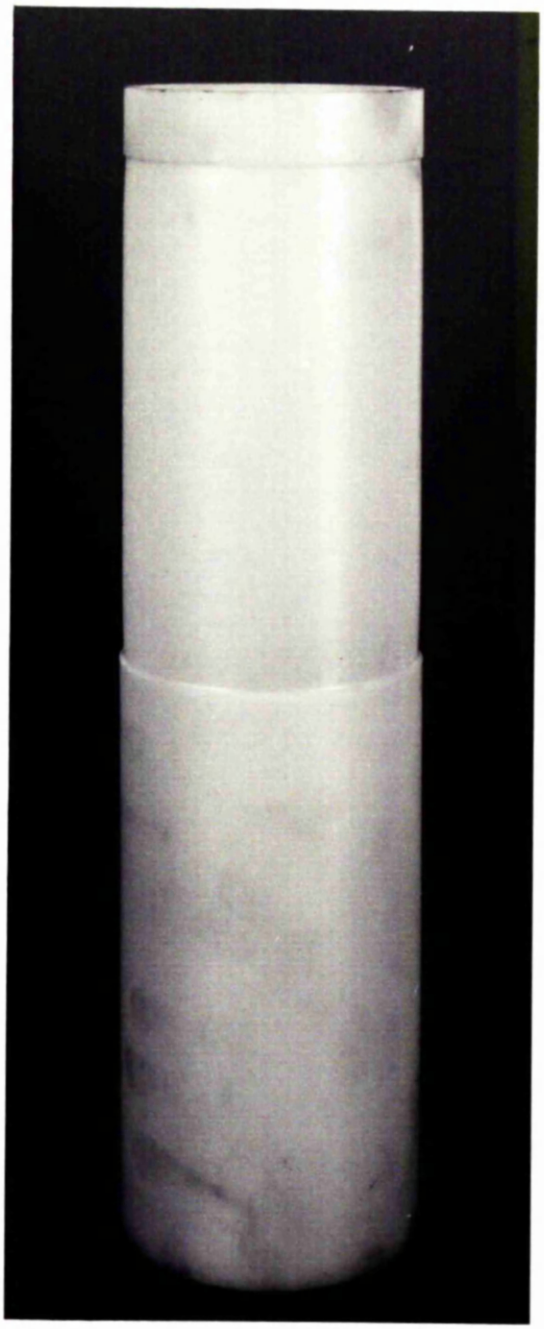

Shell specimen after 6% circumferential strain

Plate 8.2

CHAPTER 9

MODIFICATION OF THEORY

9.1 Examination of Equilibrium Equations.

When the strains are at all large the most probable source of inaccuracy in the mathematical description of the loaded shell (Chapter 2) would appear to be the equilibrium equations, which were obtained with the stress resultants assumed to act on the undeformed shell geometry. If this simplification is discarded completely the resulting equilibrium equations are very intractable. However, a useful compromise can be achieved by considering the equilibrium of a shell element, in its deformed position, while ignoring changes in its dimensions.

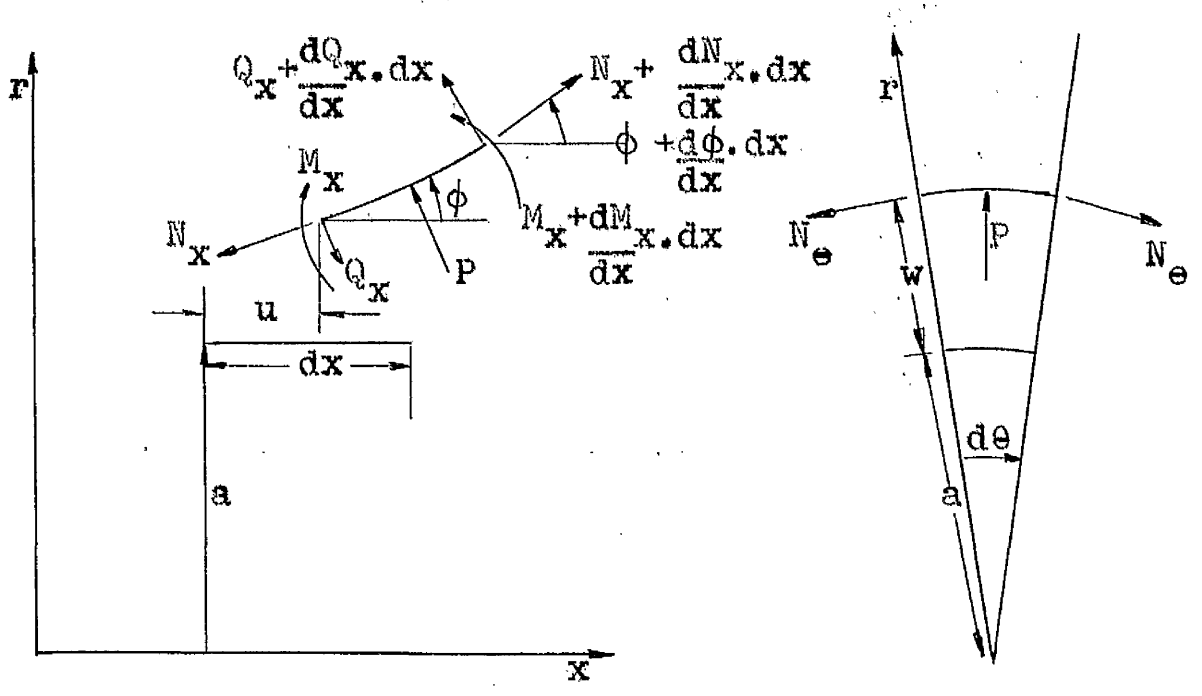

Fig. 9.1

Fig. 9.1 shows schematically a shell element before and after deformation; the deformed element is in equilibrium under the action of the stress resultants and applied load. Force equilibrium in the x direction requires that

$$-N_x \cos\phi . a d\theta + (N_x + \frac{dN_x}{dx} . dx)\cos(\phi + \frac{d\phi}{dx} . dx) a d\theta$$

$$+Q_x \sin\phi . a d\theta - (Q_x + \frac{dQ_x}{dx} . dx)\sin(\phi + \frac{d\phi}{dx} . dx) a d\theta$$

$$- P\sin(\phi + \frac{d\phi}{dx} . \frac{dx}{2}) dx . a d\theta = 0$$

ϕ is a small angle and to a first approximation $\cos\phi = 1$, $\sin\phi = \phi$, $\phi = \frac{dw}{dx}$; with terms of order dx.dx dropped, the equation then becomes

$$\frac{dN_x}{dx} - Q_x \frac{d^2w}{dx^2} - \frac{dQ_x}{dx} . \frac{dw}{dx} - P\frac{dw}{dx} = 0$$

and on integration,

$$N_x = N_a + Pw + Q_x \frac{dw}{dx} \qquad (9.1)$$

A similar treatment of force components in the radial direction leads to

$$\frac{dQ_x}{dx} - \frac{N_\theta}{a} + N_x . \frac{d^2w}{dx^2} + \frac{dN_x}{dx} . \frac{dw}{dx} = -P \qquad (9.2)$$

The moment equilibrium equation is unchanged i.e.

$$\frac{dM_x}{dx} + Q_x = 0 \qquad (9.3)$$

The relative importance of the terms containing the displacement w in equations (9.1) and (9.2) may be judged

by estimating their orders of magnitude from experimental measurements and small deflection solutions. Table 9.1 shows estimates of the maximum values of these terms obtained from the experimental results of Fig. 8.6 and the associated theoretical solution for small deflections at the fixed end (m=3). Examination of these values and equa-

	Max.^{m} value	Value of x (Fig. 8.6)
Pw	0.14P lb/in	12in
$Q_x \cdot \frac{dw}{dx}$	0.033P lb/in	14.8in
$N_x \cdot \frac{d^2w}{dx^2}$	2.4P lb/in^2	15in
$\frac{dN_x}{dx} \cdot \frac{dw}{dx}$	0	all x

Shell radius a=2in; $N_a = \frac{Pa}{2} = P$ lb/in

Table 9.1

tions (9.1) and (9.2) indicates that the dominant term near the fixed end is $N_x \cdot \frac{d^2w}{dx^2}$. If this displacement term alone is retained the equilibrium equations (9.1)-(9.3) may be combined as,*

* This form of the equilibrium equations is used in the analysis of buckling problems-see, for example, [45].

$$N_x = N_a$$

$$\frac{d^2M_x}{dx^2} + \frac{N_\theta}{a} - N_a\frac{d^2w}{dx^2} = P$$

When the non-dimensional variables (2.3) are introduced these equations become

$$\begin{aligned} n_x &= n_a \\ m_x'' + n_\theta - \frac{a\epsilon_o}{h}.n_a\bar{w}'' &= p \end{aligned} \tag{9.4}$$

These linear equations can be used in place of (2.7) in analyses such as those of Chapters 3-6, and their application to the problem of the cylindrical shell governed by the steady state relations (5.1) is now considered.

9.2 Re-formulation of Steady State Creep Problem

In a shell undergoing creep and governed by the equilibrium equations (9.4) no steady state, i.e. time independent, solution can exist, since the solution at any time depends on the prevailing deformation. However, the steady state analyses of Chapters 5 and 6 may be adapted to show, approximately, the influence of the deformation term in (9.4), if a simple proportionality is assumed between the radial displacement and velocity functions i.e.

$$\bar{w}(x) = s\dot{\bar{w}}(x) \tag{9.5}$$

Equations (9.4) may then be written

$$\begin{aligned} n_x &= n_a \\ m_x'' + n_\theta - \lambda n_a.\dot{\bar{w}}'' &= p \end{aligned} \tag{9.6}$$

where $\lambda = s\frac{a}{h}\varepsilon_o$. (9.7)

For any particular shell s can be taken as the ratio of the displacement and velocity of the uniformly strained membrane region. Equation (9.7) then becomes

$$\lambda = \frac{\dot{\bar{w}}_{mem}}{\dot{\bar{w}}_{mem}} \cdot \frac{a}{h}\varepsilon_o$$

$$= \frac{1}{\dot{\bar{w}}_{mem}} \cdot \frac{w_{mem}}{h}$$

since by definition $\bar{w} = \frac{w}{a\varepsilon_o}$. $\dot{\bar{w}}_{mem}$ is determined by the values assigned to the loading parameters p, n_a-Section 2.3 e.g. for internal pressure loading

$$\dot{\bar{w}}_{mem} = \frac{\sqrt{3}}{2}$$

and therefore, $$\lambda = \frac{2}{\sqrt{3}} \cdot \frac{w_{mem}}{h} \qquad (9.8)$$

In the manner described in Chapter 5, the equilibrium equations (9.6) are combined with the constitutive equations (5.1) and the time derivatives of the deformation-displacement equations (2.8) to form the governing differential equation:

$$\left[\phi \dot{\bar{w}}''\right]'' + k_1\phi\dot{\bar{w}} - k_3\dot{\bar{w}}'' = k_2 \qquad (9.9)$$

ϕ, k_1, k_2 are as previously defined, and

$$k_3 = 3^{\left(\frac{m}{2m+1}\right)} \cdot k_1 \lambda n_a$$

With equation (9.9) in place of (5.5) a new set of

solutions for the cylindrical shell with fixed ends can be obtained by the iterative method of Chapter 5. When m=0, equation (9.9) reduces to the linear equation

$$\dddot{\bar{w}}'''' + 9\dddot{\bar{w}} - 9\lambda n_a \dddot{\bar{w}}'' = 9(p-\frac{n_a}{2})$$

The form of the solution of this equation depends on the magnitude of λn_a. For a shell with a clamped edge at $\bar{x}=0$ and of semi-infinite length, the solution is

$$\begin{aligned}
\dddot{\bar{w}} &= (p-\tfrac{1}{2}n_a)\left[1-e^{-c_1\bar{x}}(\cos d_1\bar{x}+\frac{c_1}{d_1}\sin d_1\bar{x})\right], && \lambda n_a < \tfrac{2}{3} \\
\dddot{\bar{w}} &= (p-\tfrac{1}{2}n_a)\left[1-e^{-\sqrt{3}\bar{x}}(1+\sqrt{3}\bar{x})\right], && \lambda n_a = \tfrac{2}{3} \qquad (9.10) \\
\dddot{\bar{w}} &= (p-\tfrac{1}{2}n_a)\left[1-\frac{1}{c_2-d_2}(c_2e^{-d_2\bar{x}}-d_2e^{-c_2\bar{x}})\right], && \lambda n_a > \tfrac{2}{3}
\end{aligned}$$

In these equations

$$\begin{aligned}
c_1 &= \sqrt{3}\cos\left\{\tfrac{1}{2}\tan^{-1}\left[\frac{2\sqrt{1-\frac{9}{4}\lambda^2 n_a^2}}{3\lambda n_a}\right]\right\} \\
d_1 &= \sqrt{3}\sin\left\{\tfrac{1}{2}\tan^{-1}\left[\frac{2\sqrt{1-\frac{9}{4}\lambda^2 n_a^2}}{3\lambda n_a}\right]\right\} \qquad (9.11) \\
c_2 &= \sqrt{\tfrac{9}{2}\lambda n_a + 3\sqrt{\tfrac{9}{4}\lambda^2 n_a^2 - 1}} \\
d_2 &= \sqrt{\tfrac{9}{2}\lambda n_a - 3\sqrt{\tfrac{9}{4}\lambda^2 n_a^2 - 1}}
\end{aligned}$$

The analysis of Chapter 6 can be similarly adapted to give the corresponding solutions for a cylindrical shell with an abrupt thickness change.

9.3 Comparison of Solutions with Experimental Results

The steady state velocity measurements of Figs. 8.6 and 8.7 are reproduced in Figs. 9.2 and 9.3 and compared with distributions obtained from the modified analysis. The values of λ are calculated in each case from equation (9.8), w_{mem} being taken as the average membrane displacement in the thinner shell during steady state creep.

In Fig. 9.3 the measured and predicted velocity profiles agree within the limits of the accuracy of the experimental measurements. In this case, as previously mentioned, the power law with m=0.7 is a fairly good representation of material behaviour. In the shell of Fig. 9.2 the stress exponent m varies considerably; the theoretical distribution with m=1.4 is shown at the discontinuity-with this value of m, measured and theoretical results agree in the membrane region of both halves of the shell-while at the fixed end m=3, giving a better description of material behaviour, is used. These theoretical curves are much closer than the original solutions-Fig. 8.6-to the measured values. The difference that does exist can reasonably be attributed to the material equations not being of simple power type, to the assumption that the radial displacement is proportional to the radial velocity-equation (9.5), and perhaps to the effects produced by the changes in shell geometry which have been neglected.

In Figs. 9.4-9.6 steady state velocity profiles from the other shells tested are shown together with appropriate theoretical distributions.

From the comparisons of Figs. 9.2-9.6 it is clear that the major cause of the disagreements observed in Chapter 8, is the omission, in the original analysis, of the radial force component produced by the axial load acting on the deformed shell. The importance of this force is determined by the magnitude of the parameter λ, or-equation (9.8)-by the ratio of the radial displacement and shell thickness. The larger this ratio the greater is the influence of the deformation dependent force. The value of λ at which the effect of the additional force becomes negligible may be judged from examination of the linear (m=0) solution. When $\lambda=0$, equations (9.11) yield

$$c_1 = d_1 = \sqrt{\frac{3}{2}}$$

and the solution (9.10) becomes that of small deflection shell theory. This solution will give a good approximation to shell behaviour provided that the coefficients c_1, d_1 differ little from $\sqrt{\frac{3}{2}}$. From equations (9.10) this restriction requires

$$\lambda \ll \frac{2}{3n_a} \qquad (9.12)$$

For internal pressure loading $n_a=\frac{1}{\sqrt{3}}$, and equations (9.12) and (9.8) combine to produce the requirement:

$$\frac{w_{mem}}{h} \ll 1 \qquad (9.13)$$

When this condition is fulfilled small deflection analysis is adequate.

It should be noted that the strain components need not be large for the inequality (9.13) to be violated. If the shell is very thin, elastic deformation alone may be sufficient to make the ratio $\frac{w_{mem}}{h}$ significant.

If radial loading alone is applied to the shell the additional force disappears from the equilibrium equations (9.4), and the solution for any value of λ is that of small deflection theory. Experiments on shells subject to radial loading alone, therefore, will provide a critical test of the modified theory.

9.4 Influence of λ on Deformations and Stresses

The nature of the influence of λ on the solutions for a shell with fixed ends is shown in Figs. 9.7 and 9.8, where $\dot{\bar{w}}$ and m_x are plotted against $\bar{x}$ for internal pressure loading, m=1 and several values of λ. As λ increases the oscillation of the velocity function diminishes and eventually disappears, and $\dot{\bar{w}}$ tends asymptotically to its membrane value. This change in the form of the solution is similar to that of the linear (m=0) problem-equations (9.10). The decay length increases with λ, the effect of

the edge clamping extending further and further along the shell.

An interesting result emerges from the linear solution of the problem. From equations (9.10) and (9.11) it can be shown that for any value of λn_a

$$\dot{\bar{w}}''(0) = 3(p-\tfrac{1}{2}n_a)$$

Thus, the greatest curvature rate $\dot{k}_x(0)\left[=\dot{\bar{w}}''(0)\right]$, and hence -equation (5.1) with m=0- the greatest bending moment $m_x(0)$, are independent of λ. The numerical values of these quantities for non-zero m change very little with λ (points representing $m_x(0)$ in Fig. 9.8 for three values of λ are indistinguishable), suggesting that the invariance might extend to all values of m.

The maximum shear force (not an important quantity when the deformations are small), however, increases considerably with λ as is shown in Fig.9.9 where $q_x(0)$ is plotted against λ for m=0 and 1. The linear (m=0) curve tends asymptotically to the function $q_x(0)=\frac{4\sqrt{3}}{2}\sqrt{\lambda}$.

The important effect of λ on a shell with a thickness change is to diminish the greatest strain at the discontinuity, as is shown in Fig. 9.10 where $\dot{\bar{\varepsilon}}^*_d$ is plotted against λ for internal pressure, m=1, R=2 and 4. This decrease in $\dot{\bar{\varepsilon}}^*_d$ with λ (as with m, for small values of R- Chapter 6) can be attributed to the growth of the decay length.

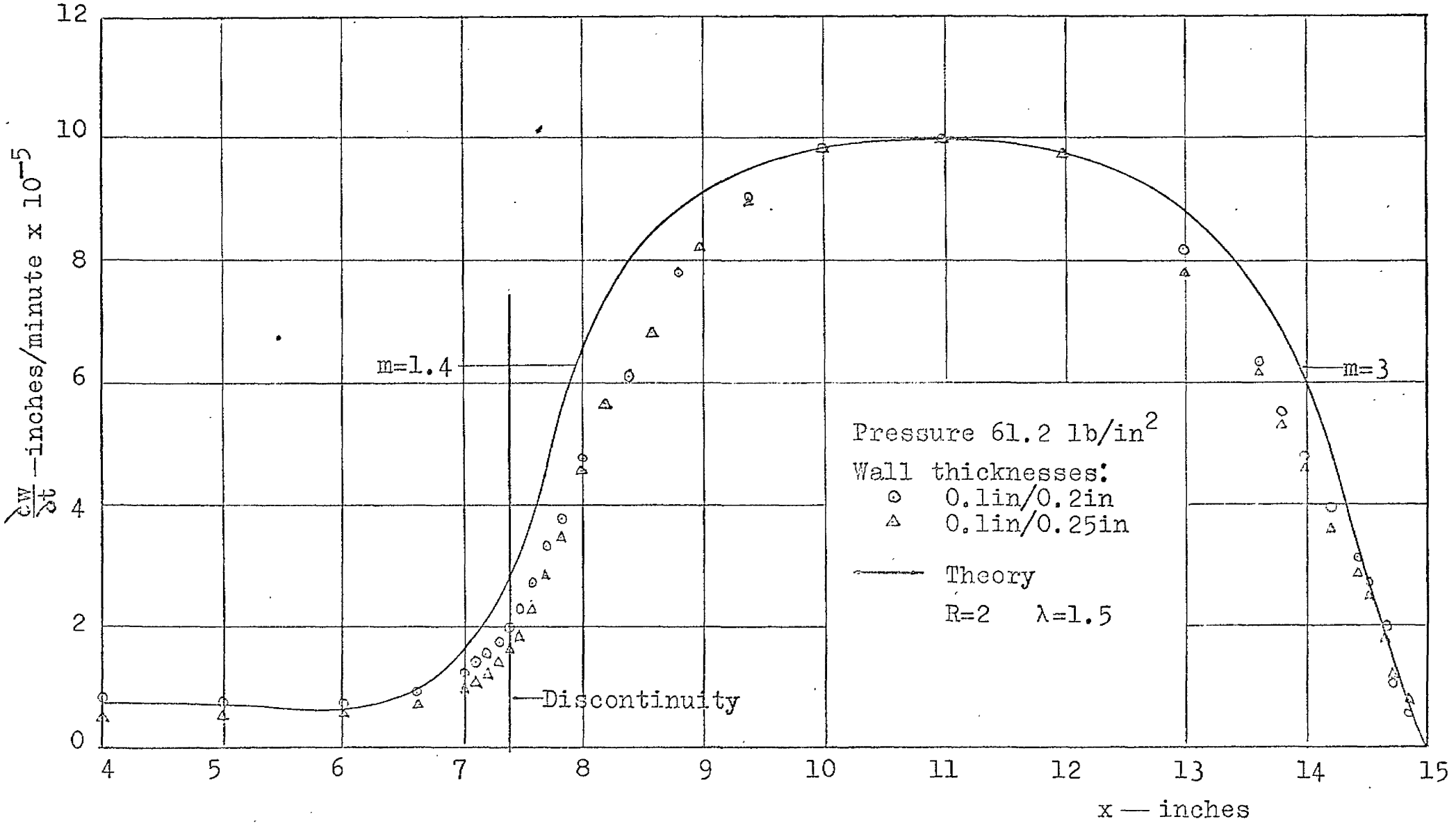

Fig.9.2 Comparison of steady state velocity profiles obtained by experiment and from modified theory

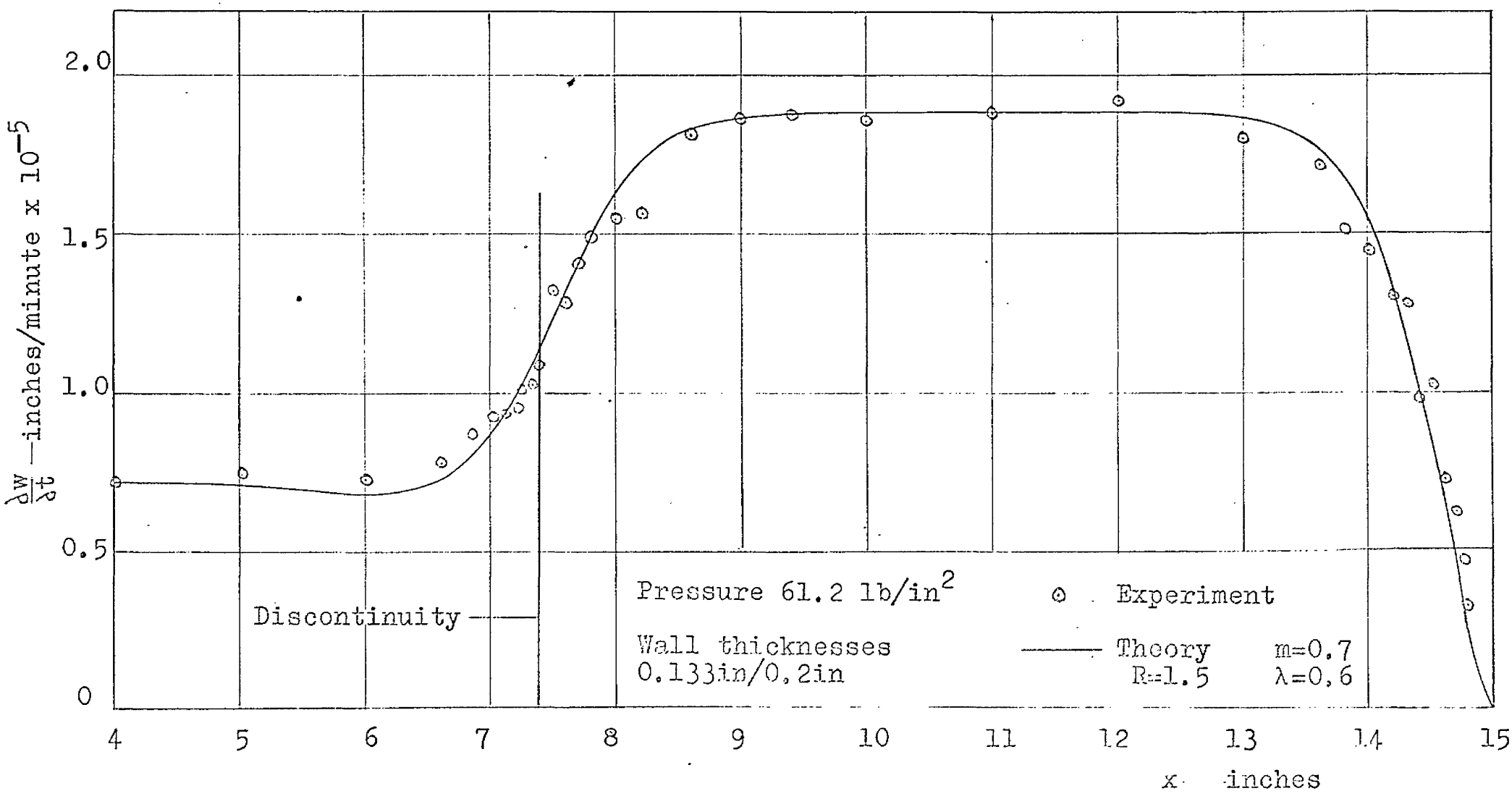

Fig.9.3 Comparison of steady state velocity profiles obtained by experiment and from modified theory

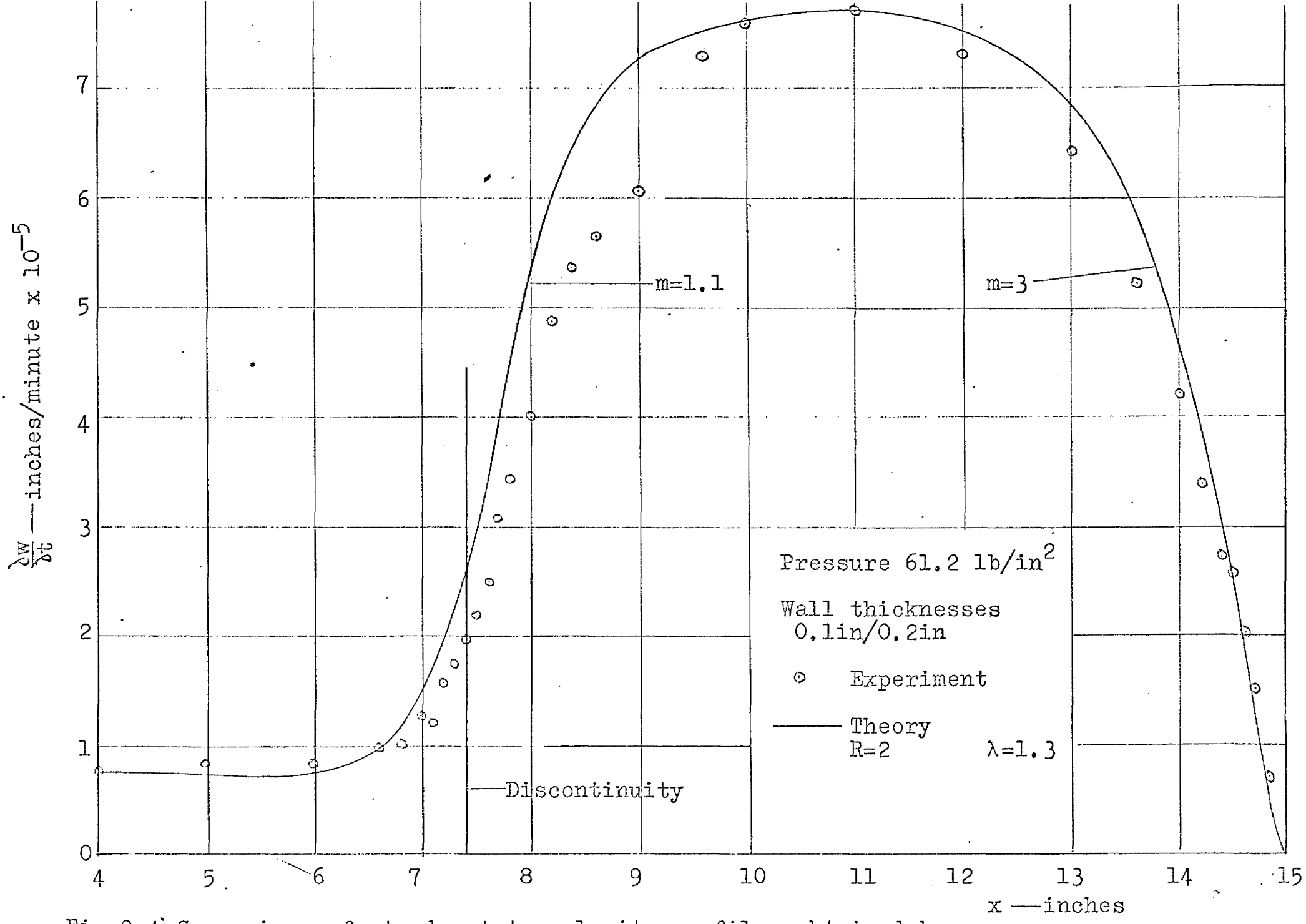

Fig.9.4 Comparison of steady state velocity profiles obtained by experiment and from modified theory

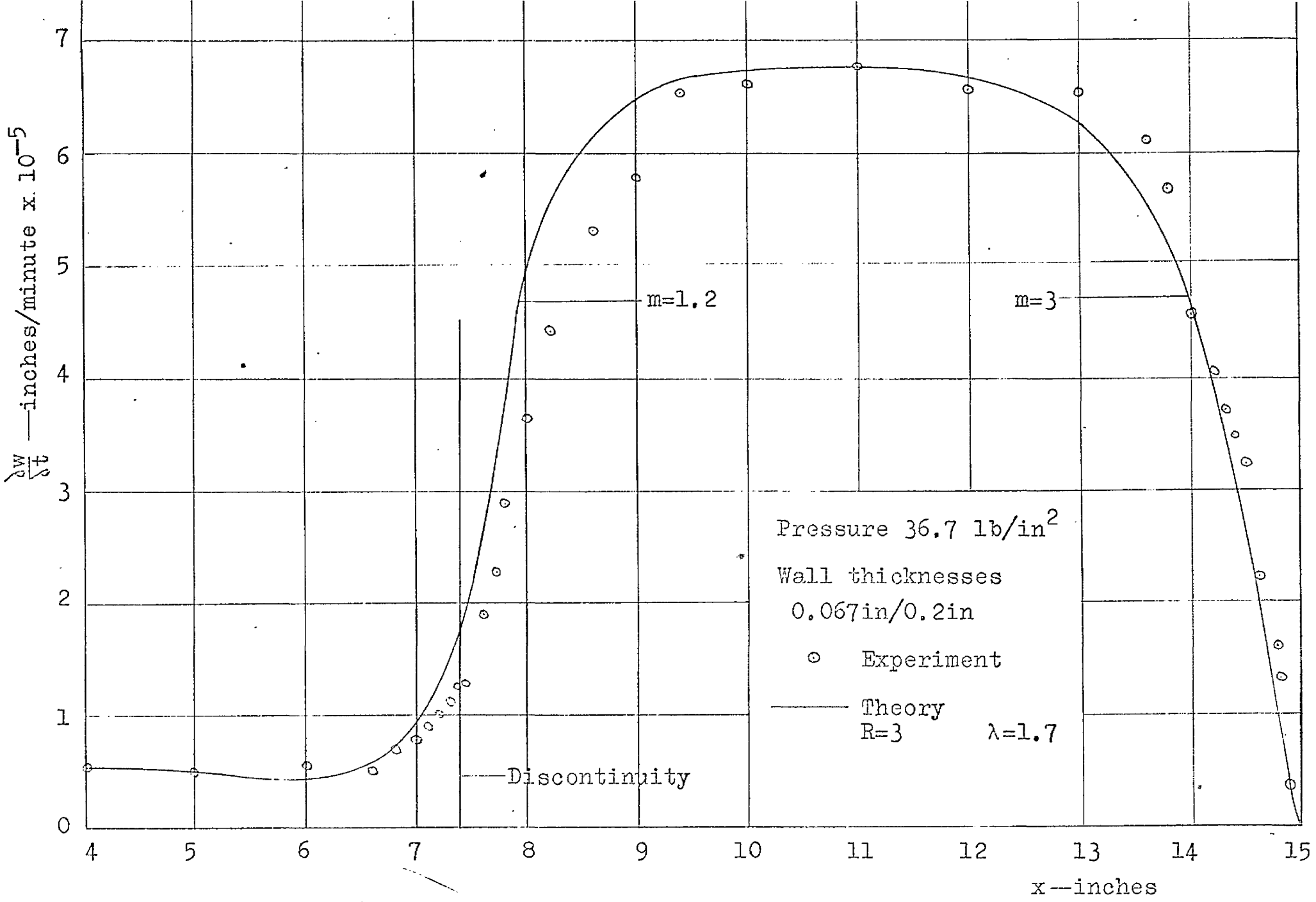

Fig.9.5 Comparison of steady state velocity profiles obtained by experiment and from modified theory

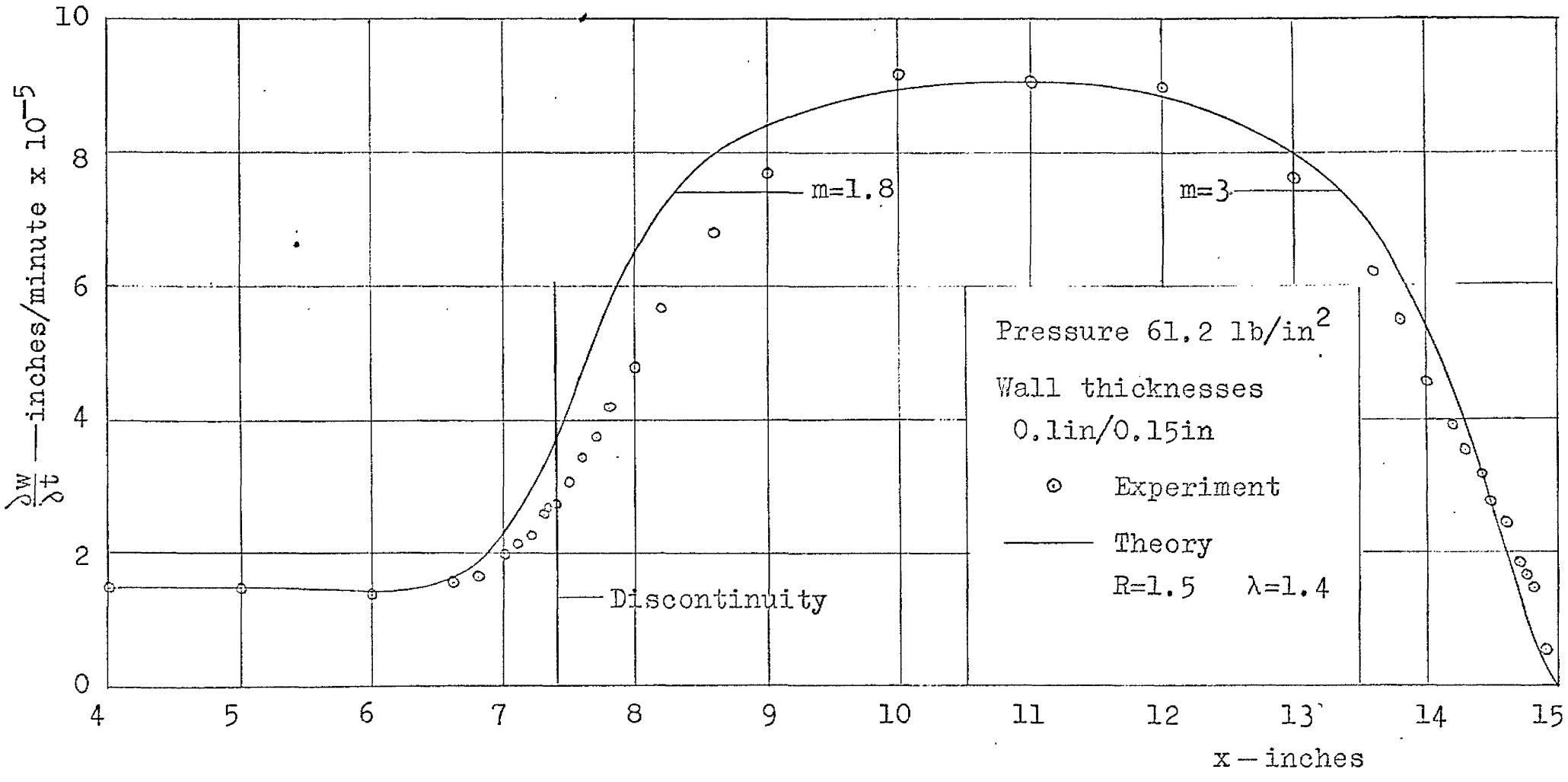

Fig.9.6 Comparison of steady state velocity profiles obtained by experiment and from modified theory

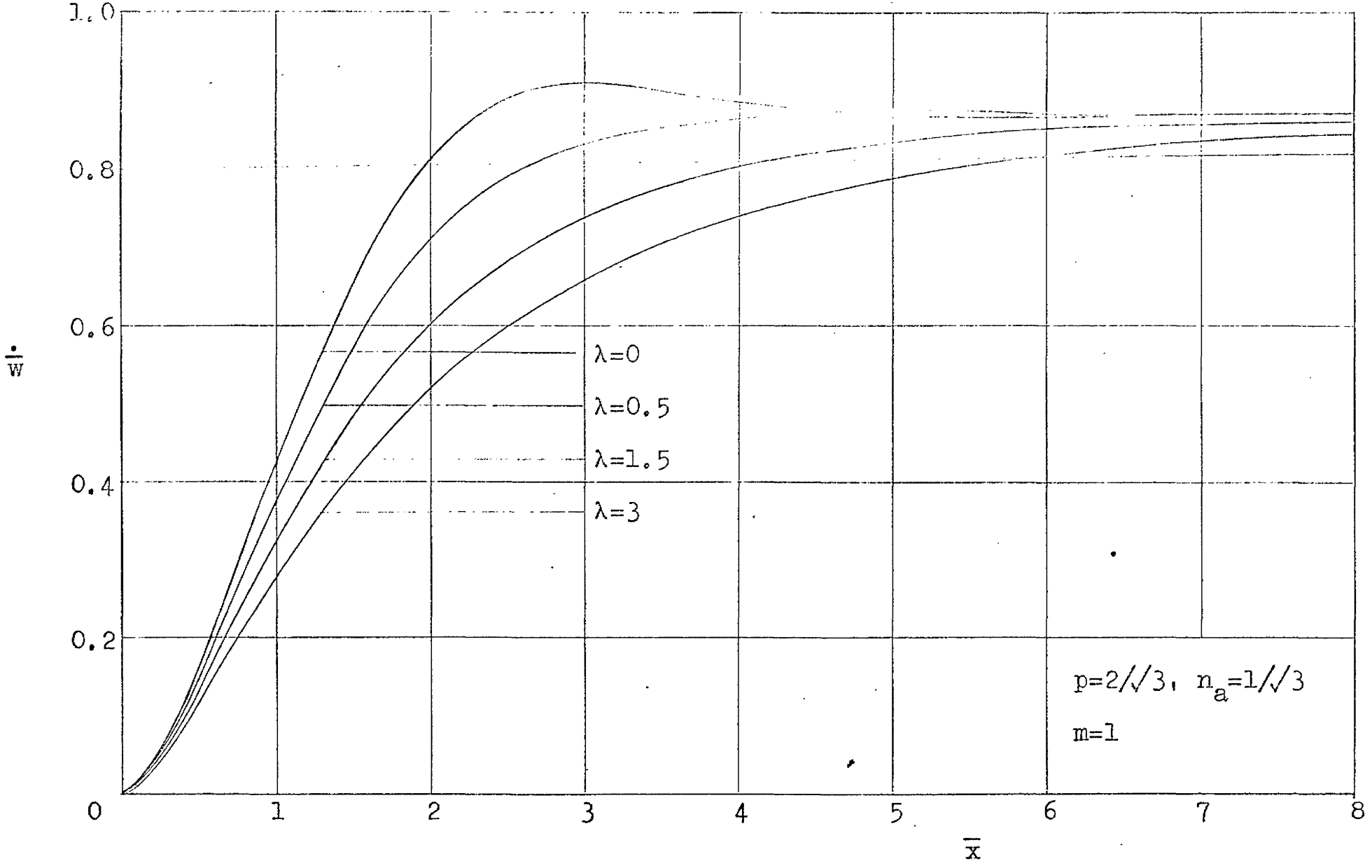

Fig.9.7 Influence of λ on steady state radial velocity distribution

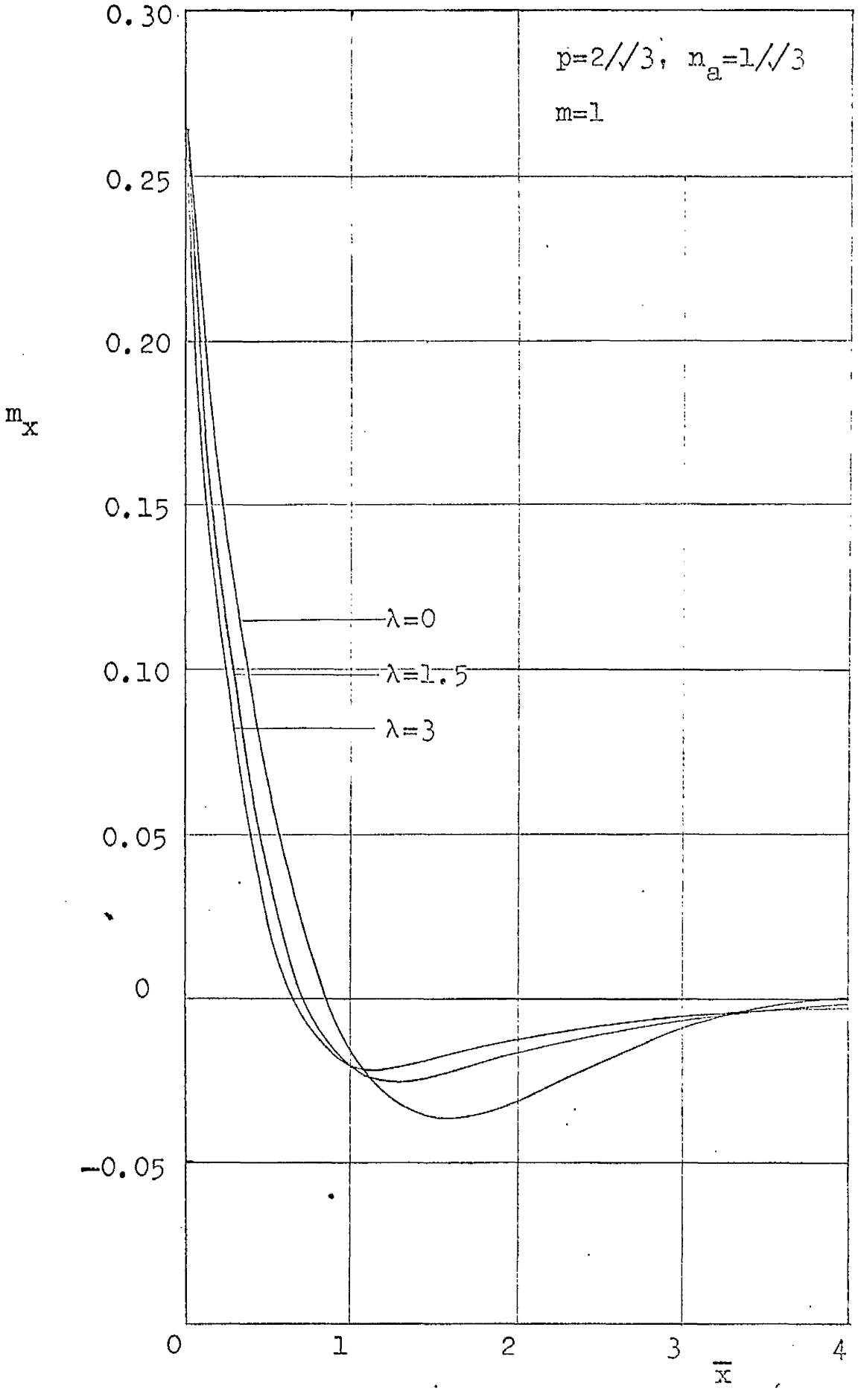

Fig.9.8 Influence of λ on steady state bending moment distribution

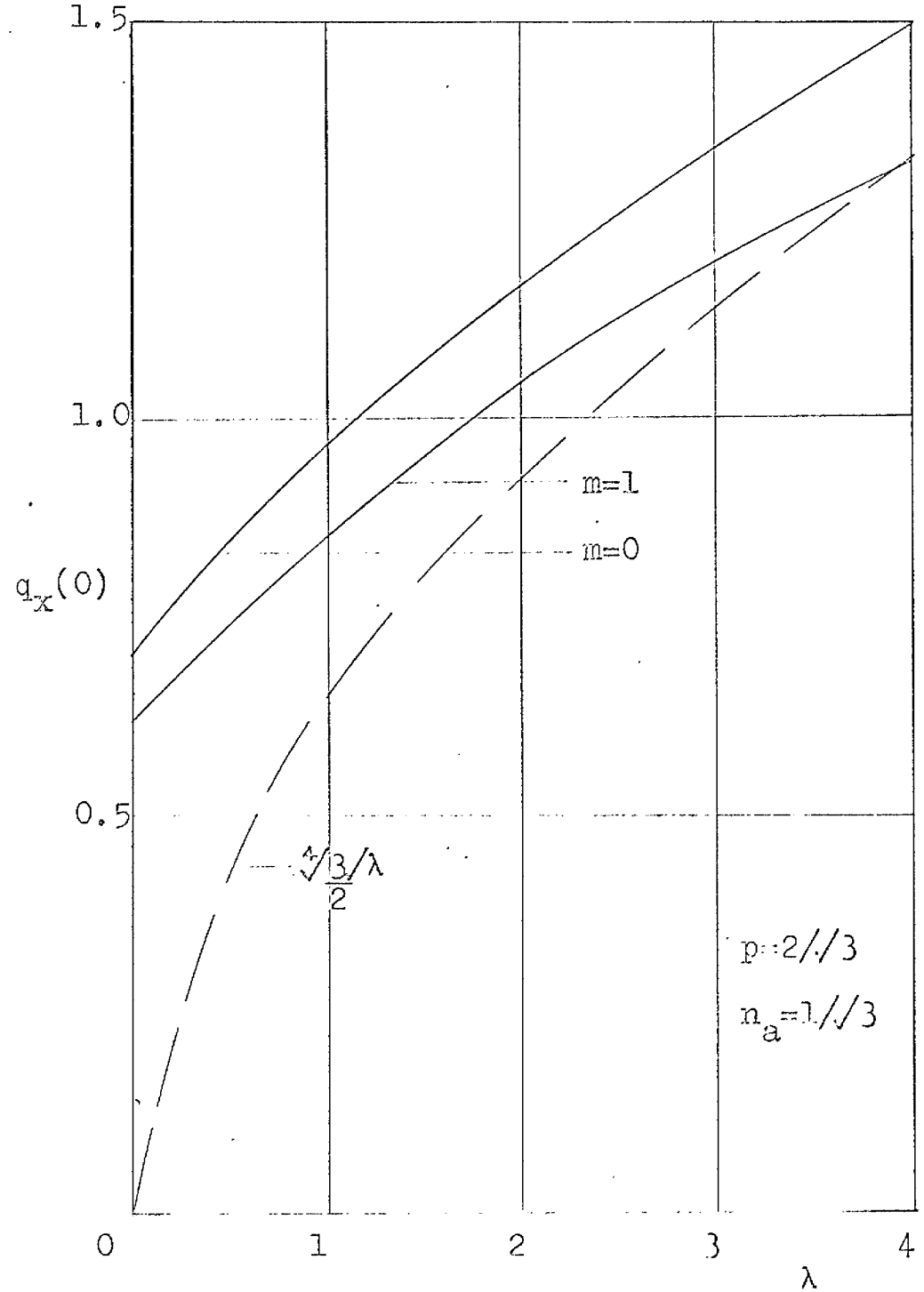

Fig.9.9 Influence of λ on greatest shear stress resultant

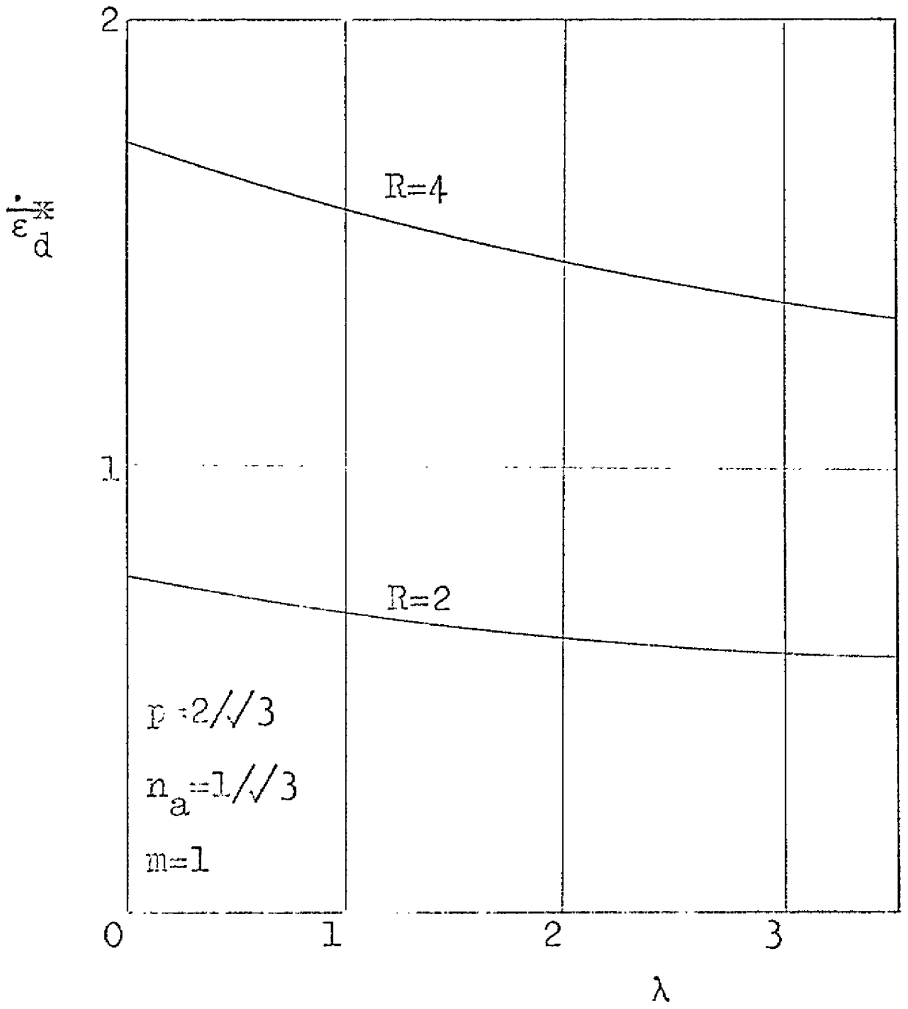

Fig.9.10 Influence of λ on greatest effective strain at discontinuity

CHAPTER 10

CONCLUSIONS

1) Considerable stress redistribution can take place in cylindrical shell structures during creep, the extent of the redistribution being determined by Poisson's ratio and the stress exponent of the creep strain rate law. In all the cases investigated the stress changes do not have much influence on the growth of total strains, and the latter can be estimated with satisfactory accuracy from the initial elastic strains and the steady state creep strain rates.

2) The approximate relations proposed for steady state analysis in references [21] and [22] are useful for indicating the general influence of the stress exponent on shell behaviour, but they cannot in general be relied on to provide more detailed information accurately.

3) Solutions obtained for a cylindrical shell with an abrupt thickness change suggest that, if an elastic analysis with Poisson's ratio equal to a half shows no strain concentration at the junction of two shells, a concentration will not develop during creep unless the stress exponent is very large.

4) If the radial displacement and thickness of a cylindrical shell are of the same order of magnitude, the conditions for equilibrium are not obtained with sufficient

accuracy by assuming the stress resultants to act on the undeformed shell geometry, and an additional force action, dependent on the deformation and axial load, must be taken into account.

5) When this additional force was included in the theoretical analyses satisfactory agreement was obtained with the measured steady state velocity profiles of polypropylene shells.

6) Polypropylene is a suitable material for short term creep tests, though to obtain consistent results it is necessary to use fairly thick sections and moderate stress levels.

APPENDIX 1

R E F E R E N C E S

1. Finnie, I., Heller, W.R., "Creep of engineering materials", McGraw-Hill, 1959.

2. Marin, J., "Mechanics of creep and combined stresses", Proc. IUTAM Coll. on Creep in Structures, Springer-Verlag, 1962, 79-95.

3. Johnson, A.E., Henderson, J., Khan, B., "Multiaxial creep-strain complex-stress/time relations for metallic alloys with some applications to structures", Proc. Joint Int. Conf. on Creep, Inst. Mech. Engrs., 1963.

4. Johnson, A.E., Henderson, J., Mathur, V., "Creep under changing complex stress systems", The Engineer, 1958, Aug. 8, 209-216, Aug. 15, 251-257, Aug.22, 287-291.

5. Marriott, D.L., Leckie, F.A., "Some observations on the deflections of structures during creep", Proc. Conf. on Thermal Loading and Creep, Inst. Mech. Engrs., 1964.

6. Frederick, C.O., Lewis, D.J., "Primary creep deformation of beams", Proc. Conf. on Thermal Loading and Creep, Inst. Mech. Engrs., 1964.

7. Smith, E.M., "Primary creep behaviour of thick tubes", Proc. Conf. on Thermal Loading and Creep, Inst. Mech. Engrs., 1964.

8. Leckie, F.A., Martin, J.B., "Deformation bounds for bodies in a state of creep", Brown University Report, 1965.

9. Mendelson, A., Hirschberg, M.H., Manson, S.S., "A general approach to the practical solution of creep problems", J. Basic Eng., 1959, 585-598.

10. Poritsky, H., "Effect of creep on stresses in cylindrical shells", Proc. Coll. on Creep in Structures, IUTAM, Springer-Verlag, 1962, 79-95.

11. Hoff, N.J., "Effects thermiques dans le calcul de la resistance des structures d'avions et d'engins", AGARD Report No. 52, 1956(Jan.).

12. Wahl, A.M., "A comparison of flow criteria applied to elevated temperature creep of rotating discs with consideration of the transient condition", Proc. Coll. on Creep in Structures, IUTAM, Springer-Verlag, 1962, 195-214.

13. Gubser, J.L., Sidebottom, O.M., Shammamy, M.R., "Creep torsion of prismatic bars", Proc. Joint Int. Conf. on Creep, Inst. Mech. Engrs., 1963.

14. Bailey, R.W., "Utilization of creep test data", Proc. Inst. Mech. Engrs., 1935, vol. 131, 131-350.

15. Patel, S.A., "Creep of annular plates under symmetric lateral pressure", Proc. Conf. on Thermal Loading and Creep, Inst. Mech. Engrs., 1964.

16. Venkatraman, B., "Creep in the presence of a concentrated force at a point", Proc. Conf. on Thermal Loading and Creep, Inst. Mech. Engrs., 1964.

17. Bieniek, M.P., Freudenthal, A.M., "Creep deformation and stresses in pressurised, long cylindrical shells", J. Aerospace Sci., 27, 10, 1960, 763-766.

18. Onat, E.T., Yuksel, H., "On the steady creep of shells", Proc. 3rd U.S. Nat. Congr. Appl. Mech., 1958, 625-630.

19. Calladine, C.R., "The steady creep of shells: a method of analysis", Proc. Symp. on Nuclear Reactor Containment Buildings and Pressure Vessels, Butterworths, 1960.

20. Gemma, A.E. "The creep deformation of symmetrically loaded circular cylindrical shells", J. Aerospace Sci., 1960, 27(12), 953.

21. Rozenblium, V.I., "Approximate equations of creep of thin shells", PMM, 1963, 27(1), 217-226.

22. Mackenzie, A.C., "On the equations for steady state creep of thin shells", J. Mech. Eng. Sci., 1965, 7(1), 114.

23. Flugge, W., "Stresses in Shells", Springer-Verlag, 1962.

24. Johnson, A.E., Henderson, J., Khan, B., "The behaviour of cylindrical pressure vessels and thick-walled tubes under internal and external pressure at elevated temperatures", Proc. Inst. Mech. Engrs., 1961, 175(25), 1043.

25. Shinozuka, M., Spillers, W.R., "Axisymmetric reinforced viscoelastic cylindrical shell", Int. J. Mech. Sci., 8, 1963, 1-12.

26. Timoshenko, S., "Vibration problems in engineering", van Nostrand, 1937.

27. Rayleigh, J.W.S., "Theory of sound", Constable, 1945.

28. Rose, W.N., "Mathematics for engineers", Chapman and Hall, 1928.

29. Wilson, W.K., Davis, E.A., "Creep and relaxation of heavy walled cylinders with specific axial boundary conditions", Proc. Joint Int. Conf. on Creep, Inst.

Mech. Engrs., 1963.

30. Hartree, D.R., "Numerical analysis", O.U.P., 1952.

31. Fox, L., "Numerical solution of two point boundary value problems", O.U.P., 1957.

32. Hodge Jr., P.G., "Limit analysis of rotationally symmetric plates and shells", Prentice-Hall, 1963.

33. Smith, E.M., "An investigation of the creep of thick tubes subjected to internal pressure", Ph.D. thesis, University of Glasgow, 1962.

34. King, R.H., "Creep of thick-walled cylinders under internal pressure", Ph.D. thesis, University of Glasgow, 1964.

35. Turner, S., "Creep in thermoplastics: polythene", British Plastics, Sept. 1964.

36. Turner, S., "Creep in thermoplastics: polypropylene", British Plastics, Aug. 1964.

37. Turner, S., "Creep in thermoplastics: unplasticized PVC", British Plastics, Dec. 1964.

38. Turner, S., "Creep in thermoplastics: nylon 66", British Plastics, Jan. 1965.

39. Sully, A.H., "Metallic creep", Butterworths, 1949.

40. Finnie, I., "An experimental study of multiaxial creep in tubes", Proc. Joint Int. Conf. on Creep, Inst. Mech. Engrs., 1963.

41. Johnson, D.P., Newhall, D.H., "The piston gauge as a precise pressure measuring instrument", Trans. A.S.M.E., 1953, vol. 75, no. 3, 301.

42. Singh, D.N., "A manometric piston gauge", D.S.I.R., M.E.R.L. Fluid Mechs. Div. Report 66, Feb. 1958.

43. Crossland, B., "The effect of fluid pressure on the shear properties of metals", Proc. Inst. Mech. Engrs., 1954, vol. 168.

44. Tobolsky, A.V., "Properties and structure of polymers", John Wiley, 1962.

45. Timoshenko, S., Gere, J.M., "Theory of elastic stability", McGraw-Hill, 1961.

APPENDIX 2

2.1 Elastic and Viscous Solutions

From equations (2.4),(2.5),(2.8) and the elasticity equations (3.2), the initial stress resultants may be expressed in terms of displacements:

$$\begin{aligned} m_{xo} &= \frac{1}{12(1-\nu^2)}\,\bar{w}_o'' \\ n_{xo} &= \frac{1}{1-\nu^2}(\bar{u}_o' + \nu\bar{w}_o) \\ n_{\theta o} &= \frac{1}{1-\nu^2}(\bar{w}_o + \nu\bar{u}_o') \end{aligned} \qquad (A2.1)$$

When these expressions are used with the equilibrium equations (2.7) the differential equation governing the initial elastic response of the shell may be written

$$\bar{w}_o'''' + 12(1-\nu^2)\bar{w}_o = 12(1-\nu^2)(p-\nu n_a) \qquad (A2.2)$$

The solution of this equation is

$$\begin{aligned} \bar{w}_o = p-\nu n_a &+ e^{-\alpha_1\bar{x}}(A_1\cos\alpha_1\bar{x}+B_1\sin\alpha_1\bar{x}) \\ &+ e^{\alpha_1\bar{x}}(C_1\cos\alpha_1\bar{x}+D_1\sin\alpha_1\bar{x}) \end{aligned} \qquad (A2.3)$$

where A_1, B_1, C_1, D_1 are constants and $\alpha_1^4 = 3(1-\nu^2)$. The associated resultants, from equations (A2.1) and (A2.3), are

$$\begin{aligned} m_{xo} &= \frac{\alpha_1^2}{6(1-\nu^2)}\Big[e^{-\alpha_1\bar{x}}(A_1\sin\alpha_1\bar{x}-B_1\cos\alpha_1\bar{x}) \\ &\qquad - e^{\alpha_1\bar{x}}(C_1\sin\alpha_1\bar{x}-D_1\cos\alpha_1\bar{x})\Big] \\ n_{\theta o} &= p + e^{-\alpha_1\bar{x}}(A_1\cos\alpha_1\bar{x}+B_1\sin\alpha_1\bar{x}) \\ &\qquad + e^{\alpha_1\bar{x}}(C_1\cos\alpha_1\bar{x}+D_1\sin\alpha_1\bar{x}) \end{aligned} \qquad (A2.4)$$

The purely viscous solution is obtained from the above by setting $\upsilon=\frac{1}{2}$, and replacing displacements by velocities. Thus

$$\dot{\bar{w}}_\infty = p-\frac{1}{2}n_a + e^{-\alpha_2\bar{\bar{x}}}(A_2\cos\alpha_2\bar{\bar{x}}+B_2\sin\alpha_2\bar{\bar{x}}) + e^{\alpha_2\bar{\bar{x}}}(C_2\cos\alpha_2\bar{\bar{x}}+D_2\sin\alpha_2\bar{\bar{x}})$$

$$m_{x\infty} = \frac{1}{3}\left[e^{-\alpha_2\bar{\bar{x}}}(A_2\sin\alpha_2\bar{\bar{x}}-B_2\cos\alpha_2\bar{\bar{x}}) - e^{\alpha_2\bar{\bar{x}}}(C_2\sin\alpha_2\bar{\bar{x}}-D_2\cos\alpha_2\bar{\bar{x}})\right] \qquad (A2.5)$$

$$n_{e\infty} = p + e^{-\alpha_2\bar{\bar{x}}}(A_2\cos\alpha_2\bar{\bar{x}}+B_2\sin\alpha_2\bar{\bar{x}}) + e^{\alpha_2\bar{\bar{x}}}(C_2\cos\alpha_2\bar{\bar{x}}+D_2\sin\alpha_2\bar{\bar{x}})$$

where A_2, B_2, C_2, D_2 are constants, and $\alpha_2^2 = \frac{3}{2}$.

2.2 Initial Velocity and Acceleration Functions

Equation (3.27), which controls the initial radial velocity, may be rewritten, using the expressions for the stress resultants (A2.4), as

$$\dot{\bar{w}}_o'''' + 4\alpha_1^4\dot{\bar{w}}_o = 12\left[(1-\upsilon^2)(p-\frac{1}{2}n_a) + \upsilon(1-2\upsilon)\left[e^{-\alpha_1\bar{\bar{x}}}(A_1\cos\alpha_1\bar{\bar{x}}+B_1\sin\alpha_1\bar{\bar{x}}) + e^{\alpha_1\bar{\bar{x}}}(C_1\cos\alpha_1\bar{\bar{x}}+D_1\sin\alpha_1\bar{\bar{x}})\right]\right] \qquad (A2.6)$$

To form the particular integral of this equation the function

$$I_1^{\pm} = \frac{1}{D_1^4+4\alpha_1^4}\, e^{(\pm 1+i)\alpha_1\bar{\bar{x}}}, \quad D_1 = \frac{\partial}{\partial\bar{\bar{x}}},$$

is considered. If the rules of the D-operator method (see, for example, [28]) are followed this function on integration

becomes

$$I_1^{\pm} = -\frac{\bar{x}e^{(\pm 1+i)\alpha_1\bar{x}}}{16\alpha_1^3}(\pm 1+i)$$

$$= \frac{\bar{x}e^{\pm\alpha_1\bar{x}}}{16\alpha_1^3}[\sin\alpha_1\bar{x} \mp \cos\alpha_1\bar{x} \mp i(\sin\alpha_1\bar{x} \pm \cos\alpha_1\bar{x})] \qquad (A2.7)$$

From the real and imaginary parts of equations (A2.7) the particular integral of (A2.6) is obtained, and the complete solution becomes

$$\bar{w}_o = p-\frac{1}{2}n_a + \frac{3\nu(1-2\nu)\bar{x}}{4\alpha_1^3}\Big[e^{-\alpha_1\bar{x}}[(A_1-B_1)\cos\alpha_1\bar{x}+(A_1+B_1)\sin\alpha_1\bar{x}] - e^{\alpha_1\bar{x}}[(C_1+D_1)\cos\alpha_1\bar{x}-(C_1-D_1)\sin\alpha_1\bar{x}]\Big] + e^{-\alpha_1\bar{x}}(A_3\cos\alpha_1\bar{x}+B_3\sin\alpha_1\bar{x}) + e^{\alpha_1\bar{x}}(C_3\cos\alpha_1\bar{x}+D_3\sin\alpha_1\bar{x}) \qquad (A2.8)$$

where A_3, B_3, C_3, D_3 are constants.

The initial radial acceleration is found in a similar manner. The stress resultant rates appearing in the governing equation (3.28) can be expressed as functions of $\bar{x}$ through equations (3.24),(3.26),(A2.4),(A2.8). The governing equation then becomes

$$\bar{w}_o'''' + 4\alpha_1^4\ddot{\bar{w}}_o = 12\nu(1-2\nu)\Big\{\frac{3\nu(1-2\nu)}{4\alpha_1^3}\Big[e^{-\alpha_1\bar{x}}[(A_1-B_1)\cos\alpha_1\bar{x}+ (A_1+B_1)\sin\alpha_1\bar{x}] - e^{\alpha_1\bar{x}}[(C_1+D_1)\cos\alpha_1\bar{x}- (C_1-D_1)\sin\alpha_1\bar{x}]\Big]\dot{\bar{x}} + e^{-\alpha_1\bar{x}}[(A_3-A_1)\cos\alpha_1\bar{x}+ (B_3-B_1)\sin\alpha_1\bar{x}] + e^{\alpha_1\bar{x}}[(C_3-C_1)\cos\alpha_1\bar{x}+ (D_3-D_1)\sin\alpha_1\bar{x}]\Big\} \qquad (A2.9)$$

To solve this equation the function

$$I_2^{\pm} = \frac{1}{D_1^4+4\alpha_1^4}\left[\bar{x}e^{(\pm 1+i)\alpha_1\bar{x}}\right]$$

is required. By use of standard integration procedures this function may be written

$$I_2^{\pm} = \frac{e^{\pm\alpha_1\bar{x}}}{32\alpha_1^3}\left[\left(\frac{3\bar{x}}{\alpha_1}\pm\bar{x}^2\right)\cos\alpha_1\bar{x}+\bar{x}^2\sin\alpha_1\bar{x}+i\left[\left(\frac{3\bar{x}}{\alpha_1}+\bar{x}^2\right)\sin\alpha_1\bar{x}-\bar{x}^2\cos\alpha_1\bar{x}\right]\right] \tag{A2.10}$$

From the real and imaginary parts of the expressions (A2.7) and (A2.10) the particular integral of equation (A2.9) can be constructed, and the entire solution written

$$\begin{aligned}\bar{w}_o = {} & 12\nu(1-2\nu)\left\{\frac{3\nu(1-2\nu)}{128\alpha_1^6}\times\right.\\
& \left[e^{-\alpha_1\bar{x}}\left[\left((A_1-B_1)\frac{3\bar{x}}{\alpha_1}-2B_1\bar{x}^2\right)\cos\alpha_1\bar{x}+\left((A_1+B_1)\frac{3\bar{x}}{\alpha_1}+2A_1\bar{x}^2\right)\sin\alpha_1\bar{x}\right]+\right.\\
& e^{\alpha_1\bar{x}}\left[\left((C_1+D_1)\frac{3\bar{x}}{\alpha_1}-2D_1\bar{x}^2\right)\cos\alpha_1\bar{x}+\left((D_1-C_1)\frac{3\bar{x}}{\alpha_1}+2C_1\bar{x}^2\right)\sin\alpha_1\bar{x}\right]+\\
& \frac{\bar{x}}{16\alpha_1^3}\left[e^{-\alpha_1\bar{x}}\left[(A_3-B_3+B_1-A_1)\cos\alpha_1\bar{x}+(A_3+B_3-A_1-B_1)\sin\alpha_1\bar{x}\right]\right.\\
& \left.\left.-e^{\alpha_1\bar{x}}\left[(C_3+D_3-C_1-D_1)\cos\alpha_1\bar{x}+(D_3-C_3+C_1-D_1)\sin\alpha_1\bar{x}\right]\right]\right\}\\
& +e^{-\alpha_1\bar{x}}(A_4\cos\alpha_1\bar{x}+B_4\sin\alpha_1\bar{x})+e^{\alpha_1\bar{x}}(C_4\cos\alpha_1\bar{x}+D_4\sin\alpha_1\bar{x})\end{aligned} \tag{A2.11}$$

where A_4, B_4, C_4, D_4 are further integration constants.

2.3 Determination of Series Constants

Before evaluating the integrals of equations (3.23) the behaviour of the orthogonal functions X_1-(3.17)-in the range $0\leq x\leq \bar{l}$ is considered.

The function

$$f(\beta) = \frac{\cos\beta\bar{I} - \cosh\beta\bar{I}}{\sinh\beta\bar{I} - \sin\beta\bar{I}},$$

may be rewritten in several forms when the characteristic equation (3.16) is employed. Thus,

$$f(\beta) = \tan\frac{\beta\bar{I}}{2} = -\tanh\frac{\beta\bar{I}}{2}, \quad (2n-1)\pi < \beta\bar{I} < 2n\pi \qquad \text{(A2.12)}$$

$$= -\cot\frac{\beta\bar{I}}{2} = -\coth\frac{\beta\bar{I}}{2}, \quad 2(n-1)\pi < \beta\bar{I} < (2n-1)\pi \qquad \text{(A2.13)}$$

$$n=1,2,3,\ldots$$

With $f(\beta)$ as given by equations (A2.12) the function

$$X(\bar{x}) = \cosh\beta\bar{x} - \cos\beta\bar{x} + f(\beta)(\sinh\beta\bar{x} - \sin\beta\bar{x})$$

at $\bar{x}=\bar{I}-b$ may be written,

$$X(\bar{I}-b) = \cosh\beta(\bar{I}-b) - \tanh\frac{\beta\bar{I}}{2}\sinh\beta(\bar{I}-b) - \cos\beta(\bar{I}-b) - \tan\frac{\beta\bar{I}}{2}\sin\beta(\bar{I}-b)$$

$$= \frac{\cosh\beta(\frac{\bar{I}}{2}-b)}{\cosh\beta\frac{\bar{I}}{2}} - \frac{\cos\beta(\frac{\bar{I}}{2}-b)}{\cos\beta\frac{\bar{I}}{2}}$$

$$= \cosh\beta b - \tanh\beta\frac{\bar{I}}{2}\sinh\beta b - \cos\beta b - \tan\beta\frac{\bar{I}}{2}\sin\beta b$$

$$= X(b), \qquad (2n-1)\pi < \beta\bar{I} < 2n\pi \qquad \text{(A2.14)}$$

In a similar manner it can be shown that when $f(\beta)$ is given by equations (A2.13),

$$X(\bar{I}-b) = -X(b), \qquad 2(n-1)\pi < \beta\bar{I} < (2n-1)\pi \qquad \text{(A2.15)}$$

The roots β_i of equation (3.16) lie within the ranges associated with equations (A2.14) when $i=1,3,5,\ldots$, and within those associated with (A2.15) when $i=2,4,6,\ldots$ Thus, for $0 \leq \bar{x} \leq \bar{I}$ the orthogonal functions X_i are symmetric about the line $\bar{x}=\bar{I}/2$ when i is odd, and are symmetric through the point $\bar{x}=\bar{I}/2$ when i is even.

A cylindrical shell with fixed ends subject to uniform radial and axial loading has symmetry about the centre

line $\bar{x}=\bar{I}/2$. All displacement functions, therefore, must have this symmetry, and the integrals over the range 0-$\bar{I}$ of their products with the functions X_i in equations (3.23) will be zero when i is even i.e. when X_i has the property (A2.15). Hence,

$$S_{1i} = S_{2i} = 0, \qquad i = 2,4,6,\ldots$$

ThThe integral $\int_0^{\bar{I}} X_i^2 d\bar{x}$, which appears in the denominator in equations (3.23) is evaluated on pages 335-6 of reference[26]. It may be written,

$$\int_0^{\bar{I}} X_i^2 d\bar{x} = \frac{\bar{I}}{4\beta^4}(X_i''^2)_{\bar{x}=0} = \bar{I}$$

With this value and equations (A2.5),(A2.8),(A2.11), the integrals (3.23) become, for odd i,

$$\begin{aligned}
S_{1i}+S_{2i} = \frac{1}{\bar{I}}\int_0^{\bar{I}}\Bigg\{ & \frac{1}{2}(1\pm f(\beta_i))\left[\frac{3\nu(1-2\nu)}{4\alpha_1^3}\bar{x}\right. \times \\
& \Big[e^{(\pm\beta_i-\alpha_1)\bar{x}}\left[(A_1-B_1)\cos\alpha_1\bar{x}+(A_1+B_1)\sin\alpha_1\bar{x}\right] - \\
& e^{(\pm\beta_i+\alpha_1)\bar{x}}\left[(C_1+D_1)\cos\alpha_1\bar{x}-(C_1-D_1)\sin\alpha_1\bar{x}\right] + \\
& e^{(\pm\beta_i-\alpha_1)\bar{x}}(A_3\cos\alpha_1\bar{x}+B_3\sin\alpha_1\bar{x}) + \\
& \qquad e^{(\pm\beta_i+\alpha_1)\bar{x}}(C_3\cos\alpha_1\bar{x}+D_3\sin\alpha_1\bar{x}) - \\
& e^{(\pm\beta_i-\alpha_2)\bar{x}}(A_2\cos\alpha_2\bar{x}+B_2\sin\alpha_2\bar{x}) - \\
& \qquad e^{(\pm\beta_i+\alpha_2)\bar{x}}\left.(C_2\cos\alpha_2\bar{x}+D_2\sin\alpha_2\bar{x})\Big] - \right. \\
& \frac{1}{f(\beta_i)}\left[\frac{3\nu(1-2\nu)}{4\alpha_1^3}\bar{x}\right. \times
\end{aligned}$$

$$\left[e^{-\alpha_1\bar{x}}\left[(A_1-B_1)\cos\alpha_1\bar{x}\sin^{\cos}\beta_i\bar{x}+(A_1+B_1)\sin\alpha_1\bar{x}\sin^{\cos}\beta_i\bar{x}\right]\right.$$

$$-\ e^{\alpha_1\bar{x}}\left[(C_1+D_1)\cos\alpha_1\bar{x}\sin^{\cos}\beta_i\bar{x}-(C_1-D_1)\sin\alpha_1\bar{x}\sin^{\cos}\beta_i\bar{x}\right]\Big]$$

$$+\ e^{-\alpha_1\bar{x}}(A_3\cos\alpha_1\bar{x}\sin^{\cos}\beta_i\bar{x}+B_3\sin\alpha_1\bar{x}\sin^{\cos}\beta_i\bar{x})\ +$$

$$e^{\alpha_1\bar{x}}(C_3\cos\alpha_1\bar{x}\sin^{\cos}\beta_i\bar{x}+D_3\sin\alpha_1\bar{x}\sin^{\cos}\beta_i\bar{x})$$

$$-\ e^{-\alpha_2\bar{x}}(A_2\cos\alpha_2\bar{x}\sin^{\cos}\beta_i\bar{x}+B_2\sin\alpha_2\bar{x}\sin^{\cos}\beta_i\bar{x})\ -$$

$$\left.e^{\alpha_2\bar{x}}(C_2\cos\alpha_2\bar{x}\sin^{\cos}\beta_i\bar{x}+D_2\sin\alpha_2\bar{x}\sin^{\cos}\beta_i\bar{x})\right]\Big\}\,d\bar{x}$$

(A2.16)

$$\gamma_{1i}S_{11}+\gamma_{2i}S_{21}=-\frac{1}{I}\int_0^I\Big\{\frac{1}{2}(1\pm f(\beta_i))\Big[12\nu(1-2\nu)\Big[\frac{3\nu(1-2\nu)}{128\alpha_1^6}\times$$

$$\Big[e^{(\pm\beta_i-\alpha_1)\bar{x}}\Big[\Big[(A_1-B_1)\frac{3\bar{x}}{\alpha_1}-2B_1\bar{x}^2\Big]\cos\alpha_1\bar{x}+$$

$$\Big[(A_1+B_1)\frac{3\bar{x}}{\alpha_1}+2A_1\bar{x}^2\Big]\sin\alpha_1\bar{x}\ -$$

$$e^{(\pm\beta_i+\alpha_1)\bar{x}}\Big[\Big[(C_1+D_1)\frac{3\bar{x}}{\alpha_1}-2D_1\bar{x}^2\Big]\cos\alpha_1\bar{x}+$$

$$\Big[(D_1-C_1)\frac{3\bar{x}}{\alpha_1}+2C_1\bar{x}^2\Big]\sin\alpha_1\bar{x}\Big]\Big]+$$

$$\frac{\bar{x}}{16\alpha_1^3}\Big[e^{(\pm\beta_i-\alpha_1)\bar{x}}\Big[(A_3-B_3+B_1-A_1)\cos\alpha_1\bar{x}+$$

$$(A_3+B_3-A_1-B_1)\sin\alpha_1\bar{x}\Big]-$$

$$e^{(\pm\beta_i+\alpha_1)\bar{x}}\Big[(C_3+D_3-D_1-C_1)\cos\alpha_1\bar{x}+$$

$$(D_3-C_3+C_1-D_1)\sin\alpha_1\bar{x}\Big]\Big]+$$

$$e^{(\pm\beta_i-\alpha_1)\bar{x}}(A_3\cos\alpha_1\bar{x}+B_3\sin\alpha_1\bar{x})\ +$$

$$e^{(\pm\beta_i+\alpha_1)\bar{x}}(C_3\cos\alpha_1\bar{x}+D_3\sin\alpha_1\bar{x})$$

$$-f(\beta_i)\Bigg[12\nu(1-2\nu)\Bigg[\frac{3\nu(1-2\nu)}{128\alpha_1^6}\times$$

$$\Bigg[e^{-\alpha_1\bar{x}}\Bigg[\Bigg[(A_1-B_1)\frac{3\bar{x}}{\alpha_1}-2B_1\bar{x}^2\Bigg]\cos\alpha_1\bar{x}\sin\beta_i\bar{x}+$$

$$\Bigg[(A_1+B_1)\frac{3\bar{x}}{\alpha_1}+2A_1\bar{x}^2\Bigg]\sin\alpha_1\bar{x}\sin\beta_i\bar{x}\Bigg]-$$

$$e^{\alpha_1\bar{x}}\Bigg[\Bigg[(C_1+D_1)\frac{3\bar{x}}{\alpha_1}-2D_1\bar{x}^2\Bigg]\cos\alpha_1\bar{x}\sin\beta_i\bar{x}+$$

$$\Bigg[(D_1-C_1)\frac{3\bar{x}}{\alpha_1}+2C_1\bar{x}^2\Bigg]\sin\alpha_1\bar{x}\sin\beta_i\bar{x}\Bigg]\Bigg]+$$

$$\frac{\bar{x}}{16\alpha_1^3}\Bigg[e^{-\alpha_1\bar{x}}\Bigg[(A_3-B_3+B_1-A_1)\cos\alpha_1\bar{x}\sin\beta_i\bar{x}+$$

$$(A_3+B_3-A_1-B_1)\sin\alpha_1\bar{x}\sin\beta_i\bar{x}\Bigg]-$$

$$e^{\alpha_1\bar{x}}\Bigg[(C_3+D_3-D_1-C_1)\cos\alpha_1\bar{x}\sin\beta_i\bar{x}+$$

$$(D_3-C_3+C_1-D_1)\sin\alpha_1\bar{x}\sin\beta_i\bar{x}\Bigg]\Bigg]+$$

$$e^{-\alpha_1\bar{x}}(A_4\cos\alpha_1\bar{x}\sin\beta_i\bar{x}+B_4\sin\alpha_1\bar{x}\sin\beta_i\bar{x})+$$

$$e^{\alpha_1\bar{x}}(C_4\cos\alpha_1\bar{x}\sin\beta_i\bar{x}+D_4\sin\alpha_1\bar{x}\sin\beta_i\bar{x})\Bigg]\Bigg\}\,d\bar{x}$$

(A2.17)

The integrands of equations (A2.16),(A2.17) are made up of two sets of terms, one formed from all the upper signs and functions, and the other from all the lower signs and functions. The integrations can be performed by standard analytical methods, and the constants S_{1i}, S_{2i} determined.

A computer programme was written to evaluate the arbitrary constants in the displacement, velocity and

acceleration functions-equations (A2.3),(A2.5),(A2.8), (A2.11)-and to obtain S_{1i}, S_{2i} from the integrated forms of equations (A2.16),(A2.17). These latter constants were checked by comparing, numerically, the radial velocity and acceleration functions obtained from the series (3.22) at $\bar{t}^*=0$, with the prescribed functions (A2.8),(A2.11). When the first forty non-zero terms of the series were summed good agreement was obtained.

When the programme was first written the integrals (A2.16),(A2.17) were evaluated between the limits 0 and $\bar{I}$. This calculation was found to involve substantial error because, for a reasonably long shell ($\bar{I}=15$ was chosen) the constants $C_{1,2,3,4}, D_{1,2,3,4}$, which determine the influence of the positive exponential terms in equations (A2.3),(A2.5),(A2.8),(A2.11), are of the same order of magnitude as the rounding errors incurred in their computation. Consequently, the dependent variables and their integrals could not be calculated accurately in the range $\bar{I}/2<\bar{x}\leq\bar{I}$. This computing difficulty was easily overcome for the problem considered, because the symmetry about $\bar{x}=\bar{I}/2$ made calculation of the variables beyond this point unnecessary, and allowed the integrals to be obtained by evaluating between the limits 0 and $\bar{I}/2$ and multiplying by two.

2.4 Determination of Stress Resultants

With the radial velocity $\dot{\bar{w}}(\bar{x},\bar{t}^*)$ known, the stress resultants $m_x(\bar{x},\bar{t}^*), n_\theta(\bar{x},\bar{t}^*)$ can be obtained from the differential equations (3.4). For example, the equation controlling $m_x(\bar{x},\bar{t}^*)$ is

$$(1-\nu^2)\ddot{m}_x + (2-\nu)\dot{m}_x + \tfrac{3}{4}m_x = \tfrac{1}{12}(\dot{\bar{w}}''+\dot{\bar{w}}'') \qquad \text{(A2.18)}$$

and its particular integral $P_1(\bar{x},\bar{t}^*)$ can be readily formed using equations (3.22) and (A2.5):

$$P_1 = m_{x\infty} + \sum_{i=1}^{\infty}\left[\frac{(1-\gamma_{1i})S_{1i}e^{-\gamma_{1i}\bar{t}^*}}{(1-\nu^2)\gamma_{1i}^2-(2-\nu)\gamma_{1i}+\frac{3}{4}} - \frac{(1-\gamma_{2i})S_{2i}e^{-\gamma_{2i}\bar{t}^*}}{(1-\nu^2)\gamma_{2i}^2-(2-\nu)\gamma_{2i}+\frac{3}{4}}\right]\frac{X_i''}{12} \qquad \text{(A2.19)}$$

The complete solution of equation (A2.18) then becomes

$$m_x(\bar{x},\bar{t}^*) = m_1(\bar{x})e^{-\gamma_{10}\bar{t}^*} + m_2(\bar{x})e^{-\gamma_{20}\bar{t}^*} + P_1(\bar{x},\bar{t}^*) \qquad \text{(A2.20)}$$

where m_1, m_2 are arbitrary functions to be found from initial conditions, and γ_{10}, γ_{20} are given by equation (3.21) with $\beta=0$, since, with this value of β, the complementary function of (A2.18) is the same as that of equation (3.19).

Immediately after loading

$$\begin{aligned} m_x(\bar{x},0) &= m_{xo} = m_1(\bar{x}) + m_2(\bar{x}) + P_1(\bar{x},0) \\ \dot{m}_x(\bar{x},0) &= \dot{m}_{xo} = -\gamma_{10}m_1(\bar{x}) - \gamma_{20}m_2(\bar{x}) + \dot{P}_1(\bar{x},0) \end{aligned} \qquad \text{(A2.21)}$$

where m_{xo} is given by the first of equations (A2.4), and $\dot{m}_{xo}$ can be obtained from equations (3.24) and (A2.8):

$$\dot{m}_{xo} = -\frac{(1-\nu+\nu^2)}{1-\nu^2} m_{xo} + \frac{1}{6(1-\nu^2)}\left\{\frac{3\nu(1-2\nu)}{4\alpha_1^3} \times \right.$$

$$\left[2\alpha_1\left[e^{-\alpha_1\bar{x}}(B_1\cos\alpha_1\bar{x}-A_1\sin\alpha_1\bar{x})+e^{\alpha_1\bar{x}}(C_1\sin\alpha_1\bar{x}-D_1\cos\alpha_1\bar{x})\right]\right.$$

$$\alpha_1^2\bar{x}\left[e^{-\alpha_1\bar{x}}\left[(A_1-B_1)\sin\alpha_1\bar{x}-(A_1+B_1)\cos\alpha_1\bar{x}\right] -\right.$$

$$\left.\left.e^{\alpha_1\bar{x}}\left[(D_1-C_1)\cos\alpha_1\bar{x}-(C_1+D_1)\sin\alpha_1\bar{x}\right]\right]\right] +$$

$$\left.\alpha_1^2\left[e^{-\alpha_1\bar{x}}(A_3\sin\alpha_1\bar{x}-B_3\cos\alpha_1\bar{x})+e^{\alpha_1\bar{x}}(D_3\cos\alpha_1\bar{x}-C_3\sin\alpha_1\bar{x})\right]\right\}$$

With equations (A2.19), (A2.20), (A2.21), $m_x(\bar{x},\bar{t}^*)$ can be written in the form

$$m_x(\bar{x},\bar{t}^*) = \frac{1}{\gamma_{20}-\gamma_{10}}\left[(\gamma_{20}m_{xo}+\dot{m}_{xo})e^{-\gamma_{10}\bar{t}^*}-(\gamma_{10}m_{xo}+\dot{m}_{xo})e^{-\gamma_{20}\bar{t}^*}\right]$$

$$+\left[\frac{\gamma_{10}e^{-\gamma_{20}\bar{t}^*}-\gamma_{20}e^{-\gamma_{10}\bar{t}^*}}{\gamma_{20}-\gamma_{10}}+1\right]m_{x\infty}+$$

$$\sum_{i=1}^{\infty}\left\{\left[\frac{(\gamma_{10}-\gamma_{1i})e^{-\gamma_{20}\bar{t}^*}-(\gamma_{20}-\gamma_{1i})e^{-\gamma_{10}\bar{t}^*}}{\gamma_{20}-\gamma_{10}} + e^{-\gamma_{1i}\bar{t}^*}\right]\right.$$

$$\times\frac{(1-\gamma_{1i})S_{1i}}{(1-\nu^2)\gamma_{1i}^2-(2-\nu)\gamma_{1i}+\frac{3}{4}} +$$

$$\left[\frac{(\gamma_{10}-\gamma_{2i})e^{-\gamma_{20}\bar{t}^*}-(\gamma_{20}-\gamma_{2i})e^{-\gamma_{10}\bar{t}^*}}{\gamma_{20}-\gamma_{10}} + e^{-\gamma_{2i}\bar{t}^*}\right]$$

$$\left.\times\frac{(1-\gamma_{2i})S_{2i}}{(1-\nu^2)\gamma_{2i}^2-(2-\nu)\gamma_{2i}+\frac{3}{4}}\right\}\frac{X''}{12}$$

In a similar manner the circumferential resultant $n_\theta(\bar{x},\bar{t}^*)$ can be obtained:

$$n_e(\bar{x}, \bar{t}^*) = \frac{1}{\gamma_{20}-\gamma_{10}}\left[(\gamma_{20}n_{e0}+\dot{n}_{e0})e^{-\gamma_{10}\bar{t}^*}-(\gamma_{10}n_{e0}+\dot{n}_{e0})e^{-\gamma_{20}\bar{t}^*}\right]$$

$$+\left[\frac{\gamma_{10}e^{-\gamma_{20}\bar{t}^*}-\gamma_{20}e^{-\gamma_{10}\bar{t}^*}}{\gamma_{20}-\gamma_{10}}+1\right]n_{e\infty}+$$

$$\sum_{i=1}^{\infty}\left\{\left[\frac{(\gamma_{10}-\gamma_{1i})e^{-\gamma_{20}\bar{t}^*}-(\gamma_{20}-\gamma_{1i})e^{-\gamma_{10}\bar{t}^*}}{\gamma_{20}-\gamma_{10}}+e^{-\gamma_{1i}\bar{t}^*}\right]\right.$$

$$\times\frac{S_{1i}}{1-\gamma_{1i}}+$$

$$\left[\frac{(\gamma_{10}-\gamma_{21})e^{-\gamma_{20}\bar{t}^*}-(\gamma_{20}-\gamma_{21})e^{-\gamma_{10}\bar{t}^*}}{\gamma_{20}-\gamma_{10}}+e^{-\gamma_{21}\bar{t}^*}\right]$$

$$\left.\times\frac{S_{2i}}{1-\gamma_{2i}}\right\}X_i$$

APPENDIX 3

NUMERICAL METHODS

The creep strain integrals (4.3) are evaluated by dividing the shell thickness into twenty-four equal intervals and applying Weddle's Rule (see, for example, [30]).

The cylindrical shell with fixed ends subject to uniform radial and axial loading has longitudinal symmetry about $\bar{x}=\bar{l}/2$, and it is therefore sufficient to integrate the equations over half of the shell length. If the range $0-\bar{l}/2$ is divided into equal intervals b, and the second space derivative represented by a three point central difference formula, at points $\bar{x}_i$, $\bar{w}''$ in equations (4.8) becomes

$$\bar{w}'' = \frac{1}{b^2}(\bar{w}_{i-1}-2\bar{w}_i+\bar{w}_{i+1})$$

and equation (4.5) can be written as

$$\bar{w}_{i-2}-4\bar{w}_{i-1}+6(1+2(1-\nu^2)b^4)\bar{w}_i-4\bar{w}_{i+1}+\bar{w}_{i+2} = k_i \qquad (A3.1)$$

where $k_i = 12(1-\nu^2)b^2\left[b^2(p-\nu n_a-\nu n^c_{xi}+n^c_{ei})+m^c_{xi-1}-2m^c_{xi}+m^c_{xi+1}\right]$

The boundary conditions at $\bar{x}_i=\bar{x}_o$ are

$$\bar{w}_o = 0$$

$$\bar{w}_d = -\frac{1}{3}\bar{w}_{-1}-\frac{1}{2}\bar{w}_o+\bar{w}_1-\frac{1}{6}\bar{w}_2 = 0 \qquad (A3.2)$$

where, as the less accurate forward differences must be used, the initial slope is represented by a four point

formula.

With the quantities k_i known, (A3.1) and (A3.2) form a set of linear algebraic equations which can be solved simultaneously for $\bar{w}_i$. The most suitable standard method for solving equations of this type on a high speed computer, is by the formation of a matrix equation which can be solved by expressing the coefficient matrix as the product of upper and lower triangular matrices (see, for example, (31)). However, the recurring pattern of coefficients in the difference equations (A3.1) makes it possible to construct a method of solution which requires less computer storage than the standard method, and is probably faster.

From the boundary equations (A3.2)

$$\begin{aligned} \bar{w}_0 &= 0 \\ \bar{w}_{-1} &= 3\bar{w}_1 - \tfrac{1}{2}\bar{w}_2 \end{aligned} \qquad \text{(A3.3)}$$

With these expressions, equation (A3.1) at x_1 becomes

$$3\left[3+4(1-\omega^2)b^4\right]\bar{w}_1 - \tfrac{9}{2}\bar{w}_2 + \bar{w}_3 = k_1$$

from which

$$\bar{w}_1 = N_{1,1} + N_{1,2}\bar{w}_2 + N_{1,3}\bar{w}_3 \qquad \text{(A3.4)}$$

where, with $D_1 = 3\left[3+4(1-\omega^2)b^4\right]$,

$$N_{1,1} = \frac{k_1}{D_1}; \quad N_{1,2} = \frac{9}{2D_1}; \quad N_{1,3} = -\frac{1}{D_1} \qquad \text{(A3.5)}$$

Substitution of (A3.4) and the first of (A3.3) into equation (A3.1) at x_2 yields

$$[6(1+2(1-\nu^2)b^4-4N_{1,2}]\bar{w}_2 - 4(1+N_{1,3})\bar{w}_3 + \bar{w}_4 = k_2+4N_{1,1}$$

from which

$$\bar{w}_2 = N_{2,1} + N_{2,2}\bar{w}_3 + N_{2,3}\bar{w}_4 \qquad (A3.6)$$

where, with $D_2 = 6(1+2(1-\nu^2)b^4)-4N_{1,2}$ (A3.7)

$$N_{2,1} = \frac{k_2+4N_{1,1}}{D_2};\ N_{2,2} = \frac{4(1+N_{1,3})}{D_2};\ N_{2,3} = -\frac{1}{D_2}$$

At x_3 and beyond, the boundary points $\bar{w}_0$ and $\bar{w}_1$ are absent from equations (A3.1); displacements are eliminated by substitutions of the form (A3.4) and (A3.6), and a regular pattern emerges from which the coefficients at any $\bar{x}_i$, $N_{i,1}, N_{i,2}, N_{i,3}$ can be calculated. Thus

$$\bar{w}_i = N_{i,1} + N_{i,2}\bar{w}_{i+1} + N_{i,3}\bar{w}_{i+2} \qquad (A3.8)$$

where, with $D_i = N_{i-2,2}N_{i-1,2}+N_{i-2,3}-4N_{i-1,2}$
$+6(1+2(1-\nu^2)b^4)$

$$N_{i,1} = \frac{1}{D_i}(-N_{i-2,2}N_{i-1,1}-N_{i-2,1}+4N_{i-1,1}+k_i) \qquad (A3.9)$$

$$N_{i,2} = \frac{1}{D_i}(-N_{i-1,3}N_{i-2,2}+4N_{i-1,3}+4)$$

$$N_{i,3} = \frac{-1}{D_i}$$

If $\bar{x}_v$ denotes the point $\bar{x}=\bar{l}/2$, from longitudinal symmetry,

$$\bar{w}_{v+1} = \bar{w}_{v-1};\quad \bar{w}_{v+2} = \bar{w}_{v-2}$$

Hence,

$$\bar{w}_{v-2} = N_{v-2,1} + N_{v-2,2}\bar{w}_{v-1} + N_{v-2,3}\bar{w}_{v}$$

$$\bar{w}_{v-1} = N_{v-1,1} + N_{v-1,2}\bar{w}_{v} + N_{v-1,3}\bar{w}_{v-1} \qquad \text{(A3.10)}$$

$$\bar{w}_{v} = N_{v,1} + N_{v,2}\bar{w}_{v-1} + N_{v,3}\bar{w}_{v-2}$$

These equations can be solved to yield

$$\bar{w}_v = \frac{N_{v,1}+\frac{N_{v,2}N_{v-1,1}}{1-N_{v-1,3}}+N_{v,3}\left(N_{v-2,1}+\frac{N_{v-2,2}N_{v-1,1}}{1-N_{v-1,3}}\right)}{1-N_{v,3}N_{v-2,3}-N_{v-1,2}\left(\frac{N_{v,2}+N_{v,3}N_{v-2,2}}{1-N_{v-1,3}}\right)}$$

The coefficients in this equation are known, determined through equations (A3.5),(A3.7) and (A3.9), and $\bar{w}_v$ can be calculated. $\bar{w}_{v-1}$ and $\bar{w}_{v-2}$ are then obtained from (A3.10), and the remaining $\bar{w}_i$ calculated successively from equations (A3.8),(A3.6) and (A3.4).

Since $\bar{w}$ and the other dependent variables change rapidly with $\bar{x}$ near the fixed end of the shell, while remote from the end they tend towards constant values, it is expedient to increase the integration interval b with $\bar{x}$. For computational convenience the interval was doubled at points $\bar{x}_c, \bar{x}_d$ in the range $0-\bar{l}/2$; typical values of c,d,v were 20,35,60, respectively. The finite difference representation of the differential equation is altered at points in the vicinity of an interval change (for a discussion of this see, for example, [30]), and, consequently, the coefficients $N_{i,j}$ at these points had to be individually calculated.

When iteration at any time interval is complete the stress resultants are calculated from

$$n_{\theta i} = \frac{1}{1-\nu^2}(\bar{w}_i + \nu \bar{u}_i') - n^c_{\theta i}$$

$$m_{xi} = \frac{1}{12b^2(1-\nu^2)}(\bar{w}_{i-1} - 2\bar{w}_i + \bar{w}_{i+1}) - m^c_{xi}$$

APPENDIX 4

4.1 Outline of Numerical Calculations

The finite difference representation of the differential equation (5.5), and the method of solving the finite difference equations are similar to those described in Appendix 3. At $\bar{x}_i$ the difference form of equation (5.5) is

$$\phi_{i-1}\dot{\bar{w}}_{i-2}-2(\phi_{i-1}+\phi_i)\dot{\bar{w}}_{i-1}+(\phi_{i-1}+(k_1 b^4+4)\phi_i+\phi_{i+1})\dot{\bar{w}}_i$$
$$-2(\phi_i+\phi_{i+1})\dot{\bar{w}}_{i+1}+\phi_{i+1}\dot{\bar{w}}_{i+2} = k_2 b^4$$

and the coefficients $N_{i,j}$ become

$$N_{i,1} = \frac{k_2 b^4-\phi_{i-1}(N_{i-2,2}N_{i-1,1}+N_{i-2,1})+2(\phi_{i-1}+\phi_i)N_{i-1,1}}{D_i}$$

$$N_{i,2} = \frac{-\phi_{i-1}N_{i-1,3}N_{i-2,2}+(\phi_{i-1}+\phi_i)N_{i-1,3}+2(\phi_i+\phi_{i+1})}{D_i}$$

$$N_{i,3} = -\frac{\phi_{i+1}}{D_i}$$

where $D_i = \phi_{i-1}(N_{i-2,2}N_{i-1,2}+N_{i-2,3})-2(\phi_{i-1}+\phi_i)N_{i-1,2}$
$$+\phi_{i-1}+(k_1 b^4+4)\phi_i+\phi_{i+1}$$

The coefficients $N_{i,j}$ are determined separately at the boundary and around points of interval change, and $\dot{\bar{w}}_i$ calculated as in Appendix 3.

With $\dot{\bar{w}}_i$ known, $\dot{\bar{u}}_i$ is obtained from the discreet

form of equation (5.4), and a further ϕ_i from (5.3) with the second derivative represented by a three point central difference formula. When the iteration process has converged the stress resultants are determined from equations (5.1) and the time derivatives of equations (2.8).

4.2 Calculation of Residue

Where the solutions eventually became unstable, the $\dot{\bar{w}}_i$ which made the sum of the squares of the residues a minimum was chosen as being closest to the true solution. The residue from the r^{th} cycle of the iteration is

$$R_i^r = k_2 b^4 - \phi_{i-1}^r \dot{\bar{w}}_{i-2}^r + 2(\phi_{i-1}^r + \phi_i^r)\dot{\bar{w}}_{i-1}^r - \left[\phi_{i-1}^r + (k_1 b^4 + 4)\phi_i^r + \phi_{i+1}^r\right]\dot{\bar{w}}_i^r + 2(\phi_i^r + \phi_{i+1}^r)\dot{\bar{w}}_{i+1}^r - \phi_{i+1}^r \dot{\bar{w}}_{i+2}^r$$

where the superscript r refers to quantities obtained from the r^{th} cycle. That $\dot{\bar{w}}_i^r$ was selected which gave

$$\sum_{i=0}^{n} (R_i^r)^2$$

its lowest value.

4.3 Calculation of $\psi(0)$ when m=0

For m=0 the radial velocity is (Appendix 2.1),

$$\dot{\bar{w}} = p - \tfrac{1}{2} n_a \quad {}_2 = \sqrt{\tfrac{3}{2}}\alpha_2 \bar{x}(A_2 \cos \alpha_2 \bar{x} + B_2 \sin \alpha_2 \bar{x}) + e^{\alpha_2 \bar{x}}(C_2 \cos \alpha_2 \bar{x} + D_2 \sin \alpha_2 \bar{x})$$

where $\alpha_2 = \sqrt{\tfrac{3}{2}}$. For a cylindrical shell of semi-infinite length, and with $\dot{\bar{w}}(0) = \dot{\bar{w}}'(0) = 0$, this equation becomes

$$\dot{\bar{w}} = (p - \tfrac{1}{2} n_a)\left[1 - e^{-\alpha_2 \bar{x}}(\cos \alpha_2 \bar{x} + \sin \alpha_2 \bar{x})\right] \qquad (A4.1)$$

Differentiating (A4.1) twice yields,

$$\dot{\bar{w}}'' = -2\alpha_2^2(p-\tfrac{1}{2}n_a)e^{-\alpha_2\bar{x}}(\sin\alpha_2\bar{x}-\cos\alpha_2\bar{x}) \qquad (A4.2)$$

and, from equation (5.4) with m=0,

$$\dot{\bar{u}}' = \tfrac{3}{4}n_a-\tfrac{1}{2}\dot{\bar{w}} \qquad (A4.3)$$

When m=0 equations (5.1) and (5.6) combine to give

$$\Psi = \tfrac{4}{3}(\dot{e}_x^2+\dot{e}_x\dot{e}_\theta+\dot{e}_\theta^2+\tfrac{1}{12}\dot{k}_x^2) \qquad (A4.4)$$

At $\bar{x}=0$, $\dot{\bar{w}}=0$, and from equations (2.8),(A4.2),(A4.3) and (A4.4)

$$\Psi(0) = \tfrac{4}{3}\left[\tfrac{9}{16}n_a^2+\tfrac{1}{12}\alpha_2^4(p-\tfrac{1}{2}n_a)^2\right]$$

Now $\alpha_2^4 = \frac{9}{4}$ and therefore,

$$\Psi(0) = n_a^2 - n_a p + p^2$$
$$= 1$$

since n_a and p are chosen to satisfy equation (2.24).

APPENDIX 5

ACCELERATED CREEP BEHAVIOUR OF SEVERAL POLYMERS

Each of the plastic tubes was given a suitable heat treatment to remove residual stresses, and tensile tests were carried out on specimens cut from the longitudinal direction.

a) Perspex (Polymethyl Methacrylate)

This is a fairly rigid, amorphous polymer, and it is used extensively for investigating the elastic behaviour of structures. To produce accelerated creep temperatures of around 100°C are required, and Fig. A5.1 shows the results of tensile tests in this temperature region at a stress of 1280lb/in^2. Below 99°C the creep strains were small, and the specimens fractured after about 5hr. Above this temperature the material became ductile, but also very unstable, tests under almost the same conditions producing greatly differing strains.

For plastic materials there are temperatures at which pronounced changes in molecular mobility take place often accompanied by considerable alteration of macroscopic properties. One of these temperatures for polymethyl methacrylate is usually found in the region of 100°C [44]. For the material tested such a transition point must occur about 99°C; above this temperature the material acquired the ductility necessary for short term creep tests, but

the accompanying instability made it quite unsuitable.

b) PVC (Polyvinylchloride)

At room temperature rigid PVC is a fairly tough polymer with a small degree of crystallinity. Its toughness diminishes rapidly with temperature, and at 60°C it exhibits substantial creep. Fig.A5.2 shows the deflection/time response at several stress levels. Although fracture occurs at about 3% strain the fairly large creep strain/elastic strain ratio made the material appear promising. However, when cylindrical shell specimens were tested failure occurred at about 1% circumferential strain through longitudinal cracking. As the tensile specimens were cut longitudinally, this suggested a severe anisotropy in the PVC tubing, and made the latter worthless as test material.

c) Nylon

Nylon is a very tough , though ductile, crystalline polymer. The results of two tests at 130°C-Fig. A5.3-were sufficient to reveal its basic creep characteristics and its inferiority to polypropylene as a test material. It has a very large initial elastic-plastic deformation, but thereafter it strain hardens considerably and exhibits little creep.

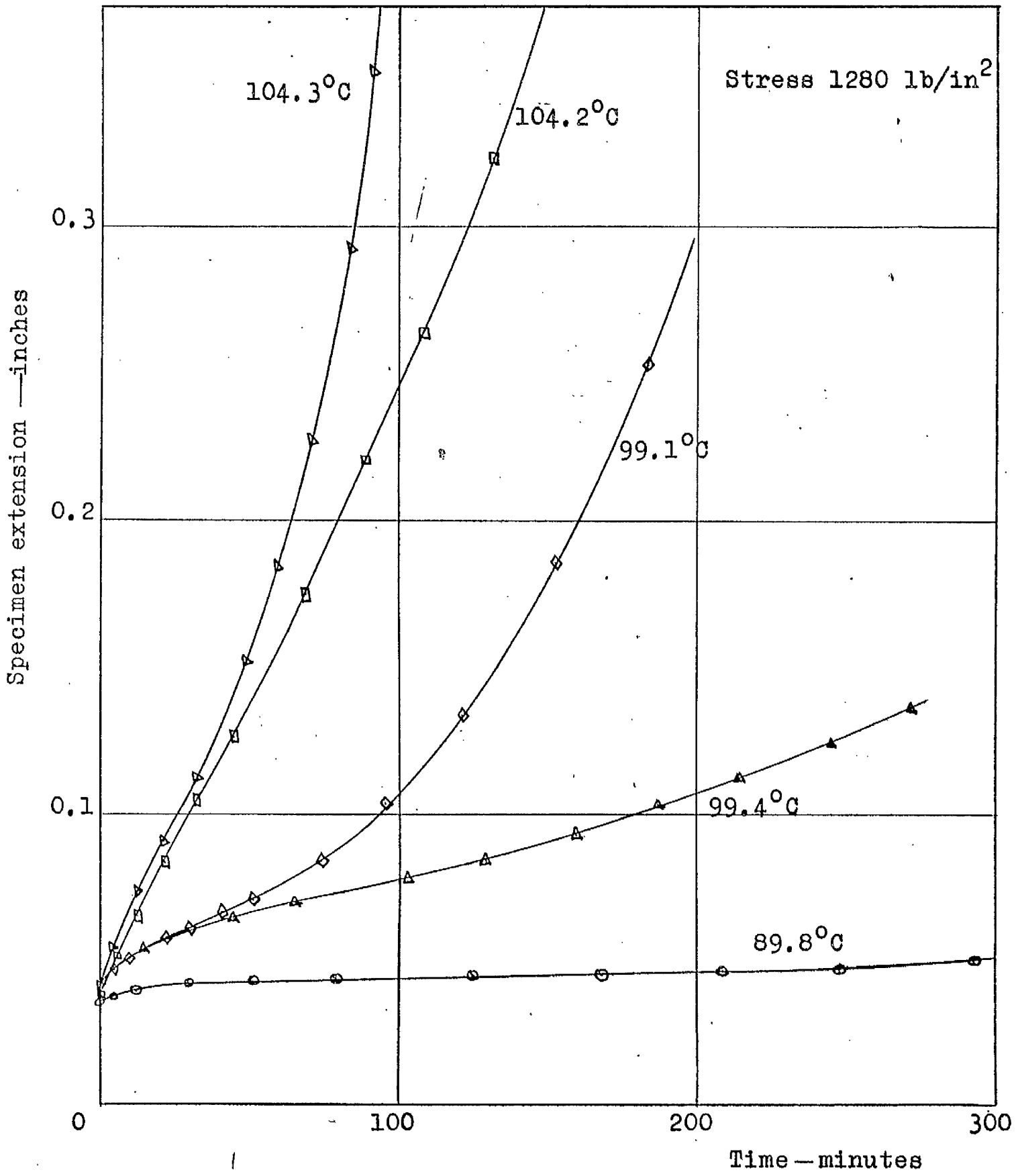

Fig. A5.1 Extension of perspex tensile specimens with time

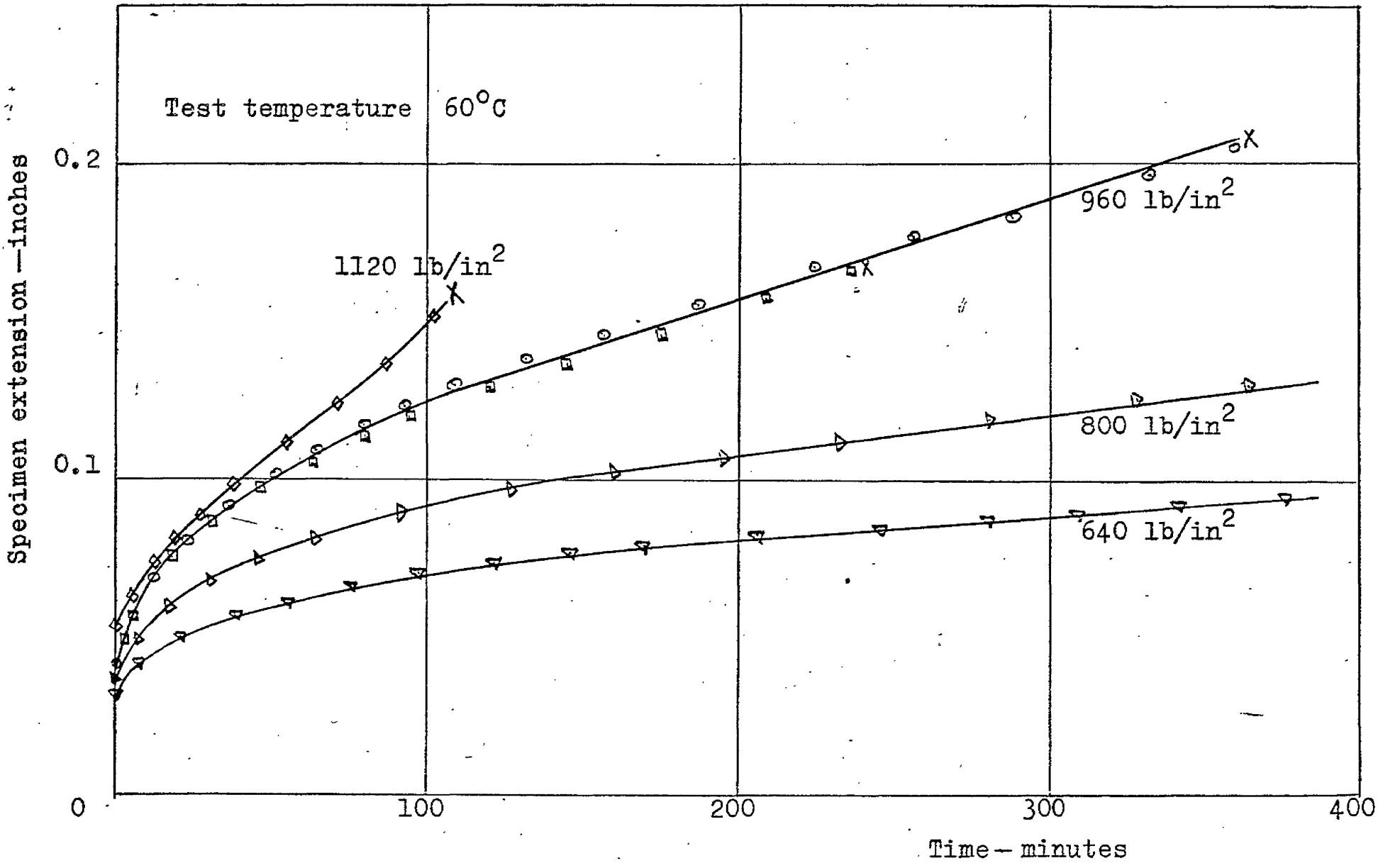

Fig. A5.2 Extension of PVC tensile specimens with time

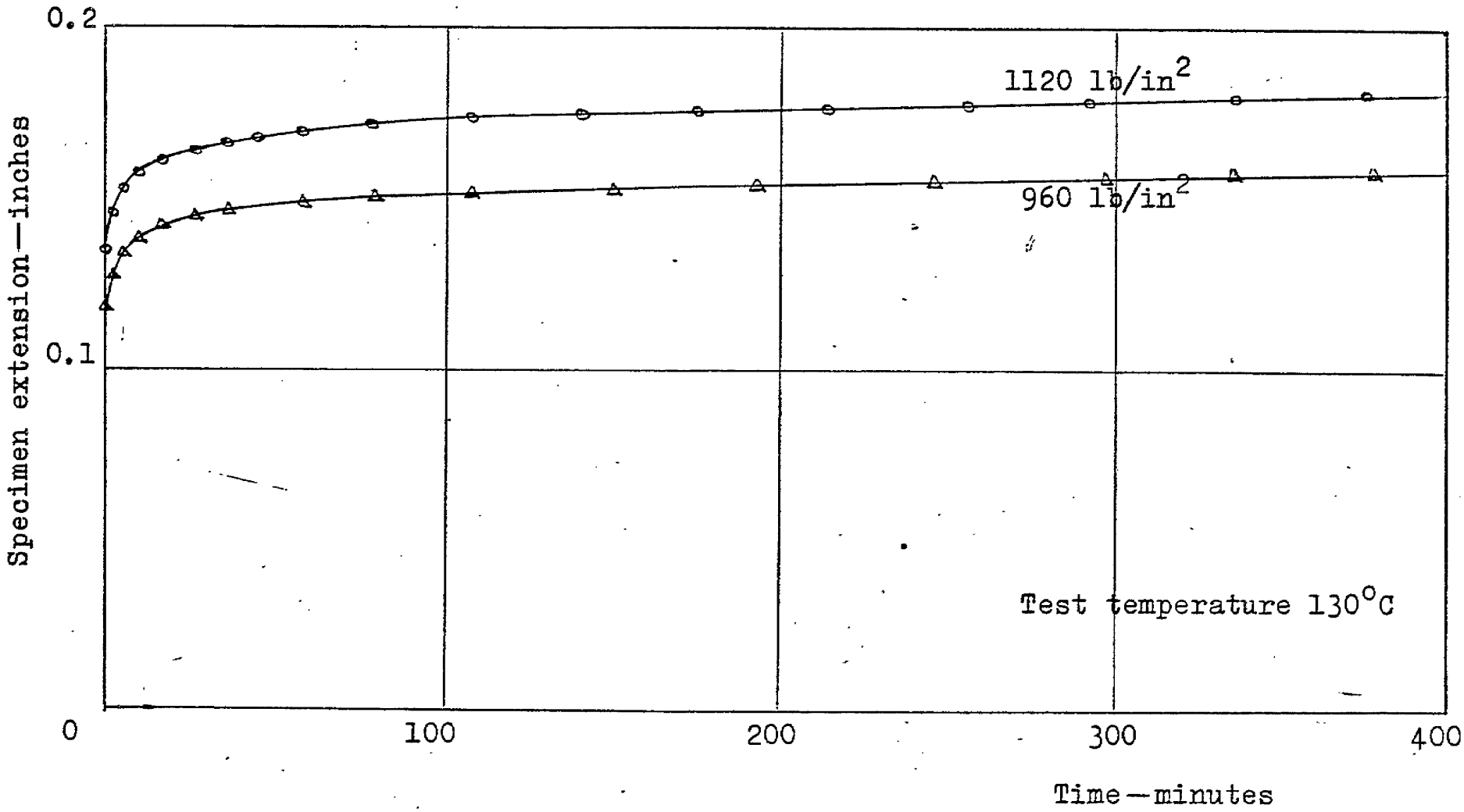

Fig. A5.3 Extension of nylon tensile specimens with time